University of Southampton
Faculty of Physical Sciences and Engineering
Optoelectronics Research Centre

DEVELOPMENT OF COMPONENTS AND FIBRES FOR THE POWER SCALING OF PULSED HOLMIUM-DOPED FIBRE SOURCES

By

NIKITA SIMAKOV

Thesis for the degree of Doctor of Philosophy

May 2017

ABSTRACT

FACULTY OF PHYSICAL SCIENCES AND ENGINEERING

OPTOELECTRONICS RESEARCH CENTRE

DOCTOR OF PHILOSOPHY

DEVELOPMENT OF COMPONENTS AND FIBRES FOR THE POWER SCALING OF PULSED HOLMIUM-DOPED FIBRE SOURCES

By Nikita Simakov

In this thesis the optimisation and peak power scaling of pulsed holmium-doped fibre lasers were investigated with the aim of demonstrating a fibre gain medium that is able to address the requirements of applications that currently rely on bulk crystalline Ho:YAG or Ho:YLF solutions.

Conventional fibre processing techniques such as cleaving, end-capping and component fabrication were improved upon using CO_2 laser processing. The resulting components and processes are also characterised under high power operating conditions and have enabled subsequent experimentation and demonstrations.

Holmium-doped silica fibres were fabricated and characterised with the aim of reducing impurity contaminations, improving composition and achieving efficient operation at 2.1 μm. These fibres were characterised passively using transmission spectroscopy and actively in a laser configuration. The most efficient of these compositions operated with a 77% slope efficiency in a core-pumped laser up to average powers of 5 W and was then processed into a double-clad geometry. The cladding-pumped fibre was operated at 70 W output power with a slope efficiency of 67% and represents one of the highest power and most efficient cladding-pumped holmium-doped fibres demonstrated to-date.

Small-signal amplifiers utilising both thulium-doped and holmium-doped silica fibres were demonstrated. These amplifiers offered a broad wavelength coverage spanning 490 nm at 15 dB gain from 1660 nm – 2150 nm. This remarkably broad wavelength coverage is attractive for a large number of disciplines looking to exploit this previously difficult-to-reach wavelength range.

In addition to these devices, the average power and peak power scaling of 2 μm fibre sources was investigated. A thulium-doped fibre laser operating at 1950 nm with >170 W of output power, a tuneable holmium-doped fibre laser producing >15 W over the wavelength span from 2040 nm –

2171 nm and a pulsed holmium-doped fibre amplifier with >100 kW peak power at 2090 nm are reported.

Finally we review the requirements for efficient scaling of mid-infrared optical parametric oscillators and analyse the non-linear effects that arise when attempting to scale the peak power in silica fibres in the 2 μm spectral region. We implement a range of strategies to reduce the onset of nonlinear effects and demonstrate a holmium-doped fibre amplifier with peak power levels exceeding 36 kW in a 5 ns pulse with a spectral width of <1 nm. This represents the highest spectral density achieved for nano-second pulse duration from pulsed holmium-doped fibre sources. This preliminary result provides an excellent platform for further peak power scaling and also in replacing conventional Q-switched Ho:YAG lasers.

Table of Contents

List of Tables

List of Figures

Declaration of Authorship

I, Nikita Simakov, declare that the thesis entitled “Development of components and fibres for the power scaling of pulsed holmium-doped fibre sources” and the work presented in it are both my own, and has been generated by me as the result of my own original research.

I confirm that:

1. This work was done wholly or mainly while in candidature for a research degree at this University;
2. Where any part of this thesis has previously been submitted for a degree or any other qualification at this University or any other institution, this has been clearly stated;
3. Where I have consulted the published work of others, this is always clearly attributed;
4. Where I have quoted from the work of others, the source is always given. With the exception of such quotations, this thesis is entirely my own work;
5. I have acknowledged all main sources of help;
6. Where the thesis is based on work done by myself jointly with others, I have made clear exactly what was done by others and what I have contributed myself;
7. Parts of this work have been published as: [see Appendix A]

Signed: .....

Date: .....

Acknowledgements

I would like to thank my family, my friends and my colleagues for their help, support and patience. To my mum and dad, thank you for always being there again. To my wife and our two wonderful sons, thank you – you have given my world meaning.

I would like to thank my supervisors, Professor Andrew Clarkson and Alexander Hemming for their support, guidance and feedback. I have been extremely fortunate to have been your student. You have always been eager to help, to provide constructive and useful criticism and to offer guidance and advice. You do this while rarely receiveing any praise or recognition, modestly and always in the background making sure that everything works and remains on track.

I would like to thank the leadership in the group and the division for ensuring that this project and I receive the necessary support. Dr. John Haub, Alasdair McInnes, Alan Towie and Dr. Jackie Craig, thank you for the opportunities that you have provided and for making this possible.

To the senior faculty members for their advice and assistance, Dr. Matthew Eckold, Dr. Pryanth Mehta, Dr. Lewis Carpenter, Dr. Peter Shardlow, Dr. Christophe Codemard, Dr. Pranabesh Barua, Dr. Masaki Tokurakawa, Dr. Shaif-ul Alam, Dr. Jacob MacKenzie, Dr. Stephen Beecher, Dr. Di Lin, Prof. David Richardson, Prof. Johan Nilsson and Prof. Jayanta Sahu.

In particular to Dr. Zhihong Li for the very rewarding conversations and collaboration. To the other members of the Advanced Solid State Sources group with whom it has been a pleasure to work especially Callum Smith and Antonin Billaud. To my colleagues in Adelaide, Dr. Keiron Boyd, Dr. Jae Daniel, Dr. Miftar Ganija, thank you for your support, your motivation, your ideas and your contribution to this and other projects. To Dr. Adrian Carter and Dr. Kevin Farley of Nufern for the quality of fibres that you have produced.

To Dr. Radan Slavik thank you for your friendship and your hospitality during my visits to Southampton. To Dr. Jackie Chan, Jared and Simon, thank you for welcoming me into your home.

To my family

Definitions and Abbreviations

AO	Acousto-optic
AOM	Acousto-optic modulator
AOTF	Acousto-optic tunable filter
AR	Anti-reflection
ASE	Amplified spontaneous emission
CLS	Cladding light stripper
CW	Continuous wave
dB	Decibels
dBm	Decibel with respect to mW
DC	Direct current
Dx	Dichroic
DFG	Difference frequency generation
EDFA	Erbium doped fibre amplifier
FBG	Fibre Bragg grating
FRIP	Fibre refractive index profile
FWHM	Full width at half maximum
HDF	Holmium-doped fibre
HDFA	Holmium-doped fibre amplifier
HOM	Higher order mode
HR	High reflector

IR	Infra-red
LMA	Large mode-area
MCVD	Modified chemical vapour deposition
MFD	Mode-field diameter
MI	Modulation instability
MM	Multi-mode
MM-FBG	Multi-mode fibre Bragg grating
MOPA	Master oscillator, power amplifier
MPE	Maximum permissible exposure
NA	Numerical aperture
NF	Noise figure
OC	Output coupler
OPG	Optical parametric generation
OPO	Optical parametric oscillator
ORC	Optoelectronics research centre
OSA	Optical spectrum analyser
PER	Polarisation extinction ratio
PM	Polarisation maintaining
PTR	Photo thermal refractive (glass)
PR	Partially reflective
QCW	Quasi-continous wave
RF	Radio Frequency

RIU	Refractive Index Units
SBS	Stimulated Brillouin scattering
SC	Supercontinuum
SM	Single-mode
SMF	Single-mode fibre
SRS	Stimulated Raman scattering
TDF	Thulium-doped fibre
TDFA	Thulium-doped fibre amplifier
TFB	Tapered fibre bundle
VBG	Volume Bragg grating
WDM	Wavelength division multiplexor
wt%	Weight percent
YAG	Yttrium aluminium garnet
YLF	Yttrium lithium fluoride
ZDW	Zero dispersion wavelength
ZGP	Zinc germanium phosphide

Chapter 1.

Introduction

1.1 Overview

There is a requirement for 2 – 2.1 µm sources in materials processing, laser surgery, generating mid-infrared sources via nonlinear conversion, remote sensing and LIDAR applications. These requirements are currently addressed by sources based on crystalline holmium materials.

Solid-state laser sources, including fibre lasers emitting at around 2 µm are typically based on direct generation using thulium and holmium rare earth ions. The wavelength range for the operation of thulium fibre lasers typically spans from 1.9 – 2.05 µm [1] and there have been numerous demonstrations of such sources in the 100 W – 1 kW average power levels [2–5]. Holmium based sources are typically required in order to operate at wavelengths longer than 2.07 µm with operation demonstrated to beyond 2.2 µm [6].

1.2 Medical applications

There are certain aspects which make the 2 µm wavelength range suitable for highly precise surgical applications [7]. The penetration depth of 0.1 – 1 mm at ~2 µm allows for efficient processing of tissue as well as subsequent cauterization.

Sources at 3 µm are able to exploit a much stronger water absorption feature; however radiation at this wavelength requires the use of a fragile soft glass delivery fibre. The 1.7 – 2.2 µm radiation from a thulium or holmium laser can be delivered over many metres with minimal attenuation in a conventional, robust all glass fused silica fibre [8].

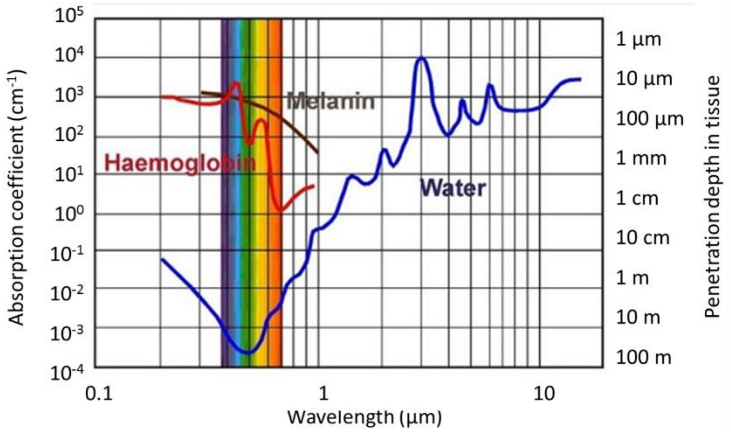

Figure 1.1: Absorption coefficient of water as a function of wavelength over the span from 200 nm to 10 µm [7]. Thulium and holmium lasers operating at 2 µm are able to address a strong absorption peak with <1 mm penetration depth, but still maintain all of the advantages of being compatible with a fused silica delivery fibre.

The typical parameters of laser sources used in surgery are 2 J pulses with a duration of 600 µs operating at a repetition rate of 50 Hz [9]. These are typically low brightness, flash-lamp pumped systems operating in a quasi-continuous wave (QCW) mode. The radiation from these sources is delivered into the patient via 200, 365 and 550 µm diameter fibres.

Both the peak and average powers of these systems are addressable by fibre lasers with the added benefit of significantly improved beam quality. The greatly improved beam quality would enable delivery via a much thinner fibre (i.e. 80 µm outer diameter), thereby allowing smaller bend radii and improved accessibility within the patient. The fibre laser geometry also allows for the flexibility of having a continuous (CW), quasi-continuous (QCW), Q-switched or mode-locked output.

1.3 Mid-infrared sources based on holmium lasers

Mid-infrared sources in the 3-5 µm spectral region are required for a range of applications including remote sensing, spectroscopy and free-space communications. Such mid-IR sources can be generated by quantum cascade lasers [10], directly from a solid-state laser [11] or by the frequency conversion of a pump laser [12,13]. The highest output powers in the mid-IR have been achieved by frequency conversion of pulsed 2 µm solid-state lasers using optical parametric oscillators (OPO) relying on Zinc Germanium Phosphide (ZGP) [12,14–16]. Consequently the development of a high power mid-IR source is reliant on the development of a suitable high power pulsed 2 µm pump

oscillator. Typically Ho:YAG laser systems are used to address this requirement and have been demonstrated at average power levels exceeding 100 W [14,15,17]. Further power scaling of Ho:YAG lasers is typically achieved by increasing the number of gain modules, the number of pump lasers and consequently the size, cost and complexity of the laser. The possibility of replacing multiple gain media with a single holmium-doped fibre (HDF) laser presents an attractive power scaling solution.

1.4 Remote sensing and LIDAR applications

A detailed summary of the requirements for fibre based LIDAR sources is presented in [18]. Depending on the range and velocity resolution requirements, the source can operate in a frequency modulated CW or an amplitude modulated/pulsed regime. The atmospheric transmission window in the 1.5 – 2.2 µm range is shown in Fig. 1.2. Pulsed sources emitting in the 2 µm range are able to operate with ~4 orders of magnitude larger peak powers in comparison to 1 µm lasers while still remaining eye-safe. Radiation in the 2.1 – 2.15 µm region is also less sensitive to scattering losses during atmospheric propagation [18]. While there is a transmission window at 2.04 µm that is addressable by thulium lasers, holmium sources are able to operate in a much wider transmission window between 2.07 – 2.2 µm.

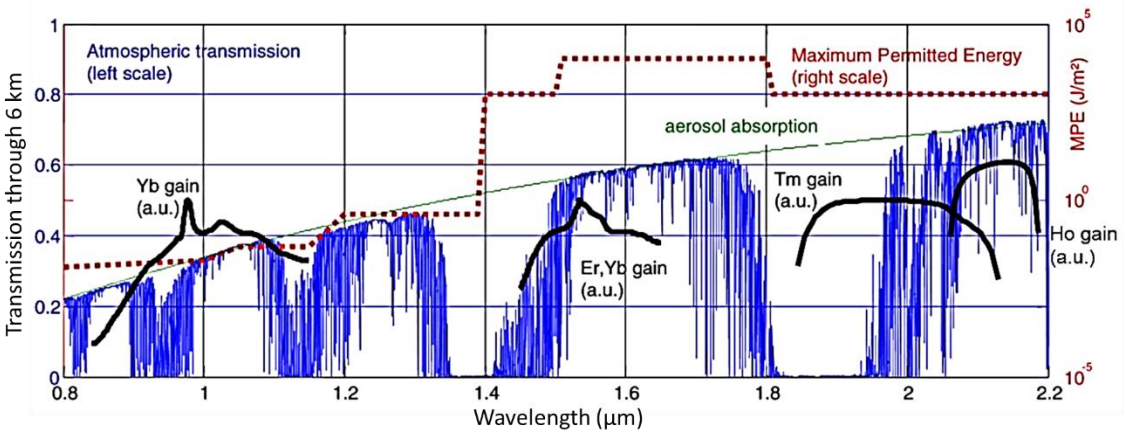

Figure 1.2: Atmospheric transmission and maximum permitted energy over a wavelength region spanning 0.8 – 2.2 µm for a 6 km propagation from ground level to 1000 m height and assuming an aerosol absorption strength of 0.18 km^{-1} at 1 µm [18,19].

As can be seen from Fig. 1.2, there are numerous absorption bands in this wavelength region. These features are due to C-H, O-H and C-O bonds. While preventing transmission in this window, it also

offers opportunities for remote sensing and measurement of these species. Thulium fibre sources are able to operate over the 1.65 – 2.05 µm wavelength region and address a number of resonances of varying strengths corresponding to a range of species.

1.5 Material processing applications

The application of 2 µm sources for material processing applications is an active area of research. Conventional 1 µm and 1.5 µm fibre laser sources are not able to address the intrinsic absorption bands in many commonly used polymers as shown in Fig. 1.3. In order to enable marking and welding, additives are incorporated into the material to increase the absorption in these wavelength regions. By operating in the 1.7 – 2.2 µm region it is possible to access strong, natural absorption features in plastics and polymers without the use of such additives [20]. Wavelength tuneable and wavelength agile sources can also enable material selective processing and provide fine depth control by tuning across absorption features. Thulium and holmium fibre lasers offer a broad operating range spanning the 1.7 – 2.2 µm region and thus are well positioned to target this application [21,22].

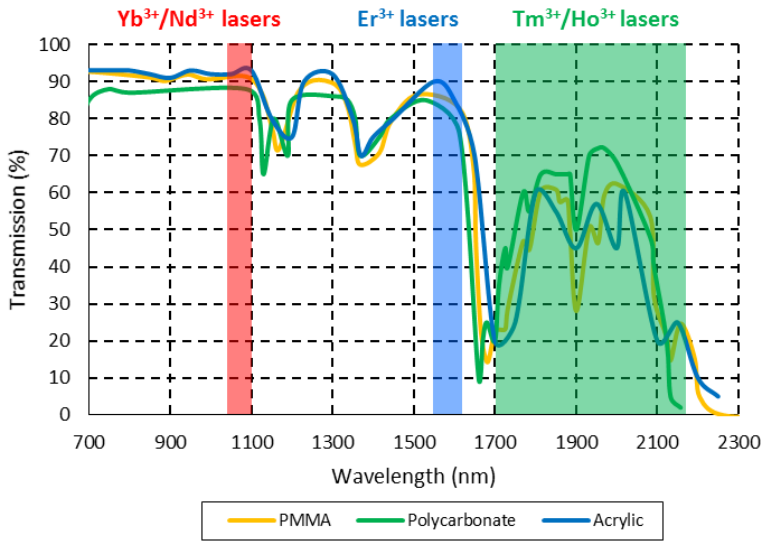

Figure 1.3: Transmission spectra though commonly used plastics and polymers with an illustration of typical operating bands for various rare-earth doped fibre lasers [23].

1.6 Summary of source requirements

Table 1.1 compares the requirements on the output powers, wavelengths and pulse formats for a range of typical applications, with the demonstrated outputs from holmium fibre lasers. With the many benefits that are offered by operating at a longer wavelength, these parameters are all readily attainable. The peak powers demanded by these sources are achievable by fibre lasers due to the geometric scaling of the core dimensions (and hence reduction of intensity) without impacting the beam quality. Furthermore the thresholds for nonlinear effects such as stimulated Raman scattering (SRS) and stimulated Brillouin scattering (SBS) are greatly increased by operating in the 2 µm spectral region.

Table 1.1: Comparison of source requirements for various applications

	Wavelength	Pulse energy/duration	Average power
Mid-IR conversion	2.09 µm	1-5 mJ in 30 ns	>100 W
Medical applications	1.7–2.15 µm	2 J in 600 µs CW operation	100 W
LIDAR – CW	2.06-2.15 µm	CW operation	10 W
LIDAR - pulsed	2.06-2.15 µm	1 mJ in 500 ns	10 W
Material processing	1.7-2.15 µm	1-10 ps CW operation	50 - 100 W >100 W

1.7 Current holmium-doped fibre sources demonstrated

Over the last 10 years there has been substantial effort in the development and power scaling of sources based on holmium-doped fibres. The pioneering work was undertaken by several groups who investigated core-pumped systems at lower power levels [24–26]. In 2011 the first resonantly, cladding-pumped HDF was demonstrated by Hemming et al [27] with 99 W of output power at a 65% slope efficiency. At the time this result was almost an order of magnitude improvement on previous investigations of holmium-doped fibres [28]. The advent of a power scalable, double-clad fibre enabled further results including a monolithic holmium-fibre laser with >400 W of average output power [29] and pulsed sources with >100 kW peak power [30]. More recent efforts on

composition optimisation have demonstrated HDFs that operate at 93% of the quantum limit with an 87% slope efficiency [31]. A variety of lower power sources have also been investigated with operation in the ultrafast regime [32], high gain amplifiers [33] and in a variety of tuneable configurations [22,34].

1.8 Outline of thesis

In this thesis the development of fibre processing and fibres to enable the power scaling of pulsed holmium fibre sources is explored. This includes measuring the basic spectroscopy of the holmium ion; undertaking an investigation into strategies for developing small-signal amplifiers; an analysis of approaches to reduce spectral broadening during high peak power operation; and finally the development of enabling components and techniques for further power scaling of pulsed holmium-doped fibres.

In Chapter 2 we introduce some of the fundamental concepts associated with fibre lasers, double-clad pumping geometries as well as covering the basic characteristics of the lasing transitions in thulium-doped and holmium-doped silica. In this chapter we also discuss the origins of noise and spurious emissions in pulsed and CW fibre lasers.

In Chapter 3 we introduce a variety of components and processes enabled by the modification of silica fibres with CO_2 laser sources. Laser cleaving is investigated, and an in-house solution is demonstrated that provides an order of magnitude improvement on conventional laser cleaved and mechanically cleaved surface topologies. Cladding surface modification is also investigated, and robust, easy-to-fabricate cladding light stripper devices are demonstrated. End-cap termination is demonstrated with excellent beam quality, strength and quality. These underlying components enable the robust construction of the high power amplifiers and oscillators that are required in the chapters that follow.

In Chapter 4 we present the basic characterisation techniques that enable rapid, low-cost iteration of holmium fibres and the subsequent testing of the composition. Hydroxyl concentration and efficiency measurements are discussed with an analysis of potential noise sources. A summary of the holmium-doped fibres developed in-house over the duration of this thesis is presented. A preform with the optimised composition was then fabricated into an all-glass, double-clad design that is compatible with pumping at 2 μm. The fibre was then operated in a free-space pumped

configuration and produced 70 W of output power at 2.1 µm with a 67% efficiency – this represents one of the most efficient cladding-pumped holmium-doped fibres currently demonstrated to date.

In Chapter 5 we investigate the wavelength coverage offered by thulium-doped and holmium-doped silica fibre lasers. Small signal amplifiers are demonstrated spanning a wavelength range from 1.65 – 2.15 µm. Various amplifier configurations including diode pumped, fibre laser pumped, single and double pass geometries are investigated. A cladding-pumped holmium laser is also presented with an operating range from 2.02 – 2.17 µm and power levels of >15 W. In the final section of this chapter, an acousto-optical tuneable filter (AOTF) is utilised to enable a wavelength agile holmium oscillator.

In Chapter 6 we focus on the pulsed operation of silica fibres in the 2.1 µm wavelength range for the application of pumping a mid-infrared parametric oscillator. A review is performed on the source requirements for the pump laser. These requirements are then considered in the context of the various nonlinear processes in silica fibres operating at high peak power in the 2 µm wavelength region. These are particularly different from the nonlinear limitations encountered in pulsed fibre sources operating at 1 µm. We propose methods to increase the nonlinear threshold and implement these in the construction of a pulsed amplifier system. These methods include spectral conditioning of the master oscillator, ultra-large mode-field diameter step-index fibre geometry, adiabatic tapering and aggressive inter-stage spectral filtering. This amplifier system is able to operate at peak power levels of 36 kW while having minimal spectral broadening. The sources in this chapter represent the highest peak power holmium-doped fibre sources demonstrated, and also achieve operating parameters that are able to equal that of conventional Q-switched Ho:YAG lasers.

In Chapter 7 we summarise the work presented throughout this thesis. A comprehensive review of the current state-of-the-art is provided illustrating the current status of holmium-doped fibre sources. We discuss future concepts for power scaling, as well as for operation in a range of pulsed regimes.

1.9 References

1. D. Y. Shen, J. K. Sahu, and W. A. Clarkson, "High-power widely tunable Tm:fibre lasers pumped by an Er,Yb co-doped fibre laser at 1.6 μm.," Opt. Express **14**, 6084–6090 (2006).

2. G. D. Goodno, L. D. Book, J. E. Rothenberg, M. E. Weber, and S. Benjamin Weiss, "Narrow linewidth power scaling and phase stabilization of 2-μm thulium fiber lasers," Opt. Eng. **50**, 111608 (2011).

3. P. Moulton, "High power Tm : silica fiber lasers : current status , prospects and challenges," Eur. Conf. Lasers Electro-Optics **Tech Focus**, TF2.3 (2011).

4. M. Meleshkevich, N. Platonov, D. Gapontsev, and A. Drozhzhin, "415W Single-Mode CW Thulium Fiber Laser in all-fiber format," CLEO/Europe Conf. Lasers Electro-Optics CP2_3 (2007).

5. A. Carter, A. Hemming, N. Simakov, A. Davidson, D. Stepanov, L. Corena, M. Hughes, N. Carmody, P. Davies, J. Haub, and A. Carter, "An Efficient, High Power, Monolithic, Single Mode Thulium Fibre Laser," in *Workshop on Specialty Optical Fibers and Their Applications* (2013), Vol. 34, p. T2.4.

6. S. O. Antipov, V. A. Kamynin, O. I. Medvedkov, A. V Marakulin, L. A. Minashina, A. S. Kurkov, and A. V Baranikov, "Holmium fibre laser emitting at 2.21 μm," Quantum Electron. **43**, 603–604 (2013).

7. K. Scholle, S. Lamrini, P. Koopmann, and P. Fuhrberg, "2 μm Laser Sources and Their Possible Applications," Front. Guid. Wave Opt. Optoelectron. 472–500 (2010).

8. T. Izawa, N. Shibata, and A. Takeda, "Optical attenuation in pure and doped fused silica in the IR wavelength region," Appl. Phys. Lett. **31**, 33 (1977).

9. Versapulse, "VersaPulse PowerSuite Powerful Surgical Solutions," (2012).

10. Daylight, "Aries High-power Lasers," www.daylightsolutions.com (2012).

11. J. J. Adams, C. Bibeau, R. H. Page, D. M. Krol, L. H. Furu, and S. A. Payne, "4.0–4.5-μm lasing of Fe:ZnSe below 180 K , a new mid-infrared laser material," Opt. Lett. **24**, 1720–1722

(1999).

12. P. A. Budni, L. A. Pomeranz, M. L. Lemons, C. A. Miller, J. R. Mosto, and E. P. Chicklis, "Efficient mid-infrared laser using 1.9-µm-pumped Ho:YAG and $ZnGeP_2$ optical parametric oscillators," J. Opt. Soc. Am. B **17**, 723–728 (2000).

13. E. Cheung, S. Palese, H. Injeyan, C. Hoefer, R. Hilyard, H. Komine, J. Gish, and W. Bosenberg, "High power optical parametric oscillator source," in *IEEE Aerospace Conference. Proceedings* (IEEE, 2000), Vol. 3, pp. 55–59.

14. E. Lippert, H. Fonnum, G. Arisholm, and K. Stenersen, "A 22-watt mid-infrared optical parametric oscillator with V-shaped 3-mirror ring resonator," Opt. Express **18**, 26475–26483 (2010).

15. A. Hemming, J. Richards, A. Davidson, N. Carmody, S. Bennetts, N. Simakov, and J. Haub, "99 W mid-IR operation of a ZGP OPO at 25% duty cycle," Opt. Express **21**, 10062 (2013).

16. I. Elder, "Thulium fibre laser pumped mid-IR source," Proc. SPIE **7325**, 73250I (2009).

17. Y.-L. J. and Y.-Z. W. Y.-J. Shen, B.-Q. Yao, X.-M. Duan, T.-Y. Dai, "Resonantly pumped high efficiency Ho:YAG laser," Appl. Opt. **51**, 7887–7890 (2012).

18. J.-P. Cariou, B. Augere, and M. Valla, "Laser source requirements for coherent lidars based on fiber technology," Comptes Rendus Phys. **7**, 213–223 (2006).

19. G. Canat, W. Renard, E. Lucas, L. Lombard, J. Le Gouët, A. Durécu, P. Bourdon, S. Bordais, and Y. Jaouën, "Eyesafe high peak power pulsed fiber lasers limited by fiber nonlinearity," Opt. Fiber Technol. **20**, 678–687 (2014).

20. C. W. Rudy, M. J. F. Digonnet, and R. L. Byer, "Advances in 2-µm Tm-doped mode-locked fiber lasers," Opt. Fiber Technol. **20**, 642–649 (2014).

21. J. Ward, "Active components for 2 µm fibre lasers," in *ISLA Workshop* (2015).

22. N. Simakov, J. M. O. Daniel, J. Ward, W. A. Clarkson, A. Hemming, and J. Haub, "Wavelength agile holmium-doped fiber laser," Proc. SPIE **9728**, 97280Q (2016).

23. ALTUGLAS, "Acrylic Sheet Plexiglas: Optical and Transmission Characteristics," (2000).

24. S. D. Jackson, "Midinfrared Holmium Fiber Lasers," IEEE J. Quantum Electron. **42**, 187–191 (2006).

25. A. S. Kurkov, E. M. Sholokhov, O. I. Medvedkov, V. V. Dvoyrin, Y. N. Pyrkov, V. B. Tsvetkov, A. V. Marakulin, and L. A. Minashina, "Holmium fiber laser based on the heavily doped active fiber," Laser Phys. Lett. **6**, 661–664 (2009).

26. J. W. Kim, A. Boyland, J. K. Sahu, and W. A. Clarkson, "Ho-doped silica fibre laser in-band pumped by a Tm-doped fibre laser," Conf. Lasers Electro-Optics **6084**, 6873 (2009).

27. A. Hemming, S. Bennetts, N. Simakov, A. Davidson, J. Haub, and A. Carter, "Resonantly Pumped 2 µm Holmium Fibre Lasers," in *Advanced Photonics* (OSA, 2011), p. SOMB1.

28. A. S. Kurkov, V. V Dvoyrin, and A. V Marakulin, "All-fiber 10 W holmium lasers pumped at λ=1.15µm," Opt. Lett. **35**, 490–492 (2010).

29. A. Hemming, N. Simakov, A. Davidson, S. Bennetts, M. Hughes, N. Carmody, P. Davies, L. Corena, D. Stepanov, J. Haub, R. Swain, and A. Carter, "A monolithic cladding pumped holmium-doped fibre laser," in *Conference on Lasers and Electro-Optics* (OSA, 2013), p. CW1M.1.

30. A. Hemming, J. Richards, N. Simakov, A. Davidson, N. Carmody, J. Haub, and A. Carter, "Pulsed operation of a resonantly pumped , linearly polarised , large mode area holmium-doped fibre amplifier," Opt. Express **22**, 4560–4566 (2014).

31. A. Hemming, N. Simakov, M. Oermann, A. Carter, and J. Haub, "Record efficiency of a holmium-doped silica fibre laser," in *Conference on Lasers and Electro-Optics* (OSA, 2016), p. SM3Q.5.

32. P. Li, A. Ruehl, U. Grosse-Wortmann, and I. Hartl, "Sub-100 fs passively mode-locked holmium-doped fiber oscillator operating at 2.06 µm," Opt. Lett. **39**, 6859 (2014).

33. N. Simakov, Z. Li, Y. Jung, J. M. O. Daniel, P. Barua, P. C. Shardlow, S. Liang, J. K. Sahu, A. Hemming, W. A. Clarkson, S.-U. Alam, and D. J. Richardson, "High gain holmium-doped fibre amplifiers," Opt. Express **24**, 13946 (2016).

34. N. Simakov, A. Hemming, W. A. Clarkson, J. Haub, and A. Carter, "A cladding-pumped, tunable holmium doped fiber laser," Opt. Express **21**, 28415–28422 (2013).

Chapter 2.

Background

2.1 Introduction

Optical fibre gain media offer many advantages over their traditional solid-state, crystalline counterparts such as improved thermal management, beam quality and cost of fabrication. The thermal load in a fibre laser is typically distributed across many meters of gain medium thereby allowing fibre lasers to generate many kW of output power without experiencing thermal degradation. The output beam quality is mostly defined by the engineered dielectric waveguide layers in the fibre and is far less sensitive to thermal gradients and external perturbations such as mechanical and mounting stresses. Finally, fibres are produced on a large scale, with a single preform yielding sufficient gain media for hundreds of high power lasers.

2.2 Fibre geometry

2.2.1 Core-pumped geometry

A core-pumped fibre source configuration occurs when the pump radiation and amplified signal radiation are confined to the same core waveguide layer. Indeed, the first diode-pumped erbium-doped fibre laser was operated in this configuration [1]. A major disadvantage of this approach is that the pump radiation is now required to have a brightness similar to that of the output signal generated in the core. This approach limits the possibility of power scaling as now there is only one or two pump sources that can be coupled to the core. While core-pumping offers some advantages in terms of reducing device length and reducing fabrication complexity, it also prevents the system from significantly improving brightness with the output beam quality having similar brightness properties to that of the input pump radiation as defined by the core waveguide. An alternative

approach that seeks to decouple the guidance of the pump and core radiation is required to make full use of the power scaling properties of optical fibres.

2.2.2 Cladding-pumped geometry

In a double-clad active optical fibre, the core radiation and pump radiation are confined by layers with small and large refractive index contrasts respectively. The refractive index contrast between the core and the cladding is usually small in order to support a much smaller number of modes (and in some cases only a single-mode) in the fibre core. In combination with the small transverse dimension of the core, this ensures that the output beam quality of any radiation that is generated by the core is significantly better than that guided by the cladding. An illustration of the refractive index of the core, cladding and coatings of double-clad fibres is shown in Fig. 2.1.

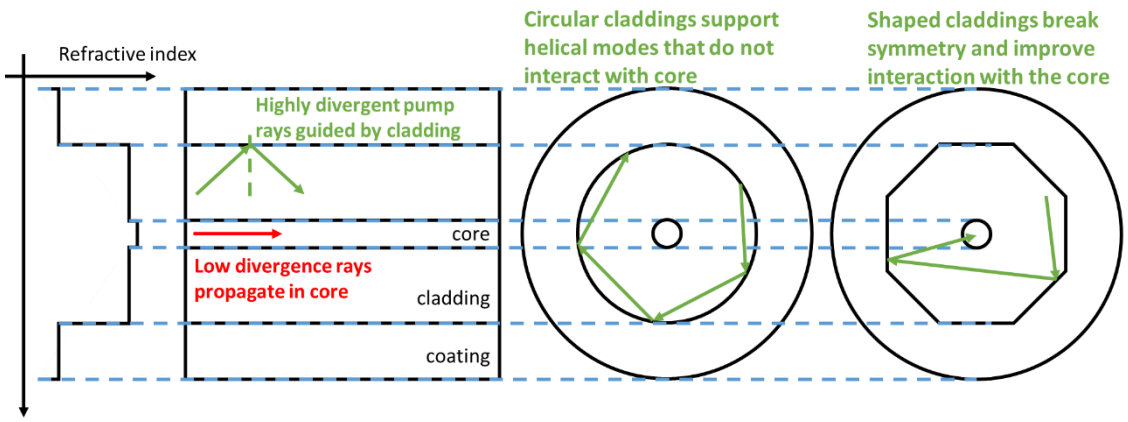

Figure 2.1: Refractive index profiles across the core, cladding and coating regions of double-clad fibres. Also shown are the cross-sections and an illustration of the impact of shaped claddings on the disruption of helical modes in active fibres.

The acceptance angle (θ) of a waveguide in an optical fibre is defined by the magnitude of the refractive index difference between the two layers. This angle is related to the numerical aperture (NA) as NA = $n_0 \sin(\theta)$ where n_0 is the refractive index of the external medium. For a core with refractive index (n_{core}) and cladding with refractive index ($n_{cladding}$) the numerical aperture can be expressed as:

$$NA = \sqrt{n_{core}^2 - n_{clad}^2} \quad , \tag{2.1}$$

2.2.3 Single-mode fibres

The number of guided modes within a step-index fibre is determined by the V-number (sometimes referred to as normalised frequency). The V-number of a circular step-index waveguide is given by [2]:

$$V = \frac{2\pi r NA}{\lambda} \quad , \tag{2.2}$$

Where r is the core radius, NA is the numerical aperture as defined by Eqn. (2.1) and λ is the operating wavelength. For a given core radius, the number of modes at a given wavelength that are supported increases with increasing NA.

For V<2.405, the fibre can only support the fundamental mode whose profile is a well-defined combination of Bessel J and K functions at the various interfaces [3] – this solution is referred to as the LP_{01} mode. This profile also resembles that of a Gaussian and is a significant aspect of fibre laser sources. A source operating on the LP_{01} mode of a fibre will have very similar spatial and propagation characteristics to that of the TEM_{00} mode of a conventional laser cavity. Higher order modes, and modes of non-step-index fibres generally have different transverse intensity profiles.

As the V-number of an optical fibre core is increased, by either increasing the radius or the magnitude of the refractive index step with respect to the cladding, the strength of the confinement of the fundamental mode within the core also increases. The mode field diameter (MFD) of the fundamental mode within a step index fibre can be related to the fibre core diameter and V-number by the Marcuse approximation [4,5] – this is valid for V>1.5.

$$MFD = 2r\left(0.65 + \frac{1.619}{V^{1.5}} + \frac{2.87}{V^{6}}\right) \quad , \tag{2.3}$$

As the V-number increases, the MFD of the fundamental mode asymptotes to 65% of the core diameter. It is important to remember that this approximation applies to step-index fibres. As the core diameter is increased in fibres that do not have a step index profile, the diameter of the fundamental mode may change drastically. This is particularly significant in fibres that have central features – whose formation are associated with the collapse stage of the MCVD fabrication process.

2.2.4 Few-mode fibres

As the V-number of the core is increased to V>2.405, the LP_{11} mode can now be supported and guided by the core. As the V-number increases further, then the waveguide can support even more modes [6].

In addition to having different propagation constants, the higher-order modes may have very different intensity profiles. If a Gaussian, diffraction limited output is desired, then measures must be taken to prevent significant generation or transfer of power into the higher order modes. Some cores also have refractive index profiles where the fundamental mode does not have a Gaussian or near-Gaussian intensity profile. In other applications such as mode-division multiplexed telecommunications or materials processing, operation on a single, but a higher order mode may be desired [7–9].

2.2.5 Multi-mode fibres

The typical cladding of a double-clad fibre has a diameter of 125 – 400 µm and an NA of 0.22 – 0.46. This yields a V-number in the order of 100-600 and thus many modes are supported by this structure. This enables the fibre cladding to confine and guide poor beam quality, lower brightness pump sources. Typically the pump source is an array of multi-mode laser diodes or fibre lasers. The active fibre acts as a brightness converter by receiving the pump input which has a poor beam quality into the multi-mode cladding and generating an output whose propagation properties are defined by the core and has excellent beam quality. The cladding layer that confines the pump radiation is also shaped as shown in Fig. 2.1 to disturb any helical modes that would otherwise experience minimal interaction with the core [10].

2.3 Active fibres

Passive fibres have been an enabling tool for many applications by allowing incredibly low loss propagation of radiation (with the lowest loss fibres achieving ~0.2 dB/km levels of attenuation). By including an active rare-earth dopant in the core, it is possible to now optically pump the ions into a metastable state and then extract that energy by stimulated emission in a spatially and temporally coherent output.

2.3.1 Thermal handling of optical fibres

A fibre laser usually contains 3-30 m of active fibre which provides an enormous surface area from which heat can be removed. Experiments and modelling suggest that these fibres can support heat loads of >300 W/m [11], and so the possible heat that can be managed by the gain medium is in the order of 1 – 10 kW [12]. Given that Yb^{3+} fibre lasers operate with >80% slope efficiencies, then this heat load represents 25% of the output power indicating that 4 – 40 kW power levels are not beyond the thermal handling limit of the fibre [13]. In reality it is rare that the heat load is distributed uniformly through the gain medium and usually quantum defect heating is not the main cause of failure, but rather the power handling of individual discrete components such as splices and combiners. Despite this, single diode pumped amplifiers at the 3 kW level and more complex systems operating at the 10 kW level have been demonstrated [12]. Further power scaling typically involves some form of combination of multiple lasers, typically spectral, coherent or incoherent [14].

2.3.2 Brightness conversion in double-clad optical fibres

The first demonstrations of diode pumped fibre lasers and amplifiers utilised core-pumped approaches [1,15]. A fundamental limitation here is that the pump source now has to be very high brightness. As a result, in order to power scale, the pump source must itself be a high brightness high power source. A solution to this was developed with the double-clad geometry [15]. Here the active fibre has multiple internal waveguides as shown in Fig. 2.2. The inner waveguide is termed the core and is typically doped with active rare-earth ions that can participate in optical pumping and stimulated emission processes – this waveguide is typically of the order of 5-30 μm in diameter and has an NA of 0.06 – 0.2 with respect to the cladding. The next largest waveguide is termed the cladding and it guides the launched pump radiation which is confined by the interface formed between it and a low index material – usually a low-index polymer. This pump waveguide typically has a diameter of 125 – 400 μm and the NA between the silica and polymer is 0.4 – 0.48. This greatly relaxes the brightness requirement on the pump source and is easily addressable in a scalable manner by multi-mode diode lasers.

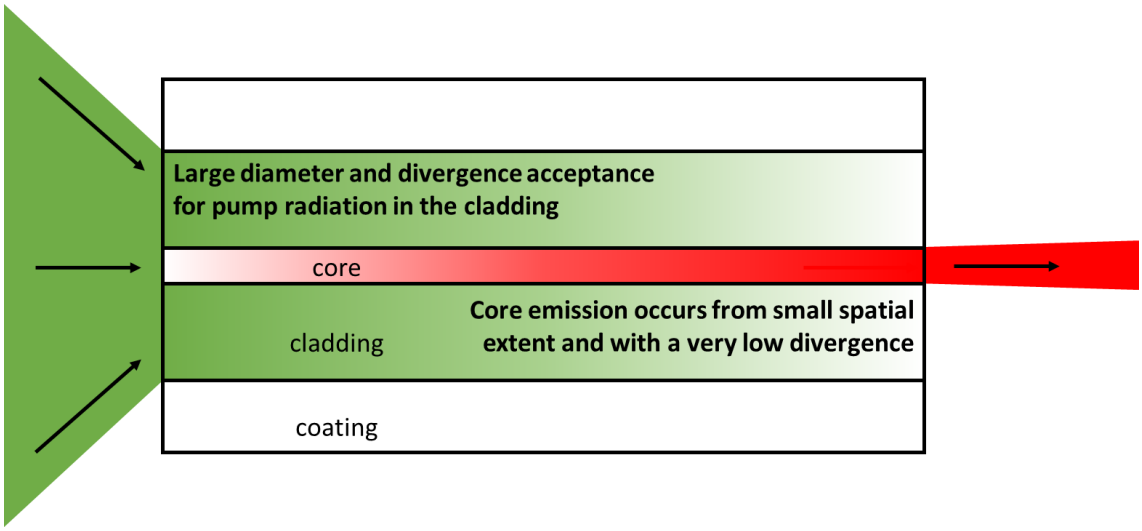

Figure 2.2: A low brightness pump beam is launched into the cladding of a fibre. This radiation is attenuated along the length of the fibre by interacting with the core. The ions in the core emit and this radiation experiences further amplification and is guided by the core. The output from the fibre core has a small spatial extent and a low divergence as defined by the core parameters.

$$Brightness\ enhancement = \frac{Cladding\ area\ \times\ Cladding\ acceptance\ cone}{Core\ area\ \times\ Core\ acceptance\ cone}\ , \qquad (2.4)$$

$$= \frac{r_{clad}^2 \times NA_{clad}^2}{r_{core}^2 \times NA_{core}^2} > 20{,}000$$

Where the 'Brightness enhancement' is the ratio of acceptance area of the cladding and the core regions (Cladding area, Core area) and the angular acceptance (Cladding acceptance solid angle, Core acceptance solid angle). This reduces to the ratio of the radii ($r_{clad,\ core}$) and NA ($NA_{clad,\ core}$) of both the cladding and the core respectively.

For a common 20 µm, 0.06 NA, 400 µm 0.46 NA fibre design, this brightness enhancement is >20000 and is routinely achieved in industrial fibre laser systems with efficiencies exceeding 80% and at power levels exceeding 1 kW. It is therefore not surprising that fibre lasers are such a widely used gain medium alongside high power but poorer beam quality semiconductor sources.

2.3.3 Gain medium quality, scalability of manufacture and efficiency

Silica is a suitable material for high power fibre lasers because of its excellent mechanical and thermal properties. However, much more importantly than the basic properties is the modified chemical vapour deposition process (MCVD) which provides a well-developed method for the fabrication of low loss, high purity silica fibres. The ability to make excellent quality, highly reproducible, low loss and high purity gain medium in relatively large volumes is an extremely important foundation for developing further systems based on this approach. Despite the many advantages that some infrared glasses present as potential hosts, the largest barrier to development is the ability to achieve the purity, the homogeneity and the volumes required.

The choice of silica as a host has several implications for 2 μm fibre lasers. The presence of a strong material infra-red background loss [16–20] and an absorption feature due to the hydroxyl ion/silica interaction (SiOH) resonances will drive the design of efficient fibre lasers at this wavelength [21]. The non-radiative decay due to multi-phonon relaxation decreases the lifetime of the upper lasing level from ~10 ms to less than 1 ms [21]. Despite these additional challenges, both thulium and holmium doped fibres have been power scaled to the >400 W from a single gain stage in various architectures.

2.4 Laser operation in rare-earth doped silica fibres

Let us consider a two level energy system where the ions are distributed between the ground state (N_1) and the upper laser level (N_2). The absorption and stimulated emission rates are related to the Einstein B coefficients (B_{12} and B_{21}) and the photon flux density ($\rho(\nu)$). The spontaneous emission rate is governed by the A_{21} coefficient. An illustration of these transitions is shown in Fig. 2.3

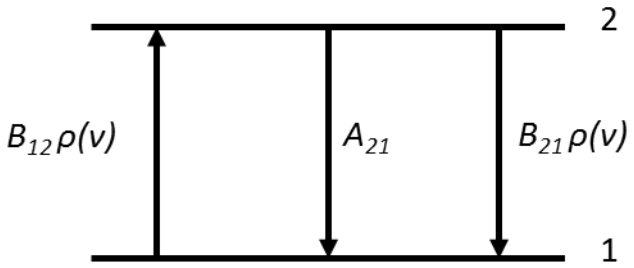

Figure 2.3: Transitions corresponding to the absorption, spontaneous emission and stimulated emission of radiation in a two-level system.

The total population of ions (N) remains constant so we can state that:

$$N = N_1 + N_2 \quad , \tag{2.5}$$

Where N_1 is the concentration of ground state ions and N_2 is the concentration of excited ions. We define the inversion parameter (β) as the fraction of ions in the upper energy state:

$$\beta = \frac{N_2}{N} \quad , \tag{2.6}$$

Based on the distribution of energy states within each manifold and the associated transition cross-sections, we can define the absorption and emission cross-sections and the effective cross-section.

$$\sigma_{effective}(\lambda) = \beta \times \sigma_{emission}(\lambda) - (1-\beta) \times \sigma_{absorption}(\lambda) \quad , \tag{2.7}$$

Where $\sigma_{effective}$ is the effective cross-section (>0 represents gain, <0 represents absorption), $\sigma_{emission}$ is the emission cross-section and $\sigma_{absorption}$ is the absorption cross-section (m^2). It is also important to bear in mind that the cross-sections are functions of wavelength (λ). The output (P_{out}) after absorption or amplification as an initial signal (P_0) propagates over a length (L) will then be:

$$P_{out} = P_0 e^{L \times N \times \sigma_{effective}(\lambda)} \quad , \tag{2.8}$$

This also assumes that the signals are sufficiently small such that there are no saturation effects. The ion concentration is typically measured by chemical analysis such as mass-spectroscopy, the absorption cross-section is easily measured using any form of optical absorption spectroscopy, and emission cross-section can be measured by creating a maximum inversion (usually with another laser source) and performing spectroscopy on the emitted fluorescence. The emission cross-section may also be estimated from the absorption spectra using the reciprocity relationship [22].

The population within each manifold is temperature dependent and is distributed according to Boltzmann statistics. It is this thermal population that is responsible for the absorption features at wavelengths longer than the zero-phonon line. As the population of ions is cooled from 295 K to 77 K we would expect that the distribution within the ground state manifold would change and more ions would occupy the lowest possible energy state. As shown in Fig. 2.4, we also observe the absorption cross-section at wavelengths greater than the wavelength corresponding to the zero-phonon transition disappear.

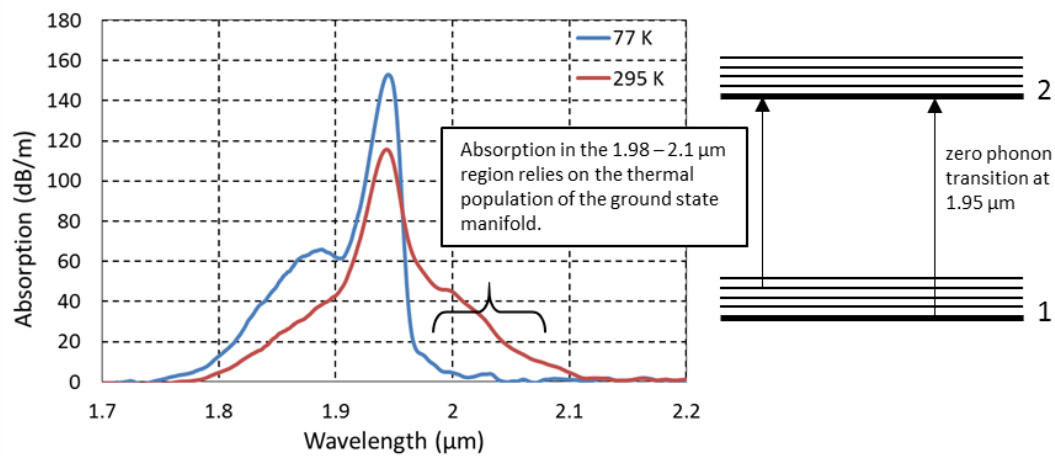

Figure 2.4: Absorption per unit length in a holmium-doped fibre at 295 K and 77 K. The absorption in the 1.98 – 2.1 µm region disappears due to the redistribution of the population in the lower level manifold.

2.4.1 Holmium-doped silica spectroscopy

The energy levels of the holmium ion in silica are shown in Fig. 2.5 [23]. The holmium ion can be pumped into either the $^5I_7$ level by 1.95 µm thulium based sources, or the $^5I_6$ level by 1.15 µm laser diodes or long wavelength ytterbium-doped fibre lasers. Pumping at 1.95 µm results in a laser transition with a very low quantum defect of <10% (absorption at 1.95 µm, emission at 2.1 µm) and is attractive for power scaling and high power applications.

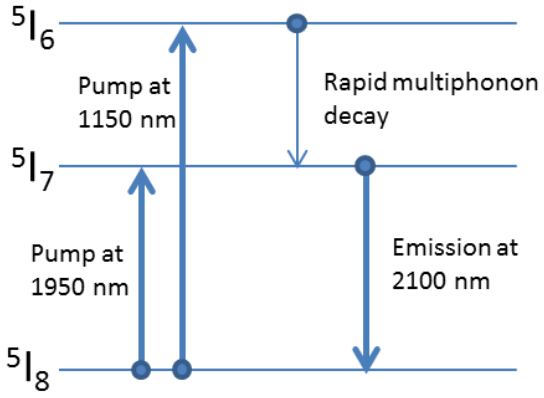

Figure 2.5: Relevant energy levels for the pumping and emission in holmium-doped silica.

The Ho^{3+} cross-section at 1.8 – 2.2 µm is shown in Fig. 2.6. The emission cross-section is estimated via reciprocity from the absorption cross-section [22]. The effective cross-section for holmium-doped silica for various inversion levels (β) as a function of wavelength is shown in Fig. 2.6.

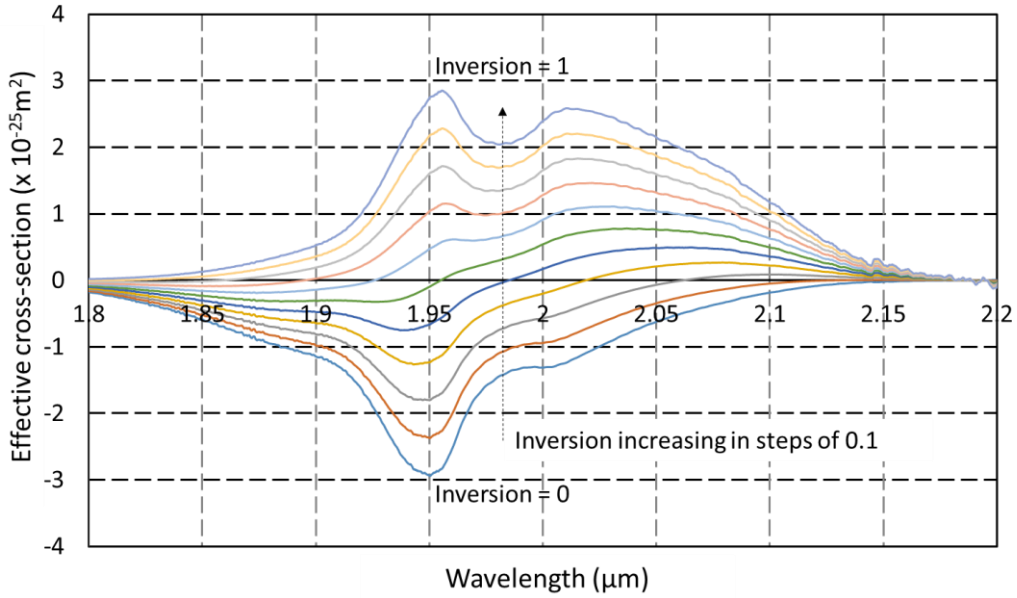

Figure 2.6: Effective cross-section of holmium-doped silica as a function of wavelength.

2.4.2 Thulium-doped silica spectroscopy

The thulium ion exhibits several broad absorption bands at 790 nm, 1550 – 1900 nm which can be addressed by diodes and fibre laser pump sources – the relevant energy levels are shown in Fig. 2.7. Several groups have demonstrated high average power levels with 608 W from a single stage

amplifier [24] and more than 1 kW from a dual stage amplifier [25]. Both of these demonstrations operated at 2.04 µm and relied on diode pumping at 0.79 µm. Other strategies for the power scaling of thulium fibre sources include resonant pumping with either erbium based sources [26] or another shorter wavelength thulium fibre laser [27]. Of these approaches, the most electrically efficient approach to generating radiation at 2 µm is achieved by using 0.79 µm diode pumping of thulium and exploiting the cross-relaxation mechanism between thulium ions.

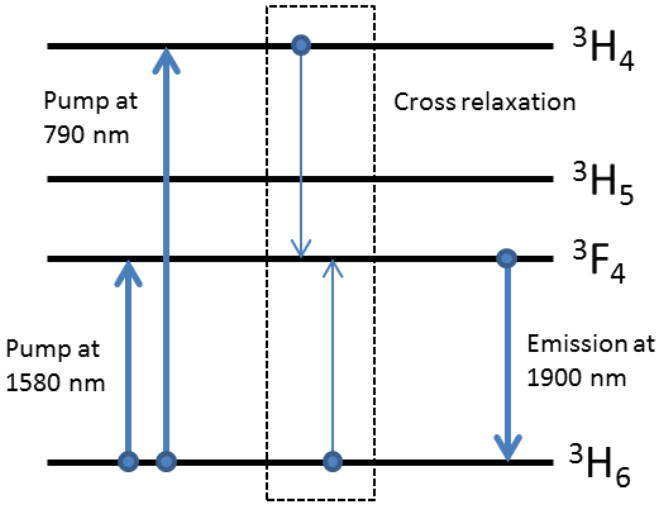

Figure 2.7: Relevant energy levels for the pumping and emission in thulium-doped silica.

Cross-relaxation is a well-known effect in thulium-doped gain media and enables a quantum efficiency >1 with up to 2 laser photons generated for a single pump photon [28]. The cross-relaxation mechanism allows for a substantial increase in efficiency when pumping at 790 nm. This 2-for-1 process increases the maximum possible yield from 790/1900 = 42% to 790/1900x2 = 83%. To date, the most efficient demonstrations of diode pumped thulium have operated at ~70% slope efficiency, with typical high power systems at 50-60% with respect to launched pump.

The thulium emission spans across 1600 – 2100 nm, and varies substantially depending on the fractional inversion as shown in Fig. 2.8. At low inversions, the gain peaks at around 2000 – 2050 nm. At higher inversions the gain can extend to the 1600 nm range, and indeed has been demonstrated to operate as short as 1650 nm [29].

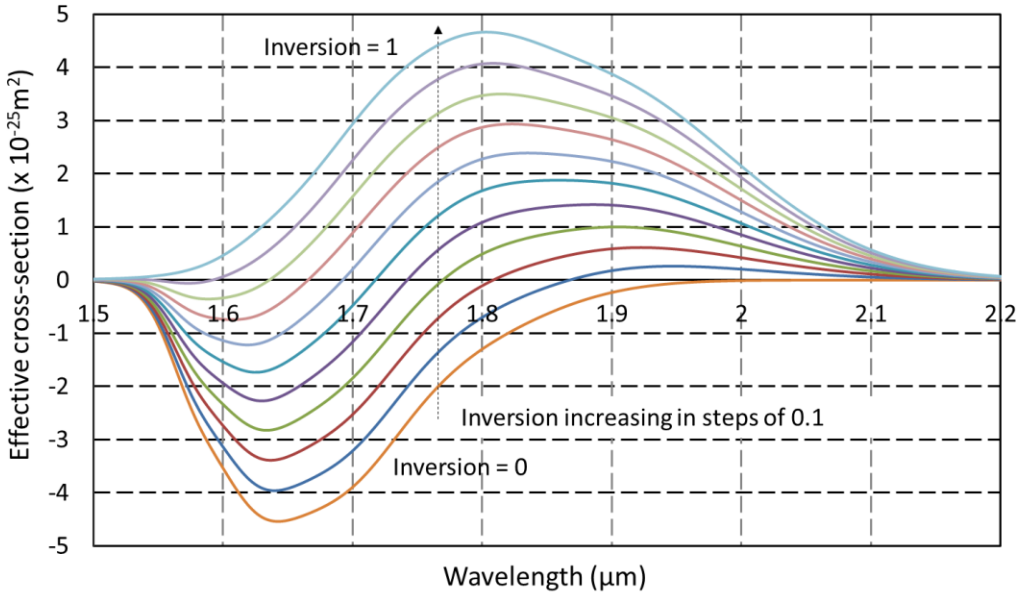

Figure 2.8: Effective cross-section of thulium-doped silica as a function of wavelength.

The inversion required to reach transparency ($\sigma_{effective} = 0$) will vary depending on the relative value of the absorption and emission cross-sections. For the longer wavelength edge of the transition, the inversion required to reach transparency will be significantly smaller than that at the zero-phonon line.

2.4.3 Lifetimes in silica host

The radiative lifetimes ($\tau_{radiative}$) associated with the 2 µm transitions in thulium and holmium are expected to be of the order of many ms. However, there are also non-radiative decay mechanisms that can contribute to this. One of the most common non-radiative decay mechanism for these transitions is due to interaction with vibrational modes within the host. This is termed as multi-phonon relaxation and occurs with a rate ($\tau_{non\text{-}radiative}$) that is dependent on the required number of interactions. Only the highest energy vibration supported by the material is significant.

The effective lifetime of the upper-state is now governed by both the radiative and non-radiative processes:

$$\frac{1}{\tau_{effective}} = \frac{1}{\tau_{radiative}} + \frac{1}{\tau_{non-radiative}} \quad , \qquad (2.8)$$

For the 2 µm transitions in silica the $\tau_{radiative}$ = 5-10 ms >> $\tau_{non\text{-}radiative}$ ~0.3 – 1 ms and so the upper-state lifetime ($\tau_{effective}$) is almost entirely determined by the non-radiative decay mechanisms. This process will significantly affect the threshold as in order to achieve a high inversion, the pump rate must be proportionally larger to compete with the non-radiative processes. This can also have significant implication for the allowed composition of the host material if the aim is to maximise the lifetime of the Tm^{3+} and Ho^{3+} ion as several of the dopants in a conventional MCVD process such as boron oxide and phosphate will increase the maximum phonon energy thereby significantly reducing the lifetimes of the transitions.

2.4.4 Discussion

When selecting the active material in a laser it is important to consider the final application. It is not sufficient to only have the necessary emission properties at the desired wavelength, but also extremely important to be able to control any out-of-band emissions that could lead to substantial levels of ASE and parasitic lasing effects.

Figure 2.9 makes a comparison between the preferred operating region for the thulium and holmium ion doped silica fibres. The maximum gain is normalised to 40 dB which is representative of the isolation strength of commercially available isolators in this wavelength region.

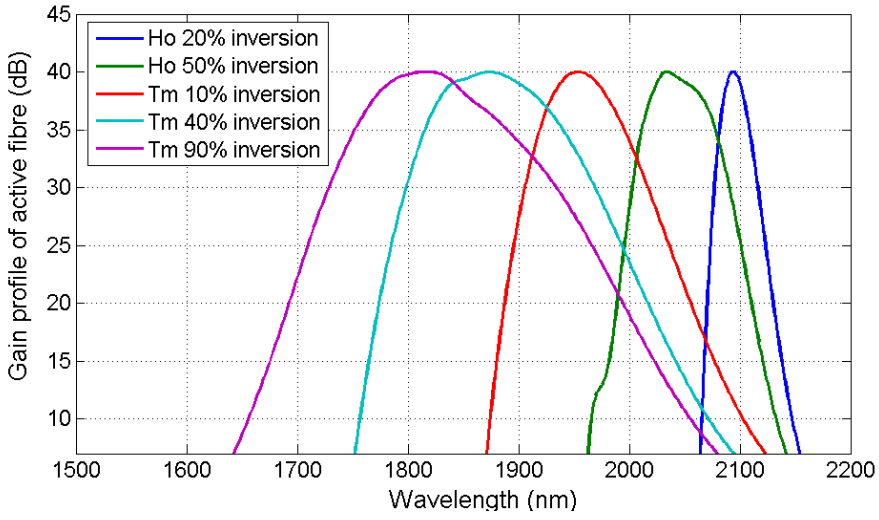

Figure 2.9: Gain profiles for thulium and holmium fibres under varying inversions normalised to an amplifier with a peak gain of 40 dB.

For example, consider the development of a pulsed 2.05 µm fibre laser as a replacement for conventional Ho:YLF solid-state lasers. A thulium-doped fibre laser operating in this region would require a long length of fibre held at a low inversion (in order to shift the maximum gain to longer wavelengths). Despite best efforts, there would still be substantial out-of-band gain at 1930 – 1980 nm. As a result, the system would be unstable and susceptible to any external feedback. Energy storage in between pulses would also be problematic. In comparison, a holmium-doped fibre would be operating on the gain peak at around 2.05 µm when at a high inversion.

Management of any out-of-band residual gain can be achieved by filter components that have a spectrally dependent loss. Ideally the losses would be distributed with the active gain medium rather than localised at either end – however the effectiveness of this approach will depend on the operating parameters of the system.

2.5 Non-radiative energy transfer effects

Rare-earth doped fibres are typically doped with concentration levels such that the ions are in close proximity and thus can interact in a non-radiative manner. It is possible for effects such as energy migration, up-conversion, transfers and impurity quenching to occur.

2.5.1 Energy migration

Energy migration and diffusion in rare earth ions have been observed in ions such as neodymium, ytterbium and erbium [30–33]. The energy transfer takes place between an excited ion and an ion in the ground state as shown in Fig. 2.10. There is no energy loss in this process. The rate of migration increases with increasing concentration of rare-earth ions and is typically several orders of magnitude faster than non-resonant up-conversion processes in crystalline material such as Ho:YAG [34].

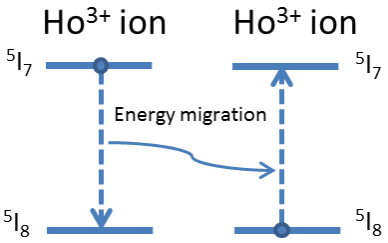

Figure 2.10: Energy migration from an excited holmium ion to a ground state holmium ion.

2.5.2 Energy up-conversion

When two excited ions are within close proximity of each other, it is possible that the energy from one is transferred to the other shifting it to a higher energy level. A diagram of this process is shown in Fig. 2.11. In holmium, this up-conversion process also relies on an additional phonon being released or absorbed. Once in the upper energy level, the phonon environment of the silica host dictates a rapid decay from the excited state to the upper lasing level. The overall energy loss in this process corresponds to the energy required to excite an additional holmium ion. The rate of this process will increase with an increasing concentration of excited holmium ions (i.e. dependant on inversion fraction and holmium concentration). A consequence of this transfer is that there is now a probability of spontaneous emission of higher energy photons from the $^5I_5$ and $^5I_6$ energy levels.

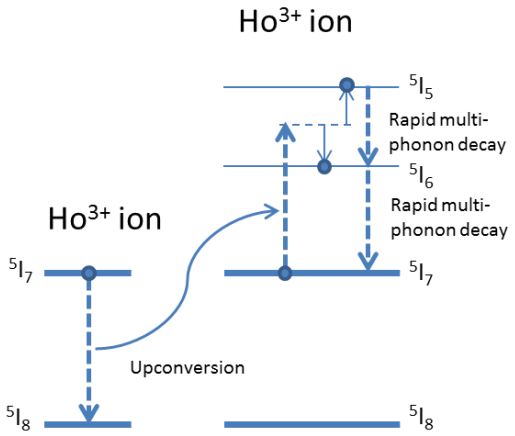

Figure 2.11: Up-conversion occurs when two excited holmium ions are in close proximity.

2.5.3 SiOH impurity quenching

The emission cross-section of a holmium ion in the $^5I_7$ level overlaps with the combination mode between the vibration of the SiO_4 tetrahedron (v_1) and the fundamental mode of the hydroxyl functional group (v_3) [35]. It is possible that an excited holmium ion in close proximity to an SiOH group will experience a rapid de-excitation due to the near resonant energy transfer. This effect will be exacerbated by energy migration within the holmium ion population. A diagram illustrating this is shown in Fig. 2.12.

Although not previously reported in holmium doped silica – this effect has been observed in the praseodymium transition at 1.3 µm which is in close proximity to the first overtone of the hydroxyl group (at ~1.38 µm) [36,37]. As a comparison, the strength of the combination mode of the fundamental resonance (at ~2.2 µm) is approximately a factor of 3 larger and this may have significant implications to the rate of energy transfer.

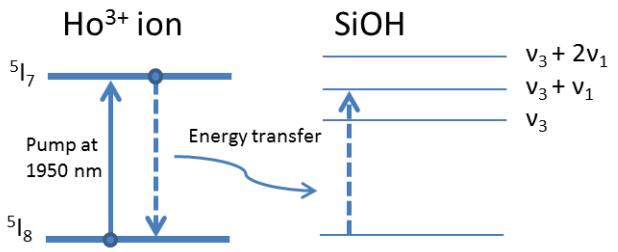

Figure 2.12: Near-resonant energy transfer between an excited holmium ion and a bonded hydroxyl group. The parameters v_3 and v_1 describe the hydroxyl fundamental mode and the SiO_4 tetrahedron vibration, respectively.

2.5.4 Clustering

Despite best efforts, the distribution of the rare-earth dopant in the host may not be uniform. This may lead to formation of rare earth ion clusters where the local concentration is far larger than the average bulk concentration. Within the cluster there will be a greatly increased rate of energy transfer and up-conversion. Furthermore if the cluster is close to an impurity such as a hydroxyl group, this can become a very efficient sink for any energy that is absorbed by any of the ions in the cluster.

2.6 Sources of noise in rare-earth amplifiers

In many applications the spectral and/or the temporal quality of the output are essential properties and any spurious emission can rapidly degrade the performance and suitability of the laser. The source of these emissions stems from spontaneous emission and subsequent amplification. We will aim to discuss the origins and how to quantify the level of this noise both in CW and pulsed systems.

As a signal is amplified within a 2-level amplifier with gain G, at frequency ν, some spontaneous emission is captured within the same spatial mode. This emission will have a random phase with respect to the incident signal, and will experience subsequent amplification. The resulting output is therefore a component of the amplified photon flux (Gρ(ν)) and a component termed amplified spontaneous emission (ASE). An illustration of this process is shown in Fig. 2.13

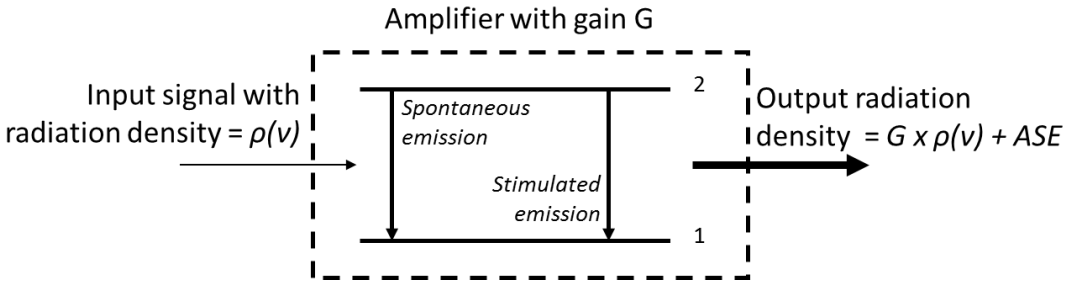

Figure 2.13: As an input signal experiences amplification, some component of the spontaneous emission is also captured in the same mode. This noise component will also experience amplification along the length of the amplifier.

2.6.1 Operation in a CW regime

Consider the spectral data in Fig. 2.14. This is an experimentally measured output from a holmium doped fibre amplifier [38]. The input seed has a -0.3 dB peak level and an optical signal-to-noise ratio of 64.5 dB. The output from the amplifier has a peak at 23.7 dB and a background at -23.6 dB. The signal peak has risen by 24 dB and the background level has experienced an increase of 40.2 dB indicating that there is indeed substantially more noise present in the system. The resolution used to perform the measurement was 0.5 nm.

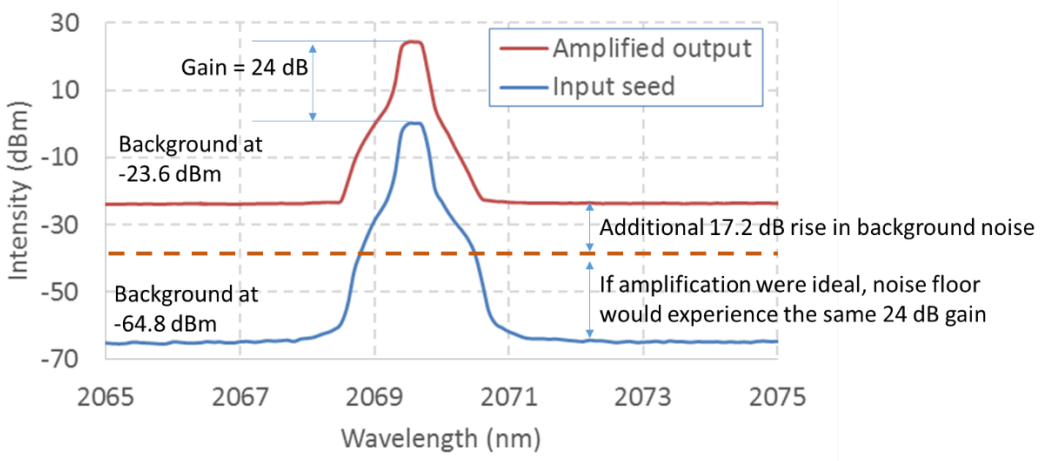

Figure 2.14: Experimentally measured input and output signals to a holmium-doped fibre amplifier [38] illustrating the non-ideal growth of the background noise. The measurement resolution was 0.5 nm.

This additional growth of background is associated with amplified spontaneous emission. In this process, ions near the start of the amplifier spontaneously decay and some radiation is coupled into the core of the active fibre and co-propagates with the input signal. This spontaneous emission also experiences the same level of amplification along the length of the amplifier as well as collecting more spurious emissions. As such the growth of such spurious emission must be very carefully controlled. In certain applications this out-of-band emission is completely unacceptable to the application.

2.6.2 Noise figure definition and measurement

In order to quantify the quality of amplifiers operating under different conditions, the noise-figure (NF) metric is introduced. The NF represents the degradation in the signal-to-noise ratio (SNR) between the input and output signals of an amplifier [22,39].

$$NF = 10 \times log_{10}\left(\frac{SNR_{in}}{SNR_{out}}\right) , \tag{2.9}$$

Where the input and output signal-to-noise ratio (SNR_{in} and SNR_{output}) are determined in terms of the currents generated by the signal and noise levels in the photodetector. It is important to note that the SNR is not the same as the optical signal-to-noise ratio (OSNR). It is also important to note that the NF is always > 0 dB as the amplifier will add noise during the amplification process. It can be shown for an ideal amplifier, the quantum limit of the noise figure is 3 dB and indeed erbium-doped fibre amplifiers with noise figures approaching this value have been demonstrated [40,41].

The NF can be experimentally determined based on the data provided in Fig. 2.14. according to the following equation [22]:

$$NF = 10 \times log_{10}\left(\frac{P_{ASE}}{h\nu\Delta\nu G} + \frac{1}{G}\right) \quad , \tag{2.10}$$

Where we estimate the ASE power level (P_{ASE} = -23.6 dBm = 0.00437 mW) at the signal wavelength by approximating it to the baseline around the main signal spectral feature. The operating wavelength was 2069.5 nm corresponding to a frequency ν = 1.449x10^{14} Hz. The bandwidth setting for this measurement was Δλ = 0.5 nm which is equivalent to a frequency bandwidth (Δν = 35 GHz). The amplifier was operating at a gain of 24 dB (corresponding to G = 251).

Based on these parameters the NF ≈ 7.1 dB. To enable accurate estimates of the NF, great care must be taken to ensure that the average power, the spectra of both input and output signals are measured correctly and with the same resolution setting on the instrument. Any systematic errors in measurement may give unrealistic estimates of the NF performance of the amplifier systems.

2.6.3 Operation in a pulsed regime

Fibre lasers typically operate in a regime where the mode-field diameters are very small, the small-signal gain and lengths are extremely large. Single pass amplification of spontaneous emission (ASE) can reach significant power levels, and is able to extract the energy relatively efficiently. Parasitic lasing can also occur from residual reflections at interfaces and even from the Rayleigh background scattering in the fibre. In many CW materials-processing applications, this residual power has little impact on the process. However in pulsed systems, these processes can be extremely detrimental.

Consider the situation of a multi-stage fibre amplifier with a pulsed seed as shown in Fig. 2.15. In the time between pulses, the ASE background from the 1st amplifier can build up to levels that are able to saturate the 2nd amplifier stage. The complete absence of a seed may not even measurably affect the average output power of the system due to how efficiently this ASE is able to extract the power from the 2nd stage. A question then arises – how to measure and quantify the amount of energy in the pulses and the amount of energy in the background noise.

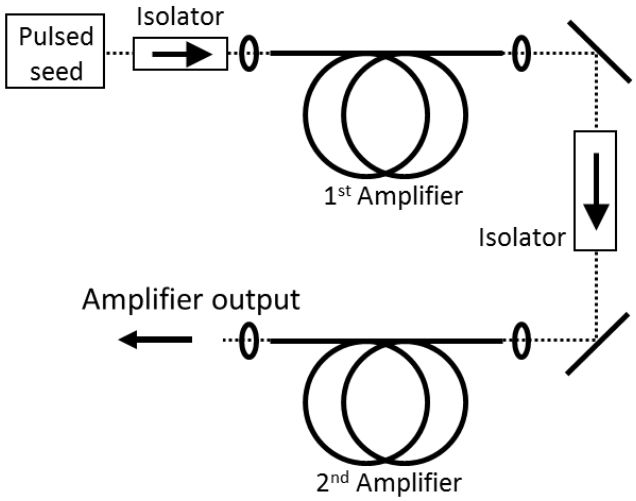

Figure 2.15: A multi-stage fibre amplifier where the parasitic background and ASE from the 1st stage can potentially extract the power from the 2nd stage independently from whether the seed is operating or not.

2.6.4 Experimental measurement of temporal quality of output

The first approach might be to rely on a DC-coupled photodiode as an attempt to make a direct measurement of the peak power and the background noise. Let us consider a source that is supposed to produce pulses with duration of 10 ns at a repetition rate of 100 kHz. Typically the output from a photodiode is observed on an oscilloscope, and the gain is configured such that the peak of the output (V_{sig}) produces a signal in the order of 1 V as shown in Fig. 2.16.

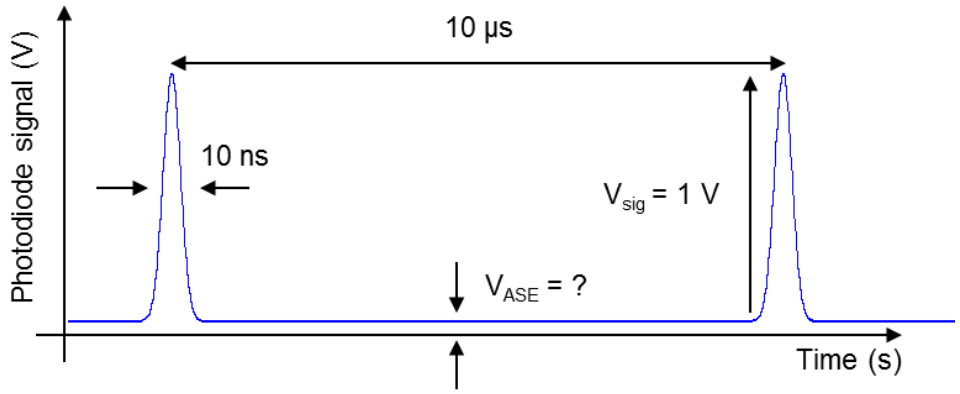

Figure 2.16: Illustration of a typical signal from a typical system operating with 10 ns pulses at 100 kHz.

Let us also make the assumption that the total power (P) is distributed between the power in the ASE background (P_{ASE}) and the power contained in the pulsed output (P_{sig}):

$$P = P_{sig} + P_{ASE} \quad , \tag{2.11}$$

If we assume that the efficiency of the photodiode and corresponding amplifiers is η_{PD} with respect to the incident power on the detector. The amplitude of the voltage signal (V) generated by incident radiation P is:

$$V = \eta_{PD} \times P \quad , \tag{2.12}$$

We can integrate the corresponding contributions for the signal and the ASE based on the pulse duration (10 ns) and the period (10 µs):

$$P_{sig} = \frac{10\ ns}{10\ \mu s} \times V_{sig} \times \frac{1}{\eta_{PD}} \quad , \tag{2.13}$$

$$P_{ASE} = \frac{10\ \mu s\ -\ 10\ ns}{10\ \mu s} \times V_{ASE} \times \frac{1}{\eta_{PD}} \approx \frac{V_{ASE}}{\eta_{PD}} \quad , \tag{2.14}$$

The minimum detectable background on an oscilloscope (i.e. the noise floor) will be typically in the range of several mV. Let us assume that the ASE level is at the minimum level we can measure reliably (V_{ASE} = 1 mV). Then the total power contained in the pulses is equivalent to the total power in the ASE.

$$P_{sig} = P_{ASE} \quad , \tag{2.15}$$

This suggests that the ASE will only become detectable when the total power contained in the DC background is equal to the power contained in the pulse. i.e. half of the total output power is contained in the DC background.

This is obviously completely unacceptable for many applications requiring the high peak power of the pulses and the absence of power in between pulses and illustrates the dangers of using a photodiode as a single measurement. The dynamic range offered by such a measurement is in the range of 20-30 dB and so will not be able to discriminate between sufficient levels of background. Additional diagnostics such as the use of an RF spectrum analyser may provide additional dynamic range and may assist in discriminating between a ‘DC’ background and a signal operating at a 100 kHz repetition rate. However this is also complicated by the fact that the ASE may not have a constant background level. Indeed, we would expect the ASE to grow as more energy is stored in the amplifier and reach a maximum shortly before the energy is extracted. In these situations, a

direct measurement of the energy contained by the pulse in comparison with the energy contained by the background is desirable.

It is possible to increase the dynamic range of the measurement by using an external fast amplitude modulator with a high extinction ratio. An acousto-optic modulator (AOM) can easily achieve extinction ratios of 30-50 dB (R_{AOM} = 10^{-3} - 10^{-5}) for the diffracted orders with rise and fall times of 100 ns. An illustration of this measurement is provided in Figs. 2.17a) and 2.17b).

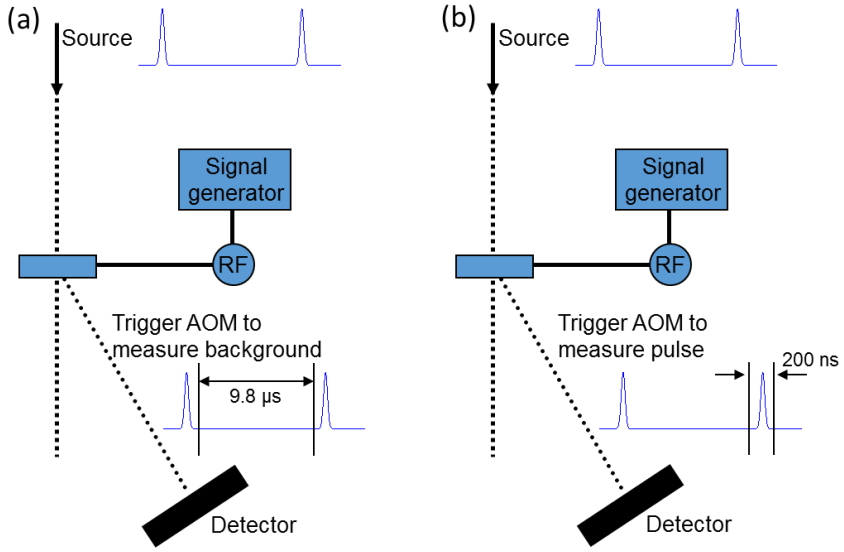

Figure 2.17: a) The AOM is triggered to diffract the background in between the pulses. b) The AOM is triggered to diffract the pulses.

In Fig. 2.17a) the AOM receives an RF pulse that is 9.8 µs duration and occurs in between the pulses. The power (P_a) on the detector in this configuration is thus equal to:

$$P_a = \eta_{AOM}\left[\left(\frac{9.8\ \mu s}{10\ \mu s}P_{ASE}\right) + R_{AOM} \times \left(\frac{0.2\ \mu s}{10\ \mu s}P_{ASE} + P_{sig}\right)\right] \quad , \qquad (2.16)$$

Where η_{AOM} is the diffraction efficiency of the AOM and can be as large as 90%, but for the purposes of this measurement is not a critical parameter. When the AOM is triggered as per Fig. 2.17b), with a 200 ns window which includes the pulse, the power (P_b) on the detector is equal to

$$P_b = \eta_{AOM}\left[\left(\frac{0.2\ \mu s}{10\ \mu s}P_{ASE} + P_{sig}\right) + R_{AOM} \times \left(\frac{9.8\ \mu s}{10\ \mu s}P_{ASE}\right)\right] \quad , \qquad (2.17)$$

Let us assume that the $P_{ASE} << P_{sig}$ (in order to analyse the sensitivity of the measurement to small amounts of ASE).

$$\frac{P_a}{P_b} \approx \frac{\frac{9.8\ \mu s}{10\ \mu s} P_{ASE} + R_{AOM} \times P_{sig}}{P_{sig}} \approx \frac{P_{ASE}}{P_{sig}} + R_{AOM} \quad , \tag{2.18}$$

Where we can see that the sensitivity of the measurement is equivalent to the dynamic range of the modulator even if we use a slow detector such as a power meter. With this approach it is possible to directly measure ASE levels which make up as little as 0.1% - 0.001% of the total output (depending on R_{AOM}).

By using a fast DC-coupled photodiode in combination with the AOM, it would be possible to further increase the sensitivity by the dynamic range of the measurement by a further 20-30 dB, thereby potentially offering an extremely high sensitivity measurement of the ASE content.

2.7 Summary

In this chapter we have outlined the basic properties of the geometries and design considerations used in active optical fibres. The geometry and engineered refractive index enables incredible power scaling and brightness conversion inside optical fibres. Combined with the relatively high gains possible, this leads to an incredibly useful amplifier platform. However, as with almost all amplification we also need to consider the possible sources of noise. We introduce the concept of noise figure and discuss how to measure spurious emissions in both CW and pulsed amplifier systems.

2.8 References

1. L. Reekie, I. M. Jauncey, S. B. Poole, and D. N. Payne, "Diode-laser-pumped operation of an Er^{3+}-doped single-mode fibre laser," Electron. Lett. **23**, 1076 (1987).

2. A. W. Snyder and J. D. Love, "Fundamental properties of modes," in *Optical Waveguide Theory* (Springer US, 1983), pp. 208–237.

3. A. W. Snyder and J. D. Love, "Waveguides with exact solutions," in *Optical Waveguide Theory* (Springer US, 1983), pp. 238–279.

4. D. Marcuse, "Loss Analysis of Single-Mode Fiber Splices," Bell Syst. Tech. J. **56**, 703–718 (1977).

5. D. Marcuse, "Gaussian approximation of the fundamental modes of graded-index fibers," J. Opt. Soc. Am. **68**, 103 (1978).

6. A. W. Snyder and J. D. Love, "Circular fibers," in *Optical Waveguide Theory* (Springer US, 1983), pp. 301–335.

7. S. Berdagué and P. Facq, "Mode division multiplexing in optical fibers," Appl. Opt. **21**, 1950 (1982).

8. J. M. O. Daniel and W. A. Clarkson, "Rapid , electronically controllable transverse mode selection in a multimode fiber laser," Opt. Express **21**, 29442–29448 (2013).

9. D. Lin, J. M. O. Daniel, M. Gecevičius, M. Beresna, P. G. Kazansky, and W. A. Clarkson, "Cladding-pumped ytterbium-doped fiber laser with radially polarized output," Opt. Lett. **39**, 5359 (2014).

10. D. Kouznetsov and J. V. Moloney, "Efficiency of pump absorption in double-clad fiber amplifiers II Broken circular symmetry," J. Opt. Soc. Am. B **19**, 1259 (2002).

11. C. A. Codemard, A. Shirakawa, J. K. Sahu, S. Yoo, Y. Jeong, and J. Nilsson, "Thermal resilience of polymer-coated double-clad fiber," in *CLEO/Europe European Conference on Lasers and Electro-Optics* (IEEE, 2009), pp. 1–1.

12. Y. Jeong, J. K. Sahu, D. N. Payne, and J. Nilsson, "Ytterbium-doped large-core fiber laser

with 1.36 kW continuous-wave output power," Opt. Express **12**, 6088 (2004).

13. H.-J. Otto, C. Jauregui, J. Limpert, and A. Tünnermann, "Average power limit of fiber-laser systems with nearly diffraction-limited beam quality," Proc. SPIE **9728**, 97280E (2016).

14. T. Y. Fan, "Laser beam combining for high-power, high-radiance sources," IEEE J. Sel. Top. Quantum Electron. **11**, 567–577 (2005).

15. J. Stone and C. A. Burrus, "Neodymium-Doped Fiber Lasers: Room Temperature cw Operation with an Injection Laser Pump," Appl. Opt. **13**, 1256 (1974).

16. E. Snitzer, H. Po, F. Hakimi, R. Tumminelli, and B. C. McCollum, "Double Clad, Offset Core Nd Fiber Laser," in *Optical Fiber Sensors* (OSA, 1988), p. PD5.

17. S. R. Nagel, J. B. Macchesney, and K. L. Walker, "Special Issue Papers An Overview of the Modified Chemical Vapor Deposition (MCVD) Process and Performance," IEEE Trans. Microw. Theory Tech. **MTT**-**30**, 305–320 (1982).

18. M. Ohashi, K. Shiraki, and K. Tajima, "Optical Loss Property of Silica-Based Single-Mode Fibers," J. Light. Technol. **10**, 539–543 (1992).

19. N. Uchida and N. Uesugi, "Infrared Optical Loss Increase in Silica Fibers due to Hydrogen," J. Light. Technol. **LT**-**4**, 1132–1138 (1986).

20. T. Edahiro, M. Horiguchi, K. Chida, and Y. Ohmori, "Spectral Loss Characteristics of GeO_2-P_2O_5-Doped Silica Graded-Index Fibres in Long-Wavelength Band," Electron. Lett. **15**, 274–275 (1979).

21. S. Sakaguchi and S. Todoroki, "Optical properties of GeO_2 glass and optical fibers.," Appl. Opt. **36**, 6809–6814 (1997).

22. S. R. Bowman, N. J. Condon, S. O. Connor, T. Ehrenreich, W. Kanxian, K. Farley, and S. Christensen, "Radiation Balanced Holmium Fiber Lasers," Proc. SPIE **7951**, 795107 (2011).

23. M. J. F. Digonnet, *Rare-Earth-Doped Fiber Lasers and Amplifiers* (Marcel Dekker, 2001).

24. S. D. Jackson, "Midinfrared Holmium Fiber Lasers," IEEE J. Quantum Electron. **42**, 187–191 (2006).

25. G. D. Goodno, L. D. Book, and J. E. Rothenberg, "Low-phase-noise, single-frequency, single-mode 608 W thulium fiber amplifier," Opt. Lett. **34**, 1204 (2009).

26. P. F. Moulton, G. A. Rines, E. V. Slobodtchikov, K. F. Wall, G. Frith, B. Samson, and A. L. G. Carter, "Tm-Doped Fiber Lasers: Fundamentals and Power Scaling," IEEE J. Sel. Top. Quantum Electron. **15**, 85–92 (2009).

27. M. Meleshkevich, N. Platonov, D. Gapontsev, and A. Drozhzhin, "415W Single-Mode CW Thulium Fiber Laser in all-fiber format," CLEO/Europe Conf. Lasers Electro-Optics CP2_3 (2007).

28. D. Creeden, B. R. Johnson, S. D. Setzler, and E. P. Chicklis, "Resonantly pumped Tm-doped fiber laser with >90% slope efficiency," Opt. Lett. **39**, 470 (2014).

29. S. D. Jackson, "Cross relaxation and energy transfer upconversion processes relevant to the functioning of 2 μm Tm^{3+}-doped silica fibre lasers," Opt. Commun. **230**, 197–203 (2004).

30. Z. Li, Y. Jung, J. M. O. Daniel, N. Simakov, M. Tokurakawa, P. C. Shardlow, D. Jain, J. K. Sahu, A. M. Heidt, W. A. Clarkson, S. U. Alam, and D. J. Richardson, "Exploiting the short wavelength gain of silica-based thulium-doped fiber amplifiers," Opt. Lett. **41**, 2197 (2016).

31. L. Zhang and H. Hu, "The effect of OH^- on IR emission of Nd, Yb and Er doped tetraphosphate glasses," J. Phys. Chem. Solids **63**, 575–579 (2002).

32. V. P. Gapontsev, S. M. Matitsin, A. A. Isineev, and V. B. Kravchenko, "Erbium glass lasers and their applications," Opt. Laser Technol. 189–196 (1982).

33. X. Feng, S. Tanabe, and T. Hanada, "Hydroxyl groups in erbium-doped germanotellurite glasses," J. Non. Cryst. Solids **281**, 48–54 (2001).

34. E. Snoeks, P. G. Kik, and A. Polman, "Concentration quenching in erbium implanted alkali silicate glasses," Opt. Mater. (Amst). **5**, 159–167 (1996).

35. N. P. Barnes, B. M. Walsh, and E. D. Filer, "Ho:Ho upconversion: applications to Ho lasers," J. Opt. Soc. Am. B **20**, 1212 (2003).

36. O. Humbach, H. Fabian, U. Grzesik, U. Haken, and W. Heitmann, "Analysis of OH absorption bands in synthetic silica," J. Non. Cryst. Solids **203**, 19–26 (1996).

37. R. Schimmel, "Towards more efficient Praseodymium Doped Fibre Amplifiers for the O-Band," PhD Thesis, Technische Universiteit Eindhoven, (2006).

38. D. W. Hewak, J. A. Medeiros Neto, B. N. Samson, J. Wang, H. J. Tate, A. Pearson, W. S. Brocklesby, G. Wylangowski, R. I. Laming, D. N. Payne, A. Jha, M. Naftaly, S. Jordery, and M. Poulain, "Spectroscopy of Pr^{3+}-doped low-phonon-energy glasses based on halides and sulfides," Proc. SPIE **2073**, 2073102 (1994).

39. N. Simakov, Z. Li, Y. Jung, J. M. O. Daniel, P. Barua, P. C. Shardlow, S. Liang, J. K. Sahu, A. Hemming, W. A. Clarkson, S.-U. Alam, and D. J. Richardson, "High gain holmium-doped fibre amplifiers," Opt. Express **24**, 13946 (2016).

40. P. C. Becker, N. A. Olsson, and J. R. Simpson, *Erbium-Doped Fiber Amplifiers : Fundamentals and Technology* (Academic Press, 1999).

41. R. Olshansky, "Noise figure for erbium-doped optical fibre amplifiers," Electron. Lett. **24**, 1363 (1988).

42. E. Desurvire, "Analysis of noise figure spectral distribution in erbium doped fiber amplifiers pumped near 980 and 1480 nm," Appl. Opt. **29**, 3118 (1990).

Chapter 3.

CO_2 Laser Processing

3.1 Introduction

CO_2 laser radiation experiences significant attenuation in silica, with typical penetration depths ranging from 5 – 30 µm at room temperature [1]. Furthermore, the absorption coefficient grows rapidly with temperature. This effect enables localised heating of the glass and can be used in a variety of applications. Previously demonstrated processes include repairing surface damage [2], fabrication of arbitrary surface profiles [3], laser polishing [4], and surface ablation of various glass surfaces [5]. The non-contact nature of CO_2 processing is an advantage for high power applications as it results in a surface that is far cleaner than if a physical contact method were to be utilised.

Figures 3.1a) – 3.1d) show the various optical fibre structures that CO_2 laser processes have been developed for as part of this project. The processes developed include fibre end-face preparation, removal of polymer coatings, cladding surface modification, chemical-free etching and bulk end-capping.

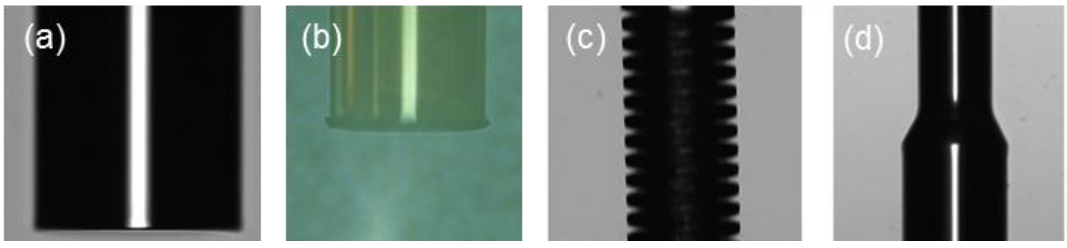

Figure 3.1: Examples of various laser processed structures for optical fibres. a) A flat-cleave fabricated using CO_2 processing in a 400 µm diameter fibre. b) A cleaved capillary with a 180 µm diameter and a 30 µm wall thickness. c) A cladding light stripper fabricated in a 250 µm diameter fibre. d) An illustration of the chemical free etching capability.

3.2 Absorption of CO_2 radiation in fused silica

In many processing applications, it is advantageous to prevent volume heating of the fibre due to the potential for dopant diffusion, surface melting, surface deformation and unwanted bulging of fibre surfaces. To avoid operating in this regime, it is necessary to perform the processes using a wavelength that has a minimal absorption depth in silica. By operating in this strongly absorbing regime, the deposition of energy is limited to the surface of the fibre and enables very precise control of ablation depth.

Silica glass is very strongly absorbing in the 9 – 11 µm spectral region. Transmission measurements reveal that <50% is transmitted through a 26 µm thick sample of pure fused silica as shown in Fig. 3.2a) [1]. Indeed, at 8-10 µm, this measurement is limited by signal-to-noise due to the strength of the absorption. Examination of the complex coefficient of propagation shows that it is several orders of magnitude stronger at 9.4 µm than that at 10.6 µm as shown in Fig. 3.2b). As a result, this wavelength can been used to measure extremely low levels of residual oxide contamination in silicon wafers due to the strength of the Si – O bond resonance at 9.4 µm [6].

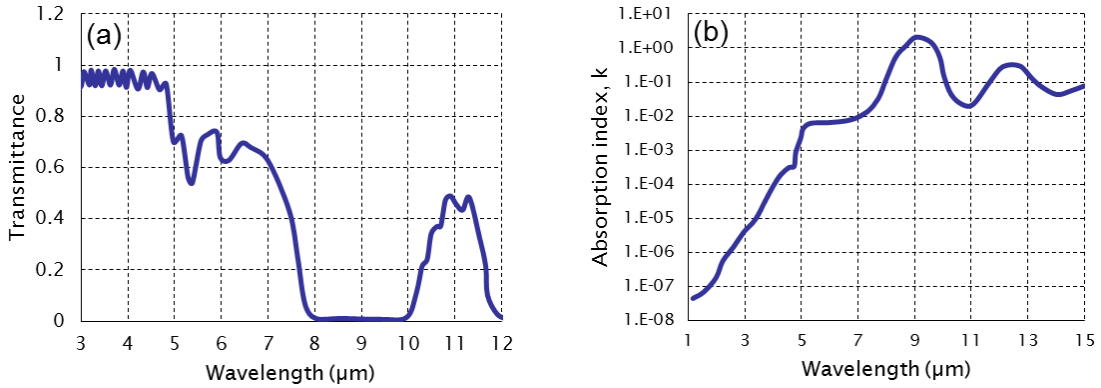

Figure 3.2: a) Transmission of radiation through a 26 µm thick sample of fused silica [1]. b) imaginary component of refractive index in silica glass from 1 – 35 µm showing a strong feature at 8.5-9.6 µm [6].

Simple transmission measurements are greatly complicated by the fact that substrates used are of a similar longitudinal dimension to the wavelength that is used to characterise them. In addition there are also complications arising from the potentially very strong reflections at the air-silica Fresnel interface. Finally as the substrate is heated, there is also an increased absorbance observed at 10.6 µm as shown in Fig. 3.3. Similar behaviour at 9.4 µm has not been reported.

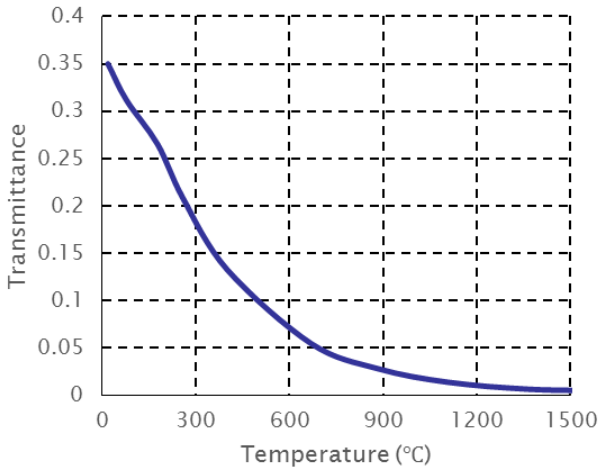

Figure 3.3: Transmission of 10.6 µm radiation through a 26 µm thick sample of fused silica as a function of temperature [1].

This strong interaction between the CO_2 laser radiation and the substrate makes it possible to achieve an almost completely surface heating effect. This is advantageous when processing fibres as it limits the temperature rise in the bulk of the material, and therefore any deformation and diffusion which could induce optical losses. We have exploited this effect to precisely machine a variety of silica structures and also in some cases, locally heat sections of bulk substrates for bonding applications.

3.3 Preform Shaping

In order to introduce the pump-scrambling shapes discussed in Section 2.2, it is necessary to machine the surface of the preform prior to drawing. Traditionally this is achieved by using an ultrasonic milling machine. However, it is also possible to use a CO_2 laser processing method to precisely etch away volumes of cladding material in order to achieve the required shape. In this section we compare these processes and discuss why the CO_2 laser processing method is more suited for our application.

3.3.1 Conventional approach: Ultrasonic milling

Ultrasonic machining is a unique non-traditional manufacturing process because it can produce parts with high precision that are made of hard and brittle materials which are often difficult to

machine using conventional techniques [7]. Here a tool bit is vibrated at an ultrasonic frequency, and gradually removes material using mechanical means. Additionally, ultrasonic machining is capable of manufacturing fragile materials such as glass and non-conductive metals. Ultrasonic machining is able to produce high-tolerance parts because there is no distortion of the worked material as there is no heat generation from the sonotrode against the work piece. Furthermore, no burrs are created in the process, thus fewer operations are required to produce a finished part. An illustration of the ultrasonic machining process is shown in Fig. 3.4.

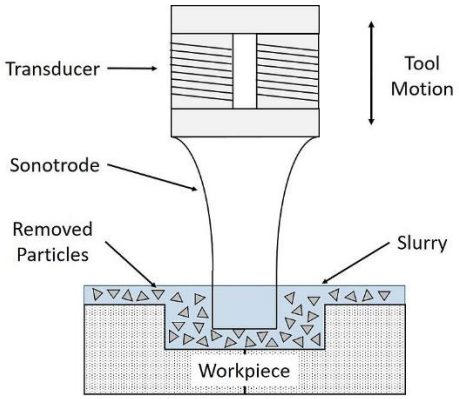

Figure 3.4: Illustration of an ultrasonic machining tool and how it interacts with the workpiece. (https://en.wikipedia.org/wiki/Ultrasonic_machining)

Because ultrasonic machining is driven by microchipping or erosion mechanisms, the material removal rate of metals can be slow and the sonotrode tip can wear down quickly from the constant impact of abrasive particles on the tool.

In some cases, the surface of the preform after ultrasonic milling is not of optical quality and has a large degree of roughness. In order to prevent scattering losses for the pump radiation, these surfaces are subsequently fire polished in an oxygen-hydrogen flame before drawing. This fire-polishing processes introduces substantial hydroxyl impurities into the surface, and is undesirable if radiation at 2 µm is propagating in the cladding. An alternative preform processing method is therefore desired.

3.3.2 CO_2 laser processing of preforms

In this section we examine the use of CO_2 laser processing to shape the outside of a preform in order to achieve a symmetry breaking structure without introducing hydroxyl contamination. This

is a technique that has been previously demonstrated [8], but has not been as widely adopted as the ultrasonic milling approach. A schematic is shown in Fig. 3.5 where the preform is mounted vertically, rotated and translated while multiple CO_2 lasers are focussed onto the surface. Intensities of >10 kW/cm^2 heat up and vaporise a thin layer of silica on the surface. The aim is to prevent and minimize bulk heating and thermal processing of the preform while performing the required machining process.

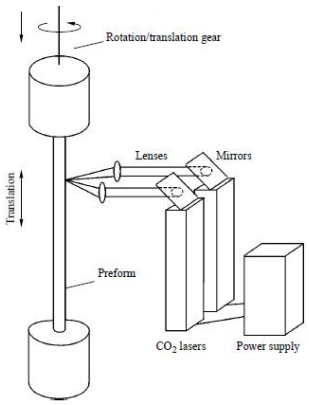

Figure 3.5: Schematic of laser based preform processing [8].

A similar system, but using only a single CO_2 laser was constructed by Shardlow et al. at the University of Southampton [9]. This system was used to fabricate a variety of surface profiles, as well as producing an optical quality finish and a very low hydroxyl contamination of the processed cladding surface. A schematic of this system is shown in Fig. 3.6.

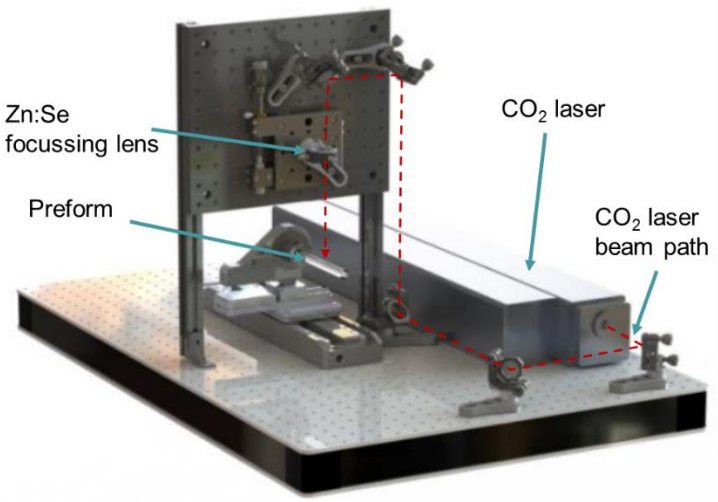

Figure 3.6: Schematic of laser based preform processing capability developed at the University of Southampton [9].

3.4 Splicing of optical fibres

The integration of active fibres into a laser or amplifier system is almost of equal importance as to the design of the fibre itself. Indeed, the most common failure mechanisms in a fibre laser arise at splices (due to excess splice loss), or at regions where there is excess cladding radiation that is able to interact with and destroy components. In the following we discuss the motivation for achieving high quality, reproducible cleaving with the intent of improving splice quality.

3.4.1 Typical splicing process

Optical fibre fusion splicing is the process by which a permanent, low-loss, high-strength, welded joint is formed between two optical fibres. The ultimate goal of optical fibre fusion splicing is to create a joint with no optical loss yet with the mechanical strength and long-term reliability that matches the fibre itself. As shown in Fig. 3.7a) the fibre end-faces are first prepared and then aligned with respect to each other. A heat source then raises the temperature to the point where the viscosity decreases (the viscosity of silica vs. temperature is shown in Fig. 3.7b)), and the fibres are pushed into each other by a controlled amount. Further heating then ensures that any residual surface defects are allowed to reflow such that the splice forms a cylinder with a continuous surface.

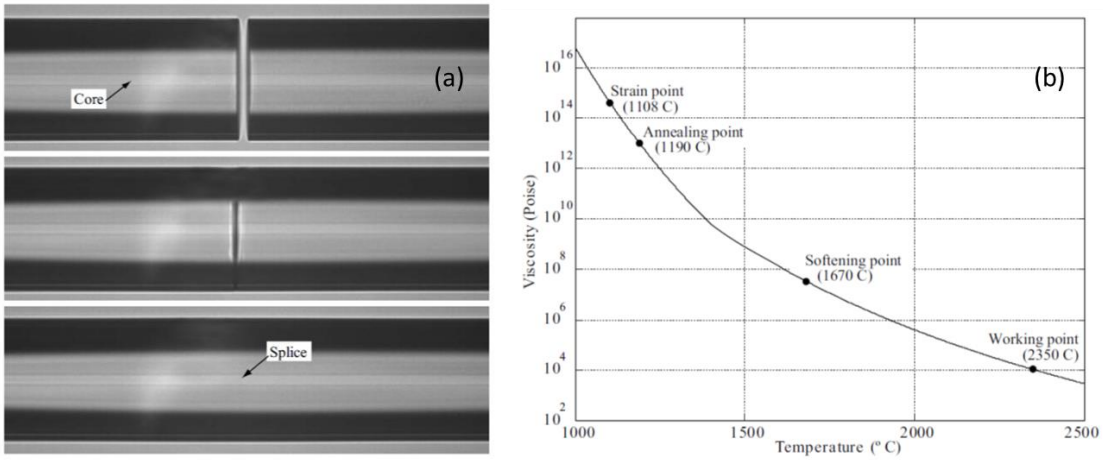

Figure 3.7: a) Images of the various stages of the alignment and splicing process [10]. b) Viscosity of silica as a function of temperature [10].

3.4.2 Splice loss

As the radiation propagates from one fibre to the other, it will experience losses depending on the properties of the individual waveguides and on the quality of the transition region. For single-mode and few-moded waveguides, the term splice loss refers to the difference between the power in the fundamental mode of the input fibre and the power in the fundamental mode of the output fibre. For very multi-mode waveguides, the term splice-loss is broader and refers to the difference in powers supported by all of the guided modes of the input and output waveguides. Understanding the losses and transformation of radiation at this point is important and an illustration of some of the complex parameters is shown in Fig. 3.8.

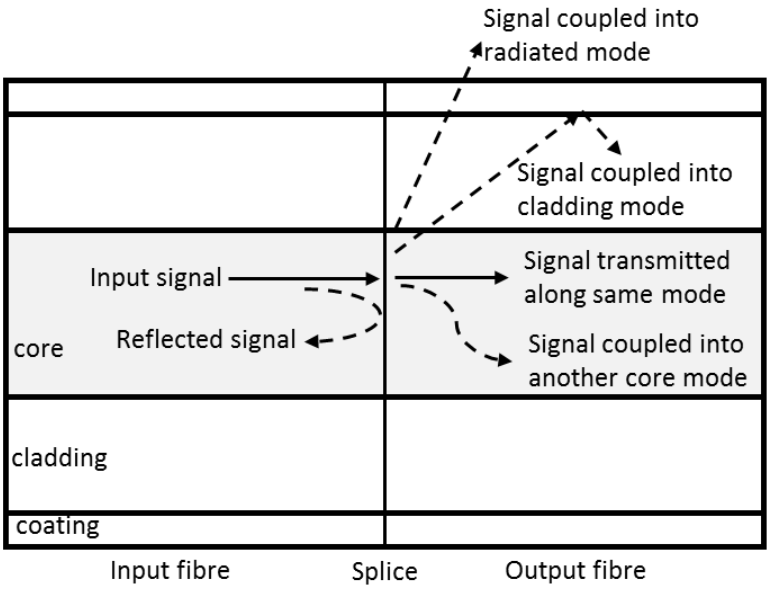

Figure 3.8: Illustration of the possible effects a splice can have on input radiation. Depending on the application, some of these will be more (or less) significant [10].

Typically a low cladding loss can be seen by visible inspection of the fibre surface with a microscope. Any defects, or rapid transitions and perturbations in the surface will lead to scattering losses as a fraction of the guided radiation is coupled into radiative modes. The core-losses can be estimated by visual inspection with a high performance vision system, or by making a measurement of the fundamental mode power levels in the input and output fibres.

The optical loss and reflectance of a fusion splice are typically much lower than alternative optical fibre connecting technologies. Fusion splices are permanent, and can exhibit mechanical strength and long-term reliability that approaches the original fibre itself – this also means that their

alignment, and hence their optical transmission, does not change over time or with temperature. Optical fibre fusion splices can also withstand extremely high temperatures or extremely high optical power densities as they do not allow dust or contaminants to enter the optical path.

3.4.3 Splice loss measurement

The term “splice loss” is one that is said very simply, but can actually mean a variety of different things. In the context of double-clad fibres using few-moded or single-mode cores, the term has many different meanings. An example of various common possibilities is summarised in Table 3.1 below.

Table 3.1: Various definitions of splice loss in the context of cladding guided pump radation, multi-moded or single-mode laser emission propagating in the core.

Source	Before splice	What happens at the splice interface?	Splice loss refers to…
Pump radiation	Multi-mode radiation guided by cladding	Radiation will be redistributed amongst the many modes of the cladding and/or scattered into modes that are not guided by the outgoing fibre	Any radiation that is scattered outside of the cladding region of the outgoing fibre
Laser emission (in the context of multi-mode lasers)	Multi-mode radiation guided by a multi-mode core (distributed amongst various modes)	Radiation can be redistributed amongst the modes in the core, coupled to cladding modes, and/or scattered into modes that are not guided by either the core or the cladding of the outgoing fibre	Any radiation that is no longer propagating in the multi-mode core
Laser emission (in the context of single-mode lasers)	Single-mode radiation guided in one of the core modes (typically the LP_{01})	Radiation can be redistributed amongst the modes in the core, coupled to cladding modes, and/or scattered into modes that are not guided by either the core or the cladding of the outgoing fibre	Any radiation that is no longer propagating in the desired single-mode (typically LP_{01}) of the core

As the definition and understanding of splice loss changes between all of these cases, it becomes important that the measurement that is used to quantify these parameters is also modified. The measurement for the first two cases (multi-mode pump and multi-mode laser emission) is relatively simple and is illustrated in Fig. 3.9.

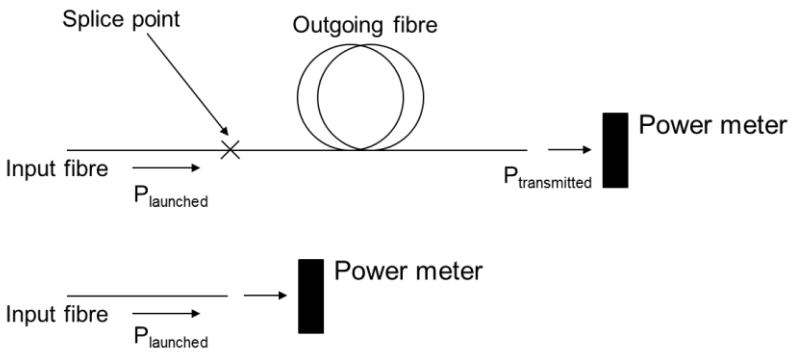

Figure 3.9: The measurement of the splice-loss between very multi-mode or robustly single-mode fibres is relatively simple and can be performed using a stable source and a power meter.

In this case the splice loss (*Loss*) can be presented as:

$$Loss = 1 - \frac{P_{transmitted}}{P_{launched}} \quad , \tag{3.1}$$

Where $P_{transmitted}$ and $P_{launched}$ are the output and input powers as illustrated in Fig. 3.9.

The situation becomes more complex if we only want to measure the radiation propagating in the core and the fibre has a double-clad geometry. Here, a cladding mode stripper device can be utilised to attenuate any radiation coupled into and guided by the cladding. Performing the measurement as shown in Fig. 3.10 will ensure that the power that is transmitted is only radiation confined to the core. This measurement is still fairly simple to make as it is easy to separate the cladding modes from the core modes using high index polymers. In fibres where an all-glass cladding is utilised, the cladding stripper will need to penetrate into the inner cladding in order to interact with those modes.

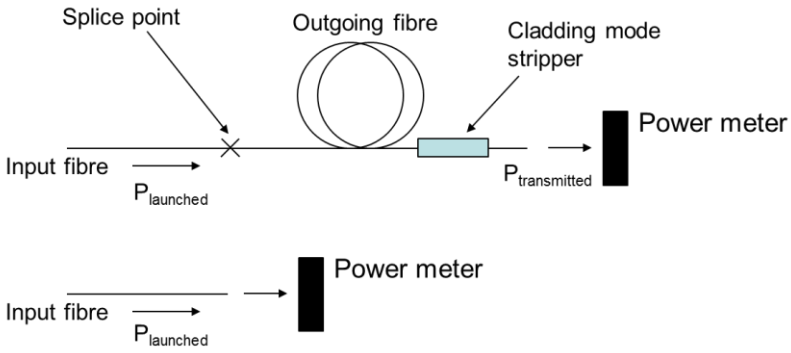

Figure 3.10: A cladding mode stripper device is inserted to remove any light that may have been scattered into the cladding modes. This ensures that the power measured is only of the core-propagating radiation.

In this case we are not concerned whether the core is single-mode or multi-mode, and again the loss of this splice can be represented as per Eqn. (3.1).

In the case where the outgoing fibre contains a few-moded core and a double-clad structure, the loss measurement increases in complexity. Typically we are concerned about the modal content in the output fibre, and ensuring that all of the radiation has been coupled into the LP_{01} mode. In order to measure the relative modal content we must perform what is commonly referred to as an S^2 measurement [11,12]. A diagram of this is illustrated in Fig. 3.11 where a broad-band, single-mode source is now launched into the outgoing fibre.

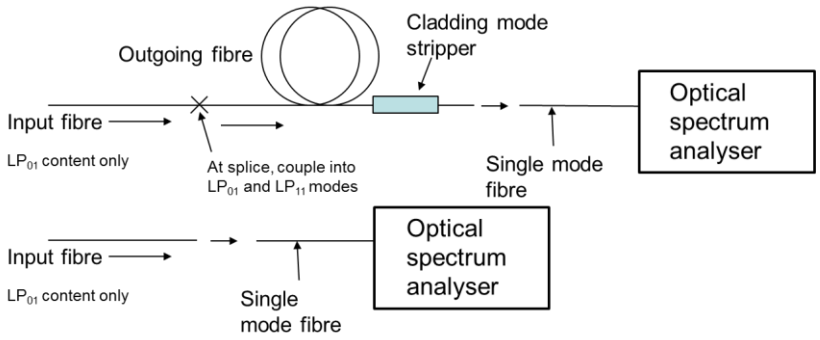

Figure 3.11: Mode coupling can be measured via the S^2 technique using a broad-band input source and an optical spectrum analyser at the output [12] .

In order to understand this measurement technique, let us assume that the input fibre only contains power in the LP_{01} mode. The splice is imperfect and some radiation is coupled into the LP_{01}, the LP_{11} and the cladding modes of the output fibre. A cladding mode stripper removes the cladding modes without perturbing the core modes and only the LP_{01} and the LP_{11} are present at the output of the fibre.

Immediately after the splice we can represent the electric fields for each mode (E_{01} and E_{11}) as follows:

$$E_{01}(\lambda, z) = E_1 e^{-ik_1 z} \quad , \tag{3.2}$$

$$E_{11}(\lambda, z) = E_2 e^{-ik_2 z} \quad , \tag{3.3}$$

$$k_{1,2} = n_{eff\ 1,2} \frac{2\pi}{\lambda} \quad , \tag{3.4}$$

Where the amplitude of each field is given by E_1 and E_2, the effective indices of each mode are given by ($n_{eff\,1}$ and $n_{eff\,2}$), with propagation constants ($k_{1,2}$) and the wavelength in vacuum is given by λ.

The wavelength and longitudinal position dependant terms contributing to the intensity of the radiation in the fibre $I(\lambda,z)$ can be expressed as:

$$I(\lambda, z) \propto |E_{01} + E_{11}|^2 \quad , \tag{3.5}$$

$$= |E_1|^2 + |E_2|^2 + 2|E_1 E_2| \cos\left(\frac{2\pi\left(n_{eff\,1} - n_{eff\,2}\right)z}{\lambda}\right) \quad , \tag{3.6}$$

By examining the expression within the cosine, we can see that there is a periodic interference that has a maximum at position ($z = L$) for wavelengths (λ_m) where the following condition is met:

$$\Delta n_{eff} \frac{L}{\lambda_m} = \left(n_{eff\,1} - n_{eff\,2}\right)\frac{L}{\lambda_m} = m \quad , \tag{3.7}$$

For integer m.

This leads to a wavelength separation ($\Delta\lambda_b$) between constructive interference peaks of:

$$\Delta\lambda_b = \lambda_{m+1} - \lambda_m = \Delta n_{eff} \frac{L}{m(m+1)} \quad , \tag{3.8}$$

Where Δn_{eff} is the difference in effective index between the two modes.

Let us consider a parameter set that is representative of a fibre laser, the length of active fibre is typically L = 5 m, modal index separation of $\Delta n_{eff} = 10^{-4}$, operating wavelength of λ = 2 µm, i.e. m = 250 and is >>1. This means that we can make the approximation that m ≈ m + 1 and the corresponding beat will have a wavelength period of:

$$\Delta\lambda_b \cong \Delta n_{eff} \frac{L}{m^2} = \frac{\lambda_m^2}{\Delta n_{eff}\, L} = 0.8\, nm \quad , \tag{3.9}$$

When measured with an OSA, the output spectrum at various transverse positions will have a modulation superimposed which will have a spectral beat corresponding to this value. The resolution of a typical OSA in this wavelength region is 0.05 nm (Yokogawa) and can easily resolve these fluctuations. The amplitude of the modulation can then be related to the relative amplitude of the LP_{01} and LP_{11} modes. Fundamentally, the modal dispersion has created a beat pattern that is superimposed on the broadband spectrum that was launched into the optical fibre.

It is important to point out that the measurement must be made in the transverse position where the field amplitudes are non-zero for the modes involved – otherwise there will be no interference and consequently no modulation. In more advanced cases and systems, the single-mode input fibre into the OSA is raster scanned in the transverse plane (x, y) to build up an entire summary of spectra at each point. This is useful when wishing to reduce the noise-floor on the measurement, or when wishing to avoid null-points when there are many modes present.

3.4.4 Splice loss optimisation - fibre design

The first significant parameter that plays a role in determining the splice loss is the mode-field diameter of input and output fibres. The loss of a splice between fibres with mismatched mode-field diameters is given by:

$$Loss = 1 - \frac{4w_1^2 w_2^2}{(w_1^2 + w_2^2)^2} \quad , \tag{3.10}$$

Where the *Loss* is the insertion loss of the splice and the mode-field diameters are w_1 and w_2. The loss estimate in Eqn. (3.10) assumes that both mode profiles are Gaussian. In some scenarios, this is not an accurate representation. In such case where the mode profiles are non-Gaussian, an overlap integral approach is necessary to estimate the splice loss [10].

It is possible, by design of the fibre and by producing a specific splice heating profile to diffuse the cores of each fibre such that the MFDs match at the splice. Care must be taken here to ensure that the transition regions are sufficiently adiabatic to ensure that there is no mode-coupling that occurs. An illustration of a mismatched splice and thermally expanded cores is shown in Fig 3.12.

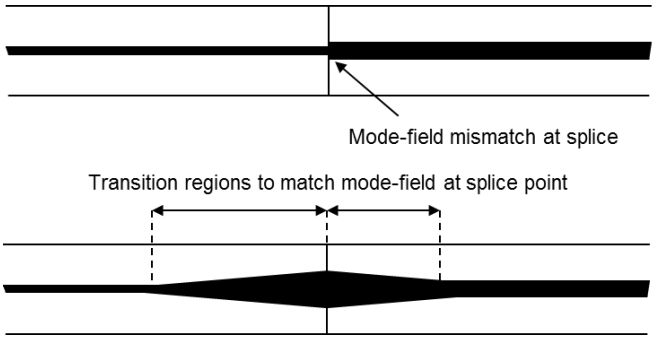

Figure 3.12: Mismatched mode-field diameters can cause excess splice losses. In some cases it is possible to mitigate these losses by further thermally processing and expanding the cores.

3.4.5 Splice optimisation – transverse alignment

Excellent transverse alignment is essential to ensure both low core and cladding losses. Figure 3.13 illustrates transverse misalignment that may occur during a splicing process. This typically places a requirement of motion resolution in the transverse dimension that is <1 µm for very multi-mode waveguides, and <0.1 µm for single-mode cores. The splice loss as a function of the transverse misalignment is given by:

$$Loss = 1 - e^{-\frac{\Delta x^2}{w^2}} , \quad (3.11)$$

Where the *Loss* is the insertion loss of the splice, Δx is the transverse misalignment of the two fibres, and w is the mode-field diameter of both fibres.

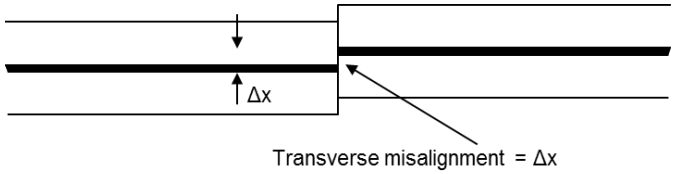

Figure 3.13: Illustration of transverse misalignment. This misalignment can lead to both core and cladding mode losses.

3.4.6 Splice optimisation – longitudinal alignment

The amount of distance that the fibres are pushed into each other during the splice – typically termed the 'hot-push' – will impact the cladding surface profile. Too much or too little hot-push can deform the cladding and also deform the core as shown in Fig 3.14. This can lead to both large cladding mode and core-mode losses as these transition regions will typically not be adiabatic. There is no general formula to describe the losses here as they are highly dependent on the geometry of the fibre and the distribution of the radiation propagating in each waveguide.

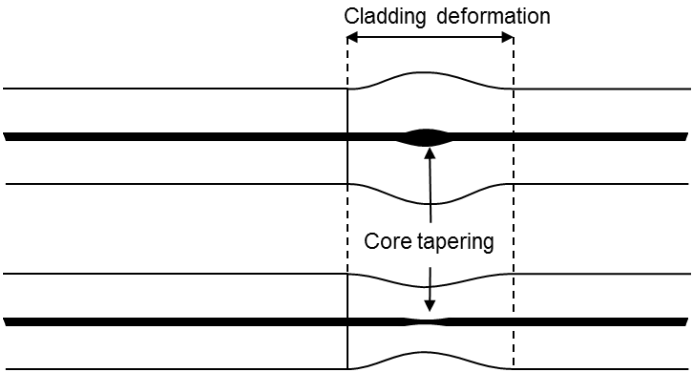

Figure 3.14: Too much or too little hot-push can lead to tapering or bulging of the fibre leading to both core and cladding losses.

3.4.7 Splice optimisation – angular alignment

A poor angular alignment of the cores can result from poor initial cleave angles and from poor angular alignment of the fibres in the splicer. This can lead to an angle remaining in the fibre after the splice as shown in Fig. 3.15, or for a kink to appear in the core. Either of these poses substantial problems – the expected loss due to an angle between two single-mode fibres with matched mode-field diameters can be predicted by using Eqn. (3.12):

$$Loss = 1 - e^{-\frac{\pi \Delta\alpha w}{\lambda n}}, \qquad (3.12)$$

Where *Loss* is the insertion loss of the splice, Δα is the angular deviation between the two fibres, w is the mode-field diameter of both fibres and n is the refractive index of both fibres.

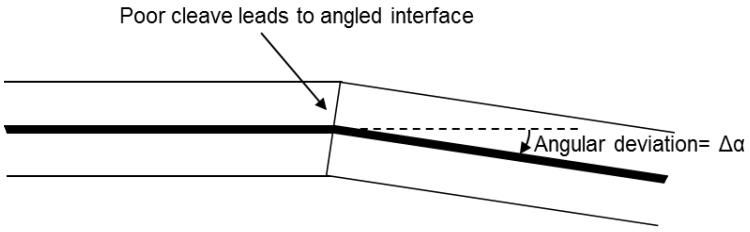

Figure 3.15: Poorly prepared or aligned fibre surfaces can lead to substantial losses at the splice point.

3.4.8 Splice optimisation – discussion

In many cases, the physical geometry of the fibres can be matched, well aligned and spliced to a high precision tolerance to produce a minimum core-loss. However residual defects in the cladding can create substantial cladding losses and ultimately degrade the performance and lifetime of the splice as shown in Fig. 3.16. Further heating of this structure can cause the surface to flow, but potentially at the cost of deforming the core. As a result, every splice may require careful consideration to maintain a balance between acceptable core losses and cladding losses and the desired mechanical stability of the splice itself.

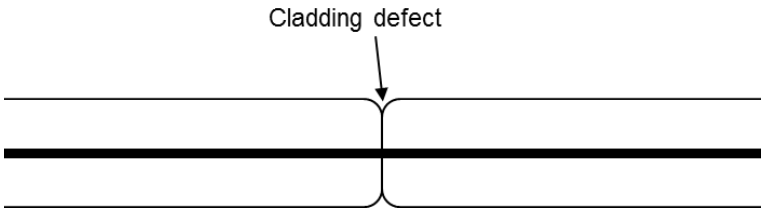

Figure 3.16: Residual defects left in the cladding may not affect the losses for the core-propagating radiation, but may mechanically degrade the splice point. It is important to maintain a balance between the acceptable splice losses as well as the mechanical stability of the splice itself.

Also it is important to point out that the various deformations can, and usually do occur in combination with each other. This does not always provide the operator with a simple solution or diagnostic as to the most significant cause of the loss. Typically in optimising a splice routine, the variables that are under the operator's control will affect more than one combination of the deformations and so it must be appreciated that splice optimisation is not always a trivial matter.

3.5 Cleaving

In order to avoid excess losses during fusion splicing, the surface of the fibre end-face must be smooth, defect-free and perpendicular to the fibre axis. A sufficiently perpendicular and planar fibre end-face can be achieved via a process termed cleaving, in which the glass fibre is fractured in a controlled manner. As we have already discussed, the cleave quality is an important factor controlling fusion splice loss. Here, we address the limitations of conventional commercial large diameter fibre cleavers by examining laser processing of optical fibres.

3.5.1 Characterisation of cleave end-face profiles

Due to the cylindrical nature of the optical fibre, inspection using side illumination can often give misleading results. With this in mind characterisation of cleaving processes was performed by measuring end-face surface profiles with a phase shifting interferometer operating with a LED source at ~650 nm (Nyfors, Cleavemeter 3D). A schematic of such a measurement system is illustrated in Fig. 3.17. A Michelson interferometer is constructed by placing the fibre surface and a reference plate in the image plane of a path matched interferometer. It is important to use a relatively low coherence source such as an LED in order to avoid interference effects from various apertures, or from the other end of the fibre. The interference pattern is then observed on a camera. Any length variation between features on the fibre surface and reference surface results in interference fringes. By adjusting the position of the reference surface, it is possible to track the motion of the interference pattern and accurately reconstruct the topology of the fibre surface.

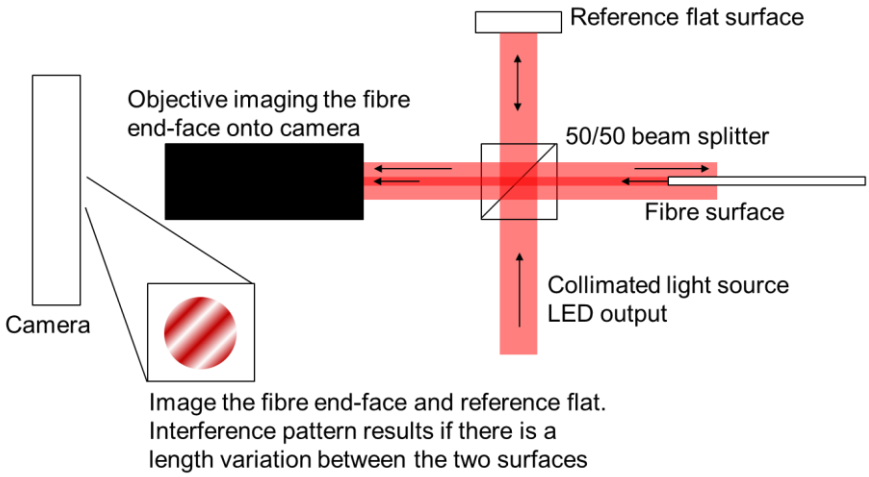

Figure 3.17: End-face interferometer configuration for the characterisation of the end-face surface of an optical fibre.

3.5.2 Mechanical cleaving techniques

Reproducible and precise cleaving of optical fibres is of significant importance to the fibre laser manufacturing and telecommunications industries. With the advent of complex optical fibre designs, including non-circular claddings, micro-structures and the presence of interfaces between materials of substantially different dopant compositions, mechanical cleaving techniques which rely on crack propagation often result in poor surface quality and a low process yield. A large variety

of solutions and products are available that aim to minimize cleave angles, yet the typical quoted value from various manufacturers is ~0.3° for a 400 µm diameter fibre [13–15]. This corresponds to a deformation of 2 µm across the fibre surface. In addition, there are process features such as the blade initiation site, misting and hackle that can lead to scattering losses and potentially cause catastrophic damage in certain applications.

For a standard tension and scribing cleaving process, selection of the optimum cleaving tension is essential to reduce the presence of initiation features, misting and hackle defects as illustrated in Figs. 3.18a) – 3.18b). Ideally the entire end-facet of the fibre should have a smooth mirror finish after the cleaving process as shown in Fig. 3.18c).

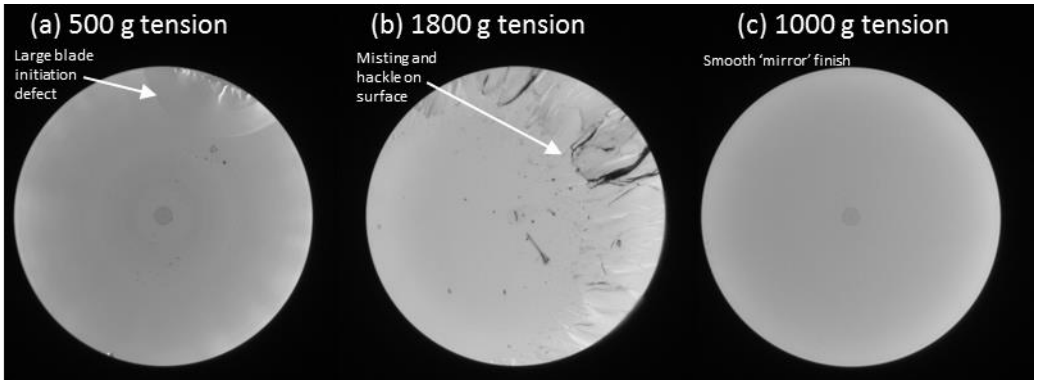

Figure 3.18: a) End-face image of mechanically cleaved optical fibre where the tension was too low. A large initiation defect is introduced as a result. b) End-face image of mechanically cleaved optical fibre where the tension was too large. This leads to a reduced mirror region and presence of mist and hackle. c) End-face image of the fibre cleaved under the optimal tension conditions showing a larger mirror finish on the surface [10].

3.5.3 Laser "cleaving" in commercially available systems

Another method capable of achieving flat fibre end-faces is to use a CO_2 laser to cut the fibre. This process is no longer a "cleave" in the traditional sense of crack propagation, but is usually referred to as such since the application and the fibre end-face produced are similar.

CO_2 laser "cleaving" naturally has no initiation features, nor any residual misting or hackle as there is no propagating shock wave. Instead the surface is typically very smooth due to it being melted and fire-polished. While fibre end-face preparation using CO_2 lasers has been previously demonstrated, these approaches have largely been limited to processing the fibre in a strong

thermal regime. As a result, the fibre end-face takes on a more rounded shape due to the highly thermal nature and reflow effects that occur during the process. The resulting end-face rounding is typically >4 µm topography over the fibre diameter [16,17].

While not presenting a problem where the application is for fibre preparation for termination or connector fabrication, this rounding is an issue for splicing applications. After splicing the rounded surfaces typically leave a defect at the edge of the fibre as shown in Fig. 3.19. This defect will cause scattering of any propagating pump radiation and degrade the mechanical strength of the splice. It is possible to remove and eliminate this defect by using an extremely hot and long splice routine, essentially melting and reflowing the glass – and this may be a satisfactory solution for highly multi-mode fibres. However, in the case of fibres with single-mode or few-moded cores, this will lead to significant diffusion and potentially distortion of the core – subsequently causing significant splice loss and mode coupling.

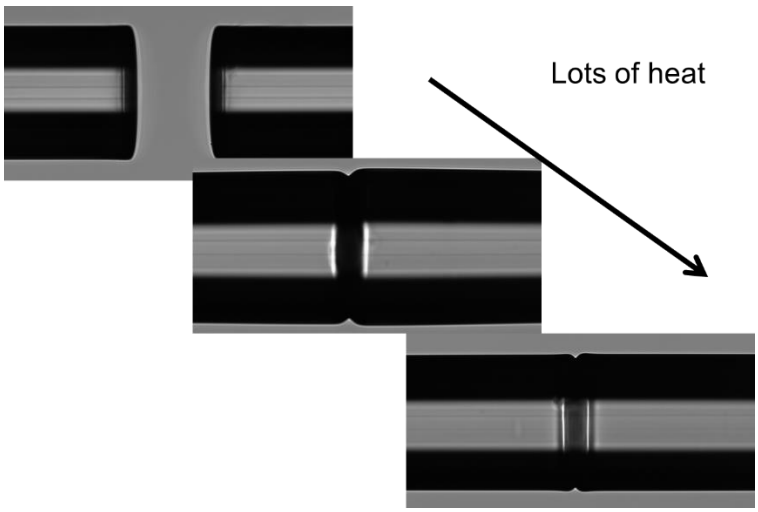

Figure 3.19: Splicing fibres that have been cleaved with a commercial laser cleaver that has a substantial amount of thermal processing. A cladding defect remains despite substantial heating and hot-push in the splice routine.

3.5.4 A new approach to laser cleaving

In contrast to commercial laser cleaver solutions, we have demonstrated a repeatable process that produces an end-face profile topography of less than 400 nm across the entire surface of a 400 µm diameter fibre with negligible rounding at the fibre edges and cleave-to-cleave reproducibility to within 200 nm [18]. The magnitude of this end-face topography is equivalent to the surface

deformation associated with that of a 0.06° angle cleave. This total deformation is also a factor of 5 smaller than the deformation associated with conventional mechanical cleaving and a factor of 10 smaller than commercial CO_2 laser cleaver solutions.

The process itself is insensitive to the original fibre end-face condition, with fibre preparation requiring only stripping of the polymer coating as shown in Figs. 3.20a) and 3.20b). Other authors have investigated and demonstrated the use of CO_2 lasers to ablate and remove the polymer coating [19]. The combination of these processes could enable a completely operator independent process of preparing, stripping and cleaving of the fibre.

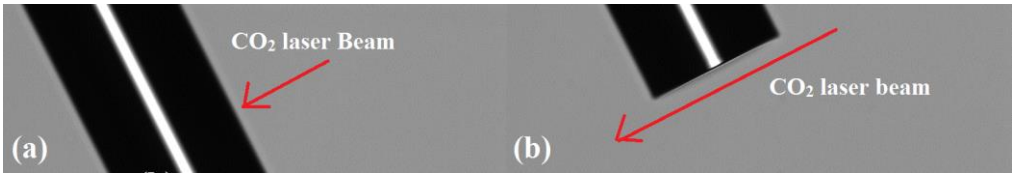

Figure 3.20: a) Only stripping of the fibre is required as a preparation process prior to cleaving. b) Resulting end-face after a CO_2 'cleaving' process [18].

3.5.5 Experimental set-up of the CO_2 laser cleaver

A schematic of the CO_2 laser fibre processing set-up is shown in Fig. 3.21a). The fibre is held in a rotary stage that can be linearly translated in three orthogonal axes and tilted in the plane of incidence of the laser. A 100 W pulse width modulated 9.6 µm wavelength CO_2 laser beam is focused on to the optical fibre using a 25 mm focal length ZnSe aspheric lens. The beam diameter of the CO_2 laser at the laser exit aperture is ~3.8 mm with a full angle divergence of 3.6 mrad and an $M^2 \approx 1.2$. The beam expands to a diameter of ~7 mm at the ZnSe lens, which focuses the beam to a spot diameter of ~50 µm at the focus. This was confirmed using a 90/10 knife-edge measurement technique. A visual indication of the spot size is shown in Fig. 3.21b) where the process feature observed is about a factor of 10 smaller than the diameter of the 400 µm fibre.

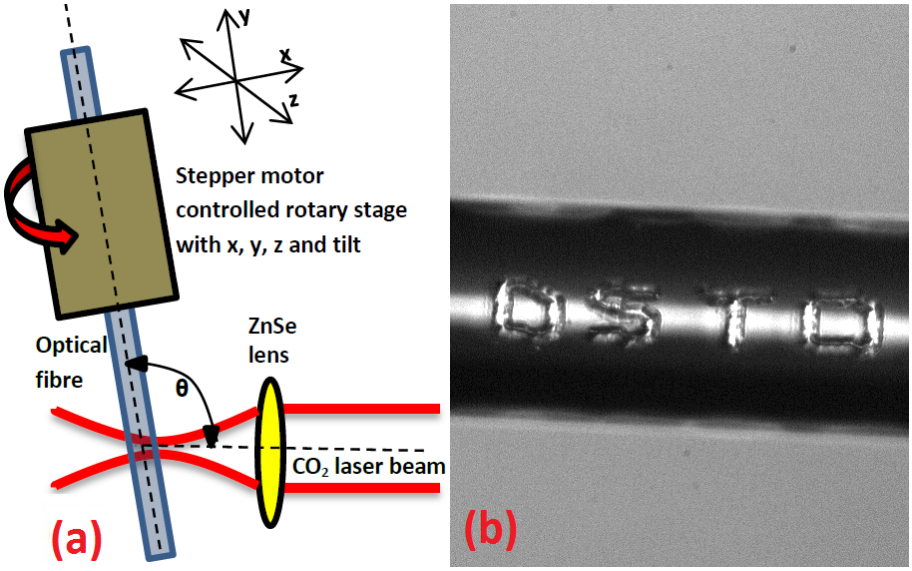

Figure 3.21: a) Schematic of the CO_2 laser cleaver b) Illustration of processing feature size [18].

In all configurations, the fibre was positioned as shown in Fig. 3.22a). Initially the laser irradiates a large volume of the glass, and there is substantial heating and material removal as shown in Fig. 3.22b). The temperature of the irradiated zones then drops below the evaporation temperature of silica glass because the fibre is no longer in the direct path of a focused Gaussian beam as shown in Fig. 3.22c) – 3.22d). At this point, the process is dominated by laser polishing of the fibre end-face surface. In this regime, the fibre end-face only interacts with a small portion of the CO_2 laser beam. It is also important to remove any heat-effected zone from the initiation of the process and the fibre is fed slowly down into the CO_2 beam. This allows for very fine control of the material removal and the subsequent production of smooth features with dimensions an order-of-magnitude less than the CO_2 laser wavelength. Final fire-polishing steps are shown in Figs. 3.22e) – 3.22f) which ensure an extremely smooth surface profile.

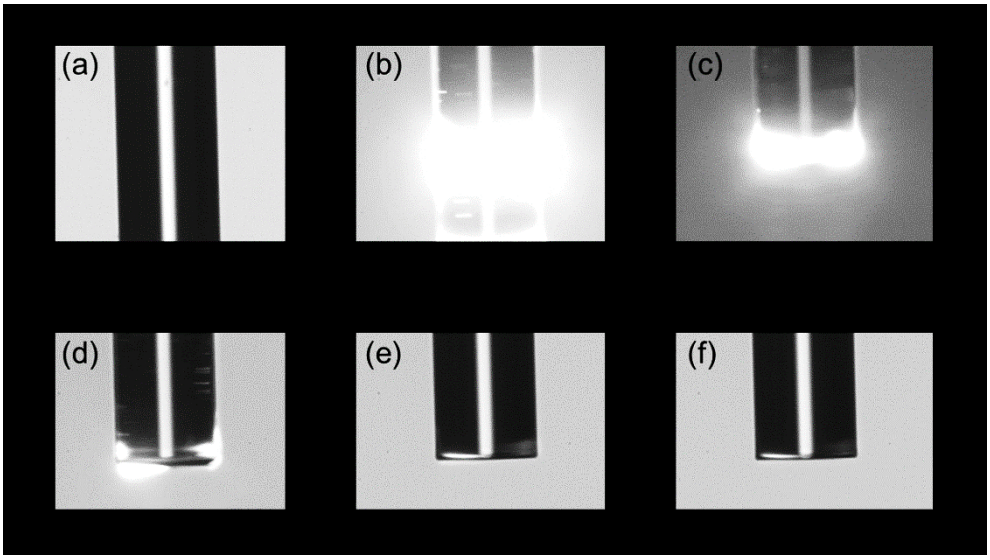

Figure 3.22: a) Initial position of the fibre in a cleave process. b) The laser illuminates the fibre resulting in a relatively large power absorbed by the fibre and large volumes of glass ablated. c) As the fibre is ablated, less radiation is intercepted and the process changes from an ablation regime to a polishing regime. d) The fibre is then moved downwards with the edge of the CO_2 laser beam effectively polishing and removing any heat-affected zone. e) Finer motion control is used to achieve a finer fire-polishing step prior to the end of the cleaving process. f) The fibre is now cleaved and can be removed from the machine [18].

3.5.6 Flexibility and reproducibility of CO_2 laser cleaving

The CO_2 laser fibre processing system described in Section 3.5.5 is capable of arbitrarily shaping fibre end-faces, resulting in profiles such as those shown in Figs. 3.23a) – 3.23f). By varying the pitch of the fibre with respect to the CO_2 laser beam, it is possible to produce profiles transitioning from convex to concave while maintaining a high degree of symmetry as shown in Figs. 3.23a) and 3.23b). The ablation depth for a fixed pitch can also be controlled by varying the pulse duration. To demonstrate the potential range of end-face structures that can be achieved a number of arbitrary structures were fabricated. In Fig. 3.23c) a ramp surface profile was created by firing the laser every 0.45° of spindle rotation, with increasing pulse durations from 40 µs to 70 µs. In Fig. 3.23d) alternating pulses of 40 µs and 45 µs created sub-micron periodic features and in Fig. 3.23e) and Fig. 3.23f) alternating pulsing for half and quarter spindle angles provides alternating high and low planes.

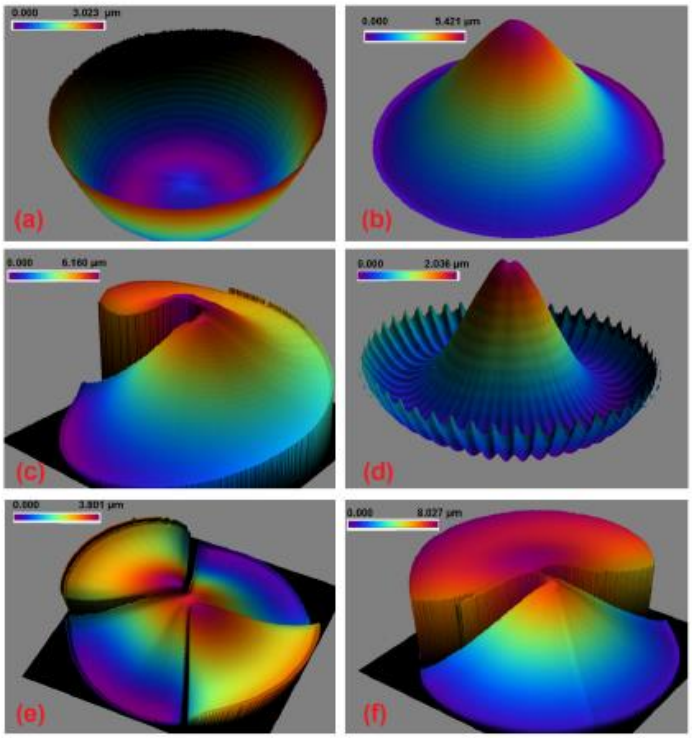

Figure 3.23: a) – f) Various end-face profiles that can be achieved by modulating the CO_2 laser pulse duration as a function of fibre rotational angle. It is possible to fabricate surfaces with concave or convex topographies and also break the circular symmetry [18].

The reproducibility of the CO_2 laser cleaving process was tested by cleaving 10 samples of 400 µm outer diameter fibre and measuring the resulting end-face profiles. Figure 3.24 shows the interference patterns obtained for each cleave. The variation between the surfaces had a standard deviation of <200 nm at each point on the surface.

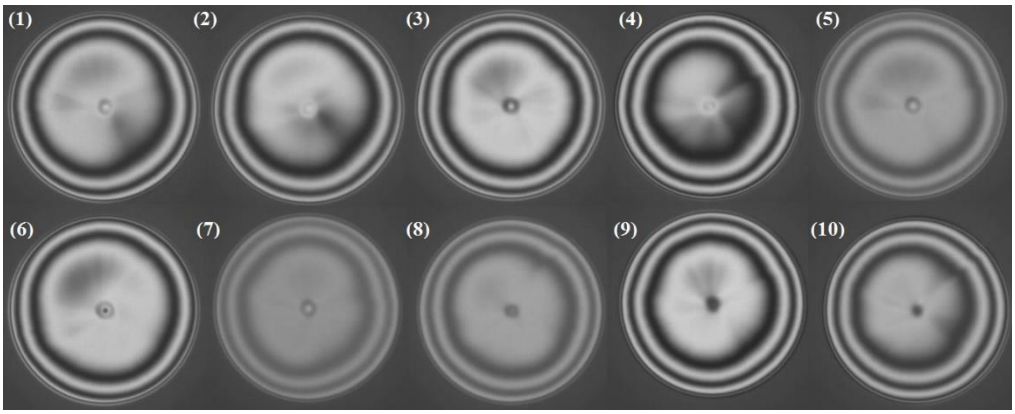

Figure 3.24: Interferometric characterisation of end-face profiles of 10 consecutive cleaves showing a high degree of reproducibility [18].

3.5.7 Discussion of the CO_2 laser cleaving approach

We have presented a 9.6 µm CO_2 laser processing technique suitable for the reproducible, rapid fabrication of near arbitrary fibre end-face profile shapes. The fabrication of a number of novel fibre end-face profiles including discontinuous phase steps and arbitrary concave and convex profiles demonstrates the versatility of this technique. Such complex profiles with sub-micron scale resolution cannot be fabricated using conventional cleaving or polishing techniques. Previous investigations of CO_2 laser cleaving have typically resulted in surfaces with a >4 µm topography over the fibre diameter [16,17,20]. In comparison, we have demonstrated a repeatable process that produces end-face profile topography of less than 400 nm across the entire surface of a 400 µm diameter fibre with negligible rounding at the fibre edges and cleave-to-cleave reproducibility to within 200 nm. The magnitude of this end-face topography is equivalent to the surface deformation associated with that of a 0.06° angle cleave.

3.6 Cladding light strippers

The efficient removal of high power excess cladding light without inducing significant core loss and beam quality degradation is of significant interest for the production and operation of robust, high power fibre lasers and amplifiers.

Light propagating in the cladding of a fibre laser can originate from a range of sources. It can be due to unabsorbed pump radiation that is transmitted through an active fibre, amplified spontaneously emitted light (ASE) leaving the core, co-propagating signal radiation leaked from the core due to splice or bend induced losses, or backwards propagating signal radiation due to reflections external to the fibre laser as illustrated in Figs. 3.25a) – 3.25b). For these reasons the cladding stripping method must ideally account for light of varying; power levels, propagating angles, direction and wavelength, without being thermally compromised.

In materials processing applications, the laser is commonly exposed to substantial back-reflections from, for example, highly reflective metal surfaces [21,22]. In such cases, isolation is necessary to prevent instability in the fibre laser. This isolation is typically achieved by applying a defocus to the beam, launching the beam in an off-centre direction or by beam quality degradation. In these cases, there may be a substantial amount of backwards propagating radiation coupled into the cladding of the fibre. It now becomes necessary to be able to remove this radiation from the cladding so that

it does not propagate to and damage the various fibre laser components or even the pump laser diodes. The power level of the radiation in the cladding can be in the many kW's of average power.

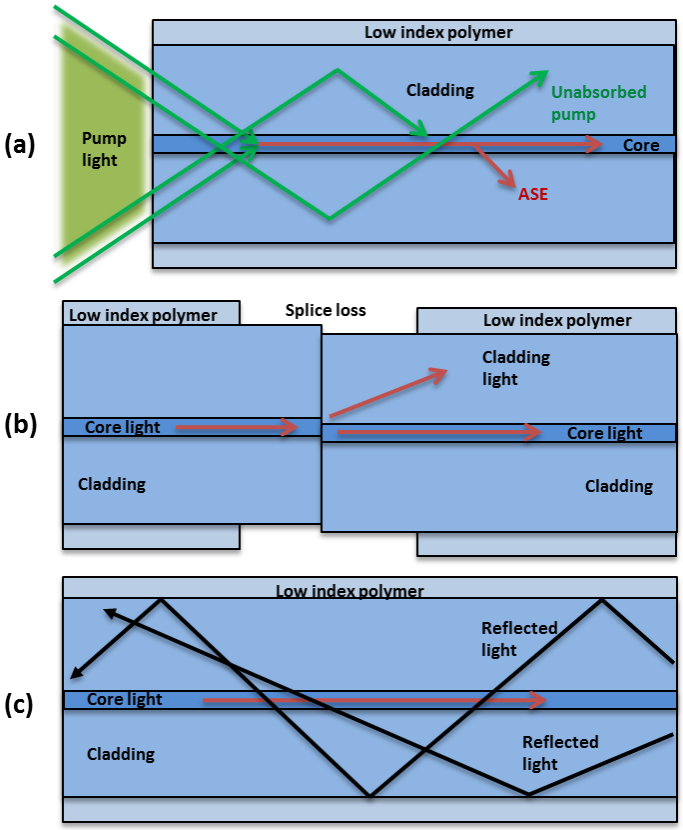

Figure 3.25: Unwanted radiation can propagate in the cladding of the fibre as a result of: a) Unabsorbed pump radiation or spontaneous emission not captured by the core. b) Scattering at splice points. c) Backward propagating radiation reflected from the end-facet of the fibre or from a work-piece being processed by the laser [23].

In Chapter 2 we have discussed parameters that could affect the efficiency of the active fibre. It was identified that complex, all-glass double-clad fibre geometries would be required in order to provide a low loss guide for the 2 µm pump radiation. While posing many advantages in terms of cleanliness and coating material flexibility, this also restricts our ability to access the inner cladding. Removing excess pump radiation is now a challenge as we cannot easily perturb the interface between the low index pump confining layer and the cladding where the pump radiation is propagating. By using a CO_2 laser, we are able to etch into the glass and perturb this layer, thereby allowing for robust, high power cladding light stripper (CLS) devices to be realised.

3.6.1 Conventional approach

A simple technique for removing excess cladding light involves coating the exposed surface of the fibre with a refractive index matched polymer. This frustrates and breaks the total internal reflection condition for the pump radiation and allows it to couple outside of the fibre. At high power levels, polymer based stripping methods [24,25] are much more likely to fail. Furthermore, standard polymers are unsuitable for use in thulium, holmium or erbium sources where the 1.5 – 2.2 µm radiation is subject to strong attenuation in the polymer, leading to localized heat zones, and rapid degradation of the polymer.

A number of groups have demonstrated all-glass CLS devices fabricated using mechanical polishing or CO_2 laser processing [26]. However there is little information provided about the exact process, the losses incurred, and the impact on the radiation propagating in the core. One group demonstrated the ablation and re-deposition of glass to create a scattering surface and achieved a device with a cladding loss of 13 dB over 8 cm [27]. Another group used soft metals as an absorptive stripping method suitable for high power operation and demonstrated up to 8.4 dB cladding loss for device lengths of 7 cm [28]. An alternative technique has been to etch the fibre and create a rough surface [29–31]. While yielding excellent results, this process involves the use of HF chemicals and a long process time to achieve reproducible results. Ideally a chemical-free approach is preferred for a production environment.

The different techniques previously demonstrated provide varying magnitudes of loss per unit length and demonstrated operating powers as shown in Table 3.2.

Table 3.2: CLS losses and power handling for various fabrication techniques [23].

Method	Loss (dB/cm)	Power stripped (W)	Ref
High index polymer	3.6	83	[25]
Soft metal coating	1.2	150	[28]
HF etched	2.9, 1.5, 1.7	90, 500, 200	[29–31]
Glass deposition	1.6	200	[27]
Cascaded polymer	3.6	150	[25]

3.6.2 CO_2 laser processing of fibres to fabricate cladding light strippers

The CLS devices developed here were fabricated using a 55 W, pulse-width-modulated (PWM) CO_2 laser (Coherent Scientific), operating at 10.6 µm. The laser was utilized to ablate channels of various depths, ranging from 5 µm to 75 µm on one side of an optical fibre. No rotational manipulation of the fibre was required in this process. 10.6 µm was selected for the CLS fabrication as opposed to 9.6 µm as was utilised in Section 3.5 due to the relaxed resolution required for the cladding surface modification as opposed to the cleaving process (10 µm vs. 0.5 µm).

The optical fibre was mounted on a vertical stepper motor controlled stage using V-groove clamps as shown in Fig. 3.26a), and a strain gauge was used to monitor the optical fibre tension. The tension was set to a value of 2 N and monitored throughout each CLS fabrication process. A drop in tension indicated overheating of the fibre and a potential subsequent core loss. A front view and a side view of the features and structures that were fabricated are shown in Fig. 3.26b) and Fig. 3.26c).

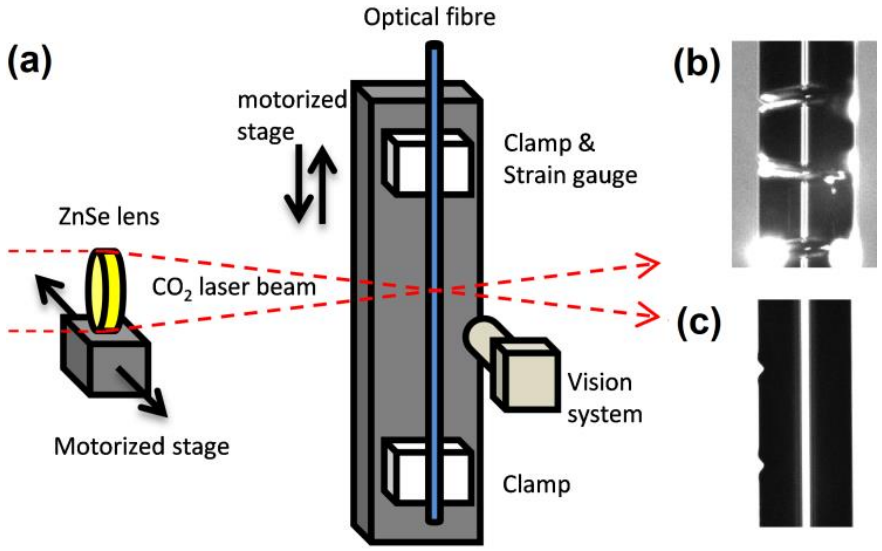

Figure 3.26: a) Schematic of CO_2 laser arrangement for the fabrication of CLS devices. b) Front view of the structures processed into the cladding of the fibre. c) Side view illustrating the depth of the grooves cut into the cladding [23].

A 25.4 mm diameter, 50 mm focal length ZnSe lens was used to focus the beam onto the optical fibre with a measured beam diameter of ~50 µm. The lens was mounted on a motorized stage enabling the lens to be swept across the beam over a distance of 1 mm. This optical layout was chosen for repeatable device fabrication as it ensured that the ablation depth was not critically dependent on the alignment of the beam to the centre of the optical fibre and the long working

distance relative to the fibre diameter ensured that there was no critical dependence on the distance between the fibre and lens.

A co-propagating He:Ne laser was used to assist in the alignment of the swept CO_2 beam to the fibre. The fabrication process was monitored visually using a CCD and a 2x telecentric objective with an 800 nm high pass optical filter. The fibre was backlit by a collimated 800 nm LED. Before fabrication, a portion of each fibre was mechanically stripped and then cleaned to remove the polymer coating. Following this, there was no other handling of the exposed glass in the process. The fibre was held by clamping over the original coating.

Control over the ablation depth of the surface features was achieved by varying the CO_2 laser pulse duration from 7.8 µs at an average power of 170 mW, up to 15.68 µs at 920 mW. The other process parameters were held fixed; pulse interval of 1.31 ms, ZnSe lens sweep rate of 2 mm s^{-1} and vertical stage velocity of 10 mm min^{-1}. These parameters resulted in the ablation depths shown in Fig. 3.27 for fibres of 250 and 400 µm outer diameter (OD).

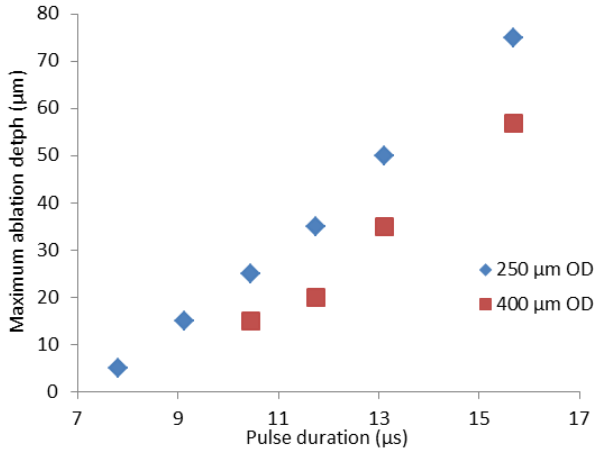

Figure 3.27: Cut depth as a function of CO_2 laser pulse duration for 2 different fibre types that are commonly used in double-clad laser construction [23].

The maximum ablation depth is greater for the 250 µm OD fibre compared to the 400 µm OD fibre as the evaporation rate of silica is temperature dependent [14] and the smaller volume reaches a higher temperature for a fixed set of CO_2 laser ablation parameters.

In order to simplify the analysis we investigated only devices fabricated with varying pulse duration, although it should be noted that there are numerous combinations of these parameters that will yield the same ablation depth.

3.6.3 Cladding loss characterisation

The optical loss of the glass cladding due to the CLS devices under investigation is a function of multiple parameters. These include ablation depth, length of the CLS, propagating angle of the radiation in the cladding fibre and pitch of the ablation channels. To investigate the device performance, the cladding loss was characterised as a function of incident angle of light and device length for CLS devices with various ablation depths at a fixed pitch.

To eliminate the noise from stray radiation that may be guided by the core, a coreless fibre with a 400 µm diameter, 0.46 NA cladding was utilized. This is representative of the cladding parameters of common fibres used to construct high power fibre lasers.

The loss was measured during the fabrication process by launching light into the optical fibre at a range of angles. To facilitate this, one fibre end was mounted on a computer controlled rotation stage, which was located 1.5 m from a collimated LED. The fibre was mounted such that the cleaved end-facet was located on the axis of rotation of the rotation stage. Irises were placed in the path of the LED to ensure that the radiation incident on the fibre was well collimated. Care was taken to ensure that the fibre was loosely spooled so as to minimize any mode-scrambling that could degrade the purity of the launched signal. By positioning the fibre near the CCD sensor without any lenses, we verified that the output radiation was propagating with the angle that corresponded to the launch conditions. The other end of the fibre was cleaved and a 4.5 mm aspheric lens with an acceptance NA of 0.48 was used to image the fibre end-face onto a CCD camera (Spiricon) as shown in Fig. 3.28. The large NA of the lens was essential to ensure that any radiation that could be guided by the 0.46 NA of the low index polymer/silica cladding interface was captured by the camera. The cladding stripper was fabricated in between these two ends. A laser line filter at 532 nm with 1 nm FWHM was used to reject stray light due to the room lights and the black body radiation associated with the heating of the fibre during fabrication.

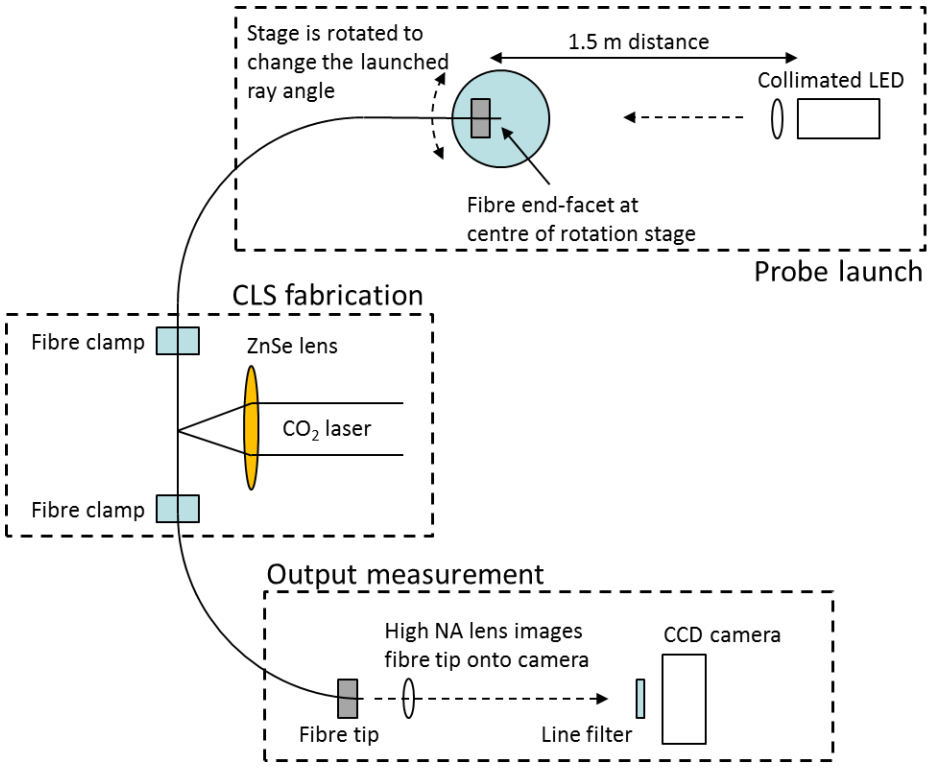

Figure 3.28: A collimated LED is launched into a fibre as it is scanned along a rotation stage. This effectively sets the internal propagating angle of the rays inside the fibre for a certain angle. By sweeping through the angle we are able to resolve the loss of the CLS as a function of internal angle [23].

This technique for the characterisation of the cladding loss is similar to those used by other groups characterising the angular dependant losses of optical fibre coatings [32]. This is also similar to techniques used by double-clad fibre manufacturers in characterising the optical quality and losses of high NA coatings. The losses for 3 different cut depths in a 400 µm fibre are shown in Fig. 3.29 and these results are summarised in Table 3.3.

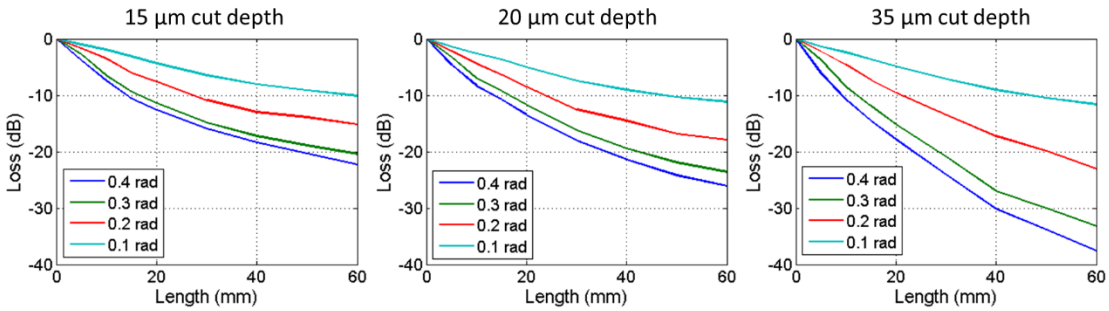

Figure 3.29: The loss of a cladding stripper in a 400 µm fibre with a 0.46 NA coating as a function of length and internal propagating angle for different cut depths [23].

Table 3.3: Loss of CLS devices written into a fibre with a 400 µm diameter at a 620 µm pitch for various ablation depths and launch angles [23].

Internal propagating angle	0.1 rad	0.2 rad	0.3 rad	0.4 rad
15 µm cut depth	1.5 dB/cm	2.0 dB/cm	3.3 dB/cm	3.6 dB/cm
20 µm cut depth	1.8 dB/cm	3.0 dB/cm	3.8 dB/cm	4.2 dB/cm
35 µm cut depth	2 dB/cm	3.8 dB/cm	5.5 dB/cm	6.1 dB/cm

3.6.4 Core loss characterisation

A diagram illustrating the core loss measurement is shown in Fig. 3.30. Here a 2 µm ASE source and an optical spectrum analyser were used to measure the core loss as a function of wavelength. For the purposes of this measurement a fibre with a 20 µm diameter, 0.09 NA core and a 400 µm diameter, 0.46 NA cladding was used. The cut-off wavelength for this core is 1950 nm. This fibre is representative of one that would be used in a high power thulium-doped fibre laser [15], and has similar core and cladding diameters to fibres commonly used in building high power ytterbium-doped fibre lasers [16].

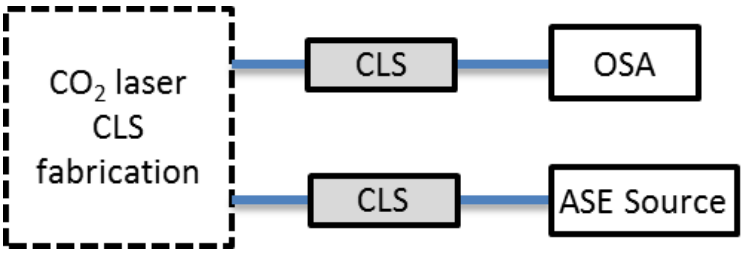

Figure 3.30: Schematic of the core-loss measurement. CLS devices were inserted before and after the fabricated device in order to remove the contribution from radiation propagating in cladding modes from the measurement [23].

The core loss measurement results are shown below in Fig. 3.31. The induced losses are measured to be <0.008 ± 0.006 dB/cm from 1950 – 2100 nm for all cut-depths. In fact, the loss measurement was limited by the noise and stability of the ASE source. As such we were unable to obtain an extremely accurate measurement of the broadband spectral losses. This measurement also confirms that there were no resonant loss features associated with the periodic CLS structure that could affect the performance of the devices over this wavelength region.

In a separate experiment, these devices where utilised on a high power, narrow band 1950 nm thulium pump laser and showed a <1% decrease in output power for a 35 µm cut, 60 mm device. This result is consistent with the low losses that were observed in-situ during fabrication.

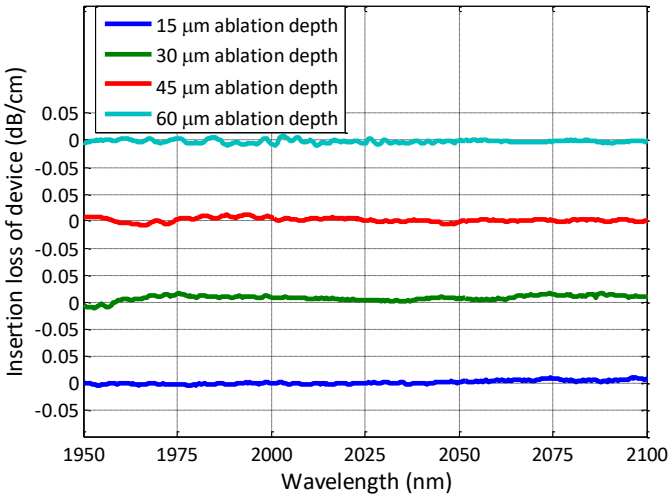

Figure 3.31: The loss of the CLS with various cut depths was measured to be less than <0.008 ± 0.006 dB/cm with the measurement limited by the stability of the ASE source [23].

3.6.5 Power handling demonstration

A device was fabricated in a fibre with a 20 µm diameter, 0.09 NA core and a 400 µm diameter, 0.46 NA cladding. The CLS device had a 60 mm length, with 35 µm deep cuts at a pitch of 500 µm. The device was suspended in air and glued into an aluminium package. To test the power handling capability of the device, a 400 µm diameter, 0.22 NA output fibre from a fibre-coupled laser diode was spliced onto this fibre. 300 W of radiation at 790 nm was then launched through the CLS device. Images taken both with a thermal camera and a normal visible camera are shown in Fig. 3.32a) and Fig. 3.32b). The maximum temperature rise from the laboratory temperature of 20°C for 300 W of stripped radiation was <60°C and was located near the stripped section of the fibre. This region is entirely glass, and is expected to be able to cope with a much larger operating temperature.

For 300 W of launched power, only 2.7 W was measured at the output yielding an extinction of >20dB. Also of note is that the fibre contained a core, which would have guided some of the launched radiation and preventing this power from being affected by the CLS device.

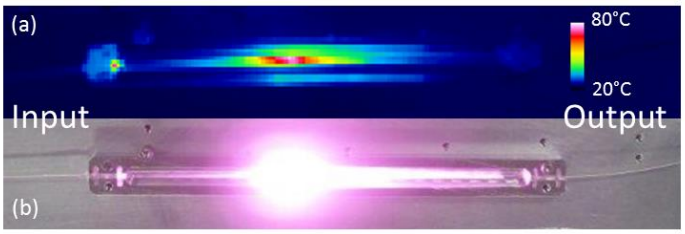

Figure 3.32: a) Thermal image of a 20 dB, 60 mm long, CLS device in a 20/400 µm passive fibre operating at 300 W launched power. b) Visible camera image of the same device under the same operating conditions. Negligible heating was observed near polymer areas suggesting that these devices are suitable for high power operation [23].

3.6.6 Discussion of cladding light stripper device development

A simple, alignment insensitive process for the fabrication of CLS devices has been presented. We have characterised the device performance in terms of core-propagation and cladding-propagation losses. Devices with large cladding losses and negligible core losses were fabricated and packaged.

Finally, we demonstrated the high power operation of such a CLS by removing 300 W of radiation from the cladding of an optical fibre, which provides adequate power removal for kW level fibre laser fabrication. Analysis of the thermal images indicated that the device was operating well below the damage threshold of the polymer fibre coating indicating that reliable long-term operation can be expected.

3.7 Fibre termination

In almost all applications, the radiation from the fibre has to exit the silica waveguide and will experience a Fresnel reflection at this glass-air interface. In order to prevent feedback from this interface from degrading the performance of the amplifier or causing other effects, it is necessary to manage this reflection and any reflected radiation properly. In this section we shall review traditional methods and discuss more advanced techniques developed to address this requirement during this project.

3.7.1 Conventional strategies

In order to reduce the back-reflections coupled into the core it is possible to use a large angle cleave or an end-cap. Fig. 3.33 shows illustrations of such conventional techniques.

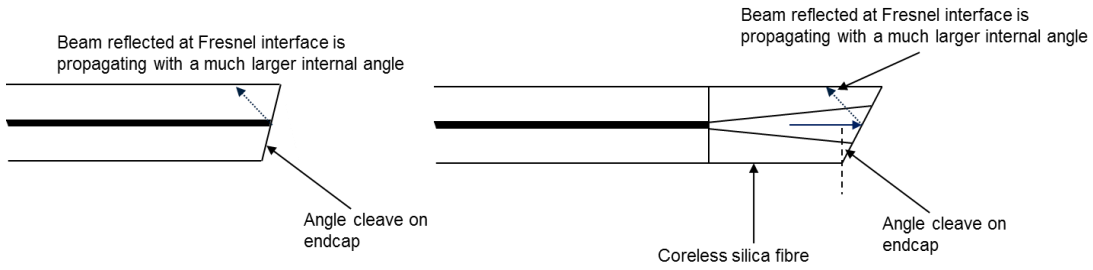

Figure 3.33: Comparison of various termination techniques illustrating some of the considerations that must be made in order to avoid feedback or end-facet damage.

Table 3.4 summarises the relative performance of either device. As can be seen, while the simple angle cleave is much more effective for reducing back reflections, it is also much less power scalable as the intensity is very high at the end-facet in comparison to the end-cap approach. Furthermore, if no AR coatings are used then both devices still suffer from having a relatively large power density at the end-face as well as a 4% power penalty. AR coating a small end-cap is problematic and only several companies have been able to demonstrate this at high power.

Table 3.4: Performance metrics of various termination processes

	Angle cleave	End-cap
Reflectivity	-50 dB	-30 dB (no AR coating) -50 dB (AR coating)
AR coating?	Only for very low power due to high power density at core	Moderate power levels
Ease of manufacture	Very simple: One cleave	More complex: Splice then re-cleave
Minimum transmission loss	4%	<4% with AR coating at moderate power levels 4% with no AR coating
Management of reflected radiation	Problematic at high power as this is now in the cladding	With AR coating, there is less radiation With no AR coating, again this is problematic

3.7.2 CO_2 laser end-capping

An alternative solution is to increase the dimension of the end-cap significantly as shown in Fig. 3.34. The output side of the substrate is now large enough to support an AR coating and the beam is allowed to expand significantly over the length of the device. However, conventional splicing techniques are no longer applicable here due to the very different thermal masses and physical dimensions of the substrate in comparison to the fibre. In order to achieve the localised heating of the substrate surface a CO_2 laser technique was utilised [33].

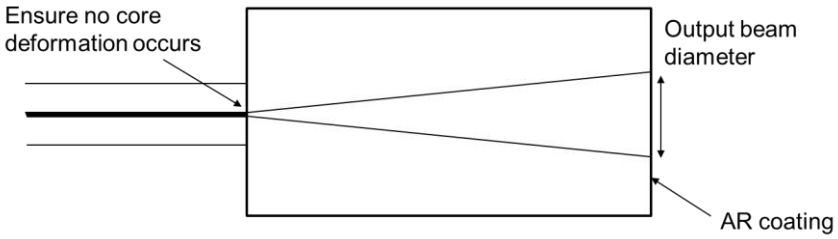

Figure 3.34: Proposed end-capping approach with a large bulk end-cap

In the process developed here, a 10 mm long end-cap with an AR coating with a reflectivity <0.25% at 1900 – 2200 nm was utilised. The estimated feedback can be predicted by comparing the diameter of the reflected beam with the diameter of the fibre core as shown in Fig. 3.35.

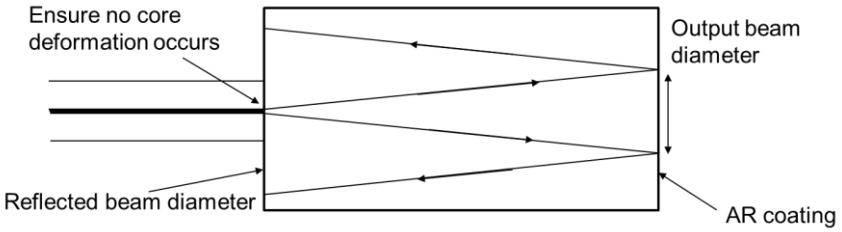

Figure 3.35: Predicted feedback protection for the reflected radiation from the AR coated surface.

The reflected beam has essentially propagated a distance of 20 mm in silica for the device described here. The initial beam is the fundamental mode of a 20 µm diameter core, 0.09 NA fibre and the mode-field radius at λ = 1950 nm can then be derived from the Marcuse equation [34]:

$$w = r\left(0.65 + \frac{1.619}{V^{1.5}} + \frac{2.87}{V^{6}}\right) , \tag{3.13}$$

$$V = \frac{2\pi r NA}{\lambda} = 2.9 , \tag{3.14}$$

$$w_0 = 9.83\ \mu m\ (radius) \quad , \tag{3.15}$$

Where w is the mode-field radius as a function of the core geometry, r is the radius of the core, V is the V-number of the core, λ is the operating wavelength, NA is the numerical aperture and w_0 is the mode-field radius of the fundamental mode.

Here the mode-field radius is essentially the radius of the waist of a Gaussian beam, and so we can calculate the expected radius after propagating through 20 mm of silica (n = 1.45) using the Gaussian beam propagation equation:

$$w(z) = w_0 \sqrt{1 + \left(\frac{z}{z_R}\right)^2} \quad , \tag{3.16}$$

$$z_R = \frac{n\,\pi\,w_0^2}{\lambda} = 0.225\ mm \quad , \tag{3.17}$$

$$w_{20\ mm} = 874\ \mu m \quad , \tag{3.18}$$

Where $w(z)$ is the radius of a Gaussian beam after propagating a distance z from an initial waist with radius of w_0. The Rayleigh length (z_R) is a function of the initial waist radius, refractive index of the medium (n) and operating wavelength (λ). The beam radius after propagating a distance of 20 mm in a silica substrate is given by $w_{20\,\mathrm{mm}}$.

We can approximate the effective overlap between a beam with a radius of 874 µm and the radius of the fundamental mode of the core at 9.83 µm using Eqn. (3.10):

$$\eta_{coupling} = 1 - Loss = \frac{4w_0^2 {w_{20\,mm}}^2}{(w_1^2 + {w_{20\,mm}}^2)^2} = 5 \times 10^{-4} \quad , \tag{3.19}$$

Where the η_{coupling} is the amount of radiation that is coupled back into the core of the fibre, the *Loss* term is the same as in Eqn. (3.10), w_0 is the mode-field radius of the core, and $w_{20\,\mathrm{mm}}$ is the beam radius after propagating 20 mm in a silica substrate as per Eqn. (3.18).

This value is an overestimate as the reflected beam has a fairly strong curvature across the wave front and is thus not at the waist of a propagating beam, whereas Eqn. (3.19) is calculated based on the assumption that the modes under comparison are both at the waist positions.

We also need to take into account the presence of the AR coating which further reduces the total feedback into the core of the fibre:

$$F = \eta_{coupling} \times R_{AR} = 1.25 \times 10^{-6} = -59\ dB \quad , \tag{3.20}$$

Where *F* is the ratio of the backwards propagating radiation that is coupled into the core in comparison to the output from the fibre, $\eta_{coupling}$ is the same term as in Eqn. (3.19), R_{AR} = 0.25% is the reflectivity of the AR coating.

Thus, the estimated resultant isolation achieved is a sufficient level of feedback protection for most applications and is comparable to the reflectivity achieved with most ultra-smooth, angle-polished connectors, but with greatly improved power handling capability.

One of the challenges in this process is ensuring that the core of the fibre does not experience significant bending or deformation at the bond to the bulk silica substrate. Such deformation will degrade the beam quality of the laser output. In order to avoid this, an intermediate core-less section of fibre was spliced to the fibre prior to end-capping as shown in Fig. 3.36. The lengths of the core-less section was chosen such that the propagating beam experiences no clipping at the fibre end-cap end-face. In this assembly, the section of the fibre with a core experiences normal splicing conditions between a matched diameter fibre and is then sufficiently removed from the CO_2 processing region when fusing the fibre to the substrates minimising any thermal distortions of the core region.

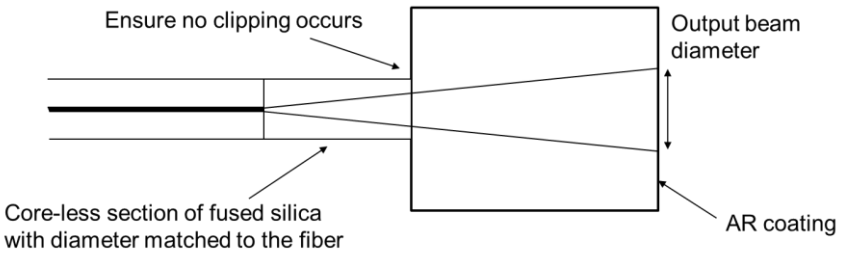

Figure 3.36: A coreless matched diameter fibre is used as an intermediate substrate in the end-capping process to avoid diffusion and deformation of the core when splicing to the bulk substrate.

Further modifications to this approach such as making an angle on the surface of the end-cap, increasing various dimensions and integrating CLS structures on the end-cap will reduce the feedback further. However, this would only be relevant to applications where further levels of feedback protection are required.

3.7.3 Characterisation of end-cap quality and high power operation

To test the end-capping process a 1 cm x 1 cm x 1 cm cube of fused silica with a single AR coated side at 1900 – 2200 nm was spliced to a fibre with a 20 µm diameter core, 400 µm diameter cladding and a core NA of 0.09. This fibre was matched to the output fibre of a 140 W, single-mode, thulium-doped fibre laser operating at 1940 nm. The output beam profile when 140 W of power is launched through the fibre is shown in Fig. 3.37 and suggests that there is negligible beam distortion in comparison to an angle cleaved facet. M^2 measurements performed before and after end-capping indicate that there is no degradation in beam quality with the output beam quality measured to be $M^2 \approx 1.1$.

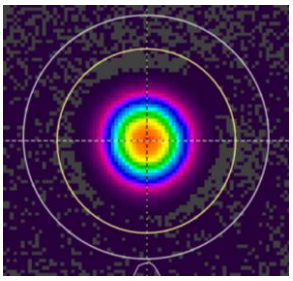

Figure 3.37: Output beam profile from a single-mode thulium laser after the bulk end-cap was attached to the output fibre. There is negligible beam distortion observed.

3.8 Summary

We have discussed a large variety of approaches to processing bulk silica glass and silica fibres. In particular the employment of a non-contact, clean, directional heat source such as CO_2 laser radiation has enabled substantial improvement of many important processes. The unique properties of this heat source has allowed extremely high performance fibre end-face preparation with features that are an order of magnitude smaller than conventional techniques to be demonstrated. High power cladding light stripper devices were fabricated by performing localised ablation of the fibre cladding surface. Finally, by locally heating only the surface of a large substrate, we have been able to weld fibres onto large substrates with dimensional differences of greater than 20x. The optical and thermal performance of the devices were tested up to the power levels available in the laboratory. It is anticipated that these techniques could be extended and demonstrated at much higher power levels; however they have been demonstrated to allow operation at power levels relevant for this project.

3.9 References

1. A. D. McLachlan and F. P. Meyer, "Temperature dependence of the extinction coefficient of fused silica for CO_2 laser wavelengths," Appl. Opt. **26**, 1728–1731 (1987).

2. E. Mendez, K. M. Nowak, H. J. Baker, F. J. Villarreal, and D. R. Hall, "Localized CO_2 laser damage repair of fused silica optics," Appl. Opt. **45**, 5358 (2006).

3. C. Weingarten, A. Schmickler, E. Willenborg, K. Wissenbach, and R. Poprawe, "Laser polishing and laser shape correction of optical glass," J. Laser Appl. **29**, 11702 (2017).

4. K. M. Nowak, H. J. Baker, and D. R. Hall, "Efficient laser polishing of silica micro-optic components," Appl. Opt. **45**, 162 (2006).

5. G. V. Vázquez, A. Harhira, R. Kashyap, and R. G. Bosisio, "Micromachining by CO_2 laser ablation: Building blocks for a multiport integrated device," Opt. Commun. **283**, 2824–2828 (2010).

6. R. Kitamura, L. Pilon, and M. Jonasz, "Optical constants of silica glass from extreme ultraviolet to far infrared at near room temperature.," Appl. Opt. **46**, 8118–33 (2007).

7. K. L. Kuo, H. Hocheng, and C. C. Hsu, "Ultrasonic Machining," in *Advanced Analysis of Nontraditional Machining* (Springer New York, 2013), pp. 325–357.

8. V. K. Sysoev, V. I. Masychev, B. P. Papchenko, S. Y. Rusanov, A. A. Yakovlev, and N. P. Glukhoedov, "High-rate IR laser evaporation of silica glass," Inorg. Mater. **39**, 532–537 (2003).

9. P. C. Shardlow, R. Standish, J. Sahu, and W. A. Clarkson, "Cladding Shaping of Optical Fibre Preforms via CO_2 Laser Machining," Eur. Conf. Lasers Electro-Optics - Eur. Quantum Electron. Conf. CJ_P_29 (2015).

10. A. D. Yablon, *Optical Fiber Fusion Splicing*, Springer Series in Optical Sciences (Springer-Verlag, 2005), Vol. 103.

11. A. D. Yablon, "New transverse techniques for characterizing high-power optical fibers," Opt. Eng. **50**, 111603 (2011).

12. J. W. Nicholson, A. D. Yablon, S. Ramachandran, and S. Ghalmi, "Spatially and spectrally

resolved imaging of modal content in large-mode-area fibers," Opt. Express **16**, 7233 (2008).

13. Vytran, "Vytran, LLC LDC-400 Product Tour - YouTube," https://www.youtube.com/watch?v=TuhZAx3q7s0.

14. 3SAE Technologies, "3SAE Technologies Liquid Clamp Cleaver LDF Performance," http://www.3sae.com/pdfdocuments/LCC_Nufern Results_100415.pdf.

15. Fujikura, "Large Diameter Optical Fiber Cleaver CT-105/CT-106," http://www.fujikura.co.uk/products/fusion-splicers-and-accessories/fusion-splicer-accessories-specialty/large-diameter-optical-fiber-cleaver-ct-106/.

16. A. Webb, M. Osborne, G. Foster-Turner, and D. W. Dinkel, "Precision laser processing for micro electronics and fiber optic manufacturing," Proc. SPIE **6880**, 688003 (2008).

17. W.-H. Wu, C.-L. Chang, and M.-W. Hung, "Cleaving parametes studies on glass fiber laser cutting," Proc. SPIE **8769**, 87693P (2013).

18. K. Boyd, S. Rees, N. Simakov, J. M. O. Daniel, R. Swain, E. Mies, A. Hemming, W. A. Clarkson, and J. Haub, "High precision 9.6 µm CO_2 laser end-face processing of optical fibres," Opt. Express **23**, 15065 (2015).

19. F. Barnier, P. E. Dyer, P. Monk, H. V Snelling, and H. Rourke, "Fibre optic jacket removal by pulsed laser ablation," J. Phys. D. Appl. Phys. **33**, 757–759 (2000).

20. L. Lévesque and V. Jdanov, "Optical fiber cleaved at an angle by CO_2 laser ablation: Application to micromachining," Opt. Laser Technol. **42**, 1080–1083 (2010).

21. M. Zhang, G. Chen, Y. Zhou, and S. Li, "Direct observation of keyhole characteristics in deep penetration laser welding with a 10 kW fiber laser," Opt. Express **21**, 19997 (2013).

22. M. Naeem, "Laser Processing of Reflective Materials," Laser Tech. J. **10**, 18–20 (2013).

23. K. Boyd, N. Simakov, A. Hemming, J. Daniel, R. Swain, E. Mies, S. Rees, W. Andrew Clarkson, and J. Haub, "CO2 laser-fabricated cladding light strippers for high-power fiber lasers and amplifiers," Appl. Opt. **55**, 2915 (2016).

24. W. Wang, J. Leng, J. Cao, S. Guo, X. Xu, and Z. Jiang, "Method for stripping cladding light in

the high power fiber laser," Opt. Commun. **287**, 187–191 (2013).

25. W. Guo, Z. Chen, H. Zhou, J. Li, and J. Hou, "Cascaded cladding light extracting strippers for high power fiber lasers and amplifiers," IEEE Photonics J. **6**, 1–6 (2014).

26. C. Ottenhues, T. Theeg, K. Hausmann, M. Wysmolek, H. Sayinc, J. Neumann, and D. Kracht, "Single-mode monolithic fiber laser with 200 W output power at a wavelength of 1018 nm," Opt. Lett. **40**, 4851 (2015).

27. S. Boehme, K. Hirte, S. Fabian, C. Hupel, T. Schreiber, R. Eberhardt, and A. Tünnermann, "CO_2 laser-based coating process for high power fiber application," Proc. SPIE **8968**, 89680Z (2014).

28. A. Babazadeh, R. R. Nasirabad, A. Norouzey, K. Hejaz, R. Poozesh, A. Heidariazar, A. H. Golshan, A. Roohforouz, S. N. T. Jafari, and M. Lafouti, "Robust cladding light stripper for high-power fiber lasers using soft metals," Appl. Opt. **53**, 2611 (2014).

29. R. Poozesh, A. Norouzy, A. H. Golshan, A. Roohforouz, A. Babazadeh, R. R. Nasirabad, N. T. Jafari, A. Heidariazar, K. Hejaz, A. Alavian, and A. Amidian, "A novel method for stripping cladding light in high power fiber lasers and amplifiers," J. Light. Technol. **30**, 3199–3202 (2012).

30. A. Kliner, K.-C. Hou, M. Plötner, C. Hupel, T. Stelzner, T. Schreiber, R. Eberhardt, and A. Tünnermann, "Fabrication and evaluation of a 500 W cladding-light stripper," Proc. SPIE **8616**, 86160N (2013).

31. T. Li, J. Wu, Y. Sun, Y. Wang, and Y. Ma, "An improved method for stripping cladding light in high power fiber lasers," Proc. SPIE **9255**, 92550M (2015).

32. G. Y. Chen, C. A. Codemard, P. M. Gorman, J. S. Chan, and M. N. Zervas, "Angle-Resolved Characterization and Ray-Optics Modeling of Fiber-Optic Sensors," J. Light. Technol. **33**, 5210–5217 (2015).

33. S. Boehme, E. Beckert, R. Eberhardt, and A. Tuennermann, "Laser splicing of end caps: process requirements in high power laser applications," Proc. SPIE **7202**, 720205 (2009).

34. D. Marcuse, "Loss Analysis of Single-Mode Fiber Splices," Bell Syst. Tech. J. **56**, 703–718 (1977).

Chapter 4.

Optimisation of Holmium-Doped Fibres

4.1 Introduction

Achieving efficient operation in holmium-doped fibre (HDF) lasers requires a careful understanding of the various loss mechanisms that can impact the fibre efficiency. We review the impacts of various materials that can be included in the composition on the background loss of the fibre and the expected impact on the phonon energy of the host. A range of holmium-doped fibres were fabricated using the modified chemical vapour deposition (MCVD) technique and characterised. We measure the properties of the fibres and describe a simple method for accurately measuring the efficiency without having to resort to a complicated fibre design.

Once an efficient composition is identified, it is transitioned into a double-clad geometry. This is further complicated due to the requirement for low-loss propagation of 1.95 µm pump radiation in the cladding region. Finally an all-glass, double-clad, HDF is fabricated and tested in a laser configuration. The fibre laser produced a CW output power of 70 W at 2.1 µm, with a diffraction limited beam quality and an efficiency of 67% with respect to absorbed pump power.

4.2 Loss mechanisms in silica

Absorption due to hydroxyl contamination and background infrared absorption are the main loss mechanisms present in silica over the 2 µm wavelength range [1,2]. The development of low-loss silica fibres for long-haul telecommunications applications has resulted in much effort being devoted to the elimination of SiOH impurities from silica fibres. In the telecommunications domain,

it is the presence of the overtone at 1.38 µm which affects the losses in the 1.55 µm region. This absorption feature at 1.38 µm is shown in Fig. 4.1a) and is the most common method of measuring hydroxyl group content in fibres. The combination mode of the SiO_4 tetrahedron with the fundamental hydroxyl resonance leads to a loss arising near 2.3 µm. Fig. 4.1b) shows the effect that trace amounts of SiOH contamination can have on the background loss in the 2 µm region [3].

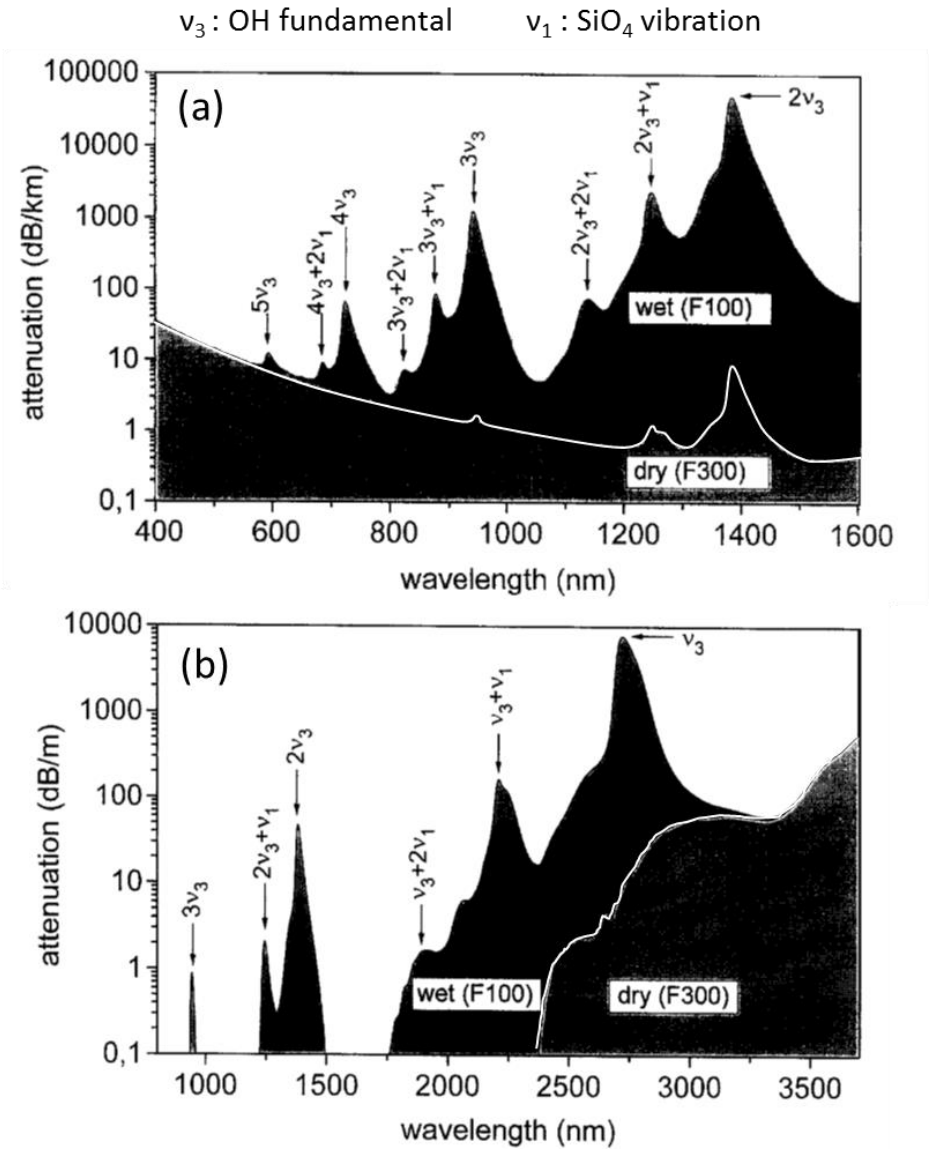

Figure 4.1: Absorption due to SiOH impurities in silica in the a) Visible/Near Infrared (400 – 1600 nm) region and b) Near/Mid Infrared (1000 – 3000 nm) region [3].

The origin of hydroxyl impurities can be from multiple sources, these include the gases used in the MCVD fabrication and starting materials. By controlling these processes and incorporating chemical drying passes, passive fibres fabricated by the MCVD process typically achieve hydroxyl

concentrations of <<10 ppb [1]. The level of contamination increases in rare-earth doped fibres due to the additional process of solution doping which involves exposing the preform to the atmosphere and to solutions including ethanol and dissolved rare-earth salts [4]. Despite this added challenge, holmium-doped fibres with SiOH concentrations of 1-3 ppm have been demonstrated commercially and more recently holmium-doped fibres with <0.5 ppm hydroxyl contamination have been reported [5]. The hydroxyl induced loss in comparison to the background infrared absorption is shown in Fig. 4.2 and suggests that hydroxyl levels of <1 ppm reduces the contribution to the loss to an order of magnitude lower than that of the background infrared loss at 2100 nm.

As an example, the minimum background loss that is achievable in silica at 2100 nm is ~0.074 dB/m. For a ~5 m length (as is typical of a fibre laser) of passive fibre this leads to a transmission loss of 0.37 dB (8.2%) loss. In comparison the actual loss experienced in a fibre laser will be reduced due to the non-uniform signal intensity throughout the gain medium. The presence of this background loss will drive the design of the fibre or device geometry to minimize the physical length of the amplifier or laser cavity to maximise the efficiency. This requirement will need to be balanced with maintaining a sufficient fibre length to dissipate the quantum defect related thermal load as well as providing sufficient gain length.

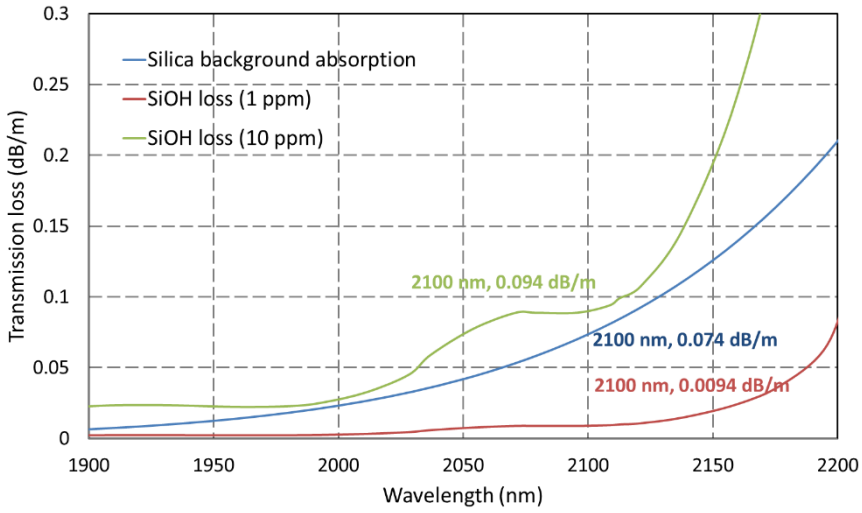

Figure 4.2: Silica background infrared absorption [1] and losses arising due to hydroxyl contamination [3].

4.3 Fabrication and materials

Different compositions of silica based glasses can increase the material background loss of the fibre [6–9]. Indeed, as shown in Fig. 4.2, silica itself exhibits absorption in the 2 µm wavelength range. Despite other compositions such as germanate or multi-component silicate glasses exhibiting lower IR loss, a scalable method of producing extremely high purity and low loss fibres with these materials has not been developed. For example, typical losses for germanate fibres fabricated using rod-in-tube techniques are reported at around 0.3 dB/m in this wavelength region and these are typically associated with scattering losses at the core-cladding interface. In comparison, the background losses that we have measured in typical MCVD fabricated, solution doped fibres are of the order of <0.02 dB/m in the 1500 nm region. This is significantly larger than passive fibres which routinely achieve losses in the range of 0.0003 dB/m, however this loss is consistent with commercial silica fibre manufacturer's background loss specifications for typical rare-earth doped fibres.

4.3.1 Modified chemical vapour deposition process

A comprehensive overview of the MCVD process for fabricating a fibre is provided in [1]. A basic overview is provided here for the purpose of describing the materials involved and the origins of hydroxyl contamination.

The MCVD process is illustrated in Fig. 4.3 and relies on the high temperature oxidation of reagents inside a rotating tube which is heated by an external heat source. Chemical reagents are converted into gas form by passing a carrier gas such as O_2, Ar, or He through a liquid precursor. Halides which have high vapour pressures at room temperature are suitable for this and include $SiCl_4$, $GeCl_4$, BCl_3, PCl_3 and $POCl_3$. The process relies on the fact that the vapour pressure of these dopants is significantly larger than that of any transition metal impurities which may be present in the starting materials. As a result the gases that enter the rotating tube are essentially free of these metallic contaminants. An important fact to note is that hydrogenated species have very similar vapour pressure to the dopants and are able to introduce hydroxyl contamination.

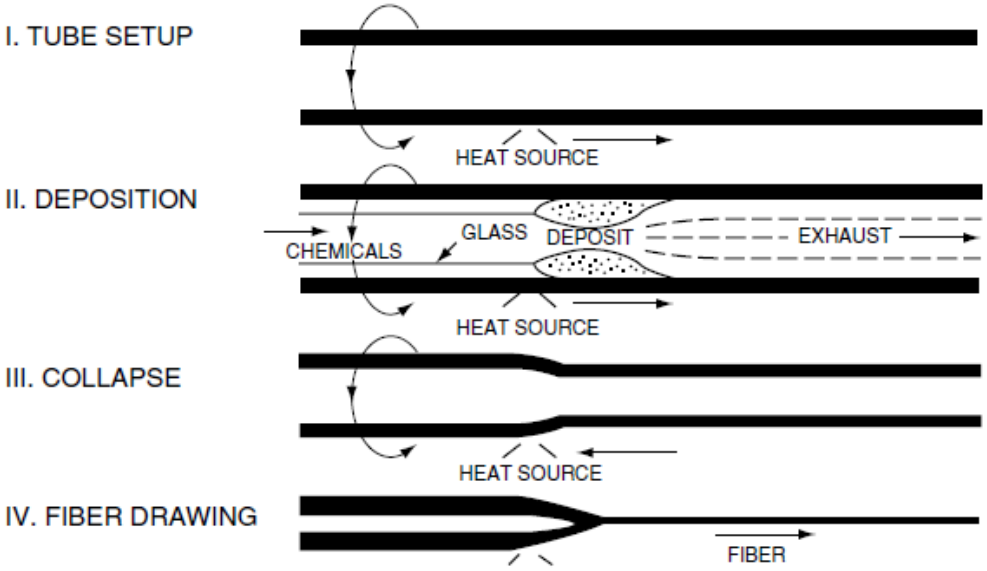

Figure 4.3: Illustration of typical MCVD process for fabrication of the preform and then drawing to a fibre [1,10].

4.3.2 Solution doping

Unfortunately, the vapour pressure of rare-earth and aluminium salts are too low at room temperature to allow a similar deposition method. As a result, incorporation of rare-earth ions and aluminium oxide is thus achieved by solution doping. Here a porous layer of soot is deposited during the MCVD process – typically under much lower temperatures than standard soot layers for passive fibres. Instead of immediately consolidating this layer, the preform is cut from the lathe and soaked in a solution of the required rare-earth chloride, aluminium chloride and ethanol. The rare-earth ion and any co-dopants are absorbed into the soot matrix. The preform is then spliced back onto the lathe and the soot layer is dried and consolidated [11,12]. An illustration of this process is shown in Fig. 4.4.

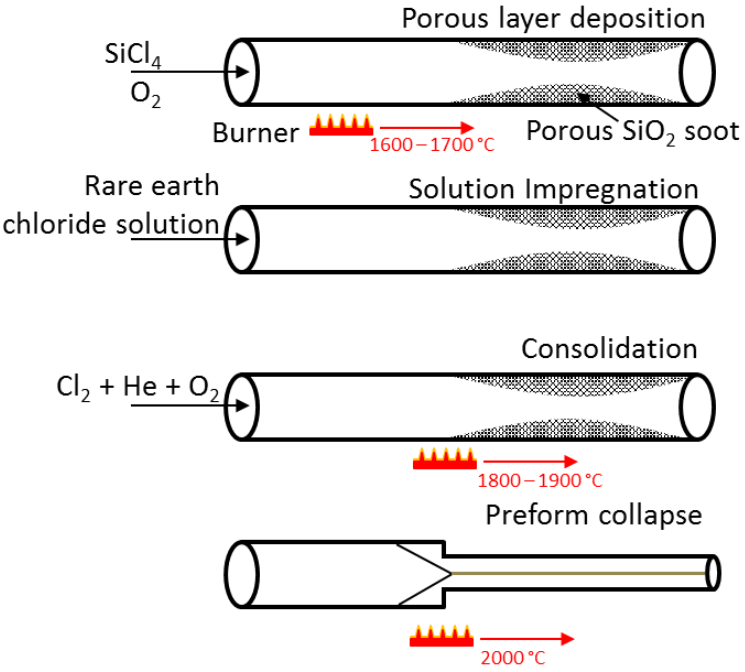

Figure 4.4: Illustration of solution doping process for incorporation of a rare-earth into the core of a fibre [10].

The solution doping process introduces further possible sources of contamination in addition to the sources that are present during the conventional MCVD fabrication of a passive optical fibre. Moisture in the air can ingress when the preform tube is removed from the lathe for solution doping and residual moisture may be present in the rare-earth chemicals and the ethanol solution. As a result additional chemical drying steps such as purging with dry nitrogen and chlorine drying are typically employed to reduce the residual moisture and hydroxyl contamination [13].

4.3.3 Discussion

A summary of the possible materials that can be included in the fibre core composition is provided in Table 4.1. If the aim is to achieve efficient operation at 2 µm then P_2O_5 and B_2O_3 should not be included as part of the core composition. Boron is well known to provide a large loss for both the pump (1.95 µm) as well as the signal (2.1 µm) radiation.

The $^5I_7$ level of holmium is heavily quenched by the multi-phonon transition in the silica host. Thus, only materials which reduce the host glass phonon energies are suitable for incorporation into the core composition, which includes Al_2O_3 and GeO_2. In order to prevent clustering it is likely that a high concentration of Al_2O_3 is required to increase the solubility of the rare earth [14–16].

Table 4.1: List of possible materials for composition of rare-earth doped fibres

Material	IR transmission edge vs SiO_2	Host properties	Refractive index vs SiO_2
Al_2O_3	No effect	Enhances solubility Reduces phonon energy, improves lifetime	Increase
GeO_2	Slight improvement	Photosensitive	Increase
F	No effect	-	Decrease
P_2O_5	Worse With hydroxyl has additional absorption features	Enhances solubility Increases local phonon energy, Quenches lifetime [17]	Increase
B_2O_3	Much worse	Quenches lifetime [17] Increases local phonon energy, Commonly used for stress rods	Decrease
Ho_2O_3	Unknown	Lasing ion Enhances photosensitivity with GeO_2 [18]	Increase

4.4 Double-clad fibres suitable for pumping at 2 µm

An additional challenge for holmium-doped fibres is the necessity to provide low loss guidance of the pump radiation. In standard double-clad fibres, a low-index polymer is typically used to both protect the fibre and confine the pump light to the cladding. However, these polymers are strongly absorptive at 2 µm due to infrared chemical resonances which precludes the use of polymer coatings for confining pump radiation at this wavelength. As a result power scaling of holmium-doped fibre lasers has traditionally been limited by the lack of a double-clad fibre that exhibits low-loss at the pump wavelength of 1.95 µm. To alleviate this issue, alternative cladding materials such as fluorine doped silica and air-jacketed fibres have been investigated with promising results [19]. Double-clad, holmium-doped fibres with all-glass or air-cladding geometries are shown in

Figs. 4.5a) – 4.5c). The NA possible with fluorine doping (0.26-0.28 NA) is not as large as air-clad fibres (>0.6 NA). However, the impact of the reduced NA (vs. fluoropolymer ~0.46) is mitigated in the case of a resonantly pumped geometry due to the high brightness of the fibre laser pump source. Single-mode thulium lasers at 1.95 µm suitable for cladding pumping holmium-doped fibre lasers have been demonstrated at the >180 W level [20–22]. A solid all-glass fibre is also preferred from the cleaving and splicing perspective.

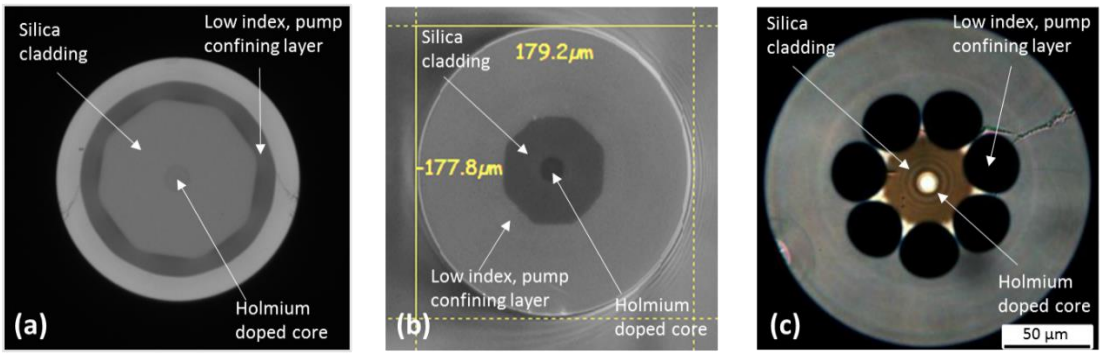

Figure 4.5: a) A fluorine layer confines the pump light to an octagon shaped silica cladding of a commercially available holmium-doped fibre [23]. b) Holmium-doped fibre fabricated at the University of Southampton with an octagon silica cladding surrounded by a fluorine-doped silica layer. c) An air-jacket design provides pump guidance in a holmium-doped fibre [24].

4.5 Impact of cladding and core dimensions on device efficiency

Designing an efficient holmium-doped fibre is achieved by considering all of the possible loss mechanisms and the relevant constraints that they impose on the system.

Literature reports in bulk crystalline materials suggest that holmium suffers from up-conversion losses at higher dopant concentrations [25]. The choice and purity of host material will be equally important to avoid quenching the already extremely short lifetime and minimising excess propagation losses. An all-glass cladding geometry is also necessary to avoid excess propagation losses at the pump wavelength.

Even with the best choice of available materials, the device length needs to be kept at a minimum to reduce the loss of the 2.1 µm signal due to background absorption. Given this constraint, let us

consider the impact of background losses on the performance of a laser for various fibre dimensions and dopant concentrations.

The small-signal core absorption at 1950 nm will typically achieve a strength of 140 dB/m for a 1 wt.% dopant concentration.

$$\alpha_{core}(1950\ nm)\left(\frac{dB}{m}\right) = 140\left(\frac{dB}{m}\right) \times C(wt.\%) \quad , \tag{4.1}$$

Where α_{core}(1950 nm) is the small-signal core absorption at 1950 nm, and *C* is the dopant concentration of the holmium ion in wt.% of the rare-earth oxide Ho_2O_3.

Assuming uniform pump distribution, the pump absorption in the cladding ($\alpha_{cladding}$) scales as:

$$\alpha_{cladding}(1950\ nm)\left(\frac{dB}{m}\right) = \alpha_{core}(1950\ nm)\left(\frac{dB}{m}\right) \times \frac{A_{core}}{A_{cladding}} \quad , \tag{4.2}$$

Where $\alpha_{cladding}$(1950 nm) is the cladding absorption at 1950 nm, A_{core} and $A_{cladding}$ are the core and cladding areas respectively.

This greatly depends on the exact geometry of the fibre cladding which can be and usually is non-circular in nature. For a simple geometry where the core and cladding are both circular, then the core:cladding area ratio can be represented by:

$$\frac{A_{core}}{A_{cladding}} = \frac{\pi r_{core}^2}{\pi r_{cladding}^2} \quad , \tag{4.3}$$

Where r_{core} and $r_{cladding}$ are the radii of the core and the cladding respectively.

Let us assume that a significant proportion of the pump radiation is absorbed. The length of the gain medium for a given device will be taken to correspond to a 95% (13 dB) pump absorption coefficient. In this case we also make the assumption that the background loss for the 1950 nm pump radiation is negligible. The length of fibre required is then:

$$L(m) = \frac{13\ dB}{\alpha_{cladding}(1950\ nm)\left(\frac{dB}{m}\right)} \quad , \tag{4.4}$$

Where L is the length of fibre required to achieve a 13 dB attenuation of the 1950 nm pump radiation.

As the signal is being amplified along the length of the fibre, the signal intensity at 2100 nm along the gain medium is not constant and will depend on the pump direction, small-signal gain, and cavity finesse. Let us assume that the effective length of the gain medium is ~0.66 of the actual length. Based on the previous review of background loss in silica, the attenuation coefficient at 2100 nm is taken as 0.074 dB/m. The excess loss due to infrared absorption of silica can be expressed as follows:

$$Excess\ loss(dB) = 0.66 \times 0.074\left(\frac{dB}{m}\right) \times L(m) \quad , \tag{4.5}$$

Where the *Excess loss* is the additional loss due to infrared absorption and *L* is the length of the fibre as obtained in Eqn. (4.4).

Figure 4.6 shows the expected slope efficiency assuming an excess loss for various clad:core diameter ratios and a device length corresponding to a pump absorption of 95% with the excess loss contribution of Eqn. (4.5). The device configuration will affect the effective length parameter – taken here as 0.66 in Eqn. (4.5). Despite this, Fig. 4.6 is still useful to illustrate the impact of doping concentration on device length and the subsequent efficiency achieved.

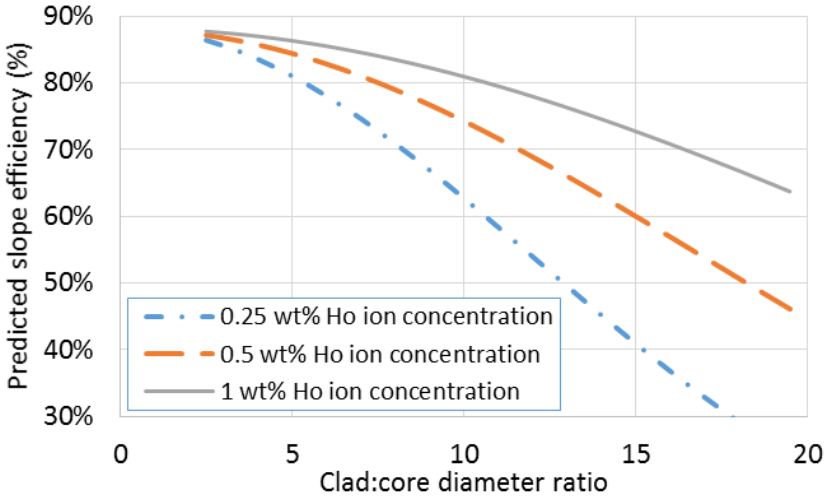

Figure 4.6: Expected slope efficiency with respect to launched pump power as a function of clad:core diameter ratio for various Ho^{3+} dopant concentrations. The only loss mechanism that is considered here is the background loss of the fibre at the 2100 nm holmium emission.

It should also be pointed out that typically the fibre will need to operate at a non-zero inversion (typically ~ 20% for holmium at room temperature as illustrated in Fig. 2.6) and as such the effective pump absorption coefficient will be reduced due to the large emission cross section at the pump

wavelength. This is illustrated in Fig. 2.6 where the absorption at 1950 nm varies significantly with increasing inversion. In situations where the holmium ion population is held at a high inversion, the length of the gain medium for efficient absorption at 1950 nm will be larger than expected in these derivations.

Figure 4.6 suggests that minimising the clad:core ratio is the method for maximising efficiency, and while it is certainly possible to operate with an extremely small clad:core ratio (i.e. 3:1), it is not necessarily practical. The requirement to decrease the clad:core area ratio also has to be balanced with the restrictions associated with the fabrication of the multi-mode fibre combiners for launching multiple thulium pump lasers into the cladding of a single holmium-doped fibre.

4.6 Measurement of hydroxyl concentration in holmium-doped fibres

A list of allowable materials and possible strategies to fabricating an efficient holmium-doped fibre laser has been presented earlier in this chapter. As discussed, a significant factor is also the presence of hydroxyl impurities. The presence of the 1.38 µm absorption feature which corresponds to the overtone of the 2.7 µm resonance provides a useful absorption feature that does not overlap with any absorption features associated with the holmium ion. This makes measurements of very low hydroxyl concentrations possible. In order to facilitate as accurate a measurement as possible, the fibre should be drawn to be single-mode at 1300 nm such that there is no resulting modal-interference phenomena as discussed in Section 3.4.3 in the wavelength region of interest.

Typical measured transmission spectra of a broad-band supercontinuum source through a holmium-doped fibre is shown in Fig. 4.7a). A 1 ppm hydroxyl contamination is associated with 0.06 dB/m peak absorption at 1385 nm [3]. Given that typically a 100 m length of fibre is available after the fibre drawing, and that the noise level and fluctuations of the supercontinuum source is of the order of 0.3 dB, this provides a lower bound of 0.003 dB/m to the measurement or equivalent to a 0.05 ppm concentration of SiOH. By comparing the two traces and scaling for the cutback length of fibre (94.8 m) the background loss is obtained as shown in Fig. 4.7b). A 0.12 dB/m strong absorption was measured at 1385 nm corresponding to a hydroxyl contamination of ~ 2 ppm.

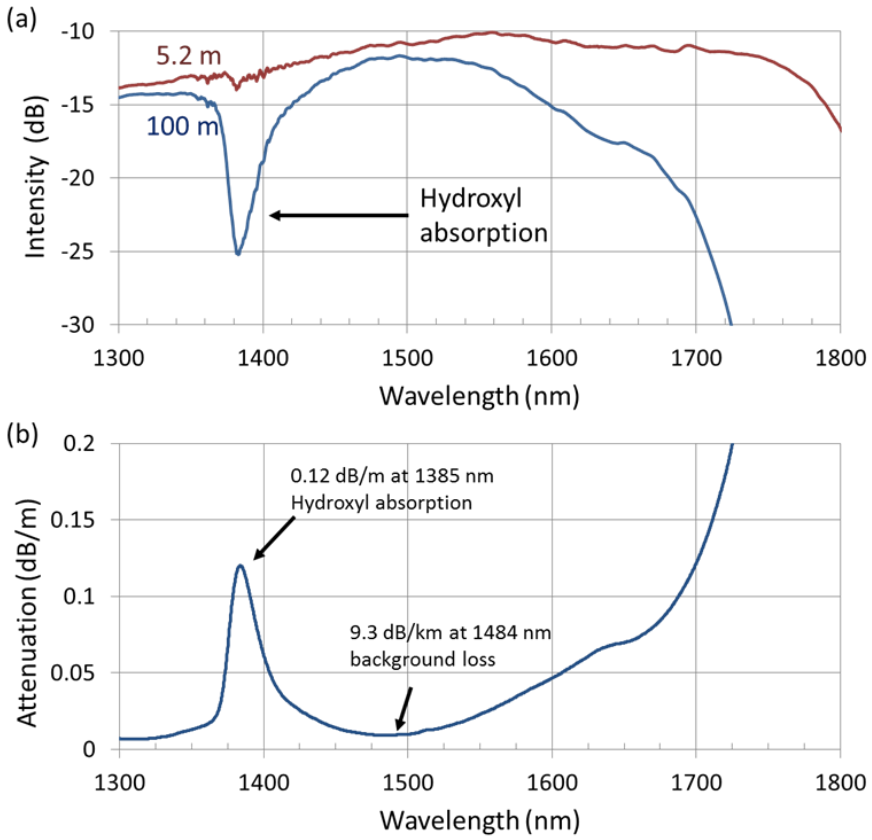

Figure 4.7: a) **T**ransmission spectra of a broad-band supercontinuum source through a length of holmium-doped fibre. b) Resulting absorption spectrum showing a 0.12 dB/m absorption peak at 1385 nm corresponding to a hydroxyl concentration of ~ 2 ppm.

4.7 Holmium concentration measurement

The holmium concentration incorporated into the fibre is measured by performing a cutback on a length of fibre drawn to be single-mode at 1.9 µm and typical transmission spectra are shown in Fig. 4.8a). A 0.5 wt.% concentration can be associated with a 70 dB/m absorption at 1950 nm based on reports in the literature [14,26–28]. It is expected that different core compositions correspond to different absorption strengths due to variations in the local environment for the holmium ion. Due to the strong absorption, a much shorter length of fibre is used in this cut-back experiment typically 0.3 – 1 m. The resulting absorption is scaled against the length as shown in Fig. 4.8b). In this case, the holmium-doped fibre had a peak absorption of 27 dB/m at 1950 nm which corresponds to a dopant concentration of 0.2 wt.%.

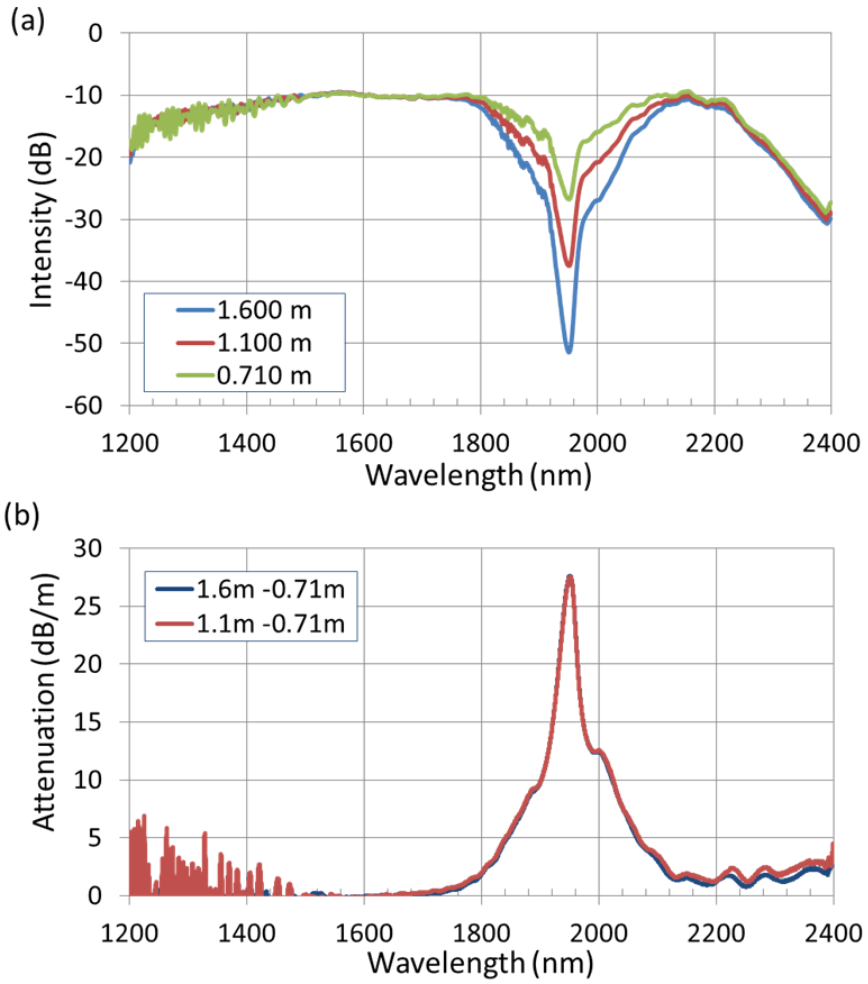

Figure 4.8: a) Example of a transmission measurement through a length of holmium-doped fibre to characterise the holmium ion concentration. b) Resulting absorption spectrum showing a 27 dB/m absorption peak at 1950 nm corresponding to ~0.2 wt.% holmium oxide concentration.

4.8 Efficiency measurement of core-pumped lasers

In order to test the efficiency of the HDFs, the fibres are tested in a core-pumped laser configuration as shown in Fig. 4.9. A single-mode, FBG stabilised thulium laser operating at 1.95 µm, providing pump power up to ~10 W, is spliced to an isolator and then to a HR FBG at 2.1 µm. A length of holmium-doped fibre is spliced to the output of the grating. A laser cavity is then formed between the HR FBG and the Fresnel reflection from the normal cleaved end-face of the fibre. A dichroic is used to separate the residual thulium pump power and the holmium output power. A series of cutback measurements are performed on the HDF to determine the peak operating point, and also to determine the pump launch efficiency at the input of the holmium-doped fibre.

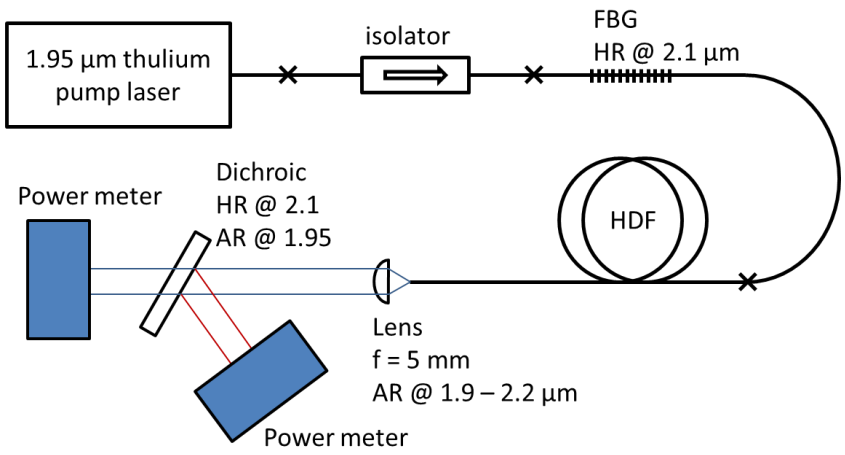

Figure 4.9: Experimental arrangement used to test the efficiency of various holmium-doped fibres by measuring the performance of a core-pumped laser oscillator.

The measurements are reconciled to obtain the internal efficiency of the holmium-doped fibre. Due to the large output coupling (T = 96%), the laser is less sensitive to the loss at the splice between the HR grating and the HDF in comparison to a laser oscillator with a lower output coupling fraction.

In order to investigate the reproducibility of this technique, we analyse the cavity configuration and the possible variables that can impact the measurement. This also allows us to isolate the key parameters that are required to make the measurement as accurately as possible and reduce the possible errors on the slope efficiency estimate. A diagram of the cavity model is shown in Fig. 4.10a). Under steady-state (CW) lasing conditions, the following relationship holds:

$$G^2 \times (1-\eta)^2 \times R_{HR} \times R_{OC} = 1 \quad , \tag{4.6}$$

Where G is the single-pass gain of the active fibre, R_{HR} is the reflectivity of the HR FBG ($R_{HR}\approx 1$), R_{OC} is the reflectivity of the output coupler – in this case the Fresnel interface between silica and air ($R_{OC}\approx 0.04$) and the splice loss (η) is the unknown variable but assumed to be <10%. By substituting these parameters into Eqn. (4.6) the following relationship is recovered:

$$G \times (1-\eta) = 5 \quad , \tag{4.7}$$

Note that the gain of the active fibre will vary between G ≈ [5, 5.6] as η varies from [0, 0.1]. As shown in Fig. 4.10a) we measure the total output power at 2.1 µm ($P_{2.1\mu m}$) and the pump launched into the active fibre at 1.95 µm ($P_{1.95\mu m}$).

By considering that the power reflected from the output coupler is R_{OC} x $P_{2.1\mu m}$ / (1 - R_{OC}) we can derive the expression for the total power at 2.1 µm that is lost (P_{Lost}) in the splice region propagating in either direction:

$$P_{Lost} = \eta \times G \times R_{OC} \times \frac{P_{2.1\mu m}}{1 - R_{OC}} + \eta \times (1 - \eta) \times G \times R_{HR} \times R_{OC} \times \frac{P_{2.1\mu m}}{1 - R_{OC}} \quad , \qquad (4.8)$$

Where P_{Lost} is the power lost at the splice and $P_{2.1\mu m}$ is the total output power at 2.1 µm.

If we assume that η is small, then $\eta^2 \rightarrow 0$ and by substituting the various parameters, we recover the following relationship:

$$\frac{P_{Lost}}{P_{2.1\mu m}} = 2 \times \eta \times G \times \frac{0.04}{0.96} = 0.42 \times \frac{\eta}{1 - \eta} \cong 0.42 \times \eta \quad , \qquad (4.9)$$

This is represented by the curve in Fig. 4.10b). For a splice loss as large as 10%, the output power is reduced by a maximum of <5%. Here the splice loss results in the measured slope efficiency representing an underestimate of the actual internal slope efficiency.

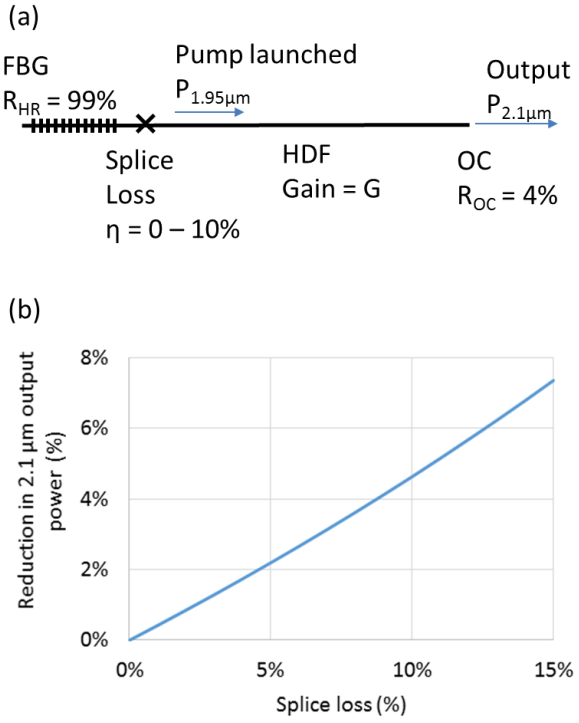

Figure 4.10: a) Diagram of the cavity used to measure the slope efficiency. b) Variation in output power from the holmium laser as a function of excess splice loss.

Providing that care is taken to select the appropriate fibres for the HR grating to ensure that the mode-field diameters are well matched, then this level of splice loss is readily achievable. The splice loss can also be estimated by cutting back the fibre laser. By cutting to a length of 20 mm of HDF, there is insufficient gain for the HDF to lase or generate any significant spontaneous emission. As a result, we can expect that at high intensity, the pump will completely bleach this short length of fibre. Typical examples of this behaviour are shown in Fig. 4.11. By then cutting away the HDF completely and measuring the pump radiation that is able to propagate through the HR grating, we can estimate the magnitude of the splice loss at the pump wavelength. While the splice may have different properties at the signal wavelength, by considering the change in the MFD in both the active and passive fibres, we are able to get an estimate for the magnitude of the splice loss. The typical splice losses illustrated in Fig. 4.11 are in the region of 12%, which suggests an error of 6% (or ±3 %) of the slope efficiency according to Fig 4.10b).

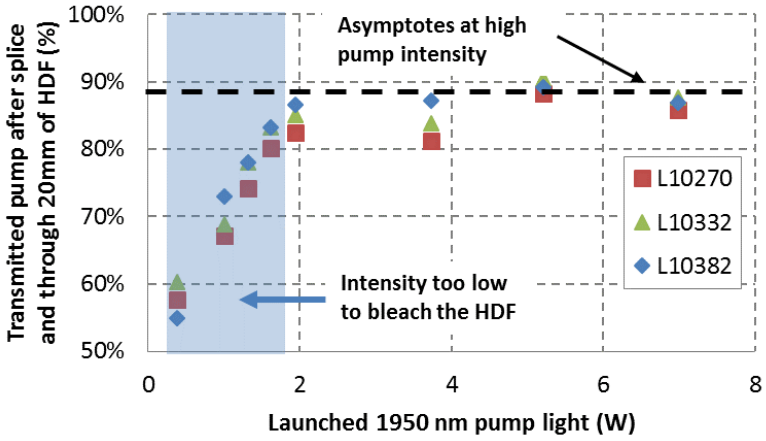

Figure 4.11: Transmitted pump power through 20 mm of HDF for different pumping rates for various fibres. This illustrates the bleaching of the pump radiation and also provides an estimate of the splice loss.

Another advantage of the core-pumped experiment is that the infrared background loss is low, as the length of the fibre is relatively short (<5 m) for all tested doping concentrations. This then allows a valid comparison of efficiency between fibres with varying compositions.

The main disadvantage of this measurement is that the fibre must now be operated at a large inversion to achieve the small-signal gain required to reach threshold in the low-Q cavity. As a result, the efficiency may be reduced by stronger up-conversion and energy transfer losses that would not be present in a cladding-pumped system operating at a lower inversion. Increasing the cavity Q is possible by using a partially reflective output coupler grating or bulk optic, however doing

so will also increase the impact of the splice loss. This increase in uncertainty and complexity is undesirable. Another possible solution is to use a longer wavelength pump which will bleach and hold the HDF at a lower inversion. In this case a longer length of fibre would be required, and the variation in the IR background loss between different doping concentrations would become a significant factor. Overall, the use of a low-Q cavity is deemed to be sufficiently representative to provide information for compositional optimisation.

4.9 Summary of in-house core-composition optimisation

For the characterisation of in-house fabricated HDFs a 1950 nm pump laser and a 2104 nm fibre Bragg grating were employed. The typical fibre lengths required for there to be sufficient gain to achieve lasing range, from 5 m, for the lower concentrations, to 2 m, for the larger concentrations. A summary of the various holmium-doped fibres fabricated to date is shown in Table 4.2.

Table 4.2: Summary of rare-earth and hydroxyl concentrations for various holmium-doped silica fibres. Also shown is the measured efficiency from the core-pumped experiments.

Preform	Preform location (mm)	Absorption at 1.95 µm (dB/m)	Holmium concentration (wt %)	Absorption at 1.38 µm (dB/m)	Hydroxyl concentration (ppm)	Slope efficiency (%)
L10194	80	130	0.93	0.017	0.27	37 ± 2
L10244	80	27	0.19	0.12	1.94	65 ± 3
L10254	80	25	0.18	0.15	2.42	67 ± 2
L10270	80	45	0.32	0.18	2.90	55 ± 4
L10332	80	45	0.32	0.308	4.97	69 ± 3
L10332	340	43.5	0.31	0.363	5.85	60 ± 2
L10382	80	35	0.25	0.07	0.13	74 ± 3
L10382 Fluorine clad	150	1	0.25	0.07	0.13	67 ± 2

There is little explicit correlation between any of these parameters and the slope efficiency measurements. One conclusion that can be drawn is that larger concentrations are less efficient, this can be attributed to up-conversion losses. Indeed, when the fibre from L10194 was operated with a lower inversion (by operating at cryogenic temperatures) the performance improved

substantially to >60%, implying that there may have been a significant loss mechanism for this fibre associated with the upper state population which is consistent with the presence of up-conversion.

Comparing fibres drawn from preforms L10270, L10332 and L10382 it is evident that there are other parameters that contribute significantly to the efficiency. All of these have similar holmium concentration, varying hydroxyl impurity levels and efficiencies ranging from 55% to 74%. It is suspected that the additional factors that are significant in determining the efficiency of the lasers include dopant distribution uniformity and the Al_2O_3 concentration. Further investigation and quantification of these parameters is essential in order to be able to identify a strategy to increase the fibre efficiency. The best efficiency observed was in the 71 – 77% range which was larger than commercially available fibres (70%) [29] but has since been superseded with recent reports of a composition with an 87% efficiency [30].

4.10 All-glass, double-clad fibre development

Based on the compositional optimisation preform L10382 was chosen to be transitioned to a double-clad fibre. To achieve this, a part of the L10382 preform was laser processed into an octagon with the technique described in Section 3.3, and over-clad with a silica tube that contained a fluorine-doped layer on the inner surface. The refractive index of the fluorine doped silica layer with respect to the un-doped silica cladding produced a guiding NA of 0.12. The resulting preform was then drawn to a fibre with dimensions of 14/65/180 µm. An end-face image illustrating the resulting fibre structure and measurements of the fibre dimensions is shown in Fig. 4.12.

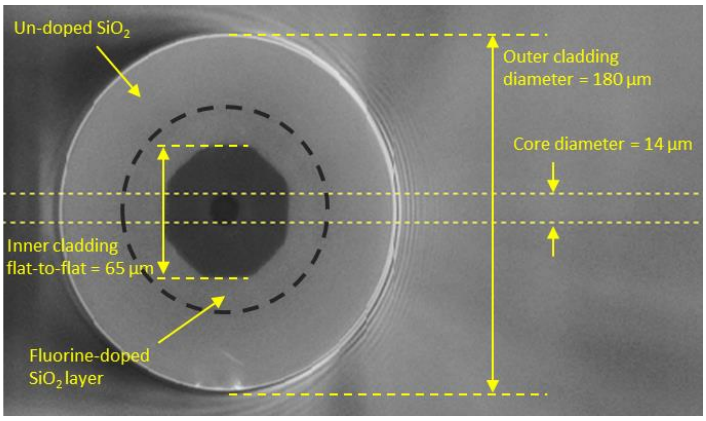

Figure 4.12: End-face image with dimensional measurements of the fluorine-clad holmium-doped fibre fabricated from the core rod L10382.

Table 4.3: Summary of core-rod performance and fluorine-clad fibre performance.

Preform	Preform location (mm)	Absorption at 1.95 µm (dB/m)	Holmium concentration (wt %)	Absorption at 1.38 µm (dB/m)	OH concentration (ppm)	Slope efficiency (%)
L10382	80	35 (core)	0.25	0.07	0.13	74 ± 3
L10382 Fluorine clad	150	1 (cladding)	0.25	0.07	0.13	67 ± 2

4.10.1 All-glass, double-clad fibre characterisation

The fluorine-clad fibre was characterised in a free-space cladding-pumped configuration. Two different configurations were investigated using the schematics as illustrated in Fig. 4.13. In both configurations the output from the 1.95 µm pump laser was collimated and then focused into the octagonal cladding of the holmium-doped fibre. At the other end of the fibre a dichroic mirror separated the residual 1.95 µm pump radiation from the 2.1 µm holmium emission. In one configuration, the distal end of the fibre had an angle cleave and the cavity was formed between the HR and 4% Fresnel reflection. In this configuration the cladding-pumped holmium-doped fibre was operated in a counter-pumped regime. One of the challenges here was ensuring stable alignment of the HR mirror at higher power levels. The transmitted pump and intra-cavity radiation at 2.1 µm caused sufficient thermal lensing in the collimating optic that the alignment degraded as a function of output power.

In order to avoid these complications with this free-space coupled feedback, the fibre was re-cleaved with a perpendicular cleave and a cavity was formed between the opposing 4% Fresnel reflections at each end. In this case the output power of the laser was split almost equally between the two beams exiting each end of the fibre. Power meters were positioned to measure the power of each output simultaneously. This configuration was observed to be much more stable and resistant to misalignment and fluctuation than the initial approach. In a final configuration, the fibre would be envisaged to be utilised in an all-fibre configuration with either FBG reflectors to provide feedback, or a master oscillator spliced onto the fibre to provide an input signal to be amplified.

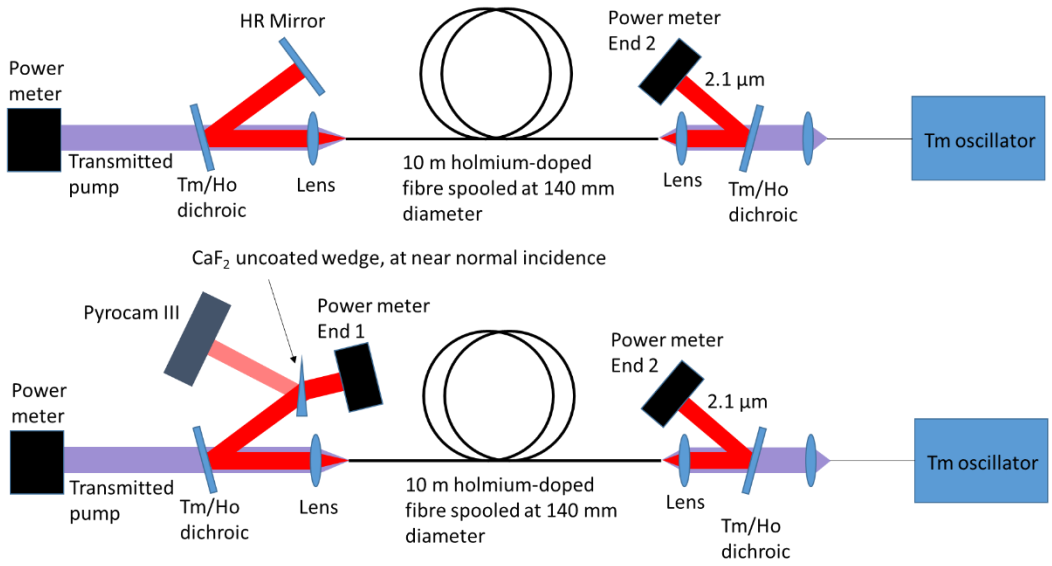

Figure 4.13: Illustration of cavities used to characterise the in-house fabricated, all-glass, double-clad, holmium-doped fibre.

In order to ensure that the pump light was launched into the inner octagonal cladding and not the outer cladding, which would also provide guidance, but with a substantially increased loss due to the low index polymers, the output pump power from the fibre at all operating power levels was monitored. Examples of bad and good launch alignment are shown in Fig. 4.14.

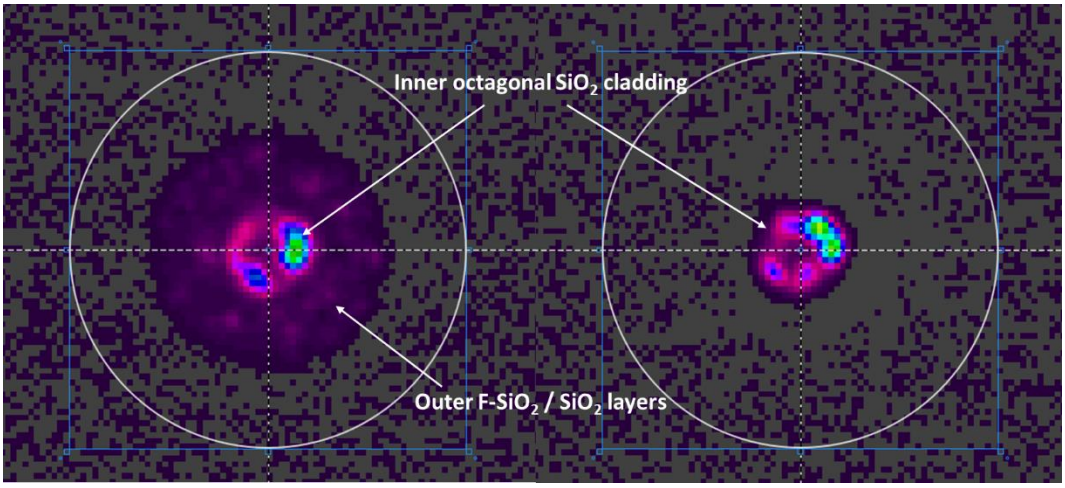

Figure 4.14: Illustration of poor (left) and good (right) alignment of the 1.95 µm pump laser into the inner cladding of the fluorine-clad, holmium-doped fibre.

4.10.2 All-glass, double-clad fibre results

The output power vs the launched pump power for the lasers shown in Fig. 4.13 is shown in Fig. 4.15. The fibre operated with an efficiency of 67% with respect to absorbed pump power. In the 10 m device, the pump absorption under operating conditions was 90% - which is in agreement with the expected area ratio and core absorption measurements. The cavity length increased from 2.5 m in the core-pumped configuration to 10 m in the cladding-pumped system as expected based on discussions in Section 4.5. The reduced slope efficiency of the cladding-pumped system can be entirely attributed to the increased fibre length and the resulting increase in IR background losses. As such an increase in the IR loss up to a maximum of 10% is expected. This is consistent with the reduction in slope efficiency that we observe (from 74% in the core-pumped configuration to 67% in the cladding-pumped configuration).

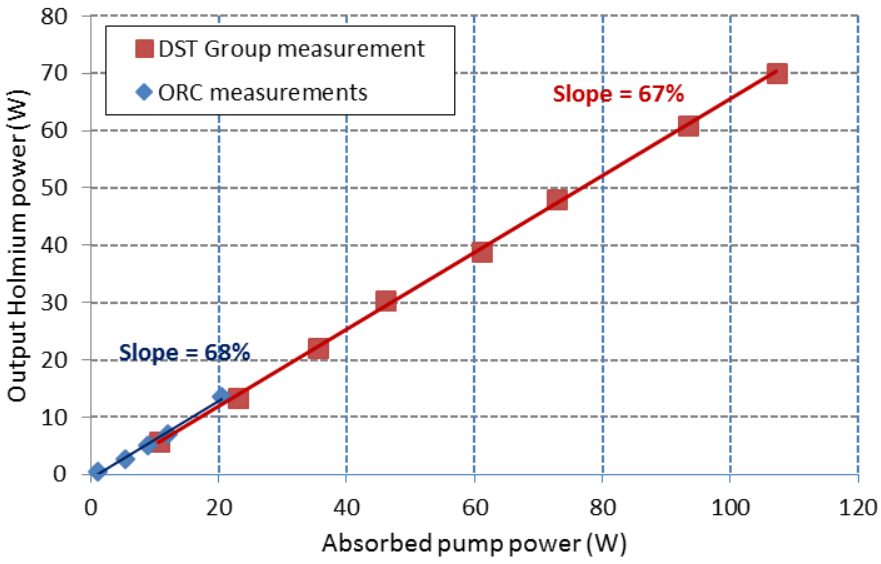

Figure 4.15: Output power at 2100 nm vs. absorbed pump power at 1950 nm. The pump absorption was measured to be ~90% for the fibre length of 10 m.

The laser operated free-running at 2100 nm as shown in Fig. 4.16a). The output beam had a Gaussian profile (shown in Fig. 4.16b)) and an $M^2_{x,y}$ = 1.04, 1.08 suggesting that the fibre was operating with a robustly single-mode and near diffraction limited output. This is also consistent with the measured fibre core parameters (14 µm diameter, 0.11 NA) which yields a V number of 2.3 at 2100 nm corresponding to single-mode operation.

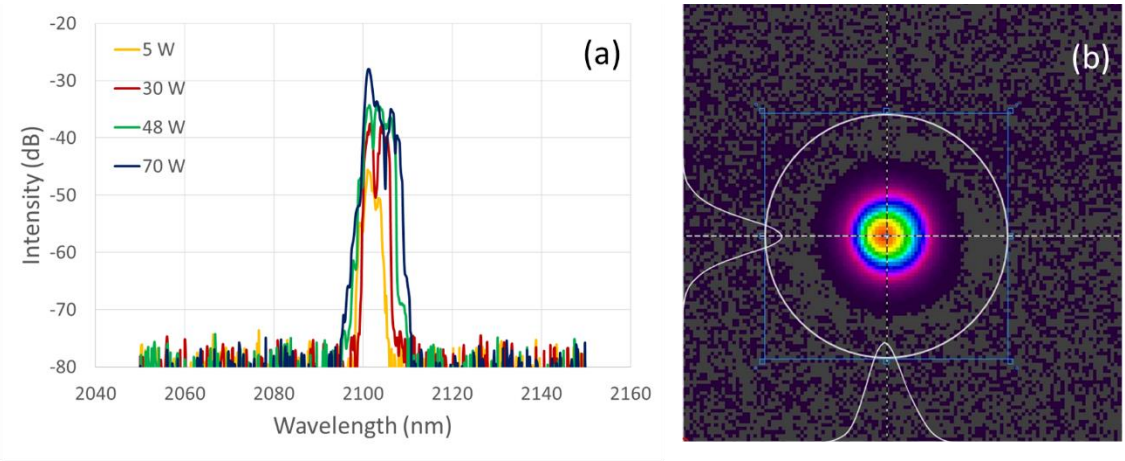

Figure 4.16: a) Spectral output and b) beam profile from the holmium-doped, all-glass, double-clad fibre.

4.11 Summary

In this chapter we have described methods for measuring and quantifying parameters which impact the efficiency of holmium-doped fibres such as dopant concentration, hydroxyl impurity concentration and background loss. We have developed and described a technique enabling efficiency measurements to be made with simple single-mode fibres and quantified the possible sources of error. This technique has enabled a rapid, low-cost iteration of the composition in order to methodically improve fibre fabrication parameters.

A summary of the various compositions that have been developed in-house as well as those reported in the literature is provided in Fig. 4.17. A common trend is the consistent reduction in slope efficiency at larger dopant concentrations. This is consistent with the expected up-conversion losses. More recent demonstrations by Hemming et al. have shown slope efficiencies of resonantly pumped holmium-doped fibres of 87% which are approaching the theoretical limit of 93% [30].

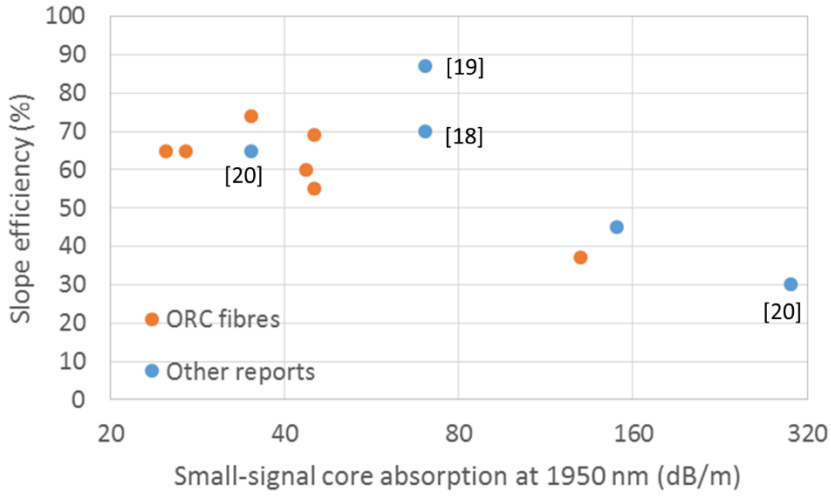

Figure 4.17: Summary of the performance of various holmium-doped silica fibres reported in the literature and developed as part of this project [29–31].

Finally we have demonstrated an all-glass, double-clad fibre based on the best performing composition developed. This fibre was then power scaled up to 70 W. The fibre operated with a 67% slope efficiency with respect to absorbed 1950 nm pump power, and equals the current record in efficiency for a cladding-pumped holmium-doped fibre [23]. Fabrication of such a fibre is particularly challenging due to the complexity associated with the fabrication of a shaped inner cladding with a Fluorine-doped silica outer layer while ensuring that there is minimal hydroxyl contamination both in the core and the cladding. The CO_2 processing of the preform and the careful optimisation and characterisation of composition were essential to achieving this result.

4.12 References

1. J. B. Macchesney, L. Walker, S. R. Nagel, J. B. Macchesney, and K. L. Walker, "An Overview of the Modified Chemical Vapor Deposition (MCVD) Process and Performance," IEEE Trans. Microw. Theory Tech. **30**, 305–322 (1982).

2. T. Izawa, N. Shibata, and A. Takeda, "Optical attenuation in pure and doped fused silica in the IR wavelength region," Appl. Phys. Lett. **31**, 33 (1977).

3. O. Humbach, H. Fabian, U. Grzesik, U. Haken, and W. Heitmann, "Analysis of OH absorption bands in synthetic silica," J. Non. Cryst. Solids **203**, 19–26 (1996).

4. J. E. Townsend, S. B. Poole, and D. N. Payne, "Solution-doping technique for fabrication of rare-earth-doped optical fibres," Electron. Lett. **23**, 329–331 (1987).

5. E. J. Friebele, C. G. Askins, J. R. Peele, B. M. Wright, N. J. Condon, S. O'Connor, C. G. Brown, and S. R. Bowman, "Ho-doped fiber for high energy laser applications," Proc. SPIE **8961**, 896120 (2014).

6. N. Uchida and N. Uesugi, "Infrared optical loss increase in silica fibers due to hydrogen," J. Light. Technol. **4**, 1132–1138 (1986).

7. Y. Ohmori, T. Miya, and M. Horiguchi, "Transmission-Loss Characteristics of Al_20_3-Doped Silica Fibers," J. Light. Technol. **LT**-**1**, 50–56 (1983).

8. M. Ohashi, K. Shiraki, and K. Tajima, "Optical loss property of silica-based single-mode fibers," J. Light. Technol. **10**, 539–543 (1992).

9. S. Sakaguchi and S. Todoroki, "Optical properties of GeO_2 glass and optical fibers.," Appl. Opt. **36**, 6809–6814 (1997).

10. M. J. F. Digonnet, *Rare-Earth-Doped Fiber Lasers and Amplifiers* (Marcel Dekker, 2001).

11. J. E. Townsend, "The development of optical fibers doped with rare earth ions," The University of Southampton (1990).

12. A. Dhar, A. Pal, M. C. Paul, P. Ray, H. S. Maiti, and R. Sen, "The mechanism of rare-earth incorporation in solution doping process," Opt. Express **16**, 12835–12846 (2008).

13. L. Cognolato, "Chemical Vapour Deposition for Optical Fibre Technology," J. Phys. IV **5**, C5-975-C5-987 (1995).

14. S. D. Jackson, "Midinfrared Holmium Fiber Lasers," IEEE J. Quantum Electron. **42**, 187–191 (2006).

15. S. D. Jackson and S. Mossman, "Efficiency dependence on the Tm^{3+} and Al^{3+} concentrations for Tm^{3+}-doped silica double-clad fiber lasers," Appl. Opt. **42**, 2702 (2003).

16. A. S. Kurkov, E. M. Sholokhov, V. B. Tsvetkov, A. V Marakulin, L. A. Minashina, O. I. Medvedkov, and A. F. Kosolapov, "Holmium fibre laser with record quantum efficiency," Quantum Electron. **41**, 492–494 (2011).

17. C. B. Layne, W. H. Lowdermilk, and M. J. Weber, "Multiphonon relaxation of rare-earth ions in oxide glasses," Phys. Rev. B **16**, 10–20 (1977).

18. M. Oermann, D. Stepanov, L. Corena, A. Hemming, N. Simakov, and J. Haub, "Single-Polarisation DBR Fibre Laser in Photosensitive Ho-doped Fibre," in *Australian and New Zealand Conference on Optics and Photonics* (2013), pp. 1–3.

19. A. Hemming, S. Bennetts, N. Simakov, J. Haub, and A. Carter, "Development of resonantly cladding-pumped holmium-doped fibre lasers," Proc. SPIE **8237**, 82371J (2012).

20. A. Carter, A. Hemming, N. Simakov, A. Davidson, D. Stepanov, L. Corena, M. Hughes, N. Carmody, P. Davies, J. Haub, and A. Carter, "An Efficient, High Power, Monolithic, Single Mode Thulium Fibre Laser," in *Workshop on Specialty Optical Fibers and Their Applications* (2013), Vol. 34, p. T2.4.

21. N. Simakov, A. Hemming, A. Carter, K. Farley, A. Davidson, N. Carmody, J. M. O. Daniel, M. Hughes, L. Corena, D. Stepanov, and J. Haub, "170 W Single-mode Large Pedestal Thulium-doped Fibre Laser," in *CLEO/Europe Conference on Lasers and Electro-Optics* (Optical Society of America, 2015), p. CJ_13_2.

22. N. Simakov, A. V. Hemming, A. Carter, K. Farley, A. Davidson, N. Carmody, M. Hughes, J. M. O. Daniel, L. Corena, D. Stepanov, and J. Haub, "Design and experimental demonstration of a large pedestal thulium-doped fibre," Opt. Express **23**, 3126 (2015).

23. A. Hemming, S. Bennetts, N. Simakov, A. Davidson, J. Haub, and A. Carter, "High power

operation of cladding pumped holmium-doped silica fibre lasers," Opt. Express **21**, 4560 (2013).

24. S. W. S. Ng, D. G. Lancaster, T. M. Monro, P. C. Henry, and D. J. Ottaway, "Air-Clad Holmium-Doped Silica Fiber Laser," IEEE J. Quantum Electron. **52**, 1–8 (2016).

25. N. P. Barnes, B. M. Walsh, and E. D. Filer, "Ho:Ho upconversion: applications to Ho lasers," J. Opt. Soc. Am. B **20**, 1212 (2003).

26. N. Simakov, A. Hemming, W. A. Clarkson, J. Haub, and A. Carter, "A cladding-pumped, tunable holmium doped fiber laser," Opt. Express **21**, 28415–28422 (2013).

27. A. Hemming, N. Simakov, J. Haub, and A. Carter, "A review of recent progress in holmium-doped silica fibre sources," Opt. Fiber Technol. **20**, 621–630 (2014).

28. A. S. Kurkov, E. M. Sholokhov, O. I. Medvedkov, V. V. Dvoyrin, Y. N. Pyrkov, V. B. Tsvetkov, A. V. Marakulin, and L. A. Minashina, "Holmium fiber laser based on the heavily doped active fiber," Laser Phys. Lett. **6**, 661–664 (2009).

29. A. Sincore, L. Shah, V. Smirnov, and M. Richardson, "Comparison of in-band pumped Tm:fiber and Ho:fiber," Proc. SPIE **9728**, 97280S (2016).

30. A. Hemming, N. Simakov, M. Oermann, A. Carter, and J. Haub, "Record efficiency of a holmium-doped silica fibre laser," in *Conference on Lasers and Electro-Optics* (OSA, 2016), p. SM3Q.5.

31. S. Hollitt, N. Simakov, A. Hemming, J. Haub, and A. Carter, "A linearly polarised, pulsed Ho-doped fiber laser," Opt. Express **20**, 16285 (2012).

Chapter 5.

Thulium and Holmium Sources

5.1 Introduction

This chapter presents the operation of thulium-doped and holmium-doped fibres in various regimes. The first section reviews the development of monolithic, robustly single-mode, thulium fibre lasers operating at 1950 nm. These act as pump sources for the holmium-doped silica fibres.

A range of small-signal thulium-doped and holmium-doped fibre amplifiers is investigated and a wavelength coverage spanning 1660 – 2150 nm with > 15 dB gain is demonstrated. A variety of amplifier geometries are considered and a host of techniques for increasing the spectral coverage are investigated. These techniques include the use of spectral filters, inversion management and amplifier geometry.

A double-clad holmium-doped fibre is characterised in a tuneable configuration with a demonstrated output of >15 W over a span from 2040 – 2170 nm. This represents one of the longest wavelength sources in a silica fibre with a power level exceeding 10 W.

Finally the concept of wavelength agility is introduced and a source that can be rapidly, electronically switched and swept across 2050 – 2140 nm based on an acousto-optical tuneable filter (AOTF) and a holmium-doped silica fibre gain medium is demonstrated.

5.2 High power 1950 nm pump source development

There have been few demonstrations of diffraction limited performance from large-mode-area (LMA) thulium-doped fibre designs incorporating a pedestal. Only a few groups have been able to report near diffraction limited (M^2<1.1) performance at power levels exceeding 50 W [1]. Typically thulium-doped fibre lasers utilising LMA-type fibres to enable power scaling to >50 W are reported

with beam qualities ranging from $M^2 = 1.2 – 3$ [2–8]. This degradation in beam quality can lead to pointing instability, lower efficiency and spectral instability of the laser [9–11] and these effects may make the laser less suitable for the target application. There is a clear need for a more robust thulium-doped fibre solution that will enable high power, diffraction limited performance from thulium-doped fibre sources.

5.2.1 Thulium-doped fibre design

In the case of 0.79 µm diode pumped thulium-doped fibre lasers, the requirement for efficient cross-relaxation results in a core composition that has a refractive index difference of ~0.02 with respect to the un-doped silica cladding, which is equivalent to a core NA of 0.23. A robustly single-mode core of this composition is then limited to a maximum core-diameter of ~6 µm for a V-number of 2.4 at 1950 nm. This presents a challenge in power scaling due to the high intensity present in such a small core. Furthermore, power scaling is typically achieved by scaling the cladding diameters to 400 µm in order to match the available diode brightness and alleviate the thermal issues. This core:cladding (6:400 µm) ratio results in a very long fibre (>20 m) for efficient pump absorption. At these lengths it will be difficult to operate at 1950 nm and the fibre gain-peak will be in the 1980 – 2020 nm region. As a result a method for increasing the core-diameter without degrading beam quality or changing composition is required to ensure that the fibre length remains sufficiently small to allow for stable operation at 1950 nm.

As the core NA cannot be reduced without degrading the efficiency of the laser, one approach is to produce a raised index cladding around the core commonly termed a pedestal [12]. In this case, the core experiences a local low-index step, and hence low NA, whilst maintaining the core composition required for good pump conversion efficiency. Figures 5.1a) – 5.1b) show the end-face images of the current commercially available 25 µm core diameter TDF and the new fibre which has a 20 µm core diameter. Both fibres have a pedestal structure and a 400 µm flat-to-flat octagonal cladding.

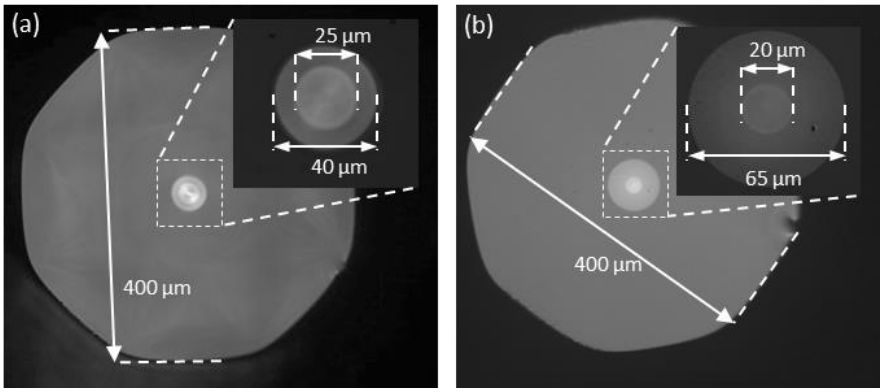

Figure 5.1: a) End-face view of a 25P/400-TDF with a 25 µm core, 40 µm pedestal and a 400 µm flat-to-flat octagonal cladding. b) End-face view of a 20LP/400-TDF (LP: large pedestal) with a 20 µm core, 65 µm pedestal and a 400 µm flat-to-flat octagonal cladding [13].

5.2.2 Impact of pedestal diameter

The choice of pedestal diameter is dictated by a trade-off between on-lathe fabrication time of the preform, preform yield and fibre laser performance. In the following sections, we examine some key parameters for fibres that incorporate a pedestal to improve beam quality, and demonstrate that an increase in laser performance and yield on device fabrication can justify the move to a more challenging, large pedestal design.

In an amplifier or laser device utilising active fibres with pedestals, the radiation coupled into the pedestal, due to either splice loss or spontaneous emission, experiences significant interaction with the core and potentially a large gain. As a result this leads to problems such as reduced hold-off in pulsed systems, and imposes a higher sensitivity to splice loss in these devices. Furthermore there may also be significant backward propagating ASE guided by the pedestal. An illustration of these various effects and how they propagate through the fibre core and cladding is shown in Fig. 5.2.

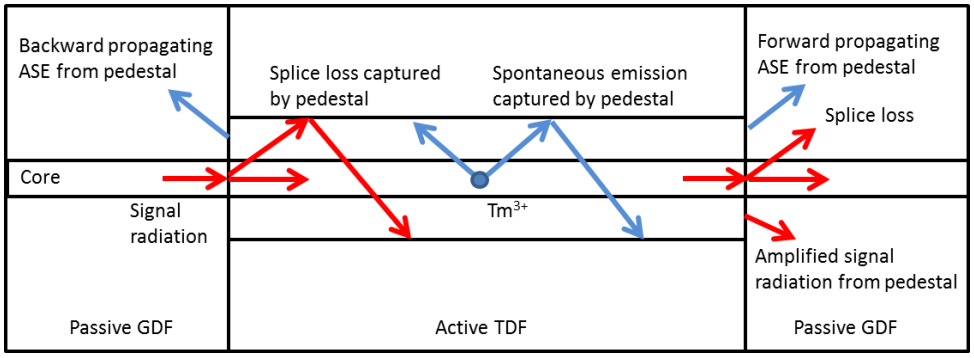

Figure 5.2: Illustration of a splice between a passive non-pedestal fibre and an active fibre containing a pedestal around the core. The majority of the radiation at the splice from the passive to the active fibre is contained by the pedestal (red arrows). This radiation will experience amplification based on the interaction with the core. The pedestal is also able to capture some of the spontaneous emission from the excited rare-earth ions (blue arrows). This radiation also experiences amplification and has components travelling in both directions along the active fibre. At the active fibre to passive fibre splices, due to the spatial overlaps, the radiation from the pedestal will be coupled into the cladding and no longer confined by the core [13].

Any radiation contained in the pedestal will not be guided by the core of the passive fibre and will thus couple to the cladding of the GDF at the splices at either end of the active fibre. As well as degrading performance these processes can degrade device lifetimes, such as fibre Bragg gratings (FBGs), fused combiners, isolators, laser diodes and cladding strippers.

The detrimental interaction between the radiation propagating in the pedestal and in the core can be estimated by considering the relative areas of both structures. For the 25P/400-TDF, the radiation propagating in the pedestal experiences only a slightly reduced (40% as shown in Fig. 5.3) interaction strength with the core. In the 20LP/400-TDF, the core diameter is reduced to 20 µm and the pedestal diameter is increased to 65 µm, substantially reducing this interaction strength from 40% to 10%.

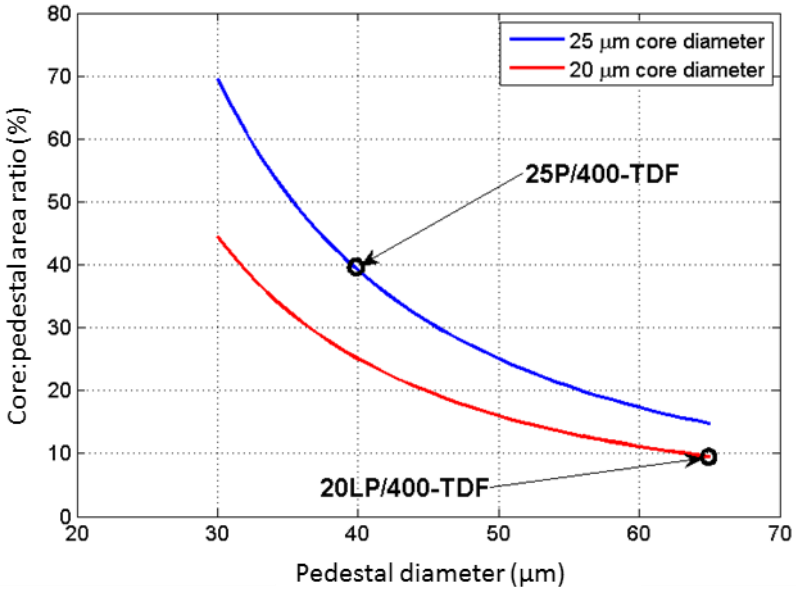

Figure 5.3: The area ratio used to estimate the effective overlap between the radiation propagating in the pedestal and the core as a function of pedestal diameter for different core diameters. Indicated are the parameters for the commercially available 25P/400-TDF and the 20LP/400-TDF fibre design used in the current work [13].

5.2.3 High power 1950 nm thulium-doped fibre laser

A schematic of the laser fabricated using the 20LP/400-TDF is shown in Fig. 5.4. The output from a fibre-coupled laser diode is tapered and then spliced to the passive fibre containing the HR FBG. The GDF passive fibre has a matched MFD to the active TDF and a 400 μm diameter cladding with a 0.46 NA. The other end of the passive fibre is spliced to a 6 m length of active thulium-doped fibre. The active fibre is mounted in a heat-sink which contains bends of 50 mm radius. The output end of the TDF is spliced to another length of 400 μm GDF passive fibre, which contains a 10% reflective output coupler (OC) FBG. The passive fibre containing the OC also contains a cladding stripper to remove any residual pump radiation and 2 μm light that may have been coupled into the cladding due to splice losses. A 1.5 mm long, 400 μm diameter core-less fused silica fibre is spliced onto the output. A 2° angle on the end-cap is used to further reduce the amount of feedback that occurs from the Fresnel reflection at the glass-air interface.

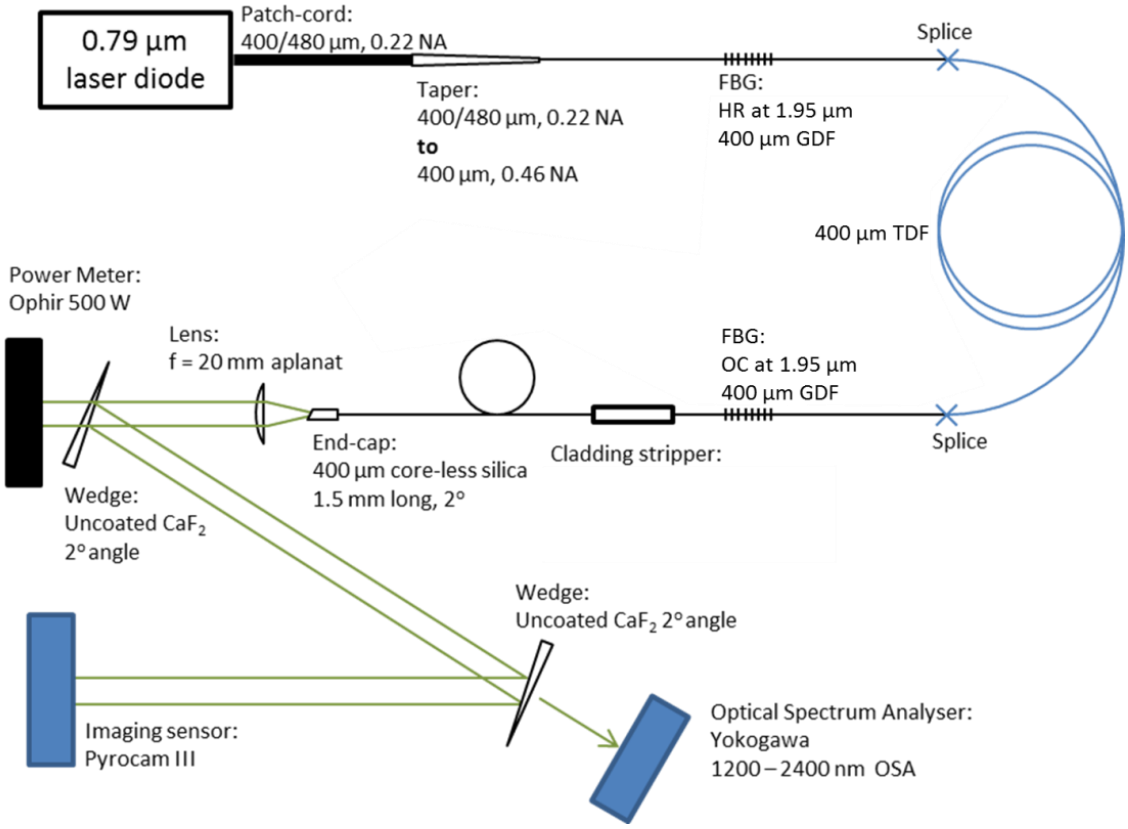

Figure 5.4: A schematic of a typical 1.95 µm thulium-doped fibre laser [13].

The output from the laser is collimated using a high power IR lens (DPM Photonics) and is attenuated by several wedges (CaF_2) before being brought to a waist using a ZnSe lens and directed onto a pyro-electric detector (Pyrocam III). The M^2 parameter of the laser output was measured by translating the Pyrocam and recording the beam parameters through the beam waist. The spectrum was measured using an optical spectrum analyser (Yokogawa, OSA) and the output power levels were monitored on calibrated thermal power meters (Ophir).

The output power from multiple lasers is shown in Fig. 5.5a). Each laser is capable of producing more than 160 W with a slope efficiency varying from 50 – 52%. The variation in slope efficiency is attributed to the variation of the exact fibre length and differences in the splice losses between lasers. A typical beam profile measurement at maximum power is shown in Fig. 5.5b). The beam diameter evolves with an $M^2_{X,Y}$ = 1.02, 1.03 indicating that the laser is operating with a diffraction limited output. The intensity profile has a >94% quality of fit to Gaussian at all points. We confirm that all of the radiation is confined to the core of the single-mode passive output fibre, with no measureable power in the cladding.

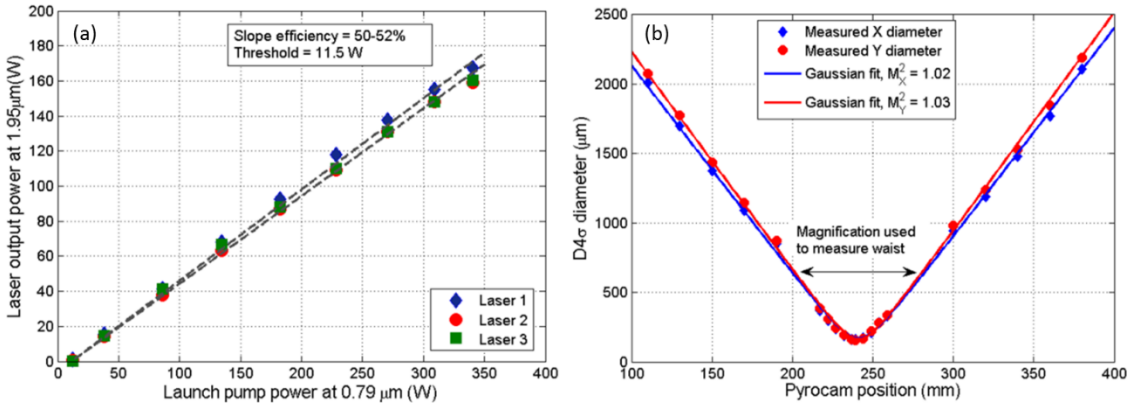

Figure 5.5: a) Slope efficiency of 1.95 µm output vs 0.79 µm launched pump power. b) Evolution of the second moment width (D4σ) beam diameter through the focus of a lens and the Gaussian fit of the output at maximum power [13].

The evolution of the spectrum with respect to output power is shown in Fig. 5.6a). The full-width half maximum (FWHM) bandwidth of the output was observed to increase from a resolution limited 0.05 nm to 0.1 nm as the laser power was increased from 16 W to 170 W. A low resolution (2 nm), high sensitivity scan of the entire thulium gain band is shown in Fig. 5.6b) confirming that there is a negligible level of ASE and no parasitic lasing at other wavelengths.

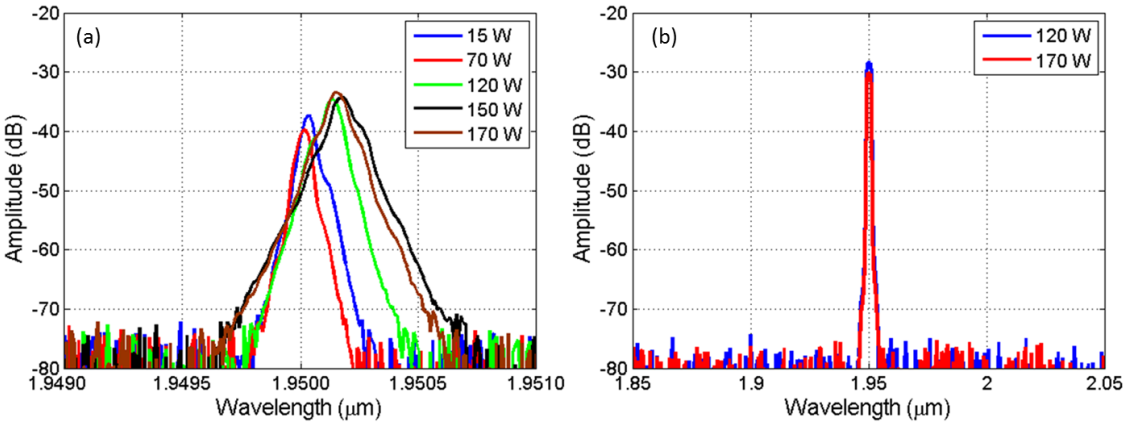

Figure 5.6: a) Evolution of the spectrum with increasing output power measured with an OSA resolution setting of 0.05 nm. b) Laser output spectrum measured with an OSA resolution setting of 2 nm showing there is negligible ASE content at the output of the laser [13].

5.2.4 Discussion

We have presented the design and characterisation of a thulium-doped fibre laser (TDFL) based on an active fibre incorporating a large-pedestal geometry. The TDFLs presented here have a relatively

low component count, are completely monolithic and produce up to 170 W output power at 1950 nm with a robustly single-mode output with an efficiency ranging from 50-52% with respect to launched pump power. By correcting for pump losses in the components before the active fibre, the total absorbed pump radiation and the Fresnel reflection from the uncoated end-cap, we estimate the internal efficiency of the thulium fibre to be ~58% with respect to absorbed pump power. This has been verified in separate cut-back measurements. This slope is still far from the ideal efficiency of 80% (assuming ideal cross-relaxation) and suggests that there are still potentially significant efficiency gains that can be made by optimizing both the composition and the fibre design.

The output beam propagated with a Gaussian fit of $M^2_{X,Y}$ = 1.02, 1.03 at the full output power of the laser. No pointing instability or variation in beam quality was observed while changing the pump power. The output spectrum has a spectral linewidth of <0.2 nm and shows no evidence of higher order modes supported by the FBG which are typically reported in systems that operate with multiple transverse modes [8].

We have demonstrated sources relying on these and similar fibre designs operating at 1908 nm, for the pumping of room temperature and cryogenic Ho:YAG solid-state lasers, 1940 nm, for the pumping of Ho:YLF lasers, and at 1950 nm, for the pumping of Ho:silica, as well as at wavelengths as large as 2050 nm [14].

5.3 Small-signal amplifiers in thulium-doped and holmium-doped fibres

The availability of practical, high-performance optical amplifiers is a critical enabler for many important photonics applications. For instance, the erbium-doped fibre amplifier (EDFA) operating from 1530–1625 nm revolutionized the field of optical telecommunications, eliminating fibre attenuation as a fundamental limit to long distance optical fibre communications. Here we report the demonstration of a suite of practical thulium-doped and holmium-doped silica fibre based amplifiers, providing continuous, high-gain, low-noise small-signal amplification across a waveband extending from 1660 nm to the effective upper-edge of the silica fibre transparency window at 2150 nm, corresponding to a 490 nm gain bandwidth. The availability of such amplifiers in this previously difficult to address waveband should pave the way for a plethora of important fibre

optics applications in areas such as optical communications, sensing, medicine and laser based materials processing.

5.3.1 Amplifier configurations

The geometry of the amplifiers investigated was similar to that of the typical EDFA. These were all core-pumped systems where the pump radiation was launched into the core of the active fibre (either thulium or holmium) via a wavelength combining element such as a dichroic based WDM or a fused biconic taper WDM. We investigated both direct diode pumping using 790 nm, 1150 nm and 1550 nm diodes to address the respective absorption bands in the rare-earth ions. In situations where a larger inversion was required, either erbium-ytterbium-doped fibre lasers (EYDFL) or thulium-doped fibre lasers (TDFL) were utilised for pumping the thulium-doped and holmium-doped fibres respectively.

We investigated both single-pass and double-pass configurations as shown in Figs. 5.7a) – 5.7b). In some cases, spectral filtering mechanisms were employed within the amplifier to enable operation at the extreme wavelengths. These mechanisms include the use of bend-loss filters, absorptive filters, as well as the implementation of long-wavelength pumping for inversion management.

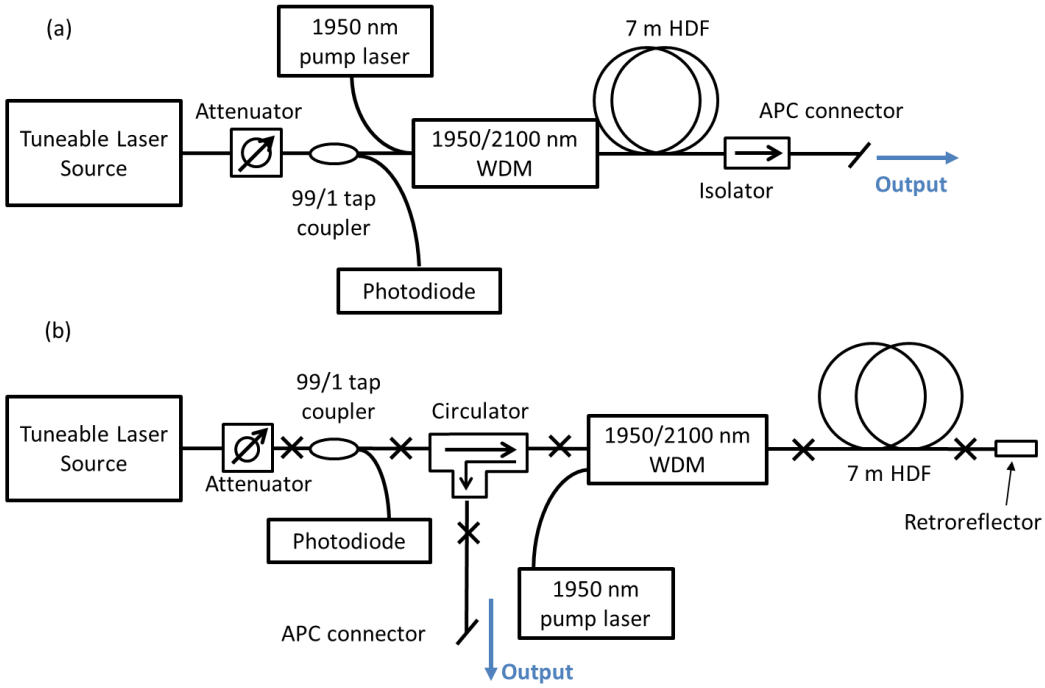

Figure 5.7: Two different amplifier configurations with a) Single-pass holmium amplifier configuration. b) Double-pass holmium amplifier configuration [15].

5.3.2 Amplifier characterisation method

In the following, we describe the measurements that were used to perform the amplifier characterisation. These measurements describe the properties of the amplifier such as noise-figure, small-signal gain, saturated gain and spectral bandwidth which is essential when applying the amplifier to a range of applications.

First, a known input signal at a known wavelength is launched into the amplifier. The input signal power level, and the level of the background ASE are measured. In practise, a monochromatic signal with a low level (>50 dB extinction) of background noise provides a suitable input source for these measurements. The output of the amplifier is characterised, with measurements taken of the output spectrum, and the average output power. In an ideal situation, the amplifiers would be characterised for a continuous range of input power levels at each wavelength; however due to the absence of an automated fibre attenuator and diagnostics, this amount of data collection was not possible. As a result, for the following characterisations, 2 different seed input power levels were chosen corresponding to a “small-signal” (-20 dBm = 0.01 mW) regime and a “saturating signal” (0 dBm = 1 mW) regime.

A schematic of the tuneable source and the associated components for diagnostic measurement that were used in the characterisation of the holmium-doped amplifiers is shown in Fig. 5.8a). The output from a tuneable Cr:ZnSe laser (IPG) was launched into a single-mode fibre and passed through an all-fibre attenuator. A 99/1 tap coupler and a photodiode were used to monitor the power levels launched into the amplifier. The spectral quality of the output was found to be excellent with an optical signal to noise ratio (OSNR) of ~65 dB as shown in Fig. 5.8b). The reproducibility and stability of the calibrated output was measured to be ±0.2 dB which was attributed in part to the stability of the fibre coupling fixture and the pointing stability of the solid-state, tuneable laser source. The laser was not operated below 2030 nm due to a degradation in performance of the 99/1 tap coupler at the shorter wavelengths and also due to potential risk of damage occurring to the tuneable laser source when tuning to <2030 nm.

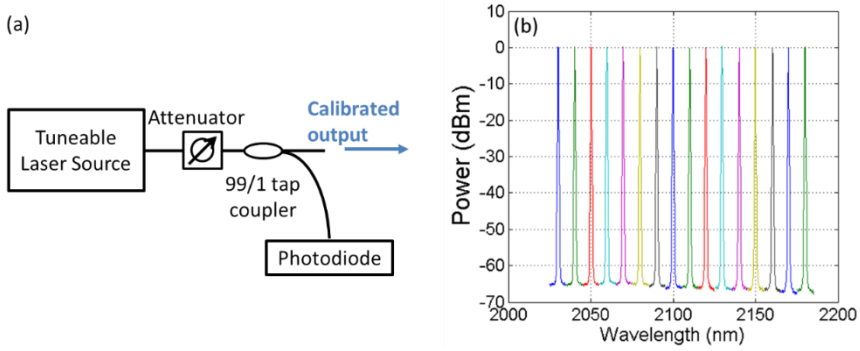

Figure 5.8: a) Schematic of tuneable laser source, attenuator and tap coupler used to monitor and calibrate the input signal level. b) The calibrated output at different wavelengths showing a >60 dB optical signal-to-noise ratio and a nearly constant power level of 0 dBm at the peak [15].

The procedure for characterising the amplifier was carefully repeated as follows:

1. The master oscillator was tuned to the desired wavelength and allowed to stabilise
2. The attenuator was adjusted to ensure the power launched into the amplifier was correct
3. The pump source to the amplifier was turned on and allowed to stabilise for 1-2 minutes
4. The average power was recorded on a thermal power meter
5. The spectrum was recorded using an OSA via a broad-band attenuator
6. The pump source was switched off and the process repeated for another wavelength

An example of a characterisation summary and the output spectra from one HDFA is shown in Figs. 5.9a) – 5.9c).

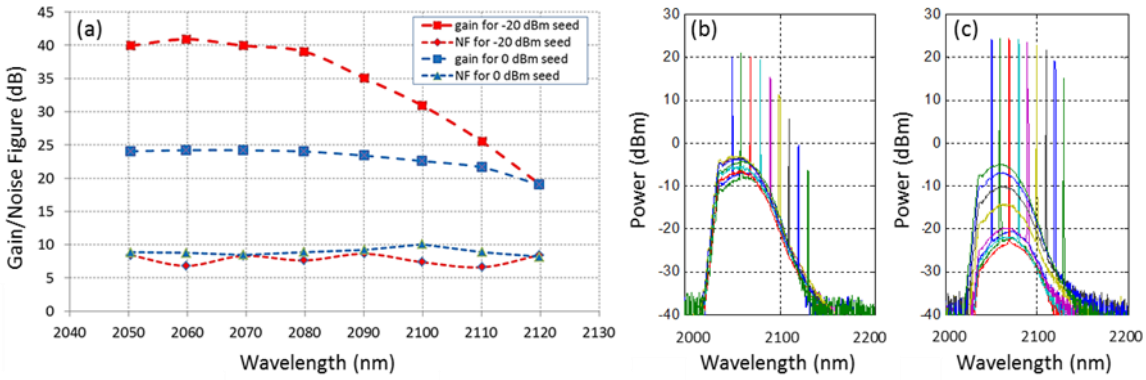

Figure 5.9: Performance of the 1950 nm fiber laser pumped HDFA. a) Summary of gain and NF vs. wavelength. b) Amplified spectra for the small-signal with a non-saturating (-20 dBm) input signal. c) Amplified spectra with a saturating (0 dBm) input signal. The spectra were measured with an OSA resolution setting of 0.5 nm [15].

5.3.3 Performance of small-signal amplifiers

Table 5.1 summarizes the various amplifiers that have been characterised and provides information about bandwidth, operating wavelengths, noise figures, pump sources and whether or not spectral filtering was employed. All of these have been fully described across various papers and in order to avoid repetitive content, this is information is not included in this thesis.

As shown in Fig. 5.10, almost a 500 nm bandwidth (at the >15 dB gain level) of continuous coverage has been demonstrated from 1660 – 2150 nm by using either thulium or holmium-doped silica fibre amplifiers. The solid data points correspond to fibre-laser pumped amplifiers and open data points correspond to diode pumped amplifiers. The fitted lines represent the small-signal gain parameter and the points represent the noise-figure performance of each of the amplifiers.

Table 5.1: Summary of the various amplifiers that have been demonstrated spanning almost 500 nm in the infrared wavelength region. Δλ refers to the 15 dB bandwidth of the amplifier.

Gain medium	Pump source	Spectral filtering	Peak gain (dB)	Gain peak (nm)	15 dB span (nm)	Δλ (nm)	Noise Figure (dB)	Ref.	Legend for Fig. 5.10
Thulium	EYDFL	Yes	29	1690	1660–1710	50	6.5-12	[16,17]	1.
Thulium	Diode, 790 nm	Yes	29	1760	1720–1800	80	9-15	[16,17]	2.
Thulium	EYDFL	Yes	33	1760	1710-1800	90	9-15	[16,17]	3.
Thulium	Diode, 1550 nm	No	35	1840	1740-1960	220	5-10	[18,19]	4.
Thulium	Diode, 1550 nm	No	36	1900	1820–2030	210	5-10	[18,19]	5.
Thulium	Diode, 1550 nm	No	33	1950	1890–2050	160	5-10	[18,19]	6.
Thulium	EYDFL	No	42	1950	1910–2020	110	5-12	[18,19]	7.
Holmium	Diode, 1150 nm	No	25	2040	2030–2100	70	5-7	[15]	8.
Holmium	TDFL	No	41	2060	2050–2120	70	6-10	[15]	9.
Holmium	TDFL	Yes	39	2090	2050–2150	100	8-14	[15]	10.

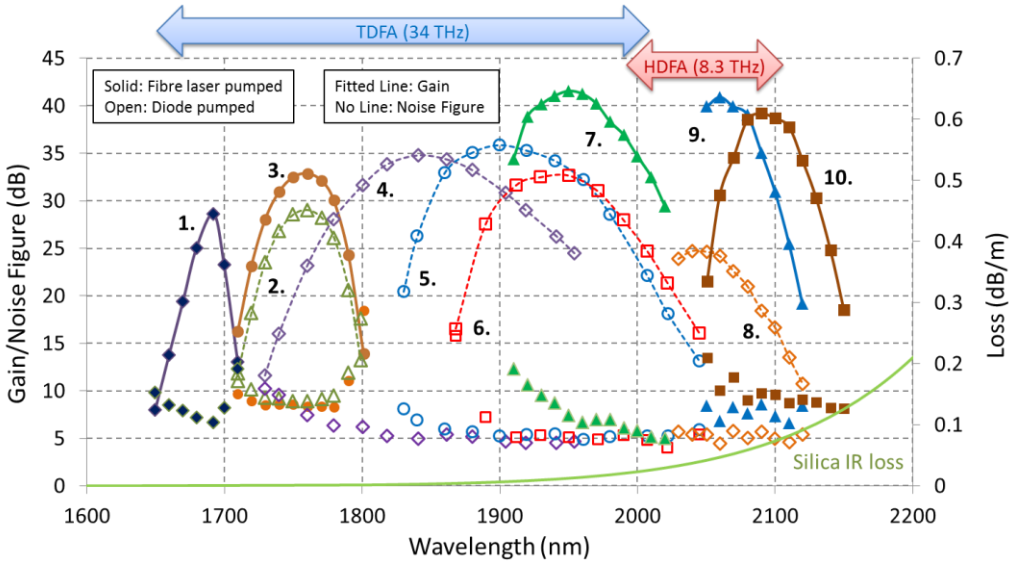

Figure 5.10: Summary of the gain curves and noise figures of various thulium-doped and holmium-doped fibre amplifiers. A continuous >15 dB gain coverage has been demonstrated from 1660 – 2150 nm [16–19].

5.3.4 Discussion

For rigorous characterisation of the amplifier architectures presented here measurements should be made at a continuously varying power level for both the master oscillator and also the pump to the amplifier, however this method was time prohibitive given the manual adjustment in the wavelength tuning, power adjustment and the quantity of amplifier experiments conducted. It is also important to note that the results presented here represent optimised amplifiers – i.e. with optimised fibre lengths, spectral filtering and operating pump powers. During the course of the development a number of iterations of the amplifiers were constructed and tested to demonstrate the optimum performance for each configuration.

In most cases the amplifier performance was limited by the performance of the available fibre coupled components. Dual-stage isolators in this wavelength range typically have an isolation rating of up to 40 dB – in comparison to 1550 nm components which are available with a single component isolation approaching 58 dB. This limits the peak gain at which the amplifiers can safely operate. Furthermore, unlike at 1550 nm, low insertion loss components are not readily available with typical insertion losses of ~1.3 dB at best. This reduces the available gain and also increases the noise figure of the various systems. As better components become available in this spectral region we anticipate that both the gain and NF of these systems will be improved, as well as the possible operating ranges.

5.4 Tuneable operation of a double-clad, holmium-doped fibre laser

As we have discussed in Section 2.4, power scaling of fibre sources requires the use of a double-clad geometry. This architecture results in a significantly lower pump intensity present in the core region. As we have analysed in Section 4.5, for efficient operation the active fibre must be sufficiently long to allow for a significant transfer of pump power to the core. The resulting parameter space and operating conditions for a double-clad holmium-doped fibre in a high power system is consequently very different to that of the small-signal amplifiers demonstrated in Section 5.3. In order to determine the operating wavelength of cladding-pumped, holmium-doped fibre lasers a tuneable laser experiment was undertaken [20].

5.4.1 Experimental set-up

A schematic layout of the experimental set-up is shown in Fig. 5.11. The output of a single-mode 1.95 µm fibre laser is collimated and launched into the cladding of a 6.5 m long double-clad holmium-doped fibre. This fibre had a robustly single-mode core with a diameter of 18 µm, and NA of 0.083. The holmium ion dopant concentration was 0.5 wt.%. The core was located within an octagonal cladding that had a flat-to-flat dimension of 112 µm and a 0.24 NA.

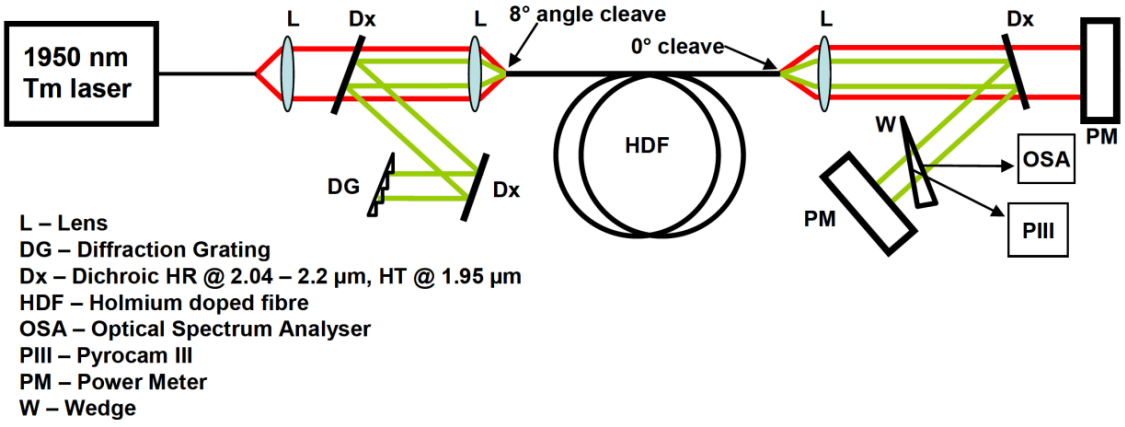

Figure 5.11: Schematic of tuneable holmium-doped fibre laser experiment [20].

Care was taken to ensure that the 1.95 µm pump light was focused into the cladding and not the core of the holmium-doped fibre in a similar manner as in Fig. 4.14. A dichroic mirror (Dx: HR @

2.04 – 2.2 µm, HT @ 1.95 µm) was placed in between the two ZnSe lenses (L, focal length = 15 mm) to separate the pump and laser light. This dichroic was angle tuned to minimize feedback between the holmium and thulium oscillators.

The laser cavity was formed between a diffraction grating (DG) and the 4% Fresnel reflection at the opposite end of the fibre. The tuning arrangement utilised a Littrow configuration. The reflectivity of the diffraction grating was >80% for P-polarized light and >90% for S-polarized light at 2.1 µm. This allowed for continuous tuning with minimal dependence on polarization state. In order to increase the threshold for parasitic lasing, the end of the HDF facing the dispersive end of the cavity was cleaved at an 8° angle. Another dichroic mirror was then used to separate the pump and laser light at the output. An uncoated CaF_2 wedge at near normal incidence provided two low power reflections which enabled monitoring of the spectrum and beam profile of the laser output on an optical spectrum analyzer (Yokogawa, AQ6375 OSA) and a pyroelectric beam profiler (Ophir, Pyrocam III). Calibrated thermal power meters (Ophir, Thorlabs) were used to monitor the residual pump power and output laser power throughout the experiment.

5.4.2 Results of tuning experiment

The typical spectrum (taken at an OSA resolution setting of 2 nm) of the output of the holmium-doped fibre laser is shown in Fig. 5.12. Parasitic lasing was observed when attempting to tune the laser beyond 2.171 µm. When attempting to tune to wavelengths <2.04 µm, there was significant feedback between the thulium-doped pump laser and holmium-doped fibre laser through the dichroic mirror, which was evident by spurious spectral emission when monitoring the spectrum of the thulium-doped pump laser. For the tuning graphs, only the operating points where parasitic or spurious lasing was absent are presented.

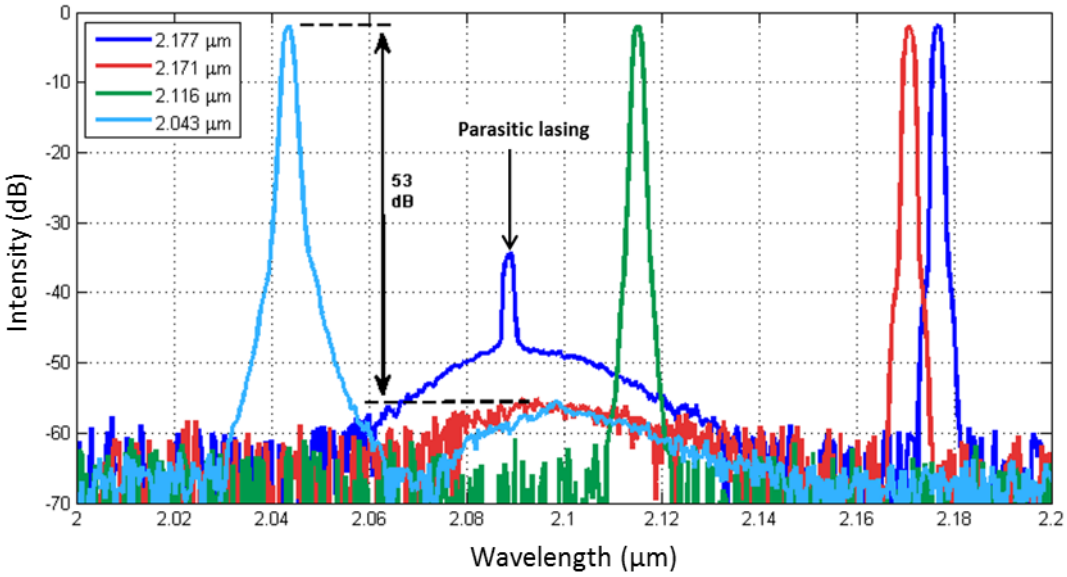

Figure 5.12: Typical spectra recorded at the output of the tuneable laser when operating at various wavelengths. These measurements are taken with an OSA resolution setting of 2 nm [20].

The results of the tuning experiments are shown in Fig. 5.13. The output from the holmium-doped fiber laser could be tuned from 2.04 µm to 2.171 µm while maintaining a signal-to-noise ratio of >53 dB

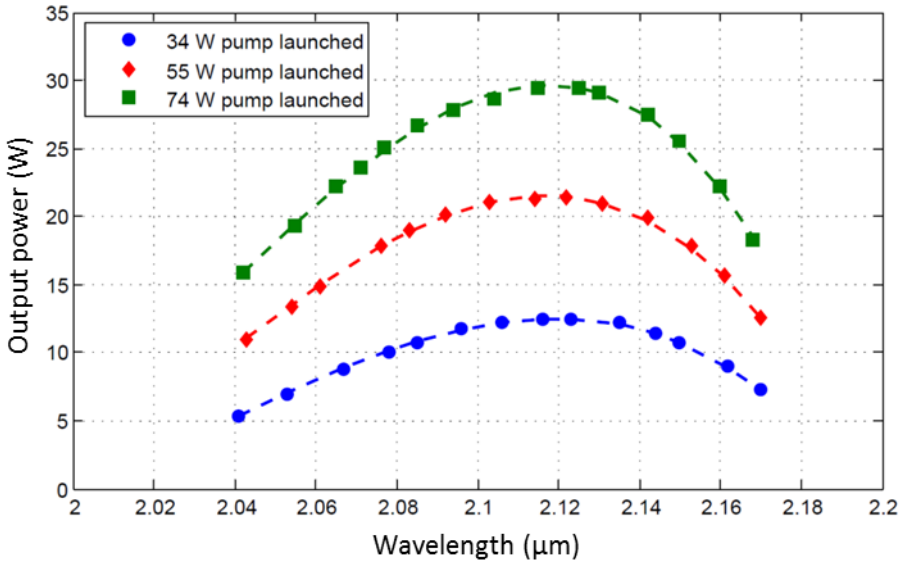

Figure 5.13: Output power vs wavelength for a range of launched pump powers. Only points with a signal-to-noise ratio of >53 dB are presented [20].

A maximum power of 29.7 W was achieved at 2.12 µm for 74 W of launched pump power. Slope efficiency measurements for operation at 2.12 µm and 2.171 µm are shown in Fig 5.14.

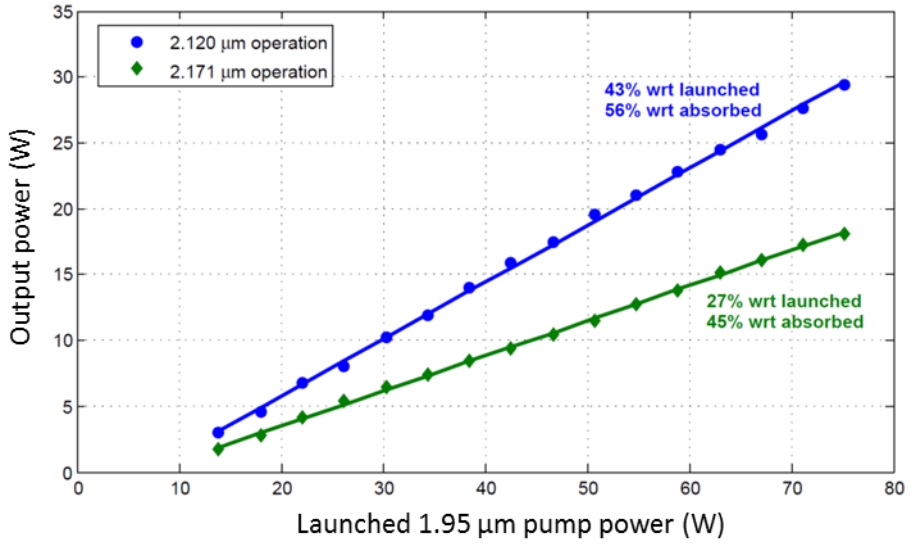

Figure 5.14: Slope efficiency of the laser when operating at 2.12 µm (peak of the tuning curve) and at 2.171 µm (longest wavelength of the tuning range) [20].

5.4.3 Discussion of tuning experiment

We have investigated the operation of a cladding-pumped, holmium-doped fibre and demonstrated a tuning range of >130 nm spanning from 2.04 µm to 2.171 µm. The peak output power was achieved at 2.12 µm. This result complements the 1.95 µm-core-pumped, small-signal, holmium-doped fibre amplifier presented in Section 5.3, which operated from 2.05 – 2.12 µm with a peak gain at 2.06 µm. The difference between the two geometries is due to the small-signal gain and inversion that the gain-medium is operated at, the difference in length of the active fibres and the difference in pumping rates along the active fibre.

The tuneable laser source is able to operate over the wavelength region where the small-signal gain of the active fibre is sufficient to match the output coupling rate of the HR/4% cavity. This typically implies a single-pass gain of ~7 dB. The longer fibre length and reduced pump interaction resulted in the distribution of the inversion across a longer distance in comparison to the core-pumped configuration. This effect is somewhat similar to the use of a longer pump wavelength for inversion management as was demonstrated in the core-pumped configuration corresponding to data 10 in Fig. 5.10. As a consequence, the 1.95 µm cladding-pumped tuneable laser was able to operate at a

much longer wavelength (2.171 µm) in comparison to the 1.95 µm core-pumped, small-signal, high-gain amplifier (2.12 µm) corresponding to data 9 in Fig. 5.10.

The achieved power of 18 W at 2.171 µm also represents the longest wavelength operation of a silica fibre laser at power levels >5 W.

5.5 Wavelength agile holmium-doped fibre source

In many spectroscopic applications there can be numerous advantages to being able to scan over multiple resonance features with a single system. The ability to operate and scan over a spectral region can aid in identifying additional compounds and chemicals, provide more specific information about temperatures and concentrations, as well as increase the range or resolution of Differential Absorption LIDAR (DIAL) systems. One of the major disadvantages of the mentioned tuning components is that when transitioning in between wavelengths, the tuneable component is usually resonant at the intermediate wavelengths. This can lead to spurious emissions, and requires the insertion of another element (similar to a Q-switch) that would prevent the laser cavity from responding. It also usually takes time to transition from one wavelength region of interest to another. Typically with mechanical components, it is possible to achieve very fast sweep rates, however this is usually a resonant effect and as shown in Fig. 5.15, only a small fraction of this entire span may provide any useful information.

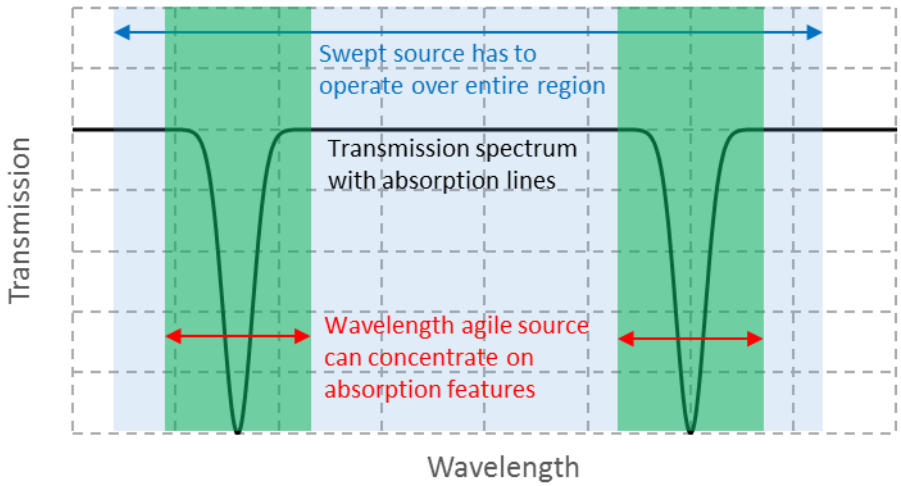

Figure 5.15: Illustration of absorption features and operation of a typical swept source in comparison to a wavelength agile source.

The term wavelength agility refers to the ability of changing wavelength with no spurious emissions and no inertia associated with the tuning mechanism. The ability to arbitrarily control the output wavelength would allow the source to sweep over only the relevant features. If such wavelength control is possible with no time penalty, this could increase the integration time substantially as the source would be able to focus only on regions of spectroscopic interest. The improved integration time would depend on the ratio of the width of the absorption features to the entire wavelength swept region and in some applications the effective integration can be increased by orders of magnitude. Such an increase in integration time would allow a significant increase in signal-to-noise in the measurement without having to change the output power of the source in any manner.

The concept of wavelength agility can have substantial implications and yield many advantages to lasers designed for spectroscopic applications. Wavelength agile operation is not restricted only to fibres, but can apply also to bulk crystalline lasers which may have discrete operating transitions, gas or chemical lasers, semiconductor gain elements and even a wavelength multiplexed arrangement of gain media with a single tuning element.

5.5.1 Methods of achieving wavelength agility

Wavelength tuning can be achieved in many ways including incorporating a mechanically tilted etalon or diffraction grating. These mechanical components, while suitable for swept sources, are typically less reliable when rapid wavelength switching is desired due to the inertia associated with rotation of the mechanical arrangement. Another demonstrated approach utilises an intra-cavity, all-fibre etalon, however these components are limited in peak power handling and are sensitive to external temperature fluctuations.

Recently, acousto-optic tunable filters (AOTFs) have attracted substantial attention as a wavelength selective element in the 2 μm range [21–23]. In this work we characterize the performance of such an AOTF designed to operate with a narrow bandwidth of <0.8 nm at 2 μm. Finally, this filter is incorporated as a wavelength selective element in a holmium-doped fibre laser cavity and an electronically-controlled wavelength agile source operating in the atmospheric transmission window around 2.1 μm is demonstrated [24].

5.5.2 Characterisation of the acousto-optical tuneable filter

The AOTF used in this experiment is a TeO_2 based device with a nominal design bandwidth of 0.8 nm and requires an RF input of ~210 mW at 27 MHz when operating at 2.1 µm. The AOTF has a much broader wavelength tuning capability than was investigated in the work described here with its operation limited by the gain bandwidth of the holmium-doped fibre and the WDM component used in the laser. The AOTF was first characterized using the optical arrangement shown in Fig. 5.16. A narrow line (0.1 nm bandwidth) thulium-doped fibre laser operating at 2050 nm was launched into port 1 of a 2 µm, polarization-insensitive circulator (AFR). The output from port 2 was then collimated by an off-axis parabolic mirror (Thorlabs RC02APC-P01) to produce a beam with diameter of 2.6 mm which was propagated through the AOTF. The two zero-order beams were directed away from the experiment so as to minimize the potential for feedback from undesirable scattered radiation. A high reflectivity (HR) mirror was aligned to retro-reflect the diffracted beam. The retro-reflected beam then double passes the AOTF and is coupled back into the fibre. A power meter and optical spectrum analyser (OSA) were then used to characterize the returning signal. The initial alignment was performed using the 2050 nm fibre laser which had a linewidth of <0.05 nm. A super-continuum (Koheras) source was then launched into the circulator to measure the spectral bandwidth of the return signal.

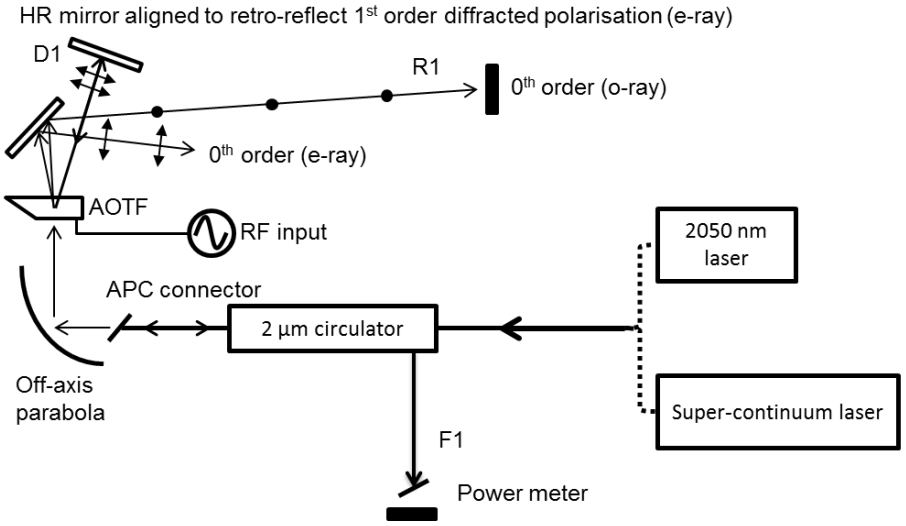

Figure 5.16: Optical characterisation of the AOTF using a narrow line 2050 nm thulium-doped fibre laser and a broadband super-continuum source [24].

The power measurements for each output from the AOTF when the narrow linewidth thulium-doped laser was used as shown in Fig. 5.16 are summarised in Table 5.2. The incident beam on the AOTF was un-polarised and the total power was 510 mW. With the AOTF off, the beam (R1) corresponding to the polarization that would experience diffraction (i.e. with the AOTF on) contained 330 mW. The RF signal was optimized to maximize the power in the diffracted order D1. At 210 mW of RF input power 260 mW of power was diffracted into beam D1. The HR mirror was then aligned to maximize the power contained in F1 up to 110 mW. Taking into account the insertion loss for the circulator (~1 dB), the total amount of power coupled back into the fibre was ~140 mW.

Table 5.2: Characterisation of power levels with the RF signal to the AOTF on or off [24].

	D1	R1	F1
RF signal off	0 mW	330 mW	0 mW
RF signal on	260 mW	70 mW	110 mW

The AOTF single-pass diffraction efficiency for the narrow-line 2050 nm source was measured to be 79% with respect to the signal power polarized in the o-ray with 260 mW diffracted from 330 mW and 70 mW remaining in the zero-order beam. The efficiency for double pass feedback strength in the diffracted arm was measured to be 43% at this wavelength for the o-ray polarization with 140 mW out of the original 330 mW coupled back into the fibre.

Replacing the narrow-band fibre laser input with the broadband super-continuum source revealed that the double-pass bandwidth through the filter had a full-width half-maximum of 1 nm as shown in Fig. 5.17. As a comparison, Fig. 5.17 also illustrates the typical line-width of the holmium-doped fibre laser when the AOTF is utilised as a tuning element.

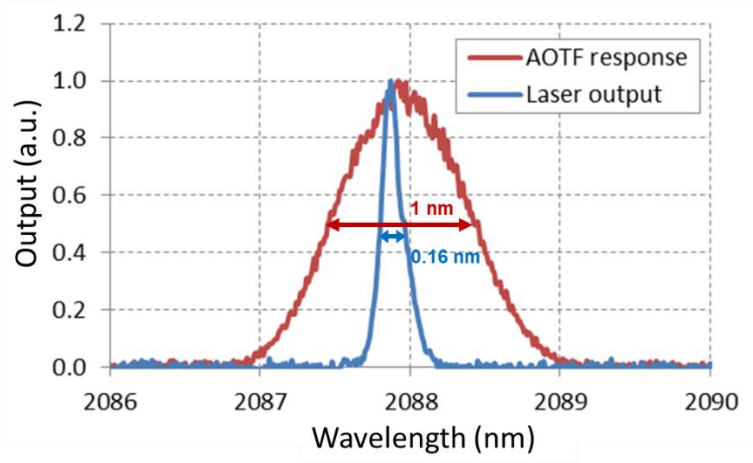

Figure 5.17: Spectral response of the AOTF showing a FWHM bandwidth of 1 nm. When incorporated into the laser cavity, the line-width of the laser is substantially smaller at ~0.16 nm. The OSA resolution setting was 0.05 nm [24].

5.5.3 Wavelength agile holmium-doped fibre laser

Having characterised the AOTF, the device was then utilised as the wavelength selective filter in a fibre laser cavity. The schematic of the resulting wavelength agile fibre laser cavity is shown in Fig. 5.18. The AOTF provides the wavelength selective feedback in the high reflectivity end of the cavity in a similar manner as demonstrated in Section 5.5.2, but with the circulator removed. A fibre coupled dichroic-based WDM was used to couple 1950 nm pump radiation from a Tm fibre laser and the 2100 nm signal into the core of a 4 m length of active holmium-doped fibre (Nufern). The pump laser was operated at 1.1 W average power. The WDM (AFR) had a large operating bandwidth with high transmission (>95%) from 2030 – 2200 nm and high reflection (>95%) from 1800 – 2010 nm. The holmium-doped fibre had a 10 µm diameter core with a 0.15 NA and core absorption of 70 dB/m at 1950 nm. This was then spliced to a 90/10 broadband fused fibre splitter (AFW). The 90% arm was used to provide the laser output and an all-fibre retro-reflector (Thorlabs) was spliced to the 10% arm. This configuration provides broadband feedback to the laser cavity with an effective reflectivity of ~1% that covers the tuning range supported by the holmium-doped fibre and the AOTF.

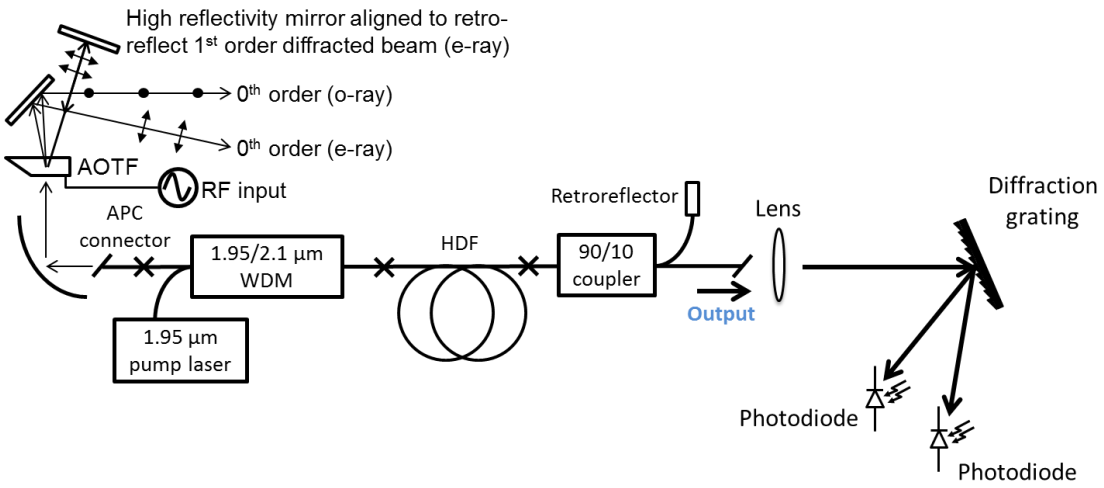

Figure 5.18: Wavelength-agile holmium-doped fibre laser with the AOTF providing the high reflectivity feedback, and the combination of 90/10 splitter and retro-reflector providing the low reflectivity feedback. The laser output was taken from the 90% port of the splitter. The laser performance was then characterized with the aid of a thermal power meter and optical spectrum analyser or collimated onto a diffraction grating and monitored using photodiodes for temporally resolved spectral characterisation [24].

The output power was measured with a thermal power meter and the output spectrum was measured on an optical spectrum analyser (Yokogawa). The temporal behaviour of the laser was measured with a DC-coupled extended InGaAs photodiode with a 20 ns response time (Thorlabs). To demonstrate the wavelength agility of the source, the output was collimated onto a diffraction grating with two photodiodes monitoring specific wavelengths in order to observe the temporal dynamics of the wavelength switching and any associated transients.

5.5.4 Characterisation of tuneable operation

For tuneable wavelength operation the AOTF was driven with a constant RF source. In this mode the laser could be tuned from 2037-2132 nm by changing the RF frequency from 25.82-27.22 MHz in discrete steps as shown in Fig. 5.19a). The output power, spectra and out-of-band ASE content at each wavelength were measured and are shown in Fig. 5.19b). The OSA resolution setting was 0.1 nm and the typical line-width of the laser is ~0.1 – 0.2 nm as shown in Fig. 5.17. The strength of the signal peak was >45 dB above the ASE background and the output power was >150 mW over this wavelength range. It is evident from the background ASE features in Fig. 5.19b) that the holmium gain-band extends down to 2010 nm; however the WDM utilised here prevented operation below 2030 nm.

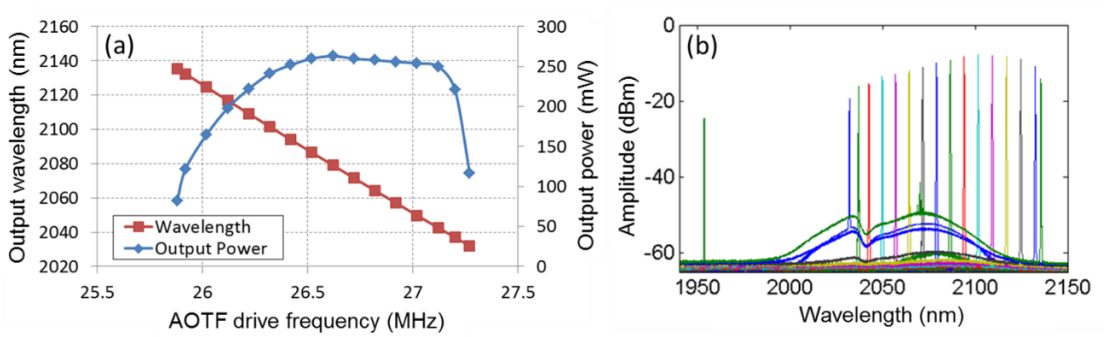

Figure 5.19: a) Output wavelength and laser power as a function of AOTF drive frequency. b) Output spectrum taken at each AOTF frequency setting. The OSA resolution setting was 0.1 nm [24].

By integrating the out-of-band emission, the total ASE content is <2% (-17 dB) for the span from 2037-2132 nm and <0.3% (-25 dB) for the range from 2040-2120 nm. Such a low ASE level makes this source suitable for further amplification without the requirement of an intermediate spectral filtering stage.

5.5.5 Characterisation of wavelength swept operation

For wavelength swept operation the AOTF was driven by a swept RF frequency, linearly scanning from 25.92 – 27.12 MHz over 10 ms. A long-hold (50 ms) OSA scan taken to measure the power spectral density at each wavelength is shown in Fig. 5.20a). In this mode, the OSA integrated the total radiation at each wavelength for the duration of the long-hold. The temporal output of the laser is shown in Fig. 5.20b). The strength of the self-pulsing in the laser varied over time despite the laser operating conditions being constant. Sweeping rates of 9 nm/ms were achieved.

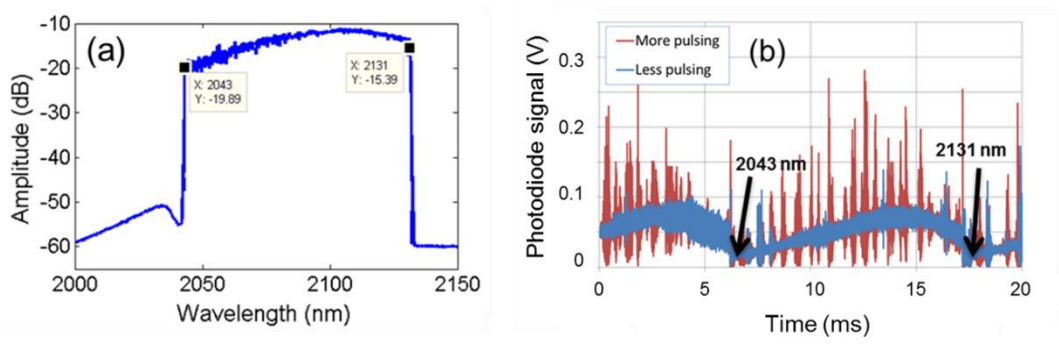

Figure 5.20: a) Long hold OSA scan demonstrating that the laser generates output across the entire swept wavelength interval. b) Temporal dynamics of the swept laser showing pulsed and near continuous operation – the laser operation fluctuated between these regimes, and in most cases there was substantial self-pulsing observed [24].

5.5.6 Characterisation of wavelength agile operation

Wavelength agile operation was achieved by driving the AOTF with a frequency modulated RF source switching between 2 discrete frequencies. This driven waveform resulted in the laser switching rapidly between two wavelengths. The output spectrum from the laser operating in this wavelength agile mode for 2 pairs of operating wavelengths is shown in Fig. 5.21a). The spectral data confirms that there is minimal ASE content emitted during this mode of operation.

The two wavelengths were then separated by the external diffraction grating and the temporal characteristics of the output at each wavelength are shown in Figs. 5.21b) and 5.21c).

The transient behaviour when switching between two different spectral regimes was also characterised. Figure 5.21b) demonstrates the temporal behaviour when switching between two wavelengths with high small signal gain (2065 and 2110 nm). Whereas Fig. 5.21c) demonstrates the temporal behaviour when switching between a wavelength on the edge of the spectrum (2122 nm) which has a relatively low small-signal gain and a wavelength near the centre of the holmium gain band (2057 nm).

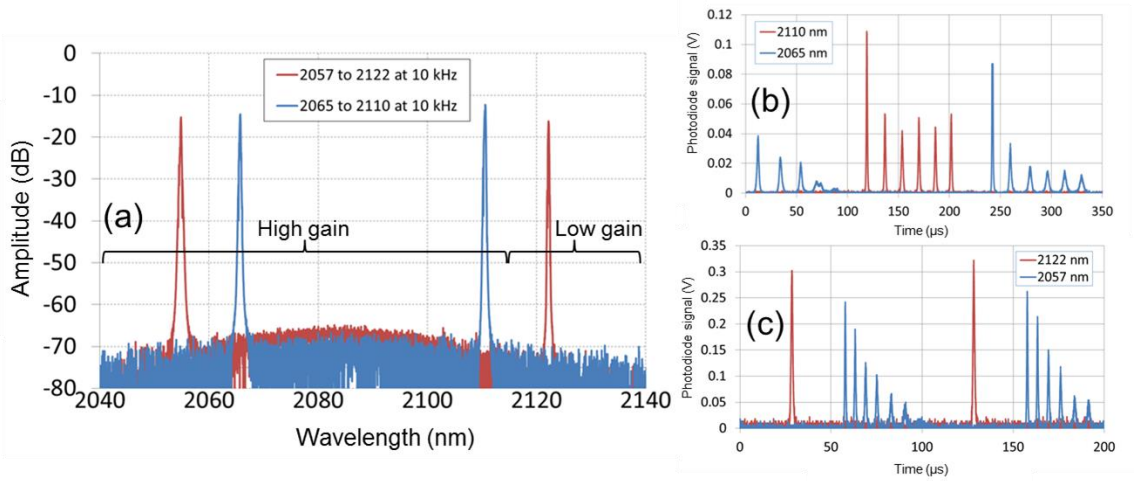

Figure 5.21: a) Spectral output when switching between wavelengths with differing small signal gain showing negligible amount of broadband ASE (red-high to low small signal gain, blue-high to high signal gain). b) Temporal dynamics of the laser output when switching between wavelengths where the laser operates efficiently. c) Temporal dynamics of the laser output when switching between a high gain region to a wavelength on the edge of the spectrum [24].

5.5.7 Discussion

We have integrated an AOTF as the wavelength selective element in a fibre laser cavity with a broad-band feedback output coupler and characterised the operation in wavelength tuneable, wavelength swept and wavelength switched configurations.

The AOTF was found to provide a diffraction efficiency of 79% with a double pass spectral FWHM of 1 nm at 2088 nm. The effective feedback for the correct polarization was 43%. While this is a substantial loss, the impact on the efficiency of the laser over most of the tuning range is minimized by operating with a very low reflectivity output coupler (1% effective feedback with a 10% insertion loss). As a result, the non-ideal feedback does not lead to a substantial penalty in terms of efficiency or performance. The line-width of the laser is significantly narrower (<0.2 nm) than the AOTF response (1 nm) due to gain saturation and the multi-pass nature of the oscillator. Despite the weak output coupler reflectivity of 1%, the residual radiation experiences multiple passes through the AOTF and subsequent spectral filtering.

The laser could be tuned over the spectral range from 2037 - 2132 nm by changing the drive frequency to the AOTF from 25.82 – 27.22 MHz. The optical signal-to-noise ratio was >45 dB and output power was >150 mW over this wavelength span. The typical laser line-width was <0.2 nm at all operating wavelengths.

The transition between wavelengths was possible with a typical response time of ~35 µs which is largely attributed to the build-up time of the acoustic field in the AOTF device. When operating at the lower gain region of the emission, the build-up time of the laser can become significant. This is evident in Fig. 5.21c) where only one pulse at 2122 nm has time to build up in the 100 µs window as opposed to when operating near the peak of the spectrum (2050 – 2110 nm) where multiple pulses are observed in a similar temporal window. Attempting to switch at a faster rate may limit the accessible spectral bandwidth of the source. With these restrictions in mind, we have demonstrated true wavelength agility with zero mechanical inertia across almost the wavelength range spanning 2040 – 2130 nm.

The laser was observed to self-pulse significantly in all operating conditions – this is largely attributed to the frequency-shifting nature of the AOTF. As a result of operating on the 1st diffracted order, the AOTF imparts a 51.64 – 54.44 MHz frequency shift every round trip of the cavity. This frequency shift potentially prevents stable formation and oscillation for a CW laser

mode as the circulating radiation sweeps through the spectral response of the filter. This is also compounded with the long cavity length and energy storage in the fibre gain stage. Transitioning to a semiconductor gain medium with a reduced cavity length could potentially eliminate some of these self-pulsing features. Employing a null-shifting AOTF device may also aid in the elimination of self-pulsing behaviour.

5.5.8 Summary of wavelength agile holmium-doped fibre source

We have characterized the performance of a narrow-band AOTF operating at 2 μm. This AOTF was then incorporated as the wavelength selective element in a holmium-doped fibre laser cavity. As a result we demonstrated a wavelength agile, digitally-controlled laser source producing >150 mW from 2043 – 2131 nm with excellent spectral quality. The laser source provided an output that could be controlled anywhere in this spectral region with a switching speed of ~35 μs. Single wavelength, swept and rapid wavelength switching operation were all demonstrated and investigated over this wavelength range. This source provides access to a wavelength region corresponding to a high atmospheric transmission and also of interest for the pumping of non-linear mid-infrared optical materials. We anticipate the use of AOTF and fibre-coupled AOTF components in future applications to enable all-fibre wavelength agile sources in this wavelength region.

5.6 Summary

In this chapter we have extensively characterised the performance of thulium-doped and holmium-doped fibre sources. Notable demonstration include high power, robustly single-mode thulium-doped fibre lasers operating at 1950 nm, monolithic all-fibre TDFAs and HDFAs, the first diode pumped holmium-doped fibre amplifier, the first tuneable operation of a resonantly cladding-pumped, holmium-doped fibre operating at >18 W from 2040 – 2170 nm, and a wavelength agile holmium source operating from 2040 – 2130 nm.

We have also summarized the key overall results from a substantial body of work undertaken over the past 5 years towards the development of ultra-wideband operation of thulium-doped and holmium-doped fibre amplifiers. We have demonstrated amplifiers spanning a combined spectral bandwidth of 490 nm (>40 THz) extending from 1660–2150 nm. This remarkably broad wavelength

coverage is attractive for a large number of disciplines looking to exploit this previously difficult-to-reach wavelength range.

The wavelength coverage demonstrated is in agreement with the modelling and predictions in Chapter 2 and enables coverage almost entirely spanning the 1530-2150 nm range in combination with EDFAs and previously investigated U-band amplifiers [25]. This potentially provides sources for a range of applications as discussed in Chapter 1. It is hoped that the comprehensive descriptions of the amplifiers as well as the development and increased availability of components, fibres and seed sources will allow the technology to be exploited in other research areas.

Indeed already there are many groups showing a great interest in various holmium and thulium amplifiers and gain media for various applications [26–29].

5.7 References

1. G. D. Goodno, L. D. Book, and J. E. Rothenberg, "Low-phase-noise, single-frequency, single-mode 608 W thulium fiber amplifier," Opt. Lett. **34**, 1204 (2009).

2. F. Wang, D. Shen, D. Fan, and Q. Lu, "Spectrum narrowing of high power Tm: fiber laser using a volume Bragg grating," Opt. Express **18**, 8937 (2010).

3. J. Liu, H. Shi, K. Liu, Y. Hou, and P. Wang, "210 W single-frequency, single-polarization, thulium-doped all-fiber MOPA," Opt. Express **22**, 13572 (2014).

4. K. Yin, B. Zhang, G. Xue, L. Li, and J. Hou, "High-power all-fiber wavelength-tunable thulium doped fiber laser at 2 μm," Opt. Express **22**, 19947 (2014).

5. L. Pearson, J. W. Kim, Z. Zhang, M. Ibsen, J. K. Sahu, and W. A. Clarkson, "High-power linearly-polarized single-frequency thulium-doped fiber master-oscillator power-amplifier," Opt. Express **18**, 1607 (2010).

6. T. S. McComb, R. A. Sims, C. C. C. Willis, P. Kadwani, V. Sudesh, L. Shah, and M. Richardson, "High-power widely tunable thulium fiber lasers," Appl. Opt. **49**, 6236 (2010).

7. J. Jiang Liu, K. Kun Liu, F. Fangzhou Tan, and P. Pu Wang, "High-Power Thulium-Doped All-Fiber Superfluorescent Sources," IEEE J. Sel. Top. Quantum Electron. **20**, 497–502 (2014).

8. T. Walbaum, M. Heinzig, T. Schreiber, R. Eberhardt, and A. Tünnermann, "Monolithic thulium fiber laser with 567 W output power at 1970 nm," Opt. Lett. **41**, 2632 (2016).

9. S. Wielandy, "Implications of higher-order mode content in large mode area fibers with good beam quality.," Opt. Express **15**, 15402–9 (2007).

10. J. W. Nicholson, A. D. Yablon, S. Ramachandran, and S. Ghalmi, "Spatially and spectrally resolved imaging of modal content in large-mode-area fibers," Opt. Express **16**, 7233 (2008).

11. H. Yoda, P. Polynkin, and M. Mansuripur, "Beam quality factor of higher order modes in a step-index fiber," J. Light. Technol. **24**, 1350–1355 (2006).

12. K. Tankala, B. Samson, A. Carter, J. Farroni, D. Machewirth, N. Jacobson, U. Manyam, A.

Sanchez, M.-Y. Chen, A. Galvanauskas, W. Torruellas, and Y. Chen, "New developments in high power eye-safe LMA fibers," Proc. SPIE **6102**, 610206 (2006).

13. N. Simakov, A. V. Hemming, A. Carter, K. Farley, A. Davidson, N. Carmody, M. Hughes, J. M. O. Daniel, L. Corena, D. Stepanov, and J. Haub, "Design and experimental demonstration of a large pedestal thulium-doped fibre," Opt. Express **23**, 3126 (2015).

14. N. Simakov, A. Hemming, A. Carter, K. Farley, A. Davidson, N. Carmody, J. M. O. Daniel, M. Hughes, L. Corena, D. Stepanov, and J. Haub, "170 W Single-mode Large Pedestal Thulium-doped Fibre Laser," in *CLEO/Europe Conference on Lasers and Electro-Optics* (Optical Society of America, 2015), p. CJ_13_2.

15. N. Simakov, Z. Li, Y. Jung, J. M. O. Daniel, P. Barua, P. C. Shardlow, S. Liang, J. K. Sahu, A. Hemming, W. A. Clarkson, S.-U. Alam, and D. J. Richardson, "High gain holmium-doped fibre amplifiers," Opt. Express **24**, 13946 (2016).

16. Z. Li, Y. Jung, J. M. O. Daniel, N. Simakov, M. Tokurakawa, P. C. Shardlow, D. Jain, J. K. Sahu, A. M. Heidt, W. A. Clarkson, S. U. Alam, and D. J. Richardson, "Exploiting the short wavelength gain of silica-based thulium-doped fiber amplifiers," Opt. Lett. **41**, 2197 (2016).

17. Z. Li, S. U. Alam, J. M. O. Daniel, P. C. Shardlow, D. Jain, N. Simakov, A. M. Heidt, Y. Jung, J. K. Sahu, W. A. Clarkson, and D. J. Richardson, "90 nm gain extension towards 1.7 μm for diode-pumped silica-based thulium-doped fiber amplifiers," in *European Conference on Optical Communication, ECOC* (2014).

18. Z. Li, A. M. Heidt, N. Simakov, Y. Jung, J. M. O. Daniel, S. U. Alam, and D. J. Richardson, "Diode-pumped wideband thulium-doped fiber amplifiers for optical communications in the 1800 - 2050 nm window," Opt. Express **21**, 26450–26455 (2013).

19. Y. Jung, Z. Li, N. Simakov, J. M. O. Daniel, D. Jain, P. C. Shardlow, A. M. Heidt, J. K. Sahu, A. Hemming, W. A. Clarkson, S. Alam, and D. J. Richardson, "Silica-Based Thulium Doped Fiber Amplifiers for Wavelengths beyond the L-band," Opt. Fiber Commun. Conf. M3D.5 (2016).

20. N. Simakov, A. Hemming, W. A. Clarkson, J. Haub, and A. Carter, "A cladding-pumped, tunable holmium doped fiber laser," Opt. Express **21**, 28415–28422 (2013).

21. J. M. O. Daniel and W. A. Clarkson, "Rapid , electronically controllable transverse mode

selection in a multimode fiber laser," Opt. Express **21**, 29442–29448 (2013).

22. E. Lallier, "2 µm lasers and Mid-IR frequency conversion," http://isla-project.eu/wp-content/uploads/2015/07/ISLA-Workshop-2-µm-lasers-for-MIR-frequency-conversion.pdf.

23. F. Gutty, A. Grisard, A. Joly, C. Larat, D. Papillon-Ruggeri, and E. Lallier, "kW-level tunable Q-switched thulium-doped fiber system," in *Advanced Solid State Lasers* (OSA, 2014), p. ATu2A.40.

24. N. Simakov, J. M. O. Daniel, J. Ward, W. A. Clarkson, A. Hemming, and J. Haub, "Wavelength agile holmium-doped fiber laser," Proc. SPIE **9728**, 97280Q (2016).

25. P. Reeves-Hall, D. A. Chestnut, C. J. S. De Matos, and J. R. Taylor, "Dual wavelength pumped L and U-Band Raman amplifier," in *Optical Amplifiers and Their Applications* (OSA, 2001), p. OMC4.

26. P. Li, A. Ruehl, C. Bransley, and I. Hartl, "Low noise, tunable Ho:fiber soliton oscillator for Ho:YLF amplifier seeding," Laser Phys. Lett. **13**, 65104 (2016).

27. P. Li, A. Ruehl, U. Grosse-Wortmann, and I. Hartl, "Sub-100 fs passively mode-locked holmium-doped fiber oscillator operating at 2.06 µm," Opt. Lett. **39**, 6859 (2014).

28. E. J. Friebele, C. G. Askins, J. R. Peele, B. M. Wright, N. J. Condon, S. O'Connor, C. G. Brown, and S. R. Bowman, "Ho-doped fiber for high energy laser applications," Proc. SPIE **8961**, 896120 (2014).

29. X. Wang, P. Zhou, Y. Miao, H. Zhang, X. Jin, H. Xiao, X. Wang, and Z. Liu, "42 W high power Ho-doped fiber laser pumped by a 1150 nm Raman fiber laser," in *Advanced Solid State Lasers* (OSA, 2014), p. AM5A.11.

Chapter 6.

Holmium-Doped Fibres for High Peak Power Operation

6.1 Introduction

Sources in the mid-infrared (mid-IR) region spanning from 3.4 – 5 µm are of interest for many applications. The excellent atmospheric transmission, shown in Fig. 6.1, coupled with the spectral chemical fingerprints of many greenhouse gases and hydrocarbon compounds makes this region extremely interesting for LIDAR and remote sensing applications. Sources in the mid-IR region are also of interest in materials processing, medical, and defence applications.

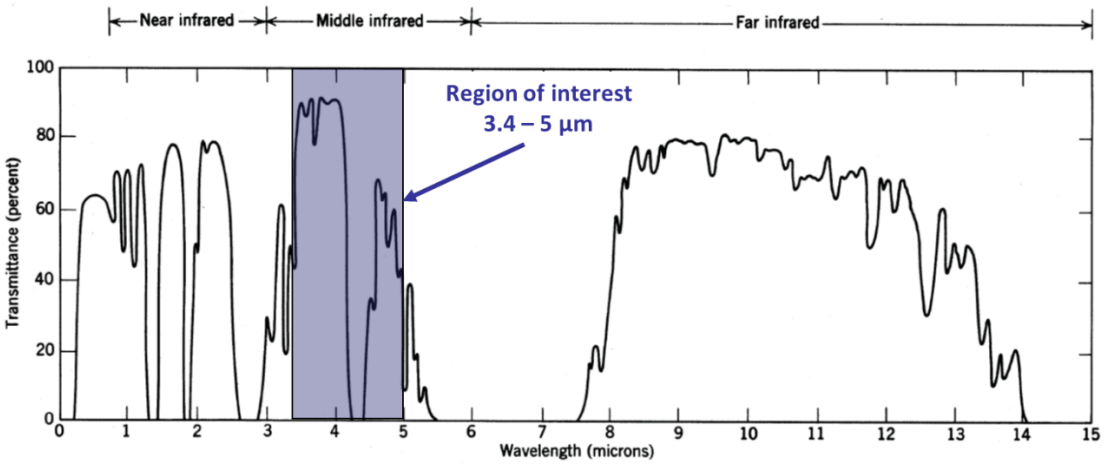

Figure 6.1: Atmospheric transmission from the UV to 14 µm. The resolution of this trace is ~50 nm, and broadly illustrates the transmission windows of the atmosphere [1].

However, the path to producing high power, solid-state laser sources in this wavelength region is challenging. Where laser transitions do exist, it is difficult to select a host material that does not significantly quench the radiative lifetime with multi-phonon processes. Such low phonon energy

materials typically do not have the necessary purity or the physical properties to act as a good host for the gain medium. A summary of various sources operating in this wavelength region is presented in Table 6.1.

While direct generation of mid-IR radiation has certainly progressed significantly, it is still a very immature technology. Only Fe:ZnS and Fe:ZnSe have been demonstrated to operate in this region at >5 W and this approach still required cryogenic cooling and a relatively exotic pump source at 3 µm. In comparison, nonlinear optics offers a much more established route to power scaling sources in the 3.4 – 5 µm region [2].

Table 6.1: Solid-state laser approaches to scaling of mid-infrared laser sources.

Approach	Wavelength	Output power	Comment
Nd:YAG → PPLN	3.5 – 4.0 µm	20 W [3,4]	Limited by thermal scaling of Nd:YAG oscillator
Nd:YAG→KTP→ ZGP	3 – 5 µm	10 W [5,6]	Limited by thermal scaling of Nd:YAG oscillator
Ho:YAG/YLF→ZGP	3 – 5 µm	20-99 W [7–9]	Limited by thermal scaling of the Ho:YAG/YLF laser
QCL	3 – 5 µm	>20 W [10]	CW scaling possible, but peak power limited
Soft glass fibres	3.44 µm	1.5 W [11–14]	Scaling possible, but thermal limitations of gain medium are significant
Fe:ZnSe	4.15 µm	35 W [15–17]	Cryogenic operation required
Supercontinuum	>3.5 µm	>1 W [18–20]	Significant power is produced in atmospheric absorption regions

6.2 Nonlinear optics background

Nonlinear optical effects are analyzed by considering the response of the dielectric material at the atomic level to the electric fields of an intense light beam. The propagation of a wave through a material produces changes in the spatial and temporal distribution of electrical charges as the electrons and atoms react to the electromagnetic fields of the wave. The main effect of the forces exerted by the fields on the charged particles is a displacement of the valence electrons from their normal orbits. This perturbation creates electric dipoles whose macroscopic manifestation is the

polarization. For small field strengths this polarization is proportional to the electric field which leads to the familiar equation:

$$\boldsymbol{P}(t) = \chi^{(1)}\boldsymbol{E}(t) \quad , \tag{6.1}$$

Where $\boldsymbol{P}$(t) is the polarisation response of the material, $\boldsymbol{E}$(t) is the driving electric field and $\chi^{(1)}$ is the linear susceptibility.

For larger electric fields, the material response is not always linear. To describe this non-linear regime, the polarisation field can be expanded in a power series in terms of the electric field:

$$\boldsymbol{P}(t) = \chi^{(1)}\boldsymbol{E}(t) + \chi^{(2)}\boldsymbol{E}^2(t) + \chi^{(3)}\boldsymbol{E}^3(t) + \cdots \quad , \tag{6.2}$$

Where the quantities $\chi^{(2)}$ and $\chi^{(3)}$ are known as the second- and third-order nonlinear optical susceptibilities. In the non-linear case, the re-radiation comes from dipoles whose amplitudes do not faithfully reproduce the sinusoidal electric field that generates them. As a result, the distorted re-radiated wave contains different frequencies from that of the original wave.

6.2.1 Operating principles of optical parametric oscillators

Optical parametric generation is a product of the second order nonlinear term where the driving electric field is composed of multiple frequencies:

$$\boldsymbol{E}(t) = E_1 e^{-i\omega_1 t} + E_2 e^{-i\omega_2 t} + c.c. \quad , \tag{6.3}$$

Where ω_1 and ω_2 are the frequency components of the electric field with corresponding amplitudes of E_1 and E_2.

We consider the second term of Eqn. (6.2):

$$\boldsymbol{P}^{(2)}(t) = \chi^{(2)}\boldsymbol{E}^2(t) \quad , \tag{6.4}$$

Where $\boldsymbol{P}^{(2)}$(t) is the second-order polarisation term and is proportional to the square of the driving electric field.

By substituting Eqn. (6.3) and expanding we retrieve the following equation:

$$\begin{aligned}&\boldsymbol{P}^{(2)}(t)\\&=\chi^{(2)}\left[E_1^2e^{-2i\omega_1 t}+E_2^2e^{-2i\omega_2 t}+2E_1E_2e^{-i(\omega_1+\omega_2)t}\right.\\&\left.+2E_1E_2^*e^{-i(\omega_1-\omega_2)t}+c.c.\right]+2\chi^{(2)}[E_1E_1^*+E_2E_2^*]\end{aligned}\quad , \qquad (6.5)$$

The various components can be grouped:

$$\boldsymbol{P}^{(2)}(t)=\sum_n P(\omega_n)e^{-i\omega_n t}\quad , \qquad (6.6)$$

Where ω_n is the respective harmonic with amplitude $P(\omega_n)$. The various harmonics and associated nomenclature are listed in Table 6.2.

Table 6.2: Various harmonic components of the second-order nonlinear polarisation term.

Component	Frequency	Terminology
$P(2\omega_1)=\chi^{(2)}E_1^2,$	$2\omega_1$	Second Harmonic Generation
$P(2\omega_2)=\chi^{(2)}E_2^2,$	$2\omega_2$	Second Harmonic Generation
$P(\omega_1+\omega_2)=2\chi^{(2)}E_1E_2,$	$\omega_1+\omega_2$	Sum Frequency Generation
$P(\omega_1-\omega_2)=2\chi^{(2)}E_1E_2^*,$	$\omega_1-\omega_2$	Difference Frequency Generation
$P(0)=2\chi^{(2)}(E_1E_1^*+E_2E_2^*)\,,$	0	Optical Rectification

Of particular interest is the difference frequency generation term (DFG) which is often illustrated as shown in Figs. 6.2a) and 6.2b).

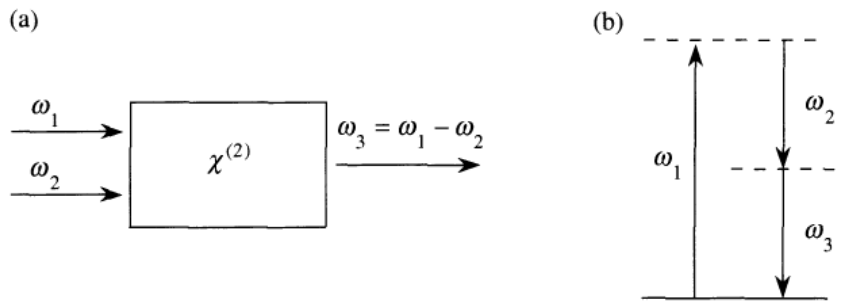

Figure 6.2: a) Schematic diagram of difference-frequency generation between two driving electric fields ω_1 and ω_2 generating a third field $\omega_3=\omega_1-\omega_2$. b) Illustration of the conservation of energy of the process in this interaction [21].

It is also possible to exploit this nonlinear phenomena by providing the nonlinear material with a feedback mechanism and a sufficiently intense driving field at ω_1 (pump). This configuration is termed an optical parametric oscillator where the other fields (signal and idler) build up from background noise (termed optical parametric generation). An illustration of the optical parametric oscillator is shown in Fig. 6.3. Equation 6.6 neglects the longitudinal evolution of the various fields in the nonlinear material. In order for the fields to coherently build up in intensity, the process must satisfy the conservation of momentum or phase matching conditions between the wave-vectors, $k = \omega \times n(\omega)/c$, where $n(\omega)$ is the refractive index of the material at angular frequency ω, of the various fields that are involved.

The output frequencies (ω_2 and ω_3) of an OPO are usually determined by the phase matching conditions for the nonlinear material which will define the spectral gain profile, wavelength selective elements in the OPO cavity and any input seed radiation, if present.

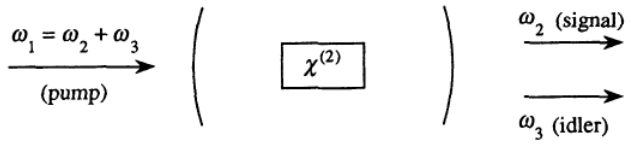

Figure 6.3: An optical parametric oscillator driven at only one frequency (pump, ω_1) in the presence of feedback that enables the recirculation of parametric generation within the cavity at either/or both the signal (ω_2) and idler (ω_3) [21].

One attractive feature of this process is the conservation of energy between the input and output electromagnetic fields. There is no energy lost in the nonlinear material due to the conversion process. In practise however, material performance is limited by either optical damage due to the peak power requirements to achieve a sufficiently strong nonlinear interaction or by thermal effects due to the residual material absorptions at either the pump, signal and/or idler wavelengths.

6.2.2 Detailed description of a high power mid-IR optical parametric oscillator

Some of the highest average power, solid-state mid-IR sources have been enabled by the frequency conversion of pulsed Ho:YAG lasers in an optical parametric oscillator. Despite issues associated with the thermal effects in bulk crystalline materials, these systems have been scaled to >40 W average power, and to 100 W at a reduced duty cycle [7–9]. The limitation to further power scaling in these systems is typically the thermal effects in the gain medium of the Ho:YAG pump laser.

Multiple rods and pump lasers are required in order to distribute the heat load, with single-rod oscillator systems typically limited to mid-IR output power levels of ~10 W [22,23].

A high power mid-IR OPO system is shown in Fig. 6.4 [8,24]. The laser system is based on a pair of 1.908 µm thulium fibre lasers which pump a dual rod Ho:YAG oscillator. The output of the Ho:YAG laser is then focused into a ring OPO; a 50% IC/OC and three HR mirrors form a cavity around a pair of 12 mm ZGP crystals.

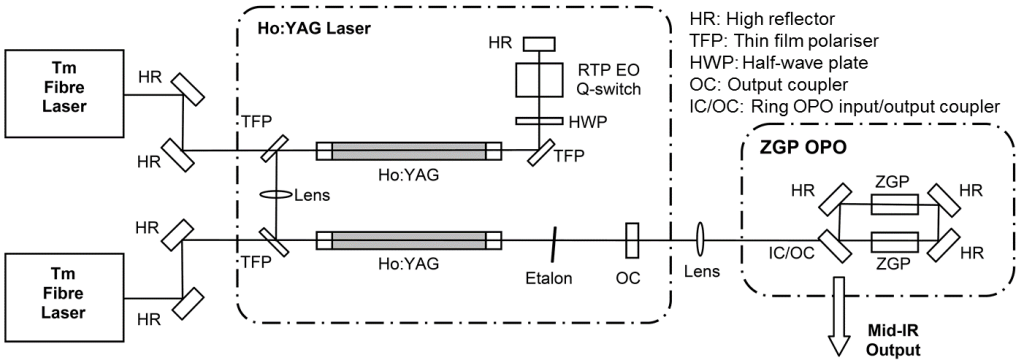

Figure 6.4: Schematic of a high power and high beam quality mid-infrared source [24].

The ZGP OPO was pumped with up to 54 W at 2.09 µm from the Ho:YAG laser. Typical pulse durations from the Ho:YAG laser had a duration of 37 ns at a repetition rate of 26 kHz providing pulse energies of 2.1 mJ resulting in peak powers of 50-100 kW. The Ho:YAG laser was tuned to operate at 2.09 µm using an intra-cavity etalon, and the beam quality at the maximum output power was measured to be $M^2 = 1.2$.

The maximum output power produced by the ZGP ring OPO was 30.2 W, Fig. 6.5a), the slope efficiency was 63%, and the optical-optical conversion efficiency 56%. The output spectrum was found to be similar to previous standing wave spectra, as shown in Fig. 6.5b). The beam quality of the signal was measured to be $M^2 = 1.3$, and a near field beam profile is depicted in Fig. 6.5c).

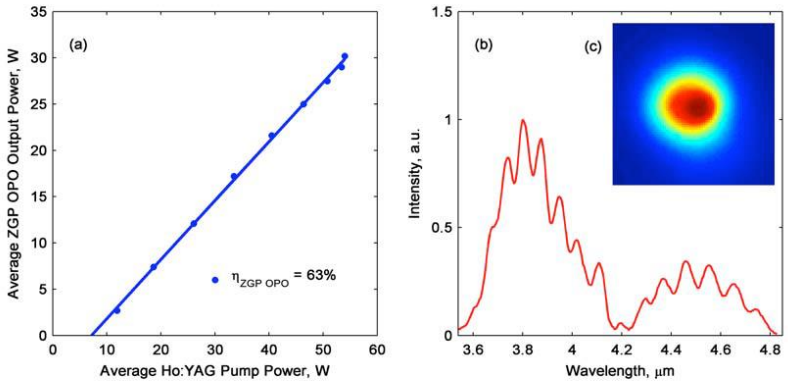

Figure 6.5: a) Output power of the ZGP optical parametric oscillator with respect to launched pump power. b) Spectrum of the output illustrating operation over 3.6 – 4.8 μm. c) Near field profile of the mid-infrared OPO output [24].

The performance of the OPO is pump limited and can be pushed to higher average powers. However scaling the Ho:YAG pump laser is not a simple matter as it will require an increase in the number of thulium-doped pump lasers and Ho:YAG rods. An alternative approach to power scaling the pump source is to replace the crystalline gain medium with a silica fibre based gain element. This should be more amenable to power scaling with single-stage thulium-doped and holmium-doped fibres having been demonstrated at >400 W in CW operation; however the peak power and spectral requirements in order to achieve efficient conversion in the OPO are much more difficult to achieve from a fibre based source.

Multiple groups have investigated the use of fibre lasers to pump ZGP OPOs with a summary provided in Table 6.3. A common trend between these results is the limited peak power, apart from the photonics crystal fibre (PCF) approach, and the subsequent thermal issues in the ZGP material. Another common feature amongst all of these demonstrations is the relatively poor slope efficiency (30-40%) which is significantly lower than the 60-70% slope efficiencies demonstrated in most solid-state-pumped ZGP OPO systems.

The reason for this is a combination of operating wavelength, extremely tight focus to compensate for the reduced peak power, walk-off between the beams which is more significant under tight focussing conditions, and the limitation in achievable peak power resulting in the OPO operating closer to threshold.

Table 6.3: A review of 2 µm fibre laser pumped mid-infrared OPOs.

Gain medium	Peak power at 2 µm/pulse duration	Output average power in mid-IR	Comment	Ref
Tm:fibre	5 kW/30 ns	2.5 W	Thermal lensing in ZGP limited scaling	[25]
Tm,Ho:fibre	4 kW/60 ns	2 W	Thermal lensing in ZGP limited scaling	[26]
Tm:fibre	7 kW/30 ns	6.5 W	Degraded M^2	[27]
Tm:PCF	20 kW/1 ns	1 W	Limited average power	[28]
Tm:fibre	4 kW/50 ns	3 W	Thermal lensing in ZGP limited scaling	[29,30]

6.2.3 Pump source requirements for optimised OPO efficiency

ZGP exhibits a defect related absorption at wavelengths <2.05 µm. With excellent growth control and post-processing irradiation, this absorption band can be pushed to allow efficient pumping at wavelengths as short as 2 µm, however the thermal effects are still pronounced at this wavelength. In order to minimise any residual absorption the target pump wavelength is >2.05 µm to enable further power scaling.

The OPO efficiency as a function of peak power is illustrated in Fig. 6.6 – in this case, the beam diameter of the 2.09 µm pump laser in the ZGP was 0.5 mm [24]. By increasing or decreasing the pump diameter, we can expect to change the conversion efficiency and the threshold. A higher peak intensity will lead to a lower threshold and better conversion. However, we should also expect thermal effects to become more pronounced at the higher average intensity. This provides a target estimate of the peak powers that are required in order to enable efficient conversion in the OPO. By aiming for peak powers in the 40 – 50 kW range we hope to ensure that the conversion efficiency is approaching 50% in the OPO.

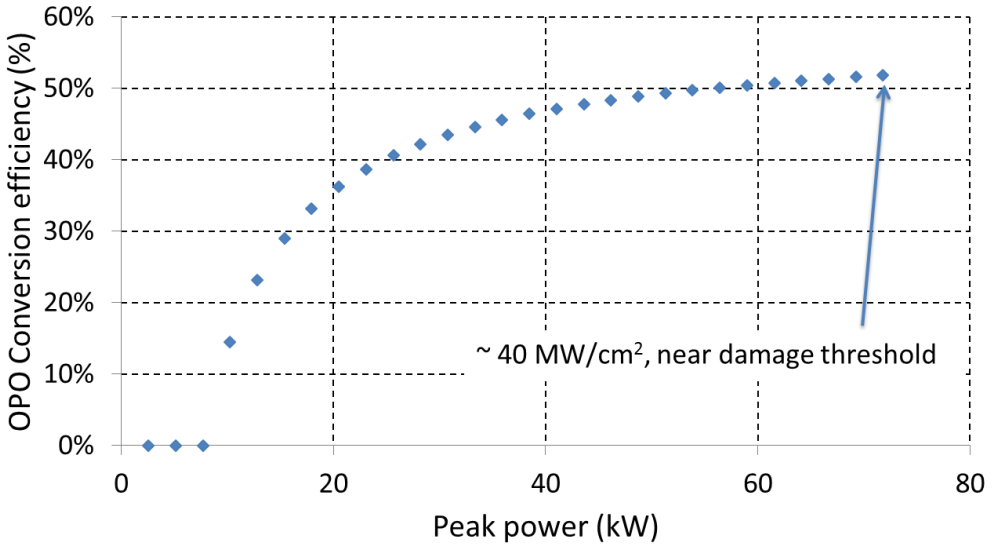

Figure 6.6: Conversion efficiency of the ZGP OPO as a function of incident peak power at 2.09 µm [24].

However we also have to be aware that the bandwidth of the seed source must be maintained within the phase matching acceptance bandwidth of the OPO otherwise we can expect to see a reduction in efficiency. As shown in Fig. 6.7, a 0.5 THz detuning (8 nm) leads to a 25% reduction in conversion efficiency and a substantial increase in threshold [31].

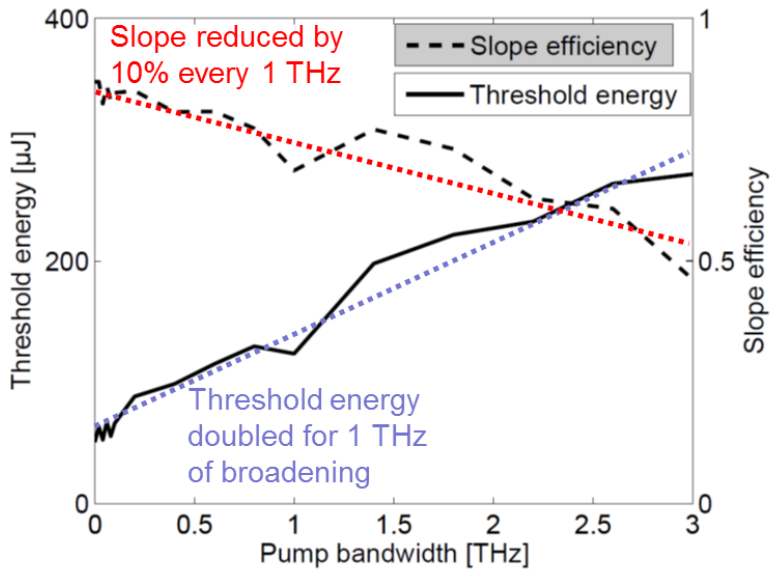

Figure 6.7: Increase in threshold and decrease in slope efficiency of a ZGP OPO as a function of pump bandwidth [31].

6.2.4 Summary of pump requirements

A summary of the various requirements on the pump source for a ZGP mid-IR OPO is provided in Table 6.4 as well as a short justification for each requirement. Some degree of flexibility does exist between these values, and they serve only as an indicative aim. In the next section we discuss the feasibility of achieving these with a pulsed fibre amplifier.

Table 6.4: A review of the pump requirements to enable efficient operation for a mid-IR ZGP OPO.

Requirement	Value	Comment
Wavelength (nm)	>2050 nm	Avoid ZGP absorption
Peak Power (kW)	>40 kW	Efficient OPO conversion
Pulse duration (ns)	1 – 100 ns	Multiple OPO round trips
Bandwidth (nm)	< 2 nm (0.2 THz)	Minimize OPO threshold and maximise slope
Beam quality (M^2)	< 1.5	Mode-overlap with OPO

6.3 Gain medium selection

The gain curves for thulium-doped and holmium-doped silica under various inversion levels are shown in Fig. 6.8. These curves are scaled to a 40 dB peak gain which is representative of the limit of commercially available isolators. In practise the scaling to achieve these gain parameters under lower inversion operation is achieved by increasing the fibre length and distributing the pump radiation over a larger volume.

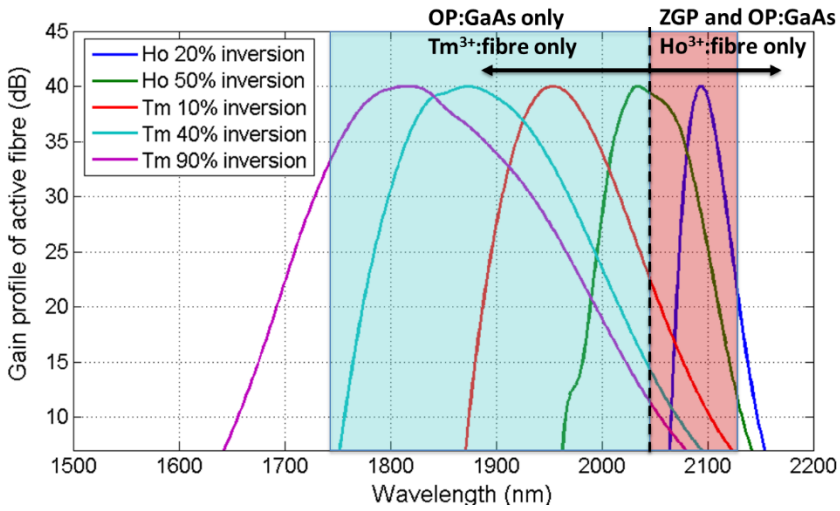

Figure 6.8: Spectral gain profile of Tm and Ho-doped silica fibres operating at different inversions and scaled to 40 dB.

In order to operate at 2.05 µm in thulium, there will a large amount of excess gain present at shorter wavelengths – as seen in Fig. 6.8 – a 22 dB gain for a Tm:fibre at a 10% inversion will result in a 40 dB gain at 1950 nm. Managing this out-of-band gain becomes increasingly more difficult in a pulsed system, especially where spurious lasing and pulses can extract significant energy and cause damage to components. Indeed, in practise, pulsed Tm:fibre systems tend to operate at wavelengths <2.02 µm [27,28,30,32]. Power scaling of ZGP OPOs is not possible at this wavelength region, and so alternative materials such as OP:GaAs must are more suited. In contrast, a pulsed system based on Ho:silica would be operating at or near the peak of its gain and is able to address the pump wavelength requirements of ZGP.

6.4 Nonlinear effects in optical fibres

Fibre lasers offer an excellent route for power scaling by distributing the thermal load over a long gain medium. The dielectric waveguide confinement also aids in defining an excellent mode quality for the output that is resistant to thermal deformations. However the high intensity radiation propagating through a long length of gain material will start to generate substantial nonlinear effects. In most cases the nonlinear effects will act to limit the peak power, degrade the spectrum or even in some cases create an effective mirror and reflect a large portion of the incoming radiation.

Nonlinear effects in fibre lasers and amplifiers have been well characterised and discussed in the literature, however most studies tend to focus for operation at 1 µm as this is the dominant wavelength for industrial fibre lasers. Typically, pulsed 1 µm fibre systems are limited in peak power by a combination of Stimulated Raman Scattering and Stimulated Brillouin Scattering. In contrast, at 2 µm the limiting nonlinear effects are similar to those seen in 1.55 µm systems due to the dispersion properties of silica. In this context, we will examine Stimulated Raman Scattering, Stimulated Brillouin Scattering and Modulation Instability with a focus on operation at 2.1 µm.

6.4.1 Stimulated Raman scattering

Stimulated Raman scattering is a nonlinear process that involves 2 optical fields, termed pump and Stokes, and a vibrational mode of the medium. The gain can be expressed as follows:

$$Gain_{SRS}(m^{-1}) = \frac{g_{SRS}\, P_0}{A_{eff}} - \alpha_{IR} + g_{Ho} \quad , \tag{6.7}$$

Where the Raman gain in silica $g_{SRS} \approx 0.5\text{x}10^{-13}$ m/W, P_0 is the incident peak power, A_{eff} is the effective mode-area, α_{IR} is the background loss at the Stokes wavelength, and g_{Ho} is the operating gain of the amplifier at the Stokes wavelength.

A spectrum of the Raman gain in fused silica is shown in Fig. 6.9. The first Raman Stokes shift from a pump operating at 2.1 µm occurs at ~2.3 µm which overlaps with the hydroxyl absorption (~0.2 dB/m/ppm), and the IR-silica background loss (~0.5 dB/m). The resulting background loss for a fibre with a 1 ppm OH^{-1} concentration is α_{IR} = 0.7 dB/m (α_{IR} = 0.16 m^{-1}). The holmium emission cross section is negligible at 2.3 µm and so g_{Ho} = 0.

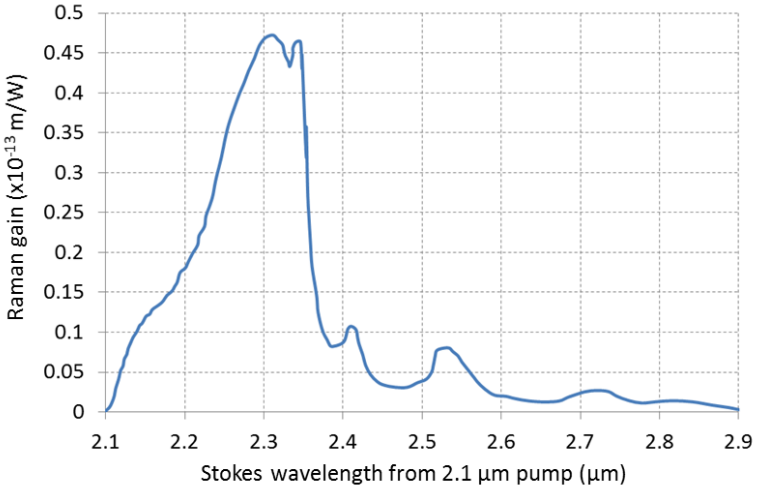

Figure 6.9: Raman gain in fused silica for a pump wavelength of 2.1 µm [33].

There are several methods for mitigating the onset of SRS. These methods typically involve increasing the mode-field diameter to reduce the peak intensity, reducing fibre length or introducing a spectrally dependant loss into the fibre. This loss mechanism can be realised by bend-loss design of the optical waveguide or by including an absorber at the Stokes wavelengths. The restriction is that any loss mechanism needs to be able to operate over a fairly large bandwidth (~100 nm as seen from Fig. 6.9 and must be able to discriminate between the original pump (2.1 µm) and the Stokes (2.3 µm).

6.4.2 Stimulated Brillouin scattering

Stimulated Brillouin scattering is a nonlinear process that involves 2 optical fields again termed pump and Stokes and an acoustic field. A high intensity and coherent pump field will create an acoustic grating in the fibre through the process of electrostriction [21]. The acoustic wave creates a modulation of the refractive index of the material in the form of a moving grating. This acoustic grating then scatters the pump radiation with a frequency shift that corresponds to the acoustic velocity of the grating and the angle of propagation of the Stokes field. The maximum scattering occurs in the backwards direction (opposite to the propagation of the pump field) and the associated frequency shift in silica (Ω_{SBS}) at 2.1 µm is ~8 GHz. This effect manifests as a reduction in forward propagating radiation and an increase in the backwards propagating radiation (a frequency shifting mirror). As the pump field is increased, the strength of the acoustic grating increases and

the Stokes field also increases. Furthermore the interference between the pump and Stokes fields further increases the strength of the acoustic grating leading to a rapid and coherent growth of the strength of the frequency shifting mirror. In a high-gain fibre amplifier, the backwards propagating radiation is able to extract a significant amount of gain as it double passes the gain medium. This can lead to a significant amount of power propagating backwards towards various components including pump diodes, isolators and fibre devices. Figure 6.10a) illustrates a thulium-doped fibre amplifier system where multiple orders of SBS were generated. As a result, the output spectrum of the laser appeared as shown in Fig. 6.10b) with the output containing every second order SBS Stokes order. Indeed, the 8th Stokes order has experienced a 0.9 nm (65 GHz) wavelength shift from the original pump yielding an approximate value for Ω_{SBS} = 8.1 GHz which agrees well with theory.

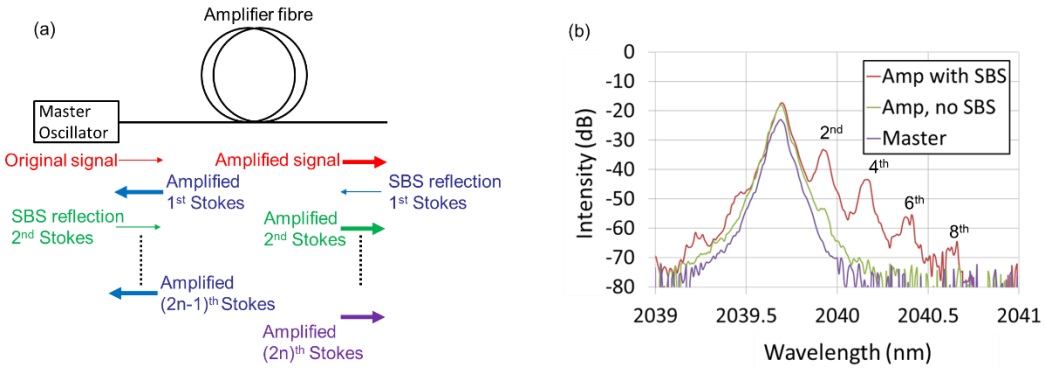

Figure 6.10: a) Illustration of cascaded SBS generation in an amplifier with the output containing the original pump signal and every 2nd order. b) Spectral output of a pulsed 2.04 µm fibre laser that has generated multiple SBS orders.

The strength of this nonlinear effect can be expressed as follows:

$$Gain_{SBS}(m^{-1}) = \frac{g_{SBS}\, P_0}{A_{eff}} - \alpha_{IR} + g_{Ho} \quad , \tag{6.8}$$

Where $Gain_{SBS}$ is the effective gain of the nonlinear mechanism, g_{SBS} is the gain peak for fused silica and is ≈ 5x10^{-11} m/W [33], P_0 is the incident peak power, A_{eff} is the effective mode-area, α_{IR} is the background loss at the Stokes and is of the order of 0.1 dB/m (α_{IR} = 0.023 m^{-1}), and g_{Ho} is the operating gain of the amplifier as the Stokes shift of 8 GHz is negligible compared to the gain bandwidth of a holmium-amplifier (>50 nm).

It is possible to reduce the onset of SBS by employing in-homogenous broadening techniques by either reducing the coherence of the acoustic grating along the length of the amplifier via

temperature, tension and composition gradients or by reducing the coherence of the pump field via phase or frequency modulation [34]. These approaches increase the bandwidth of the overall SBS gain while simultaneously reducing the peak gain [2]. Finally, more complex approaches include modifying the composition of the fibre core to reduce the overlap between the acoustic grating and the optical fields [35].

These suppression techniques have been a key element in scaling ytterbium-doped fibre amplifiers for coherent beam combination applications. The SBS line-width varies inversely with wavelength and in silica is ~10 MHz at 2.1 μm – about a factor of 4 smaller than at 1 μm – it is anticipated that these in-homogeneous techniques will be even more effective when operating in this wavelength region. Indeed, a single-frequency, CW, thulium-doped fibre amplifier was operated at 608 W of output power with no SBS – at a similar power level, a ytterbium-doped fibre amplifier system required significant spectral broadening of the input signal radiation to avoid SBS [36].

6.4.3 Modulation instability

Modulation instability (MI) occurs when operating at wavelengths in the anomalous dispersion region (D_λ = 52 ps/(nm.km) $\beta_2 \approx$ -50 ps^2/km at 2.1 μm). Here D_λ is the dispersion parameter given as $D_\lambda = -2\pi c\beta_2/\lambda^2$ and $\beta_2 = \delta^2\beta/\delta\omega^2$ is the second order dispersion coefficient. The zero-dispersion wavelength (ZDW) in silica is approximately 1300 nm with wavelengths > ZDW experiencing an anomalous dispersion. As a result of operating in this dispersion region, any intensity noise experiences exponential growth via MI. Subsequent propagation and amplification of a pulse in this regime, leads to the phenomena termed ‘pulse-break-up’, and the formation of a periodic picosecond pulse train within the envelope of the original nanosecond pulse. The peak power continues to grow as these pulses experience amplification within the amplifier. Self-phase modulation (SPM) then induces spectral broadening, which is further amplified by the available gain from the MI. These effects are typically characterised by the appearance of sidebands in the spectrum that spread symmetrically around the initial frequency of the pulse [52]. These sidebands are also able to extract a significant amount of power from the active fibre amplifier, and due to their proximity to the original signal, are difficult to spectrally filter.

The equations and parameters governing this gain profile are described as follows:

$$\gamma = \frac{n_2 \omega_0}{c\, A_{eff}} \qquad \Omega_c^2 = \frac{4\gamma P_0}{|\beta_2|} \quad , \tag{6.9}$$

Where γ is the nonlinear coefficient, $n_2 \approx 2.6 \times 10^{-20}$ m^2/W in silica, ω_0 is the centre frequency of the driving field, A_{eff} is the effective mode-area, c is the speed of light in vacuum, P_0 is the peak power and Ω_C is an introduced constant with the units of rad/s.

The gain profile of the MI can be written as follows:

$$g(\Omega) = |\beta_2 \Omega|(\Omega_c^2 - \Omega^2)^{1/2} \quad , \tag{6.10}$$

Where g(Ω) is the MI gain as a function of frequency offset Ω from the pump frequency.

Figure 6.11 illustrates the behaviour of the MI gain coefficient for a source with central wavelength of 2040 nm, $\beta_2 \approx -50$ ps^2/km and nonlinear coefficient $\gamma = 0.276$ W^{-1}/km.

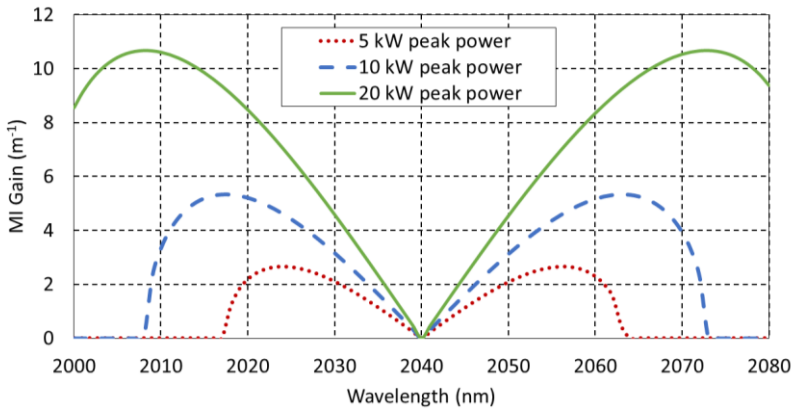

Figure 6.11: Modulation instability gain profiles as a function of wavelength for varying peak powers at a pump wavelength of 2040 nm, $\beta_2 \approx -50$ ps^2/km and nonlinear coefficient $\gamma = 0.276$ W^{-1}/km.

The frequency at which the MI gain is a maximum (Ω_{max}) occurs at:

$$\Omega_{max} = \pm \left(\frac{2\gamma P_0}{|\beta_2|}\right)^{\frac{1}{2}} \quad , \tag{6.11}$$

The resulting peak gain for MI (g_{max}) is:

$$g_{max} = g(\Omega_{max}) = \frac{1}{2}|\beta_2|\Omega_c^2 = 2\gamma P_0 \quad , \tag{6.12}$$

An example of MI occurring in a pulsed thulium-doped fibre amplifier operating at 2040 nm is illustrated in Fig. 6.12. Here the characteristic features/sidebands around the carrier can be observed along with extensive spectral broadening associated with further SPM.

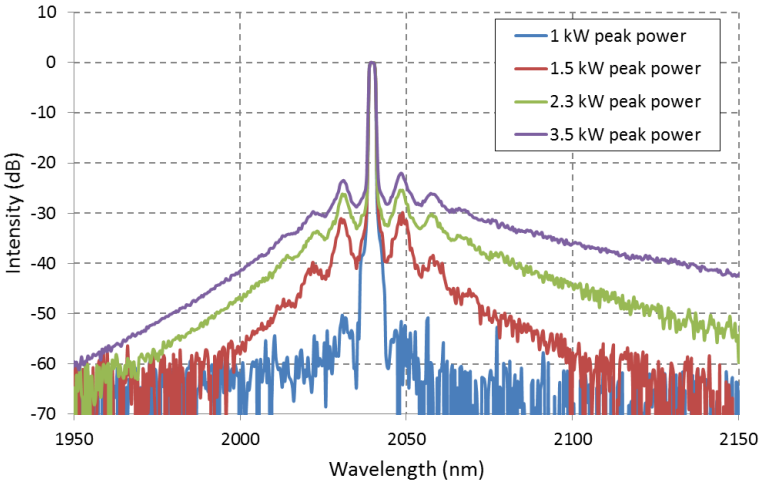

Figure 6.12: Measured performance of a 2040 nm pulsed thulium source during the onset of MI and subsequent spectral degradation due to MI and SPM.

The peak gain for modulation instability for typical peak powers occurs with a frequency shift of 10-30 nm from the original signal.

As demonstrated in Chapter 5, the operating bandwidth of holmium-doped amplifiers is typically much larger than this shift, and as a result any background noise around the signal will experience significantly more gain than the signal radiation itself. The resulting gain experienced by the MI can be expressed as:

$$Gain_{MI}(m^{-1}) = g_{max} + g_{Ho} \quad , \tag{6.13}$$

Where $Gain_{MI}$ is the peak gain experienced due to MI, g_{max} is the peak MI gain from Eqn. (6.12) and g_{Ho} is the operating gain of the holmium amplifier at the MI sidebands.

To negate the deleterious effects of MI, groups have proposed fibre designs where the dispersion of the amplified mode is shifted into the normal regime via resonant interaction with other cladding structures present in the fibre [53]. Other approaches for suppressing or avoiding MI involve improving the spectral quality of the seed laser, increasing fibre core area and reducing device lengths.

6.4.4 Comparison of nonlinear processes

Table 6.5 shows a direct comparison of the gain of each nonlinear effect for a 2.1 µm pulse with peak power P_0 = 10 kW, propagating in a fibre with an effective area A_{eff} = 300 µm^2 (MFD = 20 µm).

Table 6.5: Summary of strengths of SRS, SBS and MI nonlinear gain coefficients for a 2.1 µm pulse with 10 kW peak propagating in a fibre with an effective area of 300 µm^2.

Effect	Gain (dB/m)	Comments
MI	23 + g_{Ho}	Very little can be done to directly suppress this effect. Peak gain occurs within ±15 nm around signal.
SRS	6.5	Assume fibre has OH content of ~1 ppm. Peak gain at 2.3 µm from a 2.1 µm pump
SBS	72(7.2) + g_{Ho}	1 GHz, (10 GHz) bandwidth of master oscillator Further inhomogeneous broadening can be used. Peak gain at -8 GHz (0.1 nm) from signal

As can be seen, the dominant nonlinear effects are MI and SBS, in comparison to pulsed 1 µm systems where the dominant nonlinear effects are SBS and SRS. Suppression techniques can be used to limit the onset of SBS; however MI is much more difficult to mitigate. The strength of the spontaneous contribution of each effect is also unknown – and so it may be difficult to predict the onset of each effect if seeded by noise. Elimination of seeding mechanisms is also extremely important – for SRS and MI this involves spectral filtering and for SBS this involves elimination of any counter-propagating signal radiation that may arise from residual reflections.

6.5 Preliminary experiments with a cladding-pumped, holmium-doped fibre amplifier

An initial experiment was conducted with a large mode-area, holmium-doped fibre and a Q-switched Ho:YAG master oscillator. This was done in part to characterise the operation of the fibre in a pulsed system, but also to see if this simple approach would be sufficient to meet the requirements of an OPO pump source.

6.5.1 Polarisation maintaining, large mode-area, holmium-doped fibre design

An end view of the holmium-doped fibre is shown on Fig. 6.13. The fibre has a 45 µm diameter core with a 0.075 numerical aperture (NA). The V-number is ~5 at 2.1 µm and as a result the core is not single-mode. The holmium concentration is ~0.5 wt.% with a peak core absorption of 70 dB/m at 1.95 µm. The inner silica cladding has a diameter of 250 µm. A fluorine-doped silica layer is used to provide the pump guidance with a 0.24 NA. The fluorine-doped layer is further over-clad with fused silica out to a 400 µm diameter. Two features located in the inner silica cladding created a stress-induced birefringence of 1.5×10^{-4}.

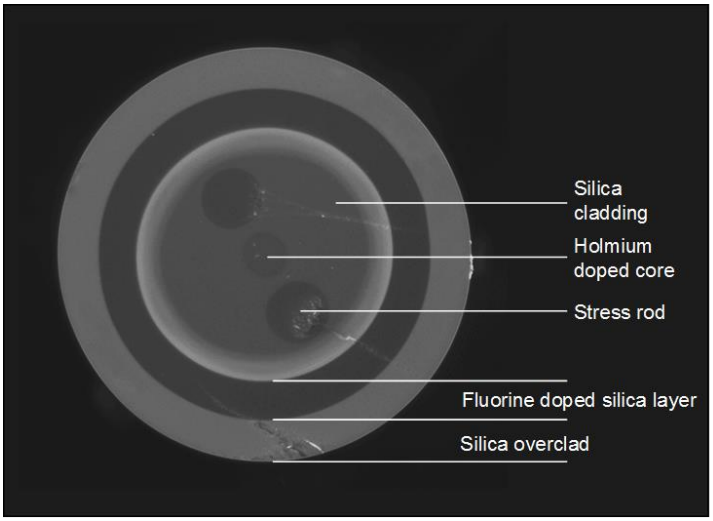

Figure 6.13: End view of the PM, LMA holmium-doped fibre. The labels detail the various types of glasses used to provide pump guidance and birefringence.

6.5.2 Q-switched Ho:YAG master oscillator

The master oscillator is a Q-switched Ho:YAG laser similar to the design presented in [22]. A schematic of the laser is shown in Fig. 6.14. A 1.908 µm thulium fibre laser is used to resonantly pump a 30 mm Ho:YAG (0.7 wt%) rod through a dichroic mirror (TFP1: HT @ 1.908 µm, HR @ 2.09 µm S-pol, HT @ 2.09 µm P-pol). The laser cavity is formed between a highly reflective mirror (HR) and a 70% reflective output coupler (OC, radius of curvature = 100 mm). The HR also ensures that the thulium pump is double passed through the rod. A quarter-wave plate (QWP) provides hold-off and a Rubidium Titanyl Phosphate (RTP) Pockels cell acts as the Q-switch. The etalon restricted output to ~2091 nm, suppressing 2097 nm emission.

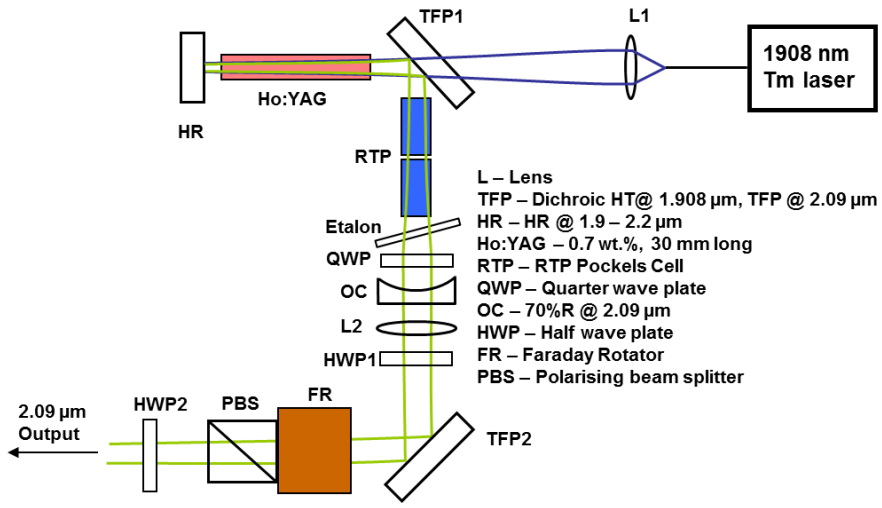

Figure 6.14: Schematic of the Q-switched Ho:YAG laser used as the master oscillator.

The output of the laser is collimated by a 100 mm lens (L2). A combination of a half-wave plate (HWP1) and thin film polariser (TFP2) provides control of the energy output of the system. A Faraday rotator (FR) and a polarising beam splitter (PBS) provide isolation protection for the master oscillator from reverse propagating signal and reflections from the amplifier. A second half-wave plate (HWP2) is used to adjust the polarisation incident onto the fibre amplifier. The output spectrum of the master oscillator is shown in Fig. 6.15. It is centred at 2091 nm and suggests that multiple longitudinal modes are present.

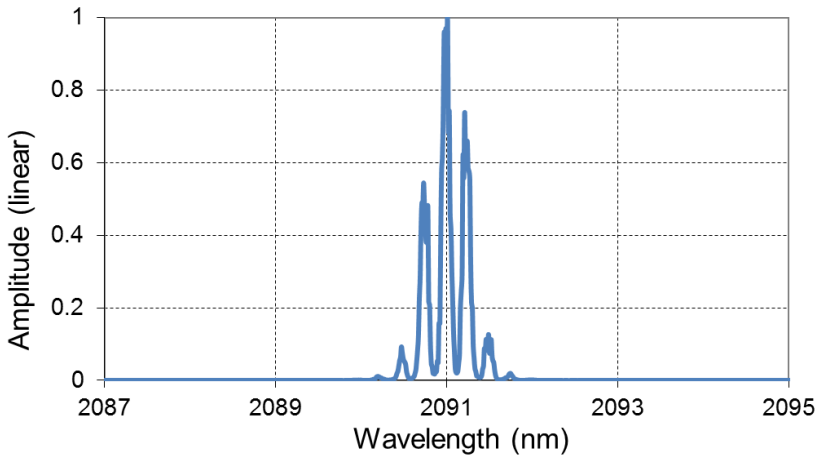

Figure 6.15: Spectrum of the output from the Ho:YAG master oscillator indicating that multiple longitudinal modes are operating.

The master oscillator provided stable pulses when operating at 20 kHz and 10 W output power. The pulse duration was 21 ns at full-width half-maximum (FWHM). The beam quality of the Ho:YAG

laser was diffraction limited. HWP1 was adjusted so as to launch 200 µJ at 20 kHz (4 W) into the PM, LMA fibre amplifier.

6.5.3 Holmium-doped fibre amplifier configuration

A schematic of the amplifier is shown in Fig. 6.16. The holmium-doped fibre is counter-pumped with a 150 W thulium-doped fibre laser at 1.95 µm [14]. The length of the holmium-doped fibre used is 10 m. A 1.5 mm long, 400 µm diameter un-doped silica end-cap with a 4° degree cleave is used at the output end. A similar dimension end-cap but with a 0° degree cleave is used at the input end. The fibre is spooled on a water-cooled mount with a diameter of 30 cm. At the time that this experiment was conducted, the bulk CO_2 end-capping capability had not yet been commissioned.

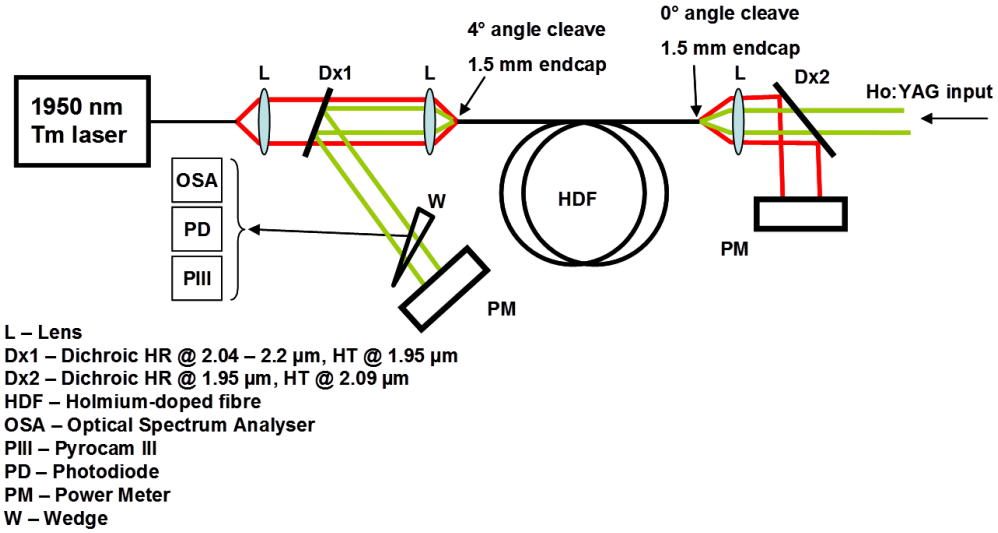

Figure 6.16: Schematic of pulsed holmium-doped fibre experiment.

A dichroic mirror (Dx1: HR @ 2.1 µm, HT @ 1.95 µm) reflects the holmium output to the diagnostics. A CaF_2 wedge provides a pick-off for imaging (PIII: Ophir Pyrocam III), spectral (OSA: Yokogawa OSA) and temporal (PD: Discovery Semiconductors) measurements. The power transmitted through the wedge is measured on a calibrated thermal power meter (Ophir). A second dichroic (Dx2: HT @ 2.1 µm, HR @ 1.95 µm) protects the master oscillator from any residual pump power transmitted through the amplifier. A ZBLAN patch-cord is used as the input to the OSA in order to avoid attenuation at wavelengths >2.1 µm due to absorption and bend loss that would be present in a silica patch-cord.

6.5.4 Double-clad, holmium-doped amplifier results

The output power vs. launched pump power is shown in Fig. 6.17. The pump absorption was 95%. The amplifier operated with a slope efficiency of 45% with respect to launched pump power up to 35 W (1.7 mJ pulse energy) and a reduced slope of 25% up to 45 W (2.25 mJ). An ASE measurement as described in Section 2.4 confirmed that there was negligible (<100 mW) ASE at the 45 W output level. There was also no significant increase in reverse propagating power towards the master oscillator. The inset to Fig. 6.17 shows that the output pulse shape was very similar to the input pulse from the master oscillator. The duration of the output pulse was 20 ns.

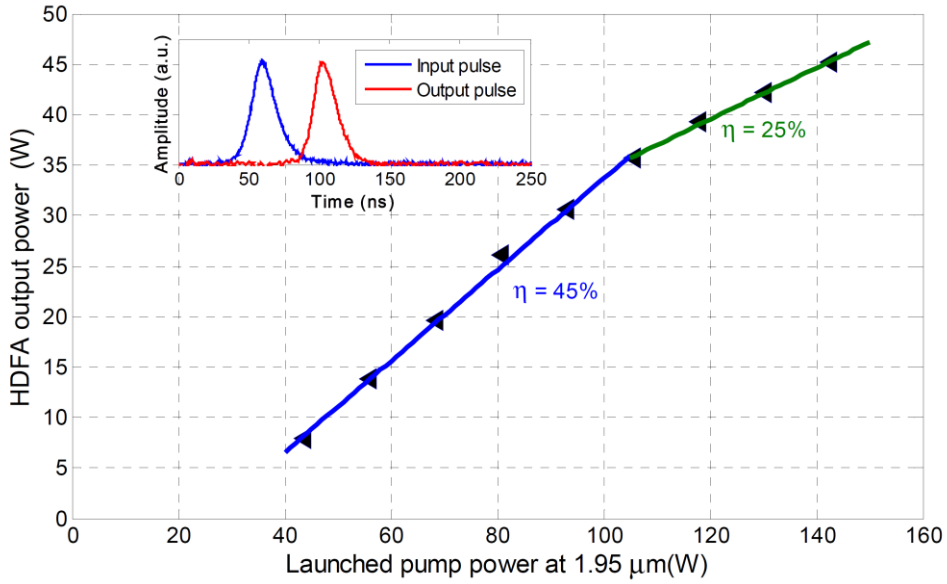

Figure 6.17: Output power of holmium-doped amplifier vs input pump power. **Inset:** the pulse before and after amplification showing no significant distortion.

The spectrum of the amplifier output is shown in Fig. 6.18. As the pumping rate was increased, there was a broad-band output generated spanning from 2.05 – 2.4 µm. The central peak was maintained at 2.09 µm. The polarisation extinction ratio was > 11.5 dB (93%) under all operating conditions.

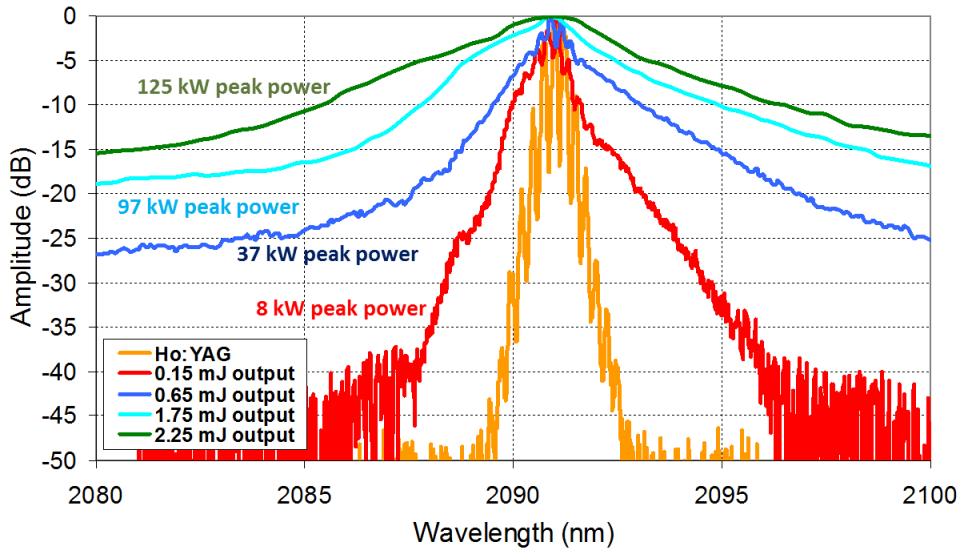

Figure 6.18: Significant spectral broadening is observed even at modest output energies. The OSA resolution setting was 0.5 nm.

The beam quality was calculated from measurements of the beam profile through the focus of a 100 mm lens. The measured values of the beam diameter using the second moment are shown in Fig. 6.19. A magnification element was attached to the Pyrocam in order to resolve the waist region. The evolution of the diameter as a function of distance corresponded to an M^2 of 1.6 in both axes, indicating that the amplifier was operating on multiple transverse modes.

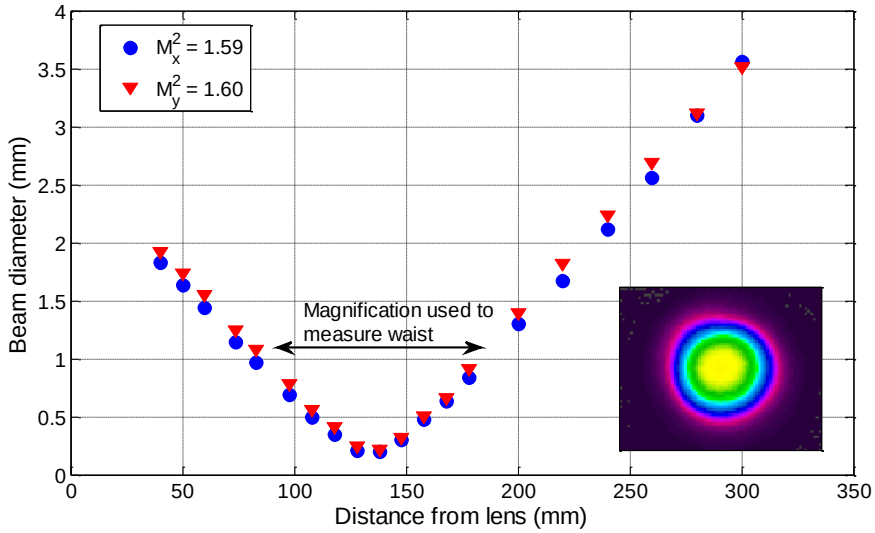

Figure 6.19: Waist measurements through a focus. $M^2_{X,Y}$ = 1.59, 1.60 were fitted to these points. The near field profile is shown.

6.5.5 Discussion

The PM, LMA holmium-doped fibre amplifier produced pulses of energy of 2.25 mJ at a repetition rate of 20 kHz with negligible CW background or ASE. The output was linearly polarised with an extinction ratio of >11.5 dB and had a beam of M^2 = 1.6. The 20 ns FWHM pulse duration at the output was almost identical to the master oscillator input and we estimate that peak powers in excess of 120 kW were achieved.

There was significant spectral broadening observed with the output spectrum extending from 2.05 – 2.4 µm with a central peak at 2.09 µm. We attribute this effect to modulation instability leading to pulse break-up and super-continuum generation. No evidence of stimulated Brillouin scattering or stimulated Raman scattering was observed.

The reduction in slope efficiency at >35 W (1.75 mJ) output power is attributed to the increase in power at wavelengths >2.2 µm due to the super-continuum generation and subsequent absorption in the active fibre or the fused silica refractive optics before the power meter.

We believe that the efficiency at low powers (45%) is below the quantum efficiency (93%) due to a combination of energy transfer processes in the holmium ion population, residual hydroxyl contamination, and significant infrared absorption at wavelengths >2.15 µm.

The summary of the amplifier output and the original requirements are summarised in Table 6.6.

Table 6.6: Summary of required and achieved source parameters.

Property	Requirement	Achieved
Wavelength (nm)	>2050 nm	2090 nm
Peak Power (kW)	> 30 kW	125 kW
Pulse duration (ns)	1 – 100 ns	20 ns
Bandwidth (nm)	< 2 nm (0.2 THz)	>20 nm
Beam quality (M^2)	< 1.5	1.6

Despite achieving sufficiently good beam quality and sufficiently large peak power, the significant spectral broadening of the source makes it unsuitable for efficient pumping of a ZGP OPO. Another approach is required. For many industrial applications such as marking and material processing, this

spectral broadening may not be a problem. However this effect is prohibitive for applications where the emission is required to pump an optical parametric oscillator for further mid-IR generation.

6.6 Alternative approach for peak power scaling

Despite operating as a fairly high performing 2 µm pulsed system, it is clear that the approach described in Section 6.5 is limited by spectral broadening and is unsuitable for constructing a pump source for the pumping of a mid-IR OPO. Over the next section we propose a new approach to peak power scaling and discuss the motivation and requirements for this approach.

6.6.1 Description of approach

The approach chosen to minimise the spectral broadening was a large mode-area, core-pumped, amplifier. This addresses the mechanisms responsible for the onset of of MI and subsequent supercontinuum generation. As discussed in Section 6.3, there are very few parameters that can be modified in order to suppress this nonlinear effect. These include reducing fibre length, increasing mode-field diameter and reducing the intensity noise present during the pulse. Other authors have proposed using resonant waveguide structures to modify the dispersion properties for the fundamental mode, to couple and propagate in a higher-order mode or to coherently combine the output from multiple fibres.

6.6.2 Overview of core-pumped approach

The device length is typically determined by a combination of the requirement for efficient transfer of the pump energy to the active material as well as providing sufficient gain for efficient extraction of this stored energy. In order to maximise the pump interaction with the core and to minimise the fibre length, a core-pumped approach was chosen. A schematic of the core-pumped approach is shown in Fig. 6.20. Here a 1.95 µm pump laser and a 2.1 µm master oscillator are combined into the core of a single fibre which is then spliced to a length of holmium-doped fibre. In order to couple the pump and the signal into the fundamental-mode of the same core, both the pump and signal radiation must originally be taken from single-mode fibres. This places a limitation on power scaling of the holmium amplifier to that of the thulium pump laser and the power handling of the

wavelength combiner (WDM). The bandwidth of the thulium-doped pump laser must also be relatively narrow in order to be able to achieve a high coupling efficiency.

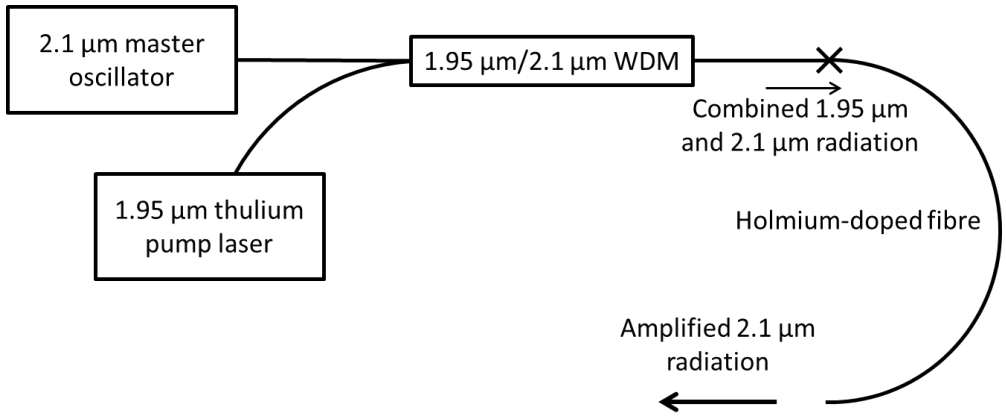

Figure 6.20: Illustration of a core-pumped amplifier approach where the master oscillator and pump are combined via a WDM device into the core of a holmium-doped fibre amplifier.

This technique also significantly reduces the cost of fabrication of the active fibre as it is now no longer necessary to have a double-clad structure. This however does come at the expense of no longer being able to exploit a double-clad architecture for power scaling. As discussed in earlier chapters, a double-clad geometry facilitates the coupling of many thulium pump lasers to a single holmium laser. However, in a core-pumped configuration, only a single thulium laser is able to be used as a pump source – thereby limiting the average power of the holmium output. With recent developments of single-mode 1.95 µm thulium fibre lasers, we anticipate that this approach is still able to scale to the 10-100 W level with relative ease.

6.6.3 Mode-area scaling in multi-mode fibre

Due to compositional restrictions, we cannot arbitrarily scale the NA of the core to lower and lower values. Recently, we have demonstrated that an efficient holmium-doped core composition that required an NA > 0.132. A robustly single-mode core with this composition therefore will have a 12 µm diameter and a mode-field diameter of ~13 µm. This relatively confined mode will reduce the thresholds for the various limiting nonlinear effects. In order to increase the fundamental mode-field without modifying the core composition, it is possible to use the pedestal technique that is common in thulium-doped fibres. With this approach, the mode-fields have been scaled to ~20 – 22 µm diameter. With the many different glass compositions in a pedestal structure, manufacturers typically will not be able to control the refractive index properties of the waveguide

and typically specify an effective NA of ~0.1 as the minimum. This is only slightly better than the original starting composition of the core at 0.132 NA and so an alternative scaling method is desirable.

Another approach is to operate with a multi-mode core and increase the core diameter. While this certainly seems simple when considering a step-index core, the variations in refractive index can affect the scaling properties of this approach. In fibres fabricated using the MCVD process it is common that there will be a central feature that typically forms as a result of additional thermal processing of the inner-most layer during the collapse stage. In our analysis we compare a step-index fibre with a 0.006 R.I.U. core with radius r and a fibre with a centre peak of height 0.001 R.I.U and extent of 0.1r. The example of both refractive indices is illustrated in Fig. 6.21a). A finite-element multi-physics computational software was utilised to solve for the guided modes of the dielectric waveguide (COMSOL).

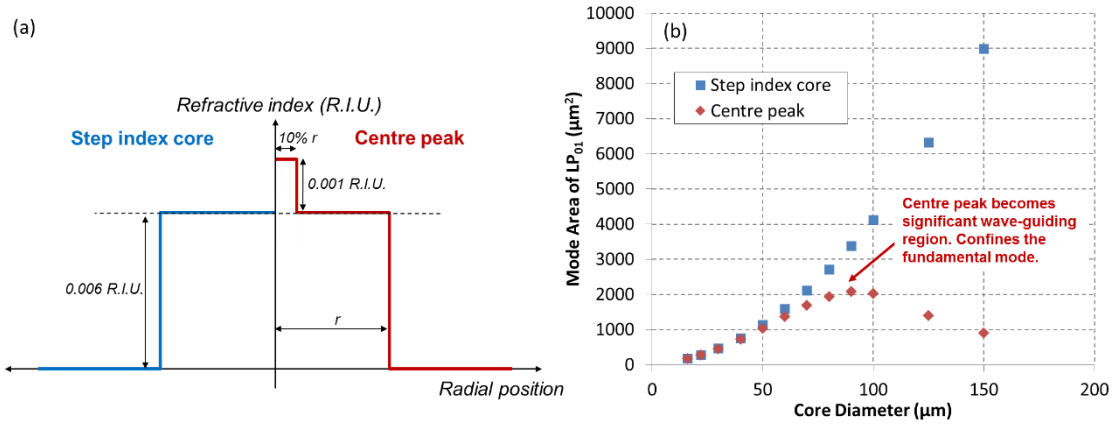

Figure 6.21: a) Step-index and a fibre with a central defect. b) Mode-area of the fundamental mode as a function of core diameter.

The level to which the MFD can be scaled will depend on the uniformity of the refractive index profile and how it scales when drawn to a larger diameter. This is shown in Fig. 6.21b). In this particular case, the central peak will limit the MFD to ~2000 μm^2. For a core diameter of >60 µm, the MFD is also greatly reduced in the presence of this feature. If there were a central dip present of a similar magnitude it would begin to distort the field profile of the LP_{01} and would no longer appear Gaussian. For the first iteration, the fibre was manufactured with a 60 µm core diameter as this is a relatively 'safe' region in which even such a significant defect will not greatly reduce the MFD.

The refractive index profile of the fibre is shown in Fig. 6.22a). Zooming in on the top of the profile we see that the peak-to-peak variation in refractive index is $4x10^{-5}$ R.I.U – shown in Fig. 6.22b). This is truly impressive for a preform fabricated by solution-doping MCVD technique and is comparable in profile quality to preforms fabricated both by the REPUSIL and chelate delivery methods [37]. It is anticipated that such a flat refractive index profile will allow MFD scaling to significantly larger dimensions than this initial attempt.

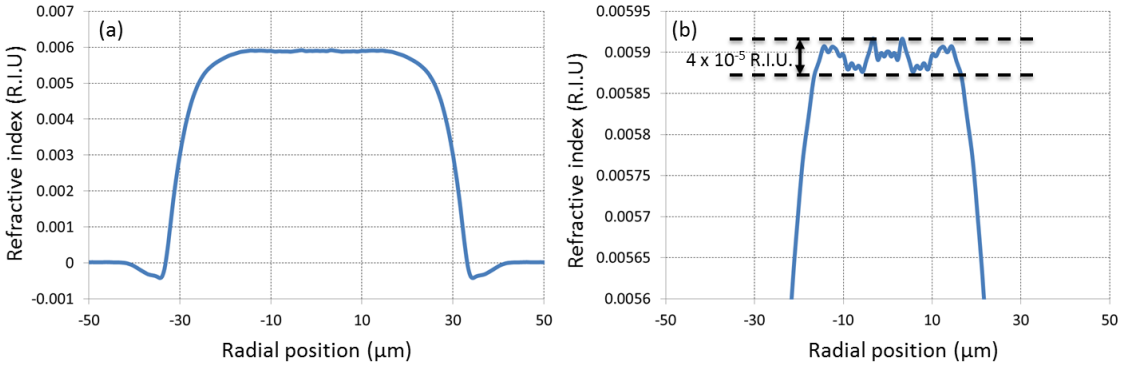

Figure 6.22: a) Measured profile of flat-top holmium-doped fibre. b) Residual ripple in the core profile achieves a peak-to-peak value of $4x10^{-5}$ R.I.U.

When drawn to a core diameter of 60 µm, the resultant fibre has a V-number of 12.0 at 2.07 µm and supports many modes. There is no mode-filtering technique that is applicable to a core with these parameters. It is therefore, essential to ensure that the launch condition into this multi-mode core is of extremely high quality into the fundamental mode only. A common method of achieving this is to use an adiabatic taper [38–41]. Here the fibre was tapered from the original 60/600 µm to a 20/200 µm (MFD = 17.1 µm) and then spliced to the 15/250 µm 0.1NA (MFD = 17.0 µm) fibre which was used in the WDM. The pointing stability and subsequent S^2 measurements were used to quantify the amount of HOM content present at the output of the active fibre after the tapering and splicing processes were performed.

The length requirement for the adiabatic taper transition is easily achievable on a GPX Vytran 3400 glass processing machine. The quality and shape of the taper was found to be of critical importance. Care must be taken to ensure that the taper is as symmetric as possible. An example of a taper that produced substantial (~40%) coupling from the LP_{01} to the LP_{11} mode of the 60 µm core is shown in Fig. 6.23a). After improvements in the fabrication process, the taper shown in Fig. 6.23b) ensured that less than 5% of the input radiation was coupled into the LP_{11} mode – i.e. the launch purity into the 60 µm core was >95% LP_{01}.

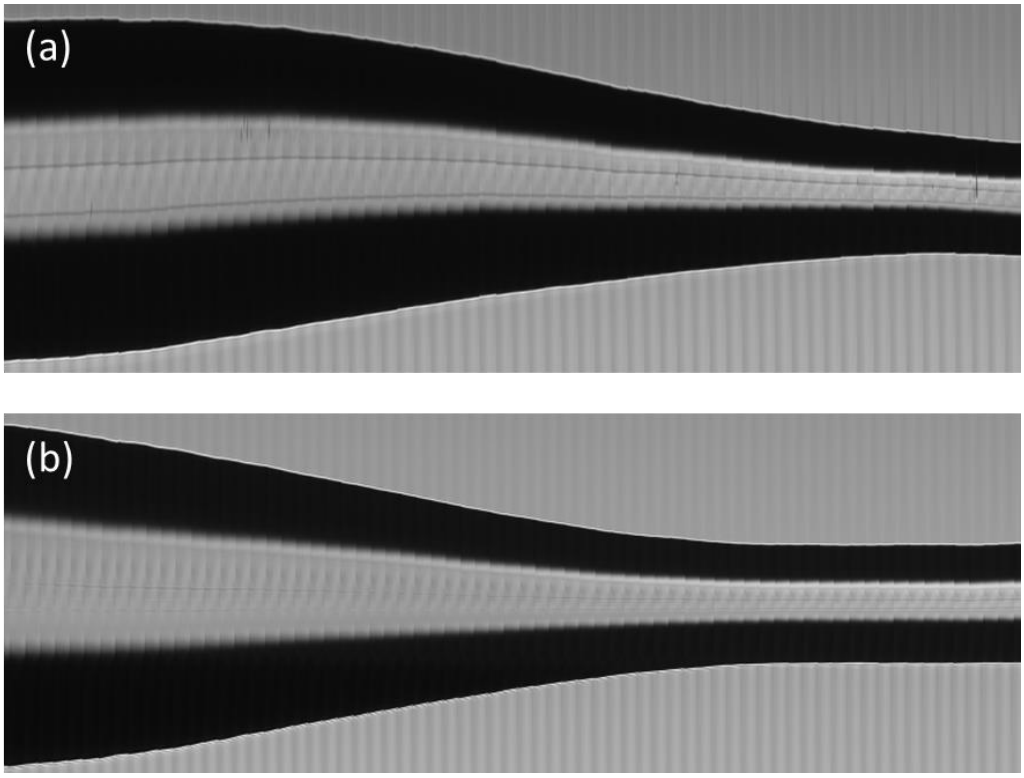

Figure 6.23: a) Initial attempt at an adiabatic taper had significant deformation and provided significant coupling from the LP_{01} to the LP_{11}. b) Taper used in final experiment provided <5% coupling to the LP_{11} mode.

A narrow band 2100 nm laser source was propagated through the taper and subsequent length of holmium-doped fibre. The beam profiles in the near and far fields from the output are shown in Figs. 6.24a) and 6.24b). By imaging the output of the fibre with a high magnification arrangement, we were able to establish that the MFD of the fundamental mode was 37 µm. To the best of our knowledge, this is the largest fundamental-mode MFD propagation demonstrated for a holmium-doped fibre. This significant increase in mode-field should enable a significant increase in the thresholds for the various nonlinear processes.

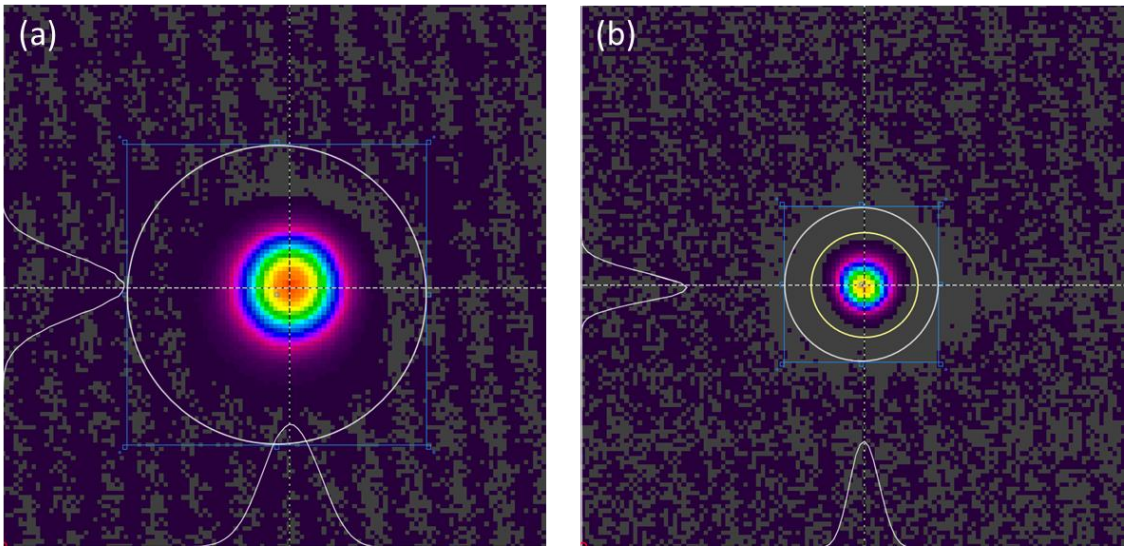

Figure 6.24: a) Near and b) Far field profiles of the beam after re-imaging of the output from the 60/600 active fibre.

6.6.4 Temporal and spectral mitigation techniques

The origin of the modal instability occurs due to the exponential growth of any intensity noise present in the system. In order to avoid the onset of this instability a source with a low relative intensity noise is required. If we examine the pulsed Ho:YAG laser used in the experiment in Section 6.5, we can see that this is indeed operating on multiple longitudinal modes. Similarly, the gain-switched fibre lasers described in [42–45] also typically operate on multiple longitudinal modes. Interference between these longitudinal modes will cause intensity modulation through the duration of the pulse and the resulting high peak power regions will suffer extensive nonlinear effects.

In order to avoid longitudinal mode-beating, it is necessary to use a source that is operating on a single longitudinal mode. However, if this is simply a single-frequency oscillator, then the SBS nonlinear effect will dominate. The linewidth of the source needs to be artificially broadened to the >10 GHz level in order to increase the SBS threshold. One common technique in high power fibre amplifier development is to use a phase modulator to rapidly dither the phase during the pulse [34]. Another approach would be to apply a frequency chirp or frequency modulation along the duration of the pulse. Such a frequency chirp can be achieved by current switching a single-mode semiconductor source [46]. The rapidly switching current will impart a frequency chirp across the pulse provided that the diode is able to respond fast enough. It is important to note that the

linewidth broadening mechanism required to suppress the SBS nonlinear effect is of the order of 10 GHz, whereas the efficiency and threshold of the mid-IR OPO begins to be significantly affected by broadening of >200 GHz. As a result we do not anticipate degradation of mid-IR conversion efficiency as a result of the artificial broadening used to suppress the SBS nonlinear effect.

6.6.5 Schematic of master-oscillator and core-pumped amplifier

As a result of the temporal and spectral mitigation techniques described above, the master oscillator is now limited to <5 mW peak power from a semiconductor seed. This then requires significant (>70 dB) amplification to achieve the 30-100 kW peak powers that are desired for the final output. Here the master oscillator is a single-mode diode (Eblana photonics) that is driven by a 5 ns flat-top current pulse (Optical pulse machines) at a 100 kHz repetition rate. The output from the seed diode passes through two stages of high gain amplification utilising similar construction to the single-pass amplifier presented in Section 5.3, but using PM fibres and components. All of the fibres in these initial stages have a 10 µm core diameter, 130 µm cladding diameter and PANDA stress rods to provide the internal stress-induced birefringence. The amplifiers are separated by dual-stage isolators as shown in Fig. 6.25. The output from the final amplifier achieves a peak power of 1.5 kW and is collimated and filtered using a volume Bragg grating (VBG, Optigrate) with a bandwidth of 0.8 nm. The VBG is able to reflect >90% of the input signal and provides excellent out-of-band rejection of any modulation instability spectral features that have appeared as a result of the high peak power in the 10 µm core.

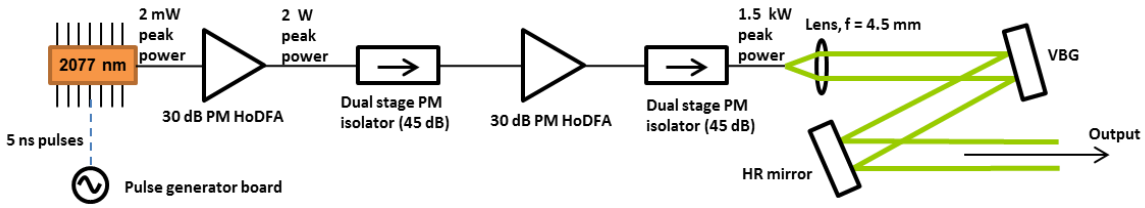

Figure 6.25: The master oscillator undergoes several stages of amplification in order to boost the 5 mW peak power to 1.5 kW. Finally, a VBG is used to spectrally filter the output in order to remove any MI that was spontaneously generated in the first stages.

The output from this master-oscillator is then coupled into one of the pigtails of the high power 1950/2080 nm WDM as shown in Fig. 6.26. A 1950 nm thulium pump laser is spliced onto the other input port of the WDM. The output fibre from the WDM is spliced to the 20/200 tapered end of the

active 60/600 HDF as discussed in Section 6.6.3. A 2 m length of 60/600 HDF is estimated to be of sufficient length to provide the necessary gain (13 - 20 dB) for the final stage of amplification. After reflecting from the VBG and with the associating losses of the free-space coupling, a pulse with ~1 kW peak power was launched into the taper of the HDF. An AR-coated, bulk end-cap as discussed in Section 3.7 was utilised to ensure that there was minimal feedback from the end-facet. This was essential to prevent instability in the thulium laser, and also to minimise the amount of broadband feedback that could potentially seed nonlinear effects such as SBS.

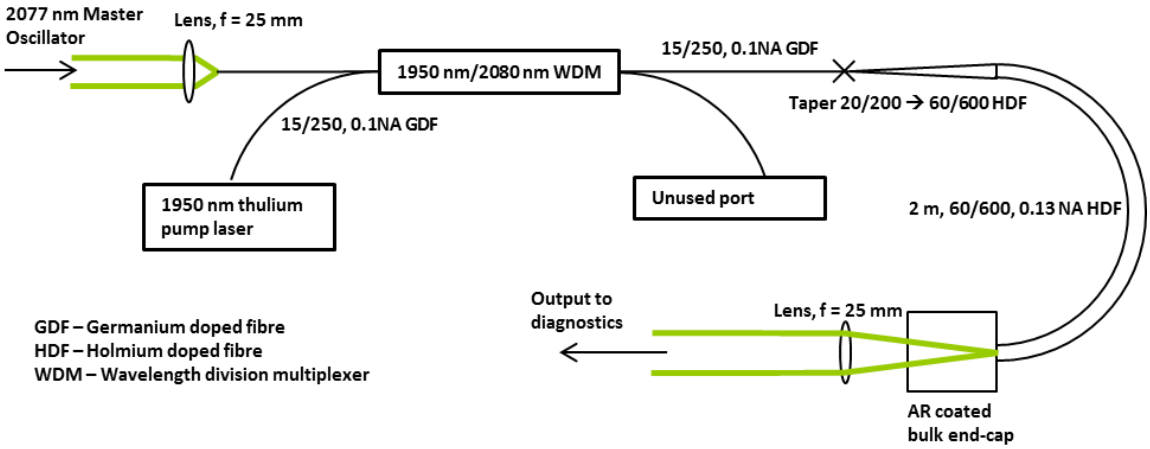

Figure 6.26: Schematic of core-pumped Ho:silica fibre amplifier.

6.6.6 Performance of core-pumped, holmium-doped fibre amplifier

The output power as a function of launched 1950 nm pump power is shown in Fig. 6.27. The inset in Fig 6.27 shows the temporal profile of the output pulse at maximum power. The amplifier produced 17 W and operated with a 38% slope efficiency. The pulse duration is ~5 ns and shows significant shaping due to gain saturation. The gain saturation occurs primarily in the final amplifier with minimal saturation in the first two stages. This level of gain shaping can be compensated by pre-shaping the current pulse to the seed diode oscillator.

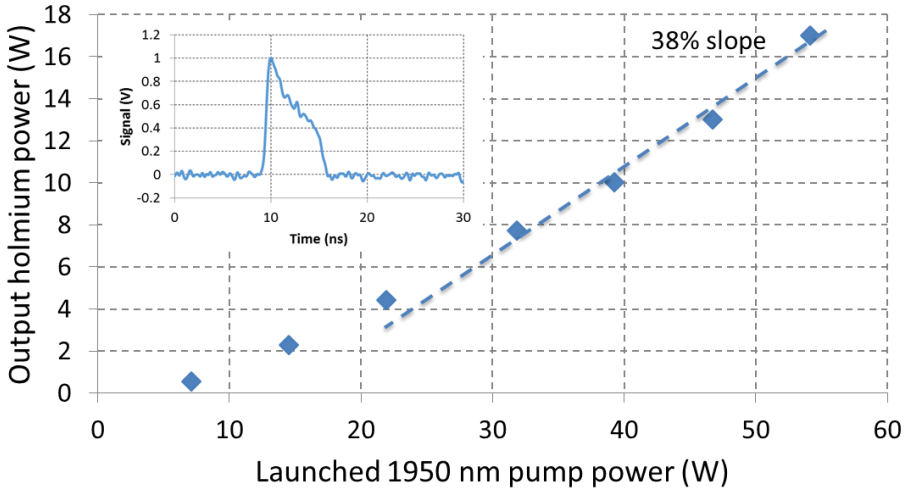

Figure 6.27: Output power of the pulsed, holmium-doped, core-pumped amplifier as a function of launched pump power **Inset:** Temporal profile of the pulse at maximum peak power.

The near and far field profiles of the output are shown in Figs. 6.28a) and 6.28b). The output of the amplifier had an $M^2 \sim 1.2$ with some distortion that was attributed to residual core distortion at the end-cap interface. The pointing stability of the source was excellent suggesting that the output was robustly single-mode.

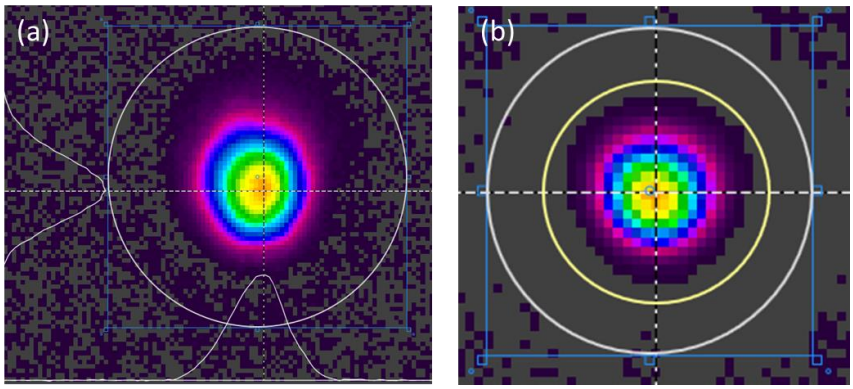

Figure 6.28: a) Near and b) Far field profiles of the amplifier output at full power.

The evolution of the spectrum as a function of peak power is shown in Fig. 6.29. The onset of modulation instability is seen by the presence of the characteristic sidebands. However there is minimal spectral broadening of the main carrier signal. Even at 36 kW peak power 99% of the power is contained within a 1 nm bandwidth.

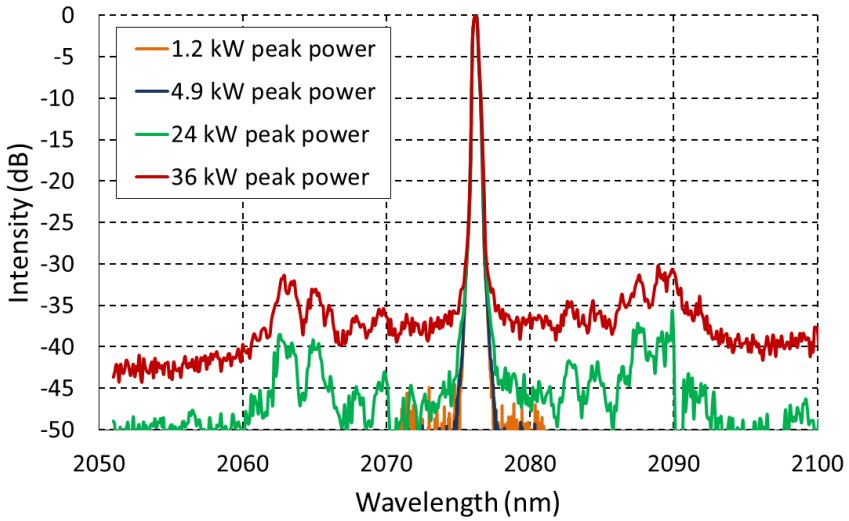

Figure 6.29: Spectrum of the output as a function of peak power showing the characteristic side bands due to MI. The OSA resolution setting used for these measurements was 0.05 nm.

6.6.7 Discussion

A number of techniques have been applied to minimise the spectral broadening observed at high peak powers. We have transitioned the final amplification stage into a core-pumped system in order to reduce the fibre length and the gain fibre has a large, step-index core with an increased mode-field area to reduce the peak intensity. As well as this, a new master oscillator configuration is used to increase the threshold for the onset of MI by eliminating longitudinal mode-beating effects. Finally, aggressive spectral conditioning using a VBG before the final stage of amplification ensures that the MI grows from spontaneous emission in the final stage as opposed to being seeded by spectral degradation from the initial pre-amplifier stages. Figure 6.30 compares the spectral output from the two pulsed MOPA systems operating at the same peak power (36 kW) presented in Section 6.5 and 6.6 overlaid on top of each other – the centre wavelength for the cladding-pumped MOPA is shifted to 2077 nm for comparison purposes.

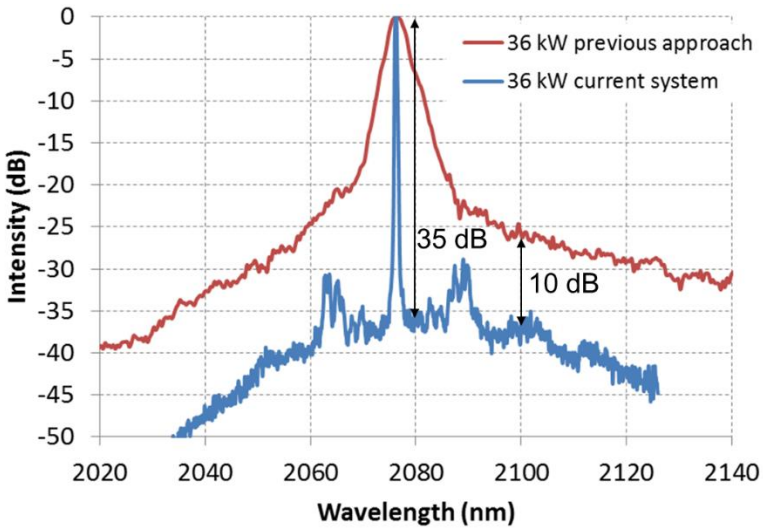

Figure 6.30: Comparison of spectral broadening between two pulsed, holmium-doped silica fibre amplifier systems at the same peak power level. The OSA resolution setting was 0.05 nm for both traces.

A significant reduction in broadening is demonstrated. The combination of the mentioned techniques has yielded an output that has a 10 dB reduction in spectral broadening over almost the entire bandwidth and a 35 dB reduction in broadening within 10 nm proximity of the signal. The integrated power within a 1 nm bandwidth is >99%. Table 6.7 lists the final output parameters of the laser amplifier system. This approach has been able to achieve all of the peak power, spectral, and beam quality requirements in order to enable efficient pumping of the ring ZGP OPO.

Table 6.7: Summary of required and achieved parameters for efficient pumping of a ZGP OPO.

Property	Requirement	Achieved
Wavelength (nm)	>2050 nm	2077 nm
Peak Power (kW)	>40 kW	36 kW
Pulse duration (ns)	1 – 100 ns	5 ns
Bandwidth (nm)	< 2 nm (0.2 THz)	1 nm (99% content)
Beam quality (M^2)	< 1.5	1.2

6.7 Summary

This chapter has presented the pump requirements for the generation of high-power mid-infrared radiation. Based on existing, demonstrated optical-parametric oscillators, a set of parameters is extracted and summarised in Table 6.4. The various possible nonlinear limitations were discussed and two approaches were investigated. A cladding-pumped, large mode-area amplifier produced an output that met most of the requirements, but was limited in application by the spectral degradation due to nonlinear effects.

A second approach was demonstrated where efforts were taken to significantly reduce the impact of these nonlinear effects, in particular MI. This was achieved by modifying the temporal properties of the seed, transitioning to a core-pumped approach and scaling the mode-field diameter of the fibre.

The strategy has yielded an output that has a significantly narrower spectral width and now meets the requirements for efficient frequency conversion in the OPO.

6.8 References

1. Naval Air Warfare Center (U.S.). Weapons Division., *Electronic Warfare and Radar Systems Engineering Handbook* (Naval Air Warfare Center, 2012).

2. V. Petrov, "Parametric down-conversion devices : The coverage of the mid-infrared spectral range by solid-state laser sources," Opt. Mater. (Amst). **34**, 536–554 (2012).

3. Y. Peng, X. Wei, W. Wang, and D. Li, "High-power 3.8 μm tunable optical parametric oscillator based on PPMgO:CLN," Opt. Commun. **283**, 4032–4035 (2010).

4. Y. Peng, W. Wang, X. Wei, and D. Li, "High-efficiency mid-infrared optical parametric oscillator based on PPMgO:CLN," Opt. Lett. **34**, 2897 (2009).

5. D. G. Lancaster, "Efficient Nd:YAG pumped mid-IR laser based on cascaded KTP and ZGP optical parametric oscillators and a ZGP parametric amplifier," Opt. Commun. **282**, 272–275 (2009).

6. E. Cheung, S. Palese, H. Injeyan, C. Hoefer, R. Hilyard, H. Komine, J. Gish, and W. Bosenberg, "High power optical parametric oscillator source," in *IEEE Aerospace Conference. Proceedings* (IEEE, 2000), Vol. 3, pp. 55–59.

7. E. Lippert, H. Fonnum, G. Arisholm, and K. Stenersen, "A 22-watt mid-infrared optical parametric oscillator with V-shaped 3-mirror ring resonator," Opt. Express **18**, 26475–26483 (2010).

8. A. Hemming, J. Richards, A. Davidson, N. Carmody, S. Bennetts, N. Simakov, and J. Haub, "99 W mid-IR operation of a ZGP OPO at 25% duty cycle," Opt. Express **21**, 10062 (2013).

9. B.-Q. Yao, Y.-J. Shen, X.-M. Duan, T.-Y. Dai, Y.-L. Ju, and Y.-Z. Wang, "A 41 W $ZnGeP_2$ optical parametric oscillator pumped by a Q-switched Ho:YAG laser," Opt. Lett. **39**, 6589 (2014).

10. R. K. Huang, B. Chann, J. Burgess, B. Lochman, W. Zhou, M. Cruz, R. Cook, D. Dugmore, J. Shattuck, and P. Tayebati, "Teradiode's high brightness semiconductor lasers," Proc. SPIE **9730**, 97300C (2016).

11. O. Henderson-Sapir, J. Munch, and D. J. Ottaway, "Mid-infrared fiber lasers at and beyond

3.5 µm using dual-wavelength pumping," Opt. Lett. **39**, 493 (2014).

12. O. Henderson-Sapir, S. D. Jackson, and D. J. Ottaway, "Versatile and widely tunable mid-infrared erbium doped ZBLAN fiber laser," Opt. Lett. **41**, 1676 (2016).

13. V. Fortin, F. Maes, M. Bernier, S. T. Bah, M. D'Auteuil, and R. Vallée, "Watt-level erbium-doped all-fiber laser at 3.44 µm," Opt. Lett. **41**, 559 (2016).

14. V. Fortin, M. Bernier, N. Caron, D. Faucher, M. El-Amraoui, Y. Messaddeq, and R. Vallee, "Monolithic mid-infrared fiber lasers for the 2-4 µm spectral region.," Proc. SPIE **8601**, 86011H9 (2013).

15. D. V Martyshkin, V. V Fedorov, M. Mirov, I. Moskalev, S. Vasilyev, and S. B. Mirov, "High Average Power (35 W) Pulsed Fe:ZnSe laser tunable over 3.8-4.2 µm," Conf. Lasers Electro-Optics SF1F.2 (2015).

16. S. B. Mirov, V. V. Fedorov, D. V. Martyshkin, I. S. Moskalev, M. S. Mirov, O. Gafarov, A. Martinez, J. Peppers, V. Smolski, S. Vasilyev, and V. Gapontsev, "Mid-IR gain media based on transition metal-doped II-VI chalcogenides," Proc. SPIE **9744**, 97440A (2016).

17. V. V. Fedorov, D. V. Martyshkin, M. Mirov, I. Moskalev, S. Vasyliev, and S. B. Mirov, "High energy 4.1-4.6 µm Fe:ZnSe laser," Conf. Lasers Electro-Optics CM3D.3 (2012).

18. C. Xia, Z. Xu, M. N. Islam, F. L. Terry, Jr., M. J. Freeman, A. Zakel, and J. Mauricio, "10.5 W Time-Averaged Power Mid-IR Supercontinuum Generation Extending Beyond 4 µm With Direct Pulse Pattern Modulation," IEEE J. Sel. Top. Quantum Electron. **15**, 422–434 (2009).

19. W. Yang, B. Zhang, K. Yin, X. Zhou, and J. Hou, "High power all fiber mid-IR supercontinuum generation in a ZBLAN fiber pumped by a 2 µm MOPA system," Opt. Express **21**, 19732 (2013).

20. O. P. Kulkarni, V. V. Alexander, M. Kumar, M. J. Freeman, M. N. Islam, F. L. Terry, Jr., M. Neelakandan, and A. Chan, "Supercontinuum generation from ~1.9 to 4.5 µm ZBLAN fiber with high average power generation beyond 3.8 µm using a thulium-doped fiber amplifier," J. Opt. Soc. Am. B **28**, 2486 (2011).

21. R. W. Boyd, *Nonlinear Optics* (Academic Press, 2008).

22. A. Hemming, J. Richards, S. Bennetts, A. Davidson, N. Carmody, P. Davies, L. Corena, and D. Lancaster, "A high power hybrid mid-IR laser source," Opt. Commun. **283**, 4041–4045 (2010).

23. E. Lippert, S. Nicolas, G. Arisholm, K. Stenersen, and G. Rustad, "Midinfrared laser source with high power and beam quality," Appl. Opt. **45**, 3839 (2006).

24. A. Hemming, J. Richards, A. Davidson, N. Carmody, N. Simakov, M. Hughes, P. Davies, S. Bennetts, and J. Haub, "A high power mid-IR ZGP ring OPO," in *Conference on Lasers and Electro-Optics* (2013), p. CW1B.7.

25. D. Creeden, P. A. Ketteridge, P. A. Budni, S. D. Setzler, Y. E. Young, J. C. McCarthy, K. Zawilski, P. G. Schunemann, T. M. Pollak, E. P. Chicklis, and M. Jiang, "Mid-infrared $ZnGeP_2$ parametric oscillator directly pumped by a pulsed 2 μm Tm-doped fiber laser," Opt. Lett. **33**, 315–7 (2008).

26. C. Kieleck, M. Eichhorn, A. Hirth, D. Faye, and E. Lallier, "High-efficiency 20–50 kHz mid-infrared orientation-patterned GaAs optical parametric oscillator pumped by a 2 μm holmium laser," Opt. Lett. **34**, 262 (2009).

27. C. Kieleck, A. Berrou, B. Donelan, B. Cadier, T. Robin, and M. Eichhorn, "6.5 W $ZnGeP_2$ OPO directly pumped by a Q-switched Tm^{3+}-doped single-oscillator fiber laser," Opt. Lett. **40**, 1101 (2015).

28. M. Gebhardt, C. Gaida, P. Kadwani, A. Sincore, N. Gehlich, C. Jeon, L. Shah, and M. Richardson, "High peak-power mid-infrared $ZnGeP_2$ optical parametric oscillator pumped by a Tm:fiber master oscillator power amplifier system," Opt. Lett. **39**, 1212 (2014).

29. N. Simakov, A. Hemming, S. Bennetts, and J. Haub, "Power scaling of 2 μm sources for frequency conversion into the mid-infrared," in *ACOFT* (2011), pp. 527–529.

30. N. Simakov, A. Davidson, A. Hemming, S. Bennetts, M. Hughes, N. Carmody, P. Davies, and J. Haub, "Mid-infrared generation in $ZnGeP_2$ pumped by a monolithic, power scalable 2-μm source," Proc. SPIE **8237**, 82373K (2012).

31. M. Henriksson, L. Sjöqvist, G. Strömqvist, V. Pasiskevicius, and F. Laurell, "Tandem PPKTP and ZGP OPO for mid-infrared generation," Proc. SPIE **7115**, 71150O–10 (2008).

32. F. Stutzki, F. Jansen, C. Jauregui, J. Limpert, and A. Tünnermann, "24 mJ, 33 W Q-switched Tm-doped fiber laser with near diffraction-limited beam quality," Opt. Lett. **38**, 97 (2013).

33. G. P. Agrawal, *Nonlinear Fiber Optics* (Academic Press, 2001).

34. A. Flores, C. Robin, A. Lanari, and I. Dajani, "Pseudo-random binary sequence phase modulation for narrow linewidth, kilowatt, monolithic fiber amplifiers," Opt. Express **22**, 17735 (2014).

35. C. Robin and I. Dajani, "Acoustically segmented photonic crystal fiber for single-frequency high-power laser applications," Opt. Lett. **36**, 2641 (2011).

36. G. D. Goodno, L. D. Book, and J. E. Rothenberg, "Low-phase-noise, single-frequency, single-mode 608 W thulium fiber amplifier," Opt. Lett. **34**, 1204 (2009).

37. K. Schuster, S. Grimm, A. Kalide, J. Dellith, M. Leich, A. Schwuchow, S. Unger, A. Langner, G. Schötz, and H. Bartelt, "The REPUSIL process and the capability of fluorine doping for the adjustment of optical and thermochemical properties in silica materials," Proc. SPIE **9359**, 935914 (2015).

38. V. N. Philippov, J. K. Sahu, C. A. Codemard, W. A. Clarkson, J.-N. Jang, J. Nilsson, and G. N. Pearson, "All-fiber 1.15-mJ pulsed eye-safe optical source," Proc. SPIE **5335**, 5335–1 (2004).

39. V. Philippov, C. Codemard, Y. Jeong, C. Alegria, J. K. Sahu, J. Nilsson, and G. N. Pearson, "High-energy in-fiber pulse amplification for coherent lidar applications," Opt. Lett. **29**, 2590 (2004).

40. J. C. Jasapara, M. J. Andrejco, A. DeSantolo, A. D. Yablon, Z. Vrallyay, J. W. Nicholson, J. M. Fini, D. J. DiGiovanni, C. Headley, E. Monberg, and F. V. DiMarcello, "Diffraction-Limited Fundamental Mode Operation of Core-Pumped Very-Large-Mode-Area Er Fiber Amplifiers," IEEE J. Sel. Top. Quantum Electron. **15**, 3–11 (2009).

41. J. W. Nicholson, A. DeSantolo, M. F. Yan, P. Wisk, B. Mangan, G. Puc, A. W. Yu, and M. A. Stephen, "High energy, 1572.3 nm pulses for CO_2 LIDAR from a polarization-maintaining, very-large-mode-area, Er-doped fiber amplifier," Opt. Express **24**, 19961 (2016).

42. N. Simakov, A. Hemming, S. Bennetts, and J. Haub, "Efficient, polarised, gain-switched

operation of a Tm-doped fibre laser.," Opt. Express **19**, 14949–54 (2011).

43. S. Hollitt, N. Simakov, A. Hemming, J. Haub, and A. Carter, "A linearly polarised, pulsed Ho-doped fiber laser," Opt. Express **20**, 16285 (2012).

44. M. Jiang and P. Tayebati, "Stable 10 ns, kilowatt peak-power pulse generation from a gain-switched Tm-doped fiber laser," Opt. Lett. **32**, 1797 (2007).

45. J. Swiderski, M. Maciejewska, W. Pichola, J. Kwiatkowski, and M. Mamajek, "Gain-switching pulse generation of a thulium-doped fiber laser pumped at 1550 nm," Proc. SPIE **8702**, 87020L (2013).

46. A. M. Heidt, Zhihong Li, and D. J. Richardson, "High Power Diode-Seeded Fiber Amplifiers at 2 μm: From Architectures to Applications," IEEE J. Sel. Top. Quantum Electron. **20**, 525–536 (2014).

Chapter 7.

Conclusion

7.1 Introduction

Throughout this thesis thulium-doped and holmium-doped fibres have been investigated under a variety of operating conditions. We have characterised sources including high average power, CW laser oscillators, high gain small-signal amplifiers, tuneable and wavelength agile sources as well as high peak power amplifiers. In addition to the laser development, a review of relevant spectroscopic and nonlinear phenomena was performed with a focus on issues relevant to the development of high peak power holmium-doped fibre sources. A compositional optimisation was undertaken with the output being one of the most efficient cladding-pumped holmium-doped fibres reported to date. The following section summarises the achievements of each chapter and discusses possible future areas of research.

7.2 Summary

In Chapter 3 we investigated some of the essential fibre processing techniques that provide an excellent fundamental platform for the construction of the subsequent sources. Indeed, while these processes are essential to achieving single-mode output from a fibre, they are rarely discussed in literature. Furthermore, we have developed cleaving and processing techniques that provide a much better surface control in comparison to conventional approaches. In addition to cleaving, we have also fabricated cladding light stripper devices and demonstrated end-capping techniques which provide robust solutions even at high average power levels.

In Chapter 4 our aim was to develop and optimise the composition of holmium-doped silica fibres. We reviewed the fabrication process and discussed some of the compositional choices as well as analysing impurities we would expect to be significant. Finally a range of fibres were analysed and tested in basic laser configurations. The composition presented here – despite achieving one of the

most efficient reported across the literature – is substantial lower than recent reports [1] which have demonstrated resonantly, core-pumped, holmium-doped fibres operating at 93% of the quantum limit. This high efficiency composition has yet to be transitioned into a cladding-pumped geometry. In addition to improving the efficiency in a core-pumped configuration, we analyse the core:clad ratios required to scale to a cladding-pumped geometry without inducing substantial infrared absorption losses. The most efficient of the developed compositions was then transitioned into a double-clad geometry – an expensive and complicated process when aiming to pump at 2 µm. This fibre is one of the first fluorine-coated, shaped inner cladding fibres demonstrated at the University of Southampton, and is also one of the most efficient cladding-pumped holmium-doped fibres demonstrated operating at 2.1 µm with output powers of 70 W with a 67% slope efficiency with respect to absorbed pump power at 1.95 µm.

In Chapter 5, we investigate the broad spectral coverage offered by thulium-doped and holmium-doped fibres. Various fibres, amplifier designs and components are developed in order to demonstrate high gain amplifiers spanning over an large aggregate wavelength range of 1660 – 2150 nm. This wavelength range is tantalisingly close to the long wavelength band (L-band) at 1625 nm. Indeed from Fig. 2.8 it certainly seems that it is possible to operate a thulium amplifier at 1600 nm. In order to achieve this an inversion of almost 100% is required, furthermore, it is also important to consider the implications and limitations of out-of-band gain. As illustrated in Fig. 2.9, achieving 10 dB gain at 1650 nm will result in 40 dB gain at 1800 nm. Pushing to shorter wavelengths will increase the gain in the 1750 – 1800 nm to the level where parasitic lasing and excess levels of ASE will be generated. In order to mitigate these effects, spectrally dependant losses will need to be introduced – ideally these losses should be distributed along the active fibre rather than lumped losses. In combination with this approach and scaling the core diameter and mode-field diameters, it is expected that thulium amplifiers can be operated at wavelengths as short as 1600 nm.

In addition to relatively simple small-signal amplifiers, we also investigated power scaling and beam quality issues with conventional thulium-doped fibres. A large-pedestal thulium fibre geometry was proposed and demonstrated to operate at 170 W CW output power with a robustly single-mode output. The large pedestal concept ensures that any radiation lost from the fundamental mode does not experience significant gain along the length of the fibre. This laser offers extremely narrow line-width operation which finds application in the pumping of cryogenic holmium-doped gain media [2] and other applications where excellent beam quality, spectral stability and performance

is required. This laser is also essential in future chapters where we pursued a core-pumped approach via a WDM device.

With the ability to build efficient, single-mode, monolithic thulium pump lasers we then constructed several holmium-doped fibre sources. A tuneable cladding-pumped holmium laser is operated at >15 W over the entire 2040 – 2170 nm range. This represents one of the longest wavelength results in silica fibres at power levels exceeding 10 W. This source also operates over an atmospheric transmission window as shown in Fig. 1.2. Acousto-optic tuneable filter components are used to create a wavelength agile holmium source operating from 2040 – 2130 nm and rapid and agile tuning operation was demonstrated. However the source was susceptible to self-pulsation effects. Given the length of the fibres and the build-up times, this resulted in pulses that had duration of the order of 1 µs. In order to reduce the pulse duration, it will be necessary to transition to a different gain medium and a much shorter cavity span. Microchip or semiconductor gain media could offer an exciting alternative to produce a source with wavelength agility and pulse durations of the order of 1-10 ns.

In Chapter 6 our focus shifted to developing fibre pump sources for the pumping of mid-infrared parametric oscillators. We reviewed the requirements on the pump laser which are typically addressed by Q-switched Ho:YAG lasers and conducted a preliminary investigation of a pulsed holmium-doped fibre amplifier system. The output of this source, while impressive, was not suitable for the pumping of an OPO due to severe spectral broadening and so we reviewed the various nonlinear processes and potential mitigation strategies. We implemented as many of these techniques as practical and demonstrated a holmium-doped fibre amplifier geometry that has the desired output characteristics for pumping ZGP optical parametric oscillators. However, we have only made preliminary efforts in this area and the strategies that we have employed can be pushed further. Table 7.1 summarises the further possible scaling opportunities using the mitigation strategies that we have proposed.

Table 7.1: Summary of mitigation strategies employed and possible future directions.

Technique	Description	Effectiveness	Possible further increase
Core-pumped approach	8 m device →2 m device length	4x (increase in thresholds	Increasing dopant concentration without reducing efficiency could allow for another factor of: x2
Mode-field area scaling	18 µm → 37 µm core diameter scaling	4x (increase in thresholds)	Possible another factor of: x4
Master oscillator spectral properties	Multi-longitudinal mode source → Chirped single frequency source	3x reduction in peak power	More accurate chirping or phase modulation of master oscillator. Possibly x1.5
Spectral filtering	Introduce VBG spectral filtering	Difficult to quantify	Distributed spectral filtering to further mitigate MI
Higher-order mode operation	Amplify on a mode that has increased area or different dispersion properties	Not employed	Other groups have demonstrated significant scaling potential [3]

One of the greatest opportunities remains in the spectral filtering aspect. In order to limit the impact of MI, it is necessary to create a loss at ±10-30 nm around the central signal. Potential mechanisms for achieving such a loss may be the use of a slanted FBG along the length of the active fibre, long period gratings or resonant waveguide structures in the fibre. With any mitigation technique it is important to bear in mind that the loss at the carrier should be minimised and that the strength of the loss mechanism should be on the order of 5-10 m^{-1} (see Fig. 6.11).

The strategies employed in the peak power scaling of the holmium-doped fibre amplifier have allowed it to produce an output that is nearly identical to Q-switched Ho:YAG lasers in peak power and spectral density. This is extremely significant in further developing and power scaling mid-infrared sources. To date, the highest average power holmium laser demonstrated has been in fibre [4] and if it is possible to transition this approach to a higher peak power output then that is certainly attractive in many applications.

By examining Table 7.1, there certainly seems to be a potential for a factor of 10x increase in peak power levels from our preliminary demonstration. This would result in a few-ns duration pulse with a peak power of ~0.5 MW while maintaining a bandwidth of <1 nm. Bearing in mind that the scaling is performed with a step-index fibre manufactured using the conventional MCVD technique and is

thus amenable to a mass-production environment. It is expected however that as the core is made increasingly larger in order to scale the MFD of the LP_{01} that thermal effects similar to those observed in a traditional bulk crystalline laser may become prevalent. Identifying where this compromise between the thermal performance of a fibre and the non-linear-free capability of a bulk crystalline geometry is extremely interesting for many applications.

Another possible area of interest is combining the wavelength agility in the pump source for the mid-IR OPO. As shown in Fig. 7.1, the mid-infrared output signal and idler can be tuned across 3100 – 5800 nm as the pump laser is tuned across 2040 – 2110nm. A wavelength agile, high peak power, holmium amplifier could enable rapid access to the entire 3- 6 µm region. In combination with a second AOTF device – potentially internal to the OPO, or perhaps in combination with a QCL, this could enable a narrow band, wavelength agile, power scalable, mid-infrared source.

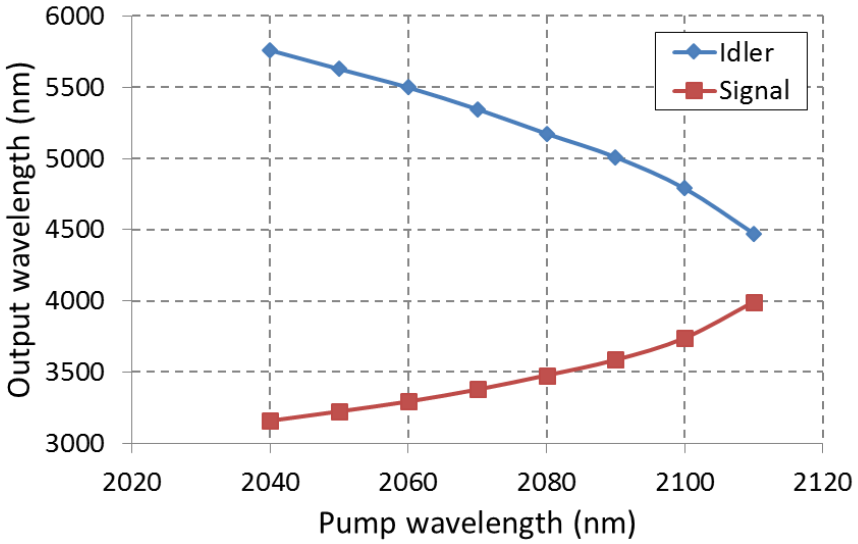

Figure 7.1: Signal and idler wavelengths as a function of pump wavelength for a 55° cut ZGP crystal [5].

Another opportunity lies in the ultrafast regime and the generation of pulses with durations in the 100 fs timescale. Holmium-doped silica can certainly support the bandwidth of a 100 fs pulse – indeed such sources have already been demonstrated [6]. In this region, the MI nonlinear effect becomes less significant and other non-linear phenomena apply. However the mode-area scaling techniques and the core-pumped approach would certainly help reduce the total accumulated non-linear phase and preserve the shape and spectral properties of the pulses. It is expected that such ultrafast sources are also of interest to the community and will be developed as passive components and active fibres become readily available.

During this project, substantial progress has been made in the development of holmium-doped fibres and holmium-doped fibre systems. We have demonstrated numerous world-leading results, improved on conventional processing techniques, assembled a host of amplifiers and sources, and investigated a variety of limiting processes. Despite this, the technology of holmium-doped fibres still remains early in its development – indeed, it has only been 6 years since the demonstration of the first double-clad holmium-doped fibre, and there are huge potentials for further scaling, both in the CW and pulsed regimes.

7.3 References

1. A. Hemming, N. Simakov, M. Oermann, A. Carter, and J. Haub, "Record efficiency of a holmium-doped silica fibre laser," in *Conference on Lasers and Electro-Optics* (OSA, 2016), p. SM3Q.5.

2. N. Simakov, A. Hemming, A. Carter, K. Farley, A. Davidson, N. Carmody, J. M. O. Daniel, M. Hughes, L. Corena, D. Stepanov, and J. Haub, "170 W Single-mode Large Pedestal Thulium-doped Fibre Laser," in *CLEO/Europe Conference on Lasers and Electro-Optics* (Optical Society of America, 2015), p. CJ_13_2.

3. S. Ramachandran, J. M. Fini, M. Mermelstein, J. W. Nicholson, S. Ghalmi, and M. F. Yan, "Ultra-large effective-area, higher-order mode fibers: a new strategy for high-power lasers," Laser Photonics Rev. **2**, 429–448 (2008).

4. A. Hemming, N. Simakov, A. Davidson, S. Bennetts, M. Hughes, N. Carmody, P. Davies, L. Corena, D. Stepanov, J. Haub, R. Swain, and A. Carter, "A monolithic cladding pumped holmium-doped fibre laser," in *Conference on Lasers and Electro-Optics* (2013), p. CW1M.1.

5. A. V. Smith, "SNLO (free version)," http://www.as-photonics.com/snlo.

6. P. Li, A. Ruehl, U. Grosse-Wortmann, and I. Hartl, "Sub-100 fs passively mode-locked holmium-doped fiber oscillator operating at 2.06 μm," Opt. Lett. **39**, 6859 (2014).

Appendix A

List of publications

A.1 Patents (1)

J. M. O. Daniel, W. A. Clarkson, N. Simakov, *"An active optical fibre,"* Publication number WO2016127208 A1 (2015), http://www.google.com/patents/WO2016127208A1?cl=en

A.2 Journal publications (8)

1. J. Daniel, N. Simakov, A. Hemming, W. Clarkson, and J. Haub, *"Metal clad active fibres for power scaling and thermal management at kW power levels,"* Opt. Express 24, 18592-18606 (2016).
2. N. Simakov, Z. Li, Y. Jung, J. Daniel, P. Barua, P. Shardlow, S. Liang, J. Sahu, A. Hemming, W. Clarkson, S. Alam, and D. Richardson, *"High gain holmium-doped fibre amplifiers,"* Opt. Express 24, 13946-13956 (2016).
3. Z. Li, Y. Jung, J. M. O. Daniel, N. Simakov, M. Tokurakawa, P. C. Shardlow, D. Jain, J. K. Sahu, A. M. Heidt, W. A. Clarkson, S. U. Alam, and D. J. Richardson, *"Exploiting the short wavelength gain of silica-based thulium-doped fiber amplifiers,"* Opt. Lett. 41, 2197-2200 (2016)
4. K. Boyd, N. Simakov, A. Hemming, J. Daniel, R. Swain, E. Mies, S. Rees, W. A. Clarkson, and John Haub, *"CO_2 laser-fabricated cladding light strippers for high-power fiber lasers and amplifiers,"* Appl. Opt. 55, 2915-2920 (2016)
5. J. Daniel, N. Simakov, M. Tokurakawa, M. Ibsen, and W. Clarkson, *"Ultra-short wavelength operation of a thulium fibre laser in the 1660-1750 nm wavelength band,"* Opt. Express 23, 18269-18276 (2015).
6. K. Boyd, S. Rees, N. Simakov, J. Daniel, R. Swain, E. Mies, A. Hemming, W. Clarkson, and J. Haub, *"High precision 9.6 µm CO_2 laser end-face processing of optical fibres,"* Opt. Express 23, 15065-15071 (2015).
7. N. Simakov, A. Hemming, W. Clarkson, J. Haub, and A. Carter, *"A cladding-pumped, tunable holmium doped fiber laser,"* Opt. Express 21, 28415-28422 (2013).

8. Z. Li, A. Heidt, N. Simakov, Y. Jung, J. Daniel, S. Alam, and D. Richardson, *"Diode-pumped wideband thulium-doped fiber amplifiers for optical communications in the 1800 – 2050 nm window,"* Opt. Express 21, 26450-26455 (2013).

A.3 Conference presenations and proceedings (18)

1. A. Billaud, P. Shardlow, K. Boyd, N. Simakov, A. Hemming, and W. A. Clarkson, *"Enhanced pump absorption in double-clad fibres using localised laser-machined mode scramblers,"* At 7th EPS-QEOD Europhoton Conference, Vienna, AT, 21 - 26 Aug 2016.
2. J. Daniel, N. Simakov, A. Hemming, W. Clarkson, and J. Haub*, "Metal Coated Active Fibres for High Power and Lightweight Laser Designs,"* in Photonics and Fiber Technology 2016 (ACOFT, BGPP, NP), OSA Technical Digest (online) (Optical Society of America, 2016), paper ATh2C.1.
3. K. Boyd, S. Rees, N. Simakov, J. Daniel, R. swain, E. mies, A. Hemming, W. Clarkson, and J. Haub*, "Precision CO_2 laser processing of optical fibres for rapid contamination free device fabrication,"* in Photonics and Fiber Technology 2016 (ACOFT, BGPP, NP), OSA Technical Digest (online) (Optical Society of America, 2016), paper AW4C.2.
4. M. Ganija, N. Simakov, A. Hemming, C. Pain, J. Mcinnes, J. Haub, P. Veitch, and J. Munch, *"Second Harmonic Generation Using a Monolithic, Linearly Polarized Thulium Doped Fiber Laser,"* in Photonics and Fiber Technology 2016 (ACOFT, BGPP, NP), OSA Technical Digest (online) (Optical Society of America, 2016), paper AW2B.2.
5. Y. Jung, Z. Li, N. Simakov, J. Daniel, D. Jain, P. Shardlow, A. Heidt, J. Sahu, A. Hemming, W. Clarkson, S. Alam, and D. Richardson, *"Silica-Based Thulium Doped Fiber Amplifiers for Wavelengths beyond the L-band,"* in Optical Fiber Communication Conference, OSA Technical Digest (online) (Optical Society of America, 2016), paper M3D.5.
6. K. Boyd, S. Rees, N. Simakov, J. M. O. Daniel, R. Swain, E. Mies, A. Hemming, W. A. Clarkson, J.Haub*, "Advances in CO_2 laser fabrication for high power fibre laser devices,"* Proc. SPIE. 9728, Fiber Lasers XIII: Technology, Systems, and Applications, 972838. (March 11, 2016) doi: 10.1117/12.2210884
7. J. M. O. Daniel, N. Simakov, A. Hemming, W. A. Clarkson, and J. Haub, *"Passively cooled 405 W ytterbium fibre laser utilising a novel metal coated active fibre,"* Proc. SPIE. 9728, Fiber Lasers XIII: Technology, Systems, and Applications, 972808. (March 09, 2016) doi: 10.1117/12.2210887

8. N. Simakov, J. M. O. Daniel, J. Ward, W. A. Clarkson, A. Hemming, and J. Haub, *"Wavelength agile holmium-doped fiber laser,"* Proc. SPIE. 9728, Fiber Lasers XIII: Technology, Systems, and Applications, 97280Q. (March 09, 2016) doi: 10.1117/12.2210880
9. J. Daniel, N. Simakov, A. Hemming, W. Clarkson, and J. Haub, *"Ultra-high Temperature Operation of a Tuneable Ytterbium Fibre Laser,"* in 2015 European Conference on Lasers and Electro-Optics - European Quantum Electronics Conference, (Optical Society of America, 2015), paper CJ_11_6.
10. Z. Li, Y. Jung, J. Daniel, N. Simakov, P. Shardlow, A. Heidt, A. Clarkson, S. Alam, and D. Richardson, *"Extreme Short Wavelength Operation (1.65 - 1.7 μm) of Silica-Based Thulium-Doped Fiber Amplifier,"* in Optical Fiber Communication Conference, OSA Technical Digest (online) (Optical Society of America, 2015), paper Tu2C.1.
11. N. Simakov, Z. Li, S. Alam, P. Shardlow, J. Daniel, D. Jain, J. Sahu, A. Hemming, W. A. Clarkson, and D. J. Richardson, *"Holmium Doped Fiber Amplifier for Optical Communications at 2.05 - 2.13 μm,"* in Optical Fiber Communication Conference, OSA Technical Digest (online) (Optical Society of America, 2015), paper Tu2C.6.
12. J. M. O. Daniel, N. Simakov, A. Hemming, W. A. Clarkson, and J. Haub*, "A double clad ytterbium fibre laser operating at 400°C,"* Proc. SPIE. 9344, Fiber Lasers XII: Technology, Systems, and Applications, 934414. (March 04, 2015) doi: 10.1117/12.2078192
13. N. Simakov, A. Hemming, W. Clarkson, A. Carter, and J. Haub*, "High Power Holmium Fiber Lasers,"* European Conference on Optical Communications 2014, Tu.3.4.1
14. Z. Li, S. Alam, J. Daniel, P. Shardlow, D. Jain, N. Simakov, A. Heidt, Y. Jung, J. K. Sahu, W. A. Clarkson, and D. J. Richardson*, "90 nm Gain Extension Towards 1.7 μm for Diode-Pumped Silica-Based Thulium-Doped Fiber Amplifiers,"* European Conference on Optical Communications 2014, Tu.3.4.2
15. K. Boyd, N. Simakov, J. Daniel, R. Swain, E. Mies, A. Hemming, W. A. Clarkson, and J. Haub, *"Novel Technique for the CO_2 Laser Fabrication of Optical Devices with Sub-Micrometer Ablation Depth Precision,"* European Conference on Optical Communications 2014, P.1.4
16. J. Daniel, N. Simakov, M. Tokurakawa, M. Ibsen, and W. Clarkson, *"Ultra-short wavelength operation of a two-micron thulium fiber laser,"* in CLEO: 2014, OSA Technical Digest (online) (Optical Society of America, 2014), paper SW1N.2.
17. J. Daniel, N. Simakov, P. Shardlow, and W. Clarkson*, "Effect of seed linewidth on few-moded fiber amplifiers,"* in CLEO: 2014, OSA Technical Digest (online) (Optical Society of America, 2014), paper STu2N.7.

18. N. Simakov, A. Hemming, W. Clarkson, A. Carter, and J. Haub, *"Tuneable Operation of Core and Cladding Pumped Holmium Fibre Lasers,"* in 2013 Conference on Lasers and Electro-Optics - International Quantum Electronics Conference, (Optical Society of America, 2013), paper CJ_10_3.